METASTABLE DYNAMICS OF CONVECTION-DIFFUSION-REACTION EQUATIONS

By

Xiaodi Sun

B. Sc. (Computational Mathematics) Nanjing University, P.R. China, 1984

M. Sc. (Numerical Analysis) Nanjing University, P.R. China, 1987

A THESIS SUBMITTED IN PARTIAL FULFILLMENT OF

THE REQUIREMENTS FOR THE DEGREE OF

DOCTOR OF PHILOSOPHY

in

THE FACULTY OF GRADUATE STUDIES

DEPARTMENT OF MATHEMATICS

INSTITUTE OF APPLIED MATHEMATICS

We accept this thesis as conforming

to the required standard

. . . . . .

. . . . . .

. . . . . .

THE UNIVERSITY OF BRITISH COLUMBIA

August 1998

In presenting this thesis in partial fulfillment of the requirements for an advanced degree at the University of British Columbia, I agree that the Library shall make it freely available for reference and study. I further agree that permission for extensive copying of this thesis for scholarly purposes may be granted by the head of my department or by his or her representatives. It is understood that copying or publication of this thesis for financial gain shall not be allowed without my written permission.

Department of Mathematics
Institute of Applied Mathematics
The University of British Columbia
2075 Wesbrook Place
Vancouver, Canada
V6T 1Z1

Date:

Abstract

Metastable dynamics, which qualitatively refers to physical processes that involve an extremely slow approach to their final equilibrium states, is often associated with singularly perturbed convection-diffusion-reaction equations. A problem exhibits metastable behavior when the approach to equilibrium occurs on a time-scale of order $O(e^{\frac{C}{\varepsilon}})$, where $C > 0$ and ε is the singular perturbation parameter. The studies of these mathematical models are not only significant in their own right, but also useful in simulating and explaining observed physical phenomena and exploring possibly certain unknown ones. A typical common characteristic associated with these convection-diffusion-reaction equations is that the linearized operator is exponentially ill-conditioned. By exponential ill-conditioning we mean that the linearized operator has an exponentially small eigenvalue. As a result, conventional analytical methods and numerical schemes may fail to provide accurate information about the metastable behavior.

This thesis is concerned with developing a systematic and robust approach based on asymptotic and numerical methods to quantify the dynamic metastability associated with various problems. Using the asymptotic method called the projection method which was originated by Ward in [108], we have succeeded in deriving ordinary differential equations (ODEs) or differential algebraic equations (DAEs) which characterize the metastable patterns for several problems, including, the phase separation of a binary alloy modeled by the viscous Cahn-Hilliard equation, the upward propagation of a flame front in a vertical channel modeled by the Mikishev-Rakib-Sivashinsky equation, and two problems in slowly varying geometries. The main role of our numerical method called the transverse method of lines is to give a numerical justification of these ODEs/DAEs and to provide

useful information about the metastable solutions in their transient phases and collapse phases during which our asymptotic method fails.

From the numerical point of view, little is known of the nature concerning the convergence and stability of any numerical scheme that computes metastable behavior, as a result of the exponential ill-conditioning of the linearized operator. In this thesis, several finite difference schemes and their convergence are analyzed rigorously for a boundary layer resonance problem. Our results from this problem are shown numerically to be also valid for other nonlinear metastable problems and some guidelines in designing effective numerical schemes are provided.

The analytical and numerical results show that our approach is a powerful and general tool to quantitatively study the metastable patterns in various physical problems. In addition, the metastable behavior revealed by our analysis appears to be also rather interesting from the viewpoint of physical applications.

Table of Contents

List of Tables

List of Figures

Acknowledgements

I would like to express my deepest gratitude to my supervisor, Dr. Michael Ward. His insight into mathematics has opened my mind to a new world and his remarkable ability in applying cutting-edge mathematics to real-world situations has guided me to one of the most interesting topics in the world. In addition, he has always been generous with his time in teaching me how to make a rigorous scientific approach and how to document material and write in English. I am fortunate in having him as a supervisor.

I am greatly indebted to Dr. Uri Ascher for his insightful comments and stimulating discussions about numerical computation and to Dr. Jim Varah, Dr. Greif Chen and Dr. Xiao-Wen Chang for their very helpful advice for solving ill-conditioning problems. My thanks also go to Dr. Anthony Peirce and Dr. Brian Seymour for their interest and input in our committee meetings. The help from Anthony, Jim, Michael and Uri was not limited to the science; they also supported my personal goals.

I acknowledge the University Graduate Fellowship committee and I.W. Killam Trusts for their financial support which made my studies at UBC possible.

Finally, very special thanks to my wife Yanping and my daughter Yuan (Amanda). Without their understanding, support and love this thesis would not have been completed.

Chapter 1

Introduction

The subject of dynamic metastability has recently generated tremendous interest in the mathematical science community and in several areas of application such as in the phase separation of binary alloys, the propagation of flames, the exit problem of a Brownian particle confined by a finite potential well, etc. Metastable dynamics, which refers to physical processes that involve an extremely slow approach to their equilibrium states, is usually associated with particular types of singularly perturbed parabolic partial differential equations. A problem exhibits metastable behavior when the approach to equilibrium occurs on a time-scale of order $O(e^{\frac{C}{\varepsilon}})$, where $C > 0$ and ε is the singular perturbation parameter. Examples of such equations include: the Cahn-Hilliard equation and the constrained Allen-Cahn equation (cf. [24], [22], [91]) modeling the slow phase separation of a binary alloy; a Burger-type equation derived in [85] and [77] for flame-front propagation in a vertical channel; the Kolmogorov's backward equation in the exit problem (cf. [72], [75], [92], [93]); the Gierner Mienhardt equation as an activator-inhibitor model in the mathematical biology (cf. [40], [56]).

There are a few common characteristics associated with these singularly perturbed problems exhibiting dynamical metastability. A typical feature is exponential ill-conditioning, by which we mean that the spectrum of the eigenvalue problem associated with the linearized equation about the steady state solution contains asymptotically exponentially small eigenvalues. As a result of this exponential ill-conditioning, the time-dependent solution approaches its steady state only over an exponentially long time

interval. Moreover, the steady state itself is often extremely sensitive to perturbations of the boundary values and the coefficients in the differential operator. The significance of such eigenvalues was first recognized for certain linear two-point problems involving boundary layer resonance in [1], [31], [60], [67], and later in [3], [14], [61], [87], [111], [112] for the Cahn-Hilliard equation, the Allen-Cahn equation and the viscous shock problem. Another consequence of this exponential ill-conditioning is that a straightforward application of the method of matched asymptotic expansions (MMAE) fails to determine the solution uniquely. Specifically, since a conventional MMAE approach is incapable of resolving the exponentially small terms that are significant for ill-conditioned problems, it typically yields an asymptotic approximation with undetermined constants.

To overcome this deficiency, various modifications of the MMAE approximations have been proposed to treat asymptotically exponentially ill-conditioned problems. A variational principle [44] and its extensions [114] were postulated and used to calculate the leading order asymptotic solutions for certain linear turning point problems exhibiting the phenomena of boundary layer resonance. Explicit matching of crucial exponentially small terms was implemented to find the shock-layer locations for the steady state Burgers equation in [63] and to construct asymptotic expansions of the solutions to several nonlinear boundary value problems in [66]. Another method is applying the nonlinear WKB–type transformation introduced in [86], [87] for the Ginzberg–Landau equation and the viscous shock problem, by which the problems are transformed to well–conditioned steady state problems. In this way, a conventional boundary layer theory or a traditional numerical method can be applied to find the equilibrium solutions. A more powerful technique to resolve this indeterminacy is the projection method that combines the MMAE approach with some information concerning the spectral properties associated with the linearized problem. This method, motivated by the work of deGroen [31], was originally developed by Ward [108] for some reaction-diffusion models and has been successfully

applied to various problems including the one dimensional exit problem in [67], the viscous shock problem in [87] and several phase separation models in [86], [88], [109] and [110]. The projection method has an advantage over other approaches in its adaptability to treat various problems involving indeterminate constants where others may fail to. In addition, using this spectral approach it is possible to derive equations of motion for the internal layers or other structure patterns pertaining to some time-dependent partial differential equations exhibiting metastability.

The characterization of these metastable patterns in various physical models in one spatial dimension has become the subject of much recent research. Metastable behavior for the time-dependent viscous shock problem was first observed numerically in [61], and a quantitative characterization of this exponentially slow dynamics was derived in [64], [65] and [87] by different approaches. The work in [26], [38] and [39] dealt with the unconstrained Allen-Cahn equation in the one-dimensional case and established the exponentially slow motion of the internal layers. The Cahn-Hilliard equation, modeling phase separation, has been studied numerically in [76], [32], [9] and the existence of metastable phase field boundaries has been proved in [3], [17], [15], [43] and [35]. An explicit characterization of metastability for the (constrained) Allen-Cahn equation and the (viscous) Cahn-Hilliard equation can be found in [86], [88] and [109], where the asymptotic projection method is used to obtain the equation of motion for the locations of the internal layers. In a multi-dimensional setting, dynamic metastability for phase separation models that conserve mass can also occur and were discussed in [3], [91] and [110]. In spite of numerous efforts devoted to study metastable dynamics in various physical problems in the past decade, there still remain many interesting problems unexplored, especially in multi-dimensional domains and for systems of reaction-diffusion equations. In addition, even for phase separation models in one spatial dimension, quite a few questions and phenomena require further explanation.

In the rest of this section, we first in §1.1, through studying the Burgers equation for viscous shocks, illustrate some basic characteristics associated with the singularly perturbed problems exhibiting dynamic metastability. Then in §1.2 we outline how the projection method can be used to calculate the undetermined constants occurring in MMAE approximations and to analyze metastable dynamics for time–dependent problems. In §1.3, we propose an algorithm based on the idea of the transverse method of lines (cf. [7]), which will be used to calculate full numerical solutions to the time–dependent singularly perturbed problems studied in this thesis and to compare them with the corresponding asymptotic approximations. Finally, the contribution of this thesis is given in §1.4.

1.1 Burgers Equation for Viscous Shocks

We investigate the following initial–boundary value problem for Burgers equation in the limit $\varepsilon \to 0$:

$$u_t + uu_x = \varepsilon u_{xx}\,, \quad 0 < x < 1\,, \ \ t > 0\,, \tag{1.1a}$$

$$u(x,0) = u_0(x)\,, \quad u(0,t) = \alpha, \quad u(1,t) = -\alpha\,. \tag{1.1b}$$

Here α is a positive constant. In this equation, the term uu_x represents a nonlinear convection or transport term, and εu_{xx} is a Fickian diffusion term. The nonlinear convection term steepens the initial waveform, while the diffusion term attempts to smear out the solution. Thus (1.1) is a balance equation between these two effects. Equation (1.1) was first suggested by Bateman [13] to describe the discontinuous motion of a fluid whose nondimensionalized viscosity ε tends to zero. This equation and its generalizations have subsequently been successfully applied in a number of fields, including turbulence, laminar transonic flow, traffic flow, supersonic flow about an airfoil, biochemistry, etc. (cf. [18], [69], [68], [19] [37] and [52]). The $\pm\alpha$ boundary values were selected so that a

traveling wave solution for (1.1a), connecting $u = \alpha$ and $u = -\alpha$, has zero speed. Consequently, the shock layer solution $u(x,t)$ of the initial–boundary value problem (1.1) converges, in time, to its steady state $u(x,\infty)$ only over exponentially long time. This sluggishness was attributed by [61] to the occurrence of the asymptotically exponentially small principal eigenvalue for the linearized equation about the steady state solution.

We first consider the equilibrium problem of (1.1):

$$\varepsilon u_{xx} - u u_x = 0, \qquad 0 < x < 1, \tag{1.2a}$$

$$u(0) = \alpha, \quad u(1) = -\alpha. \tag{1.2b}$$

This equation has an exact solution $u = u^e$ with an interior shock given by $u^e = -\beta \tanh[\beta\varepsilon^{-1}(x - \frac{1}{2})/2]$, where β satisfies

$$\alpha = \beta \tanh \frac{\beta}{4\varepsilon} . \tag{1.3}$$

Using successive approximation (as in [62]), we can solve (1.3) to obtain

$$\beta = \alpha + 2\alpha e^{-\frac{\alpha}{2\varepsilon}} + O(e^{-\frac{\alpha}{\varepsilon}}) , \qquad \text{as} \quad \varepsilon \to 0 . \tag{1.4}$$

The eigenvalue problem associated with the linearized equation about u^e can be written as

$$\varepsilon \phi_{xx} - (u^e \phi)_x = \lambda \phi, \quad 0 < x < 1 , \tag{1.5a}$$

$$\phi(0) = \phi(1) = 0 . \tag{1.5b}$$

Let λ_0^e denote the first eigenvalue of (1.5). The estimate in [61], based on the Rayleigh quotient, showed that $\lambda_0^e = O(e^{-\frac{C}{\varepsilon}})$ for some constant $C > 0$. More precisely, this eigenvalue has been explicitly calculated in [87] to be

$$\lambda_0^e \sim -2\alpha^2 \varepsilon^{-1} e^{-\alpha\varepsilon^{-1}/2} + \ldots, \quad \text{as} \ \ \varepsilon \to 0 , \tag{1.6}$$

which is exponentially small.

The exponentially ill–conditioning of the linearized problem suggests that the equilibrium solution to (1.2) is rather sensitive to the small changes in the boundary conditions and in the coefficients of the equation. In fact, for problem (1.2a) with the following boundary conditions:

$$u(0) = \alpha - A_l e^{-\alpha\varepsilon^{-1}/2} , \quad u(1) = \alpha + A_r e^{-\alpha\varepsilon^{-1}/2} , \tag{1.7}$$

where A_l and A_r are positive constants, Reyna and Ward [87] showed that the shock layer solution is given asymptotically by $u \sim -\alpha \tanh \frac{\alpha(x-x^*)}{2\varepsilon}$, where x^* is defined by

$$x^* \equiv \frac{1}{2} + \frac{\varepsilon}{\alpha} \log[\gamma + (\gamma^2+1)^{\frac{1}{2}}] , \quad \gamma \equiv (A_r - A_l)/4\alpha . \tag{1.8}$$

This example shows that the exponentially small changes in the boundary conditions result in an $O(\varepsilon)$ change in the location of the shock layer. This property is called "*supersensitivity*" in [62], [64], [64] and [65]. There are other examples in these papers showing the substantial perturbation of the shock layer location x^* resulting from exponentially small changes in the coefficients of the differential equation as well as in the boundary values.

As shown in [61], the speed of approach of the solution $u(x,t)$ of (1.1) to its steady state is determined by the principal eigenvalue λ_0^ε of (1.5). Since λ_0^ε is exponentially small, the solution of (1.1) becomes quasi-stationary and the shock creeps extremely slowly to the equilibrium position once the shock profile has been formed from initial data. Specifically, the dynamical behavior of the solution to the Burgers equation (1.1) can be divided into two different time phases: a transient $O(1)$ phase where a shock layer of width $O(\varepsilon)$, connecting $u = \alpha$ and $u = -\alpha$, is formed from monotone decreasing initial data; and an exponentially slow phase where the shock layer drifts towards its equilibrium location at an exceeding slow rate. This shock layer is closely approximated

by the traveling wave solution of (1.1a):

$$\tilde{u}^{\varepsilon}(x; x_0(t)) \equiv -\alpha \tanh\left(\frac{\alpha(x - x_0(t))}{2\varepsilon}\right) , \quad 0 < x < 1 , \tag{1.9}$$

and its initial location $x_0(0)$ depends on the initial data $u_0(x)$. In Figure 1.1, we plot the solution to the Burgers equation at various times to show these two different phases.

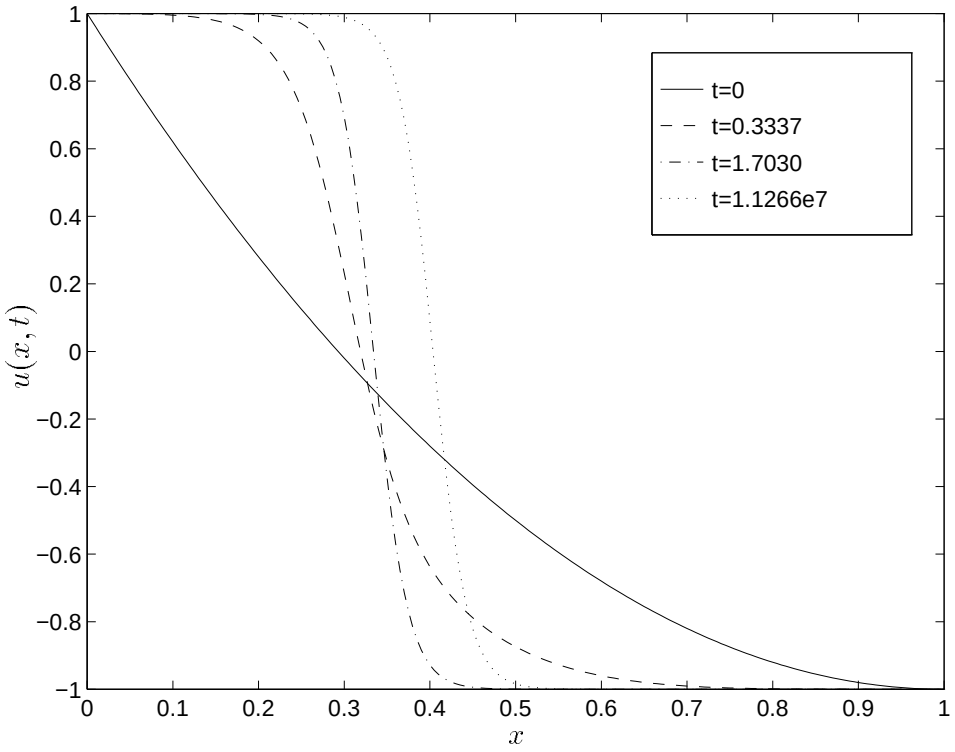

Figure 1.1: The solution to the Burgers equation (1.1) at various times with $\varepsilon = 0.02$ and initial data $u(x, 0) = 2x^2 - 4x + 1$. Notice the slow motion of the shock layer towards the equilibrium solution.

Using the Cole–Hopf transformation (cf. [30] and [49]), by which Burgers equation can be reduced to the initial-boundary value problem for the linear diffusion equation and thus can be solved analytically in closed form, Reyna and Ward [87] wrote the exact solution to (1.1) in terms of the eigenfunctions of the linear diffusion operator and derived the explicit dynamical behavior for (1.1). Specifically, if the initial data $u_0(x)$ satisfies

$u_0(0) = -u_0(1) = -\alpha$ and $u_0'(x) < 0$ for $0 < x < 1$, then, for $\varepsilon \to 0$, the slow motion of the shock layer is described by (1.9) where $x_0(t)$ satisfies

$$\tanh\left(\frac{\alpha(x_0(t) - \frac{1}{2})}{2\varepsilon}\right) = \tanh\left(\frac{\alpha(x_0^0 - \frac{1}{2})}{2\varepsilon}\right) e^{-\frac{t}{t^*}}\ , \tag{1.10}$$

with $t^* \equiv \varepsilon(2\alpha^2)^{-1} e^{\frac{\alpha}{2\varepsilon}}$ and

$$x_0^0 \equiv \frac{1}{2} + \frac{1}{2\alpha}\int_0^1 u_0(x)dx + \frac{\varepsilon^2}{2\alpha^3}[u_0'(1) - u_0'(0)] + \ldots\ , \qquad \text{as} \quad \varepsilon \to 0. \tag{1.11}$$

It is clear from (1.10) that it will take $O(t^*)$ time scale for the shock layer to reach its equilibrium position at $x_0 = \frac{1}{2}$.

Finally, we note that, for $\varepsilon \to 0$, the leading order MMAE solution to (1.2) is given by $u \sim \tilde{u}^\varepsilon(x; x_0)$, where the shock profile $\tilde{u}^\varepsilon(x; x_0)$ satisfies (1.9) and the shock location x_0 is an undetermined parameter. It is obvious that for any $x_0 \in (0, 1)$, with $x_0/\varepsilon \gg 1$ and $(1 - x_0)/\varepsilon \gg 1$, this leading order MMAE solution satisfies (1.2a) exactly and (1.2b) to within exponentially small terms. Therefore, we conclude that the correct value $x_0 = \frac{1}{2}$ can not be determined analytically even after calculating higher order boundary layer corrections near each endpoint. This indeterminacy in x_0 can be eliminated by symmetry considerations, by constructing a higher order MMAE solution accounting for exponentially small terms (cf. [62]) or by the projection method, which we will introduce below.

1.2 The Projection Method

The idea of the projection method was originally introduced by Ward [108] to determine the locations of the internal layer positions for certain nonlinear singularly perturbed boundary value problems. It was later generalized by Ward and his co-workers in [67], [79], [86], [87], [88], [89], [110], [111], [112] to study the metastable dynamics for various classes of time–dependent singularly perturbed problems. The basic idea behind this

method is to supplement the method of matched asymptotic expansions with certain spectral information associated with the linearized equation.

At the outset we illustrate the key elements of the projection method by studying the following system of linear equations

$$A_\varepsilon x = b \ , \tag{1.12}$$

where x and b are N-dimensional vectors and A, depending on a small parameter $\varepsilon > 0$, is an $N \times N$ Hermitian matrix with eigenvalues $\lambda_1 \leq \lambda_2 \leq \ldots \leq \lambda_N$ and corresponding orthonormal eigenvectors $\phi_1, \phi_2, \ldots, \phi_N$. In addition, we assume that the right-hand side b depends on a vector of unknowns, say $\boldsymbol{\alpha} \in R^m$ with $m < N$. Now, let's determine this unknown vector $\boldsymbol{\alpha}$ by assuming some properties of A specified below.

Suppose that A_ε does not have a zero eigenvalue. Then we can expand the solution x in terms of eigenvectors of A_ε:

$$x = \sum_{j=1}^{N} \frac{(b, \phi_j)}{\lambda_j} \phi_j \ , \tag{1.13}$$

where $(b, \phi_j) \equiv b^T \phi_j$. We further assume that the first m eigenvalues $\lambda_1, \ldots, \lambda_m$ are exponentially small as $\varepsilon \to 0$ so that

$$\lambda_j \sim O(\varepsilon^p e^{-\frac{C}{\varepsilon}}) \ , \quad j = 1, \ldots, m \ , \tag{1.14}$$

where $C > 0$ and p are constants independent of ε, and $\lambda_{m+1}, \ldots, \lambda_N$ are bounded away from zero as $\varepsilon \to 0$. Then, for a solution of (1.12) to exist in the limit $\varepsilon \to 0$, we require that as $\varepsilon \to 0$,

$$(b, \phi_j) \to 0 \ , \quad \text{for } j = 1, \ldots, m. \tag{1.15}$$

Setting $(b, \phi_j) = 0$, for $j = 1, \ldots, m$, we obtain a system of algebraic equations for determining the unknown vector $\boldsymbol{\alpha} \in R^m$.

We now apply this technique to resolve the indeterminacy occurring in the conventional MMAE approximations and to derive equations of motion for the shock-like layers or other localized structures pertaining to some evolution equations exhibiting dynamic metastability. Consider the following steady state nonlinear differential equation of the form

$$N_\varepsilon(u) \equiv \varepsilon u_{xx} + F(u, u_x) = 0\,, \quad 0 < x < 1\,, \tag{1.16a}$$

$$B_l u \equiv \varepsilon u_x - \kappa_l(u - u_0) = 0 \quad \text{at } x = 0\,, \tag{1.16b}$$

$$B_r u \equiv \varepsilon u_x + \kappa_r(u - u_1) = 0 \quad \text{at } x = 1\,. \tag{1.16c}$$

Here $\varepsilon \to 0$ is a small parameter, $u_0,\ u_1,\ \kappa_l > 0$ and $\kappa_r > 0$ are constants, and $F(\cdot, \cdot)$ is a nonlinear function. Assume that we can find a MMAE solution $\tilde{u}^\varepsilon[x; \alpha_1, \ldots, \alpha_m]$ to (1.16), which represents an m-parameter family of "approximate" solutions with integer $m \geq 1$ and parameter α_j belonging to some set S_j, so that for each $\alpha_j \in S_j$, $j = 1, \ldots, m$, we have

$$N_\varepsilon(\tilde{u}^\varepsilon) = O(\varepsilon^p e^{-\frac{q}{\varepsilon}})\,, \tag{1.17a}$$

$$B_l\tilde{u}^\varepsilon = O(\varepsilon^{p_0} e^{-\frac{q_0}{\varepsilon}})\,, \quad B_r\tilde{u}^\varepsilon = O(\varepsilon^{p_1} e^{-\frac{q_1}{\varepsilon}})\,, \tag{1.17b}$$

where $p,\ p_0,\ p_1,\ q > 0,\ q_0 > 0$ and $q_1 > 0$ are constants. Then the conventional MMAE does not give a uniquely determined approximation, unless exponentially small terms are taken into account.

To select the correct vector $\boldsymbol{\alpha} \equiv (\alpha_1, \ldots, \alpha_m)^T$ corresponding to a true steady state solution, we linearize (1.16) around $\tilde{u}^\varepsilon$ by writing $u = \tilde{u}^\varepsilon + v$ to get

$$L_\varepsilon v \equiv \varepsilon v_{xx} + F_2(\tilde{u}^\varepsilon, \tilde{u}^\varepsilon_\varepsilon)v_x + F_1(\tilde{u}^\varepsilon, \tilde{u}^\varepsilon_\varepsilon)v = -N_\varepsilon(\tilde{u}^\varepsilon)\,, 0 < x < 1\,, \tag{1.18a}$$

$$B_l v = -B_l\tilde{u}^\varepsilon \quad \text{at } x = 0\,, \quad B_r v = -B_r\tilde{u}^\varepsilon \quad \text{at } x = 1\,, \tag{1.18b}$$

where $F_1(u, v) \equiv \frac{\partial F(u,v)}{\partial u}$ and $F_2(u, v) \equiv \frac{\partial F(u,v)}{\partial v}$. Noting that the differential operator L_ε with homogeneous boundary conditions can always be transformed into a selfadjoint

form using a Liouville transformation in some weighted space ω, we let λ_j and ϕ_j for $j \geq 1$ be the normalized eigenpairs in this space of the associated eigenvalue problem

$$L_\varepsilon \phi = \lambda \phi \,, \quad 0 < x < 1 \,, \qquad B_l u(0) = 0 \,, \quad B_r u(1) = 0 \,. \tag{1.19}$$

Then we write the solution v to (1.18) in terms of the eigenfunctions ϕ_j as $v = \sum_{j=1}^{\infty} \frac{c_j}{\lambda_j} \phi_j$. Here the coefficient c_j can be obtained from (1.18) and the Lagrange's identity as

$$c_j = -(N_\varepsilon(\tilde{u}^\varepsilon), \phi_j)_\omega + \text{B.T. (boundary terms)} \,, \tag{1.20}$$

where the inner product is defined by $(u, v)_\omega \equiv \int_0^1 uv\omega dx$ and B.T. denotes some items depending on the values and/or derivatives of $\tilde{u}^\varepsilon$, ϕ_j and ω at the endpoints.

Let $\tilde{\phi}_j \equiv \frac{\partial}{\partial \alpha_j} \tilde{u}^\varepsilon[x; \alpha_1, \ldots, \alpha_m]$. Then, by differentiating (1.17) with respect to α_j, we get

$$L_\varepsilon \tilde{\phi}_j \;=\; \text{e.s.t. (exponentially small terms)} \,, \quad 0 < x < 1 \,, \tag{1.21a}$$

$$B_l \tilde{\phi}_j \;=\; \text{e.s.t.} \quad \text{at } x = 0, \quad B_r \tilde{\phi}_j = \text{ e.s.t.} \quad \text{at } x = 1 \,. \tag{1.21b}$$

Thus, if these functions $\tilde{\phi}_j$, $j = 1, \ldots, m$, are independent, then (1.21) suggests that (1.19) has m eigenvalues that are exponentially small. Since $L_\varepsilon \tilde{\phi}_j$ is uniformly exponentially small, we have that ϕ_j is proportional to $\tilde{\phi}_j$, except near the endpoints at $x = 0, 1$ where boundary layer corrections must be inserted in order to satisfy the boundary conditions. When the asymptotic approximations of the eigenfunctions ϕ_j , $j = 1, \ldots, m$, are obtained, we can estimate the eigenvalues λ_j, $j = 1, \ldots, m$. If these eigenvalues are shown to be exponentially small and other eigenvalues $\lambda_{m+1}, \ldots, \lambda_N$ are negative and bounded away from zero as $\varepsilon \to 0$, then a necessary condition for the solvability of (1.16) is that $c_j \to 0$ as $\varepsilon \to 0$, $j = 1, \ldots, m$. Setting $c_j = 0$ in (1.20), we obtain a system of nonlinear algebraic equations for determining the unknown parameter vector $\boldsymbol{\alpha}$

$$(N_\varepsilon(\tilde{u}^\varepsilon), \phi_j)_\omega = \text{ B.T. } \,, \quad j = 1, \ldots, m \,. \tag{1.22}$$

We now outline how the projection method can be used to analyze metastability for the time–dependent problem corresponding to (1.16):

$$u_t = \varepsilon u_{xx} + F(u, u_x)\,, \quad 0 < x < 1\,, \tag{1.23a}$$

$$B_l u(0) = 0\,, \quad B_r u(1) = 0\,; \qquad u(x,0) = u_0(x)\,. \tag{1.23b}$$

We seek a solution to (1.23) for $t \gg 1$ in the form

$$u(x,t) = \tilde{u}^{\varepsilon}[x; \alpha_1(t), \ldots, \alpha_m(t)] + v(x,t)\,, \tag{1.24}$$

where $v \ll \tilde{u}^{\varepsilon}$ and $v_t \ll \partial_t \tilde{u}^{\varepsilon}$. Linearizing (1.23) around $\tilde{u}^{\varepsilon}$, we obtain that v satisfies the quasi-steady problem

$$L_{\varepsilon} v = -N_{\varepsilon}(\tilde{u}^{\varepsilon}) + \sum_{j=1}^{m} \alpha_j' \partial_{\alpha_j} \tilde{u}^{\varepsilon}, \qquad 0 < x < 1\,, \tag{1.25a}$$

$$B_l v = -B_l \tilde{u}^{\varepsilon} \quad \text{at } x = 0\,, \qquad B_r v = -B_r \tilde{u}^{\varepsilon} \quad \text{at } x = 1\,. \tag{1.25b}$$

Here $\alpha_j' \equiv d\alpha_j(t)/dt$ and the operator L_{ε} is the same as in (1.18). Applying the similar technique used in studying the equilibrium problem (1.16), we expand v in terms of ϕ_j as $v = \sum_{j=1}^{\infty} \frac{c_j(t)}{\lambda_j} \phi_j$, where

$$c_j(t) = -(N_{\varepsilon}(\tilde{u}^{\varepsilon}), \phi_j)_{\omega} + \text{ B.T. } + \sum_{i=1}^{m} \alpha_i' (\partial_{\alpha_i} \tilde{u}^{\varepsilon}, \phi_j)\,, \quad j = 1, \ldots, m\,. \tag{1.26}$$

Since the eigenvalues $\lambda_j\,, j = 1, \ldots, m$ are assumed to be exponentially small, for a solution of (1.23) to exist in the limit $\varepsilon \to 0$, we require that $c_j \to 0$ as $\varepsilon \to 0$. Then, by letting $c_j = 0$ in (1.26), we get

$$(N_{\varepsilon}(\tilde{u}^{\varepsilon}), \phi_j)_{\omega} = \text{ B.T. } + \sum_{i=1}^{m} \alpha_i' (\partial_{\alpha_i} \tilde{u}^{\varepsilon}, \phi_j)\,, \quad j = 1, \ldots, m\,. \tag{1.27}$$

This is a system of ordinary differential equations (ODEs), from which the dynamics of m parameters $\alpha_1(t), \ldots, \alpha_m(t)$ can be derived.

In summary, the metastable dynamics for (1.23) is characterized by $u \sim \tilde{u}^\varepsilon[x; \alpha_1(t), \ldots, \alpha_m(t)]$, where the quasi-equilibrium $\tilde{u}^\varepsilon$ is the MMAE solution and $\alpha_j(t)$, $j = 1, \ldots, m$ is determined by the system of ODEs (1.27). The equilibrium values α_j^e for $\alpha_j(t)$, $j = 1, \ldots, m$, corresponding to the equilibrium solution for $u(x,t)$, satisfy (1.22) which can also be obtained by setting $\alpha_j' = 0$ in (1.27).

1.3 The Numerical Method TMOL

To verify the ODE system (1.27) and other asymptotic results in the thesis numerically, we need to compute the numerical solutions to the time-dependent singular perturbation problems directly. The numerical algorithm we will use is called the transverse method of lines (TMOL) (cf. [7]) which is applicable to various types of parabolic partial differential equations or systems, especially in one spatial dimension. For illustration purposes, we use the TMOL approach to compute numerical solutions to (1.23).

The TMOL is based on replacing the time derivative in (1.23) by a difference approximation and then solving the resulting boundary value problems in space. More specifically, suppose t_j, for $j = 0, 1, ..$, are the grid points in time that are determined in the actual computation using a time–stepping control strategy. Then, we convert the time–dependent problem (1.23) to a set of boundary value problems using the Backward Differentiation Formulas (BDF) (cf. [7])

$$\sum_{j=0}^{k} \beta_j u_{n-j}(x) = \beta_{n+1} N_\varepsilon u_n(x)\,, \qquad B_l u_n(0) = B_r u_n(1) = 0\,. \tag{1.28}$$

Here $\beta_0 = 1$ and the differential operator N_ε is defined in (1.16a). The other coefficients β_j, for $j > 0$, which depend only on $h_i \equiv t_i - t_{i-1}$, for $i = n, n-1, .., n-k+1$, can be computed numerically using Gaussian elimination in such a way that the BDF scheme (1.28) is k–th order accurate in time.

For every fixed n, (1.28) is a two–point boundary value problem which we solve using COLSYS ([6]). Although this approach is computationally expensive, it yields approximate solutions to (1.23) that are highly accurate in space. Since several time scales may occur in our problem, we found it necessary to implement a time–stepping control strategy to efficiently track the solution to (1.1) over long time intervals. To achieve this, we employed a higher (e. g. , $(k+1)$–th) order BDF scheme at each time step for the purpose of comparison, and used the l_2–norm of the difference between the solutions of the k–th and the $(k+1)$–th order BDF schemes as an error indicator to reject large inaccurate time steps or to enlarge unnecessary small time steps. In all of the calculations below we took $k = 2$.

Comparing the TMOL with the method of lines (MOL) which discretizes a time-dependent PDE in space first and then solves the resulting initial value problem (IVP) in time, we found that the TMOL is easier to implement and is rather accurate for our metastable problems. The numerical computations of various metastable dynamics showed that the global numerical errors are strongly dependent on the discretization errors in spatial variable, whereas they are usually less sensitive to the time discretization. Thus, we consider that a good implementation of a spatial discretization is critically significant for a singular perturbation problem exhibiting metastable dynamics, whose solutions often possess kinds of singularities in space such as internal layers and boundary layers. Fortunately, COLSYS is a well-known effective software to yield a numerical solution adaptively to a boundary value problem within a prescribed precision. Incorporating COLSYS into the TMOL makes it easier to treat various parabolic singular perturbation problems in this thesis. Since our time discretization (2nd order BDF scheme) does not depend on the specific nonlinearity, the major work to compute a new problem is to define the parameters and supply the subroutines required by COLSYS to solve the semi-discretized boundary value problems such as (1.28). On the other hand, if the

MOL is employed to solve the time-dependent PDEs, we will have to pay much attention to constructing the scheme and designing the corresponding mesh individually for each problem considered. This method has another obvious drawback in that the spatial mesh does not change. This means that for our metastable problems having transient regions like a moving shock layer, a fine mesh should be used throughout the whole interval in space. In other words, we do not have the flexibility in treating the spatial variation unless certain moving mesh techniques (cf. [54]) are employed. Moreover, even for problem without internal layer regions, the MOL has a severe limitation of the number of mesh points in space due to the capacity of a computer, if the resulting IVP is to be solved by an IVP software not accounting for the sparse structure of the right-hand side of the IVP. In consequence, we can not guarantee that the numerical results of the MOL are accurate enough to examine the validity of our asymptotic results.

1.4 Contribution of This Thesis

The first goal of the thesis is to further the development and application of the projection method to certain time-dependent singular perturbation problems having metastable dynamics. The problems included in this thesis research fall into three categories: an upwardly propagating flame front in a vertical channel, internal layers in a weakly varying geometry and some phase separation models.

In Chapter 2, we study a Burgers-type equation modeling an upward flame front propagation in a vertical channel. For this problem, it is shown that the principal eigenvalue associated with the linearization around an equilibrium solution corresponding to a parabolic–shaped flame–front interface is exponentially small. This exponentially small eigenvalue then leads to a metastable behavior for the time–dependent problem. This

behavior is studied quantitatively by deriving an asymptotic ordinary differential equation characterizing the slow motion of the tip location of a parabolic–shaped interface. The asymptotic results complement the rigorous, but qualitative, metastability result obtained in [16]. Similar metastability results are obtained for a more generalized Burgers equation. These asymptotic results are shown to compare very favorably with full numerical computations. Most parts of this chapter are taken from the paper [100].

In Chapter 3, the projection method is applied to study two time-dependent singularly perturbed problems related to exponentially slowly varying geometries. The first problem is a Burgers-like convection-diffusion equation which describes one dimensional transonic flow through a nozzle with a weakly variable cross-sectional area. The metastable behavior of the shock waves occurring in the nozzle is studied quantitatively by deriving an asymptotic ODE characterizing the slow motion of the shock layer. From this ODE, we found that a stable steady shock layer may exist in the convergent part of a nozzle, which seems to contradict the previous experimental and analytical result that stable steady shock layers only occur in the divergent parts of a nozzle. The disagreement is explained. The second problem we consider in this chapter is a generalized Ginzburg-Landau(G-L) equation in one dimension, which is employed to determine conditions for the existence of stable spatially-dependent steady state solutions to the Ginzburg Landau equation in several space dimensions. In a convex domain, the Ginzburg-Landau equation $u_t = \varepsilon^2 \triangle u + Q(u)$ with Neumann boundary conditions does not admit stable spatially-dependent steady state solutions. However, this result does not hold for non-convex domains. From the ODE describing the metastable dynamics of this generalized G-L equation, which arises from an asymptotic reduction of a G-L equation in a long, thin, axially symmetric channel, we show that non-constant stable steady solutions to the G-L equation may exist in some non-convex domains. Most parts of this chapter are taken from the paper [101].

In Chapter 4, we consider a viscous Cahn-Hilliard equation in one spatial dimension, from which several phase separation models, including the constrained Allen-Cahn equation, the viscous Cahn-Hilliard equation and the Cahn-Hilliard equation, can be derived by letting a continuation coefficient take on some limiting values. The metastable behavior associated with these phase separation models is quantitatively described by an asymptotic system of differential algebraic equations (DAEs) derived by applying the projection method. Through simplifying this system of DAEs, we identify the differences and similarities of the metastable behavior associated with the various phase separation models and we compare our asymptotic results with some previous results for the metastable dynamics associated with the Cahn-Hilliard equation. Our analysis is verified numerically by solving the original viscous Cahn-Hilliard equation and the asymptotic system of DAEs directly. In addition, a hybrid algorithm based on the asymptotic information and the conservation of mass condition is proposed to model the entire coarsening process associated with the phase separation models. Most parts of this chapter are taken from the paper [102].

From a numerical point of view, it seems that there is an insurmountable obstacle in solving exponentially ill-conditioned singular perturbation problems, say $L_\varepsilon u = f$. More specifically, since $u(x)$ can be exponentially sensitive to all the data in the equation, e.g., $f(x)$, a perturbation $\triangle f$ in $f(x)$ may cause rather large changes in $u(x)$, of the order $O(\lambda_0^{-1} \triangle f)$, where λ_0 (exponentially small) is the principal eigenvalue associated with the linearization operator of L_ε. Thus, one may naturally guess that the numerical truncation error must be less than the order of the principal eigenvalue λ_0 to guarantee the convergence of the numerical method. Based on this conjecture, it seems impractical to treat exponentially ill-conditioned problems by using conventional numerical methods, since λ_0 might be smaller than the machine precision. On the other hand, however, we have noticed that many classical numerical schemes with moderate size meshes have been

successfully applied to obtain approximate solutions to these ill-conditioned problems (cf. [32], [87], [88], [9], [8], [62]). Therefore, the second goal of the thesis is to explain why these classical schemes succeed and shed some light on numerical computation of exponentially ill-conditioned problems by studying the "simplest" linear metastable problem — a boundary layer resonance problem in Chapter 5.

For this resonance problem, bounds for numerical errors for the upwind scheme (cf. [90]), the coupled scheme (cf. [104]) and the Il'in scheme (cf. [5], [55]) are established rigorously. These bounds demonstrate our observations from numerical experiments that although the discrete stability estimate is not valid for a numerical scheme of an exponentially ill-conditioned problem, a truncation error may not result in very large errors in the numerical solution and a scheme may still be uniformly convergent with respect to ε (i.e., the convergence constant does not depend on ε). However, the coefficient matrix of a scheme will usually inherit the ill-conditioning from its continuous problem and consequently, we have to resort to high precision arithmetic to yield a true solution to the scheme. In addition, through solving the time-dependent problem corresponding to the boundary value resonance problem and a steady Allen-Cahn equation numerically, we further believe that the traditional finite difference schemes and other standard numerical methods may also provide accurate approximation solutions to the time-dependent metastable problems and to nonlinear problems exhibiting exponentially ill-conditioning.

Finally, a summary of the major results in this thesis and the potential problems for future research are presented in Chapter 6.

Chapter 2

Metastability in Upward Propagating Flame

2.1 A Generalized Burgers Equation

We now apply the projection method to study the dynamics of an upward propagating flame-front in a vertical channel modeled by a generalized Burgers equation. We begin with an outline of the physical background of this equation.

There are three basic distinct types of phenomena that may be responsible for intrinsic instabilities of premixed flames: body-force effects, hydrodynamic effects and diffusive-thermal effects. Within the framework of a one-dimensional slab geometry (see Figure 2.1), the weakly nonlinear flame interface evolution equation describing the effects of buoyancy under conditions of diffusive-thermal instability of the flame was proposed by Rakib and Sivashinsky [85] as

$$F_t - \frac{1}{2}U_b F_x^2 - \alpha D_{th} F_{xx} - 4D_{th} l_{th}^2 F_{xxxx} = \frac{\gamma g}{2U_b}(F - < F >) \, . \tag{2.1}$$

Here $y = F(x,t)$ is the perturbation of a planar flame front $y = U_b t$; $< F >$ is the space average over the gap between the vertical walls $x = 0$ and $x = L$; U_b is the flame speed related to the burnt gas; g is the acceleration of gravity; $\gamma = (\rho_- - \rho_+)/\rho_-$ is the thermal expansion coefficient of the gas; ρ_- and ρ_+ are the densities of the unburnt and burnt gases, respectively; D_{th} is the thermal diffusivity of the gaseous mixture; l_{th} is the thermal thickness of the flames; $\alpha = \frac{1}{2}\beta(1-Le)-1$ where β is the Zeldovich number and the Lewis number $Le = D_{th}/D_{mol}$ is the ratio of the thermal diffusivity of the mixture to the molecular diffusivity of the deficient reactant.

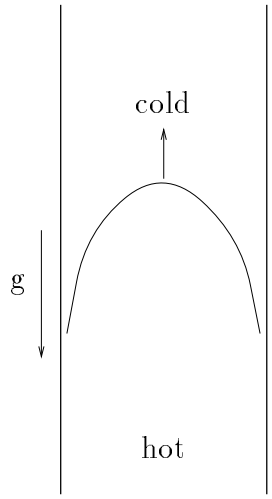

Figure 2.1: Diagram illustrating an upward propagating flame in a vertical channel.

Equation (2.1) covers the whole range of buoyancy and diffusive-thermal effects in the flame and is a rigorous asymptotic equation derived from some equations of aerothermochemistry (cf. [85], [96]). In the absence of the effects for buoyancy, the asymptotic equation (2.1) will reduce to the well known Kuramoto-Sivashinsky equation, i.e., (2.1) with a homogeneous right hand side. In a particular parameter region ($4\pi(2-\gamma)U_b^2/\gamma gL \gg 1$) (cf. [77]), a nonlinear analysis in [96] shows that one can also consider the equation

$$F_t - \frac{1}{2}U_b F_x^2 = D_{th}\left[\frac{1}{2}\beta(1-Le) - 1\right]F_{xx} + \frac{\gamma g}{2U_b}(F - < F >)\,, \tag{2.2}$$

instead of (2.1). This equation was derived within the framework of the Boussinesq model which neglects density variation everywhere except in the external forcing term. Here we assume that the Lewis number Le is large enough to ensure the positive sign of the coefficient of the second derivative. Otherwise, the corresponding evolution problem is ill-posed. Assuming that the walls are thermally insulating, we thus consider the evolution

equation (2.2) subject to the adiabatic boundary conditions

$$F_x(0,t) = F_x(1,t) = 0. \tag{2.3}$$

In terms of certain appropriate dimensionless variables, problems (2.2), (2.3) may be written as

$$y_t - \frac{1}{2}y_x^2 = \varepsilon y_{xx} + y - \int_0^1 y\,dx\,, \qquad 0 < x < 1\,, \quad t > 0\,, \tag{2.4a}$$

$$y_x(0,t) = 0\,, \quad y_x(1,t) = 0\,; \qquad y(x,0) = y_0(x)\,. \tag{2.4b}$$

Here $\varepsilon \equiv 2\alpha D_{th} U_b/\gamma g L^2 > 0$ is a small parameter and the dimensionless variables t and x have been chosen to share the same notations for the corresponding dimensional variables for convenience. Finally, the substitution $u(x,t) = -y_x(x,t)$ leads to the following Burgers type equation

$$u_t + uu_x - u = \varepsilon u_{xx}\,, \quad 0 < x < 1\,, \;\; t > 0\,, \tag{2.5a}$$

$$u(0,t) = u(1,t) = 0\,, \quad u(x,0) = u_0(x)\,. \tag{2.5b}$$

As shown numerically in [77], the solution to (2.4) (or (2.5)), for a certain class of initial conditions relevant to flame–front propagation, exhibits a phenomenon known as dynamic metastability when $\varepsilon \ll 1$. In Figure 2.2 we illustrate this metastable behavior by plotting some numerical results for the shape of the interface $y = y(x,t)$ versus x at four different values of t when $\varepsilon = 0.0115$. In Figure 1a we choose an initial condition where the flame–front assumes a somewhat concave parabolic shape. Then, as shown in Figure 2.2a–c, the tip location $x_0 = x_0(t)$ of the parabola, defined as the location of the maximum value of y at time t, moves towards the channel wall at $x = 0$ rather slowly. For other initial conditions, the tip of this interface can move slowly towards the other wall at $x = 1$. When ε is decreased, this stage of the motion, whereby the tip of the

parabolic flame–front moves towards one of the walls, becomes exceedingly slower than in Figure 2.2a–c. In [16] it was proved that this motion is asymptotically exponentially slow as $\varepsilon \to 0$. Finally, when the tip of the interface comes close enough to the wall, the rate of evolution of the flame–front increases and a final equilibrium state is attained when the tip touches the wall (see Figure 2.2c–d).

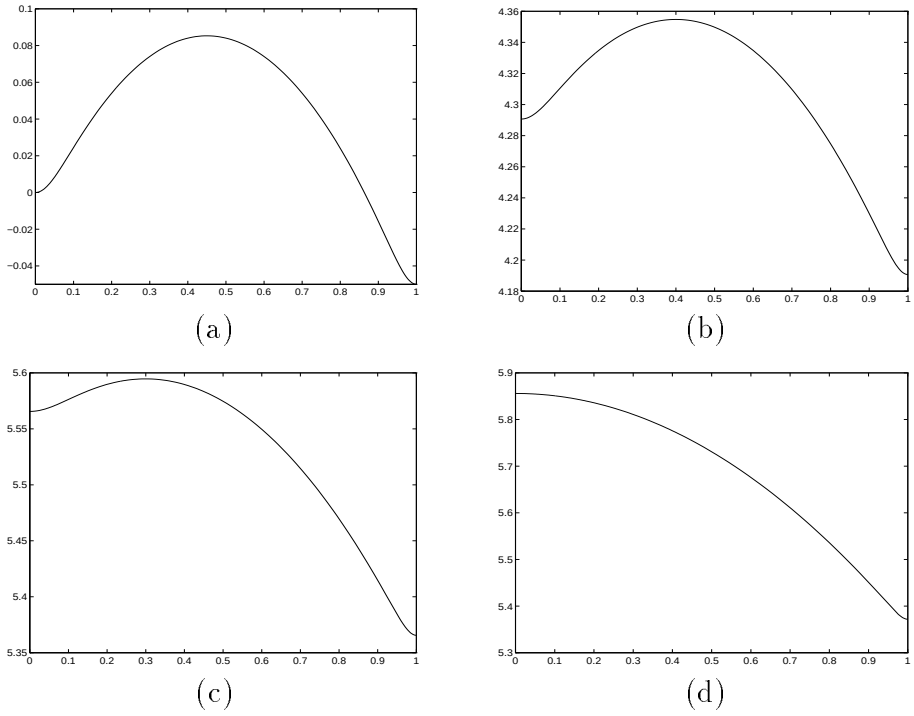

Figure 2.2: Plot of $y(x,t)$ versus x with $\varepsilon = .0115$ obtained from (2.84). (a) initial quasi–equilibrium solution $y(x,t)$ with tip location $x_0 = 0.45$ at $t = 0$; (b) quasi–equilibrium solution with $x_0 = 0.4$ at $t = 90.05$; (c) quasi–equilibrium solution with $x_0 = 0.3$ at $t = 113.69$; (d) final stable equilibrium solution at $t \geq 117.07$.

For the equilibrium problem, it was shown in [16] that (2.5) admits multiple equilibrium solutions when $\varepsilon \ll 1$. In particular, there exists a unique positive equilibrium U_ε^+ and a unique negative equilibrium U_ε^-. These solutions were found to be linearly stable. In addition, for $\varepsilon \ll 1$, it was shown that (2.5) has two unstable equilibrium solutions $U_{\varepsilon,1}^+$ and $U_{\varepsilon,1}^-$, which each have exactly one zero–crossing in the interval $(0,1)$.

Other equilibrium solutions with more than one zero–crossing are also possible. The stability of these equilibrium solutions with more than one zero–crossing and the associated time–dependent solutions were studied in [41]. In Figure 2.3 we plot the four equilibrium solutions U_ε^+, U_ε^-, $U_{\varepsilon,1}^+$ and $U_{\varepsilon,1}^-$ when $\varepsilon = 0.005$. From this figure we observe that U_ε^+ and U_ε^- have boundary layers of width $O(\varepsilon)$ near one of the endpoints, $U_{\varepsilon,1}^+$ has an internal layer of width $O(\varepsilon)$ near $x = 1/2$, and $U_{\varepsilon,1}^-$ has an $O(\varepsilon)$ boundary layer near each endpoint. Among these solutions, $U_{\varepsilon,1}^-$ corresponds to a concave parabolic–shaped equilibrium flame–front interface. We show that the linearization of (2.5) around $U_{\varepsilon,1}^-$ has an exponentially small principal eigenvalue as $\varepsilon \to 0$. Thus, it is this equilibrium solution that is the most significant for the occurrence of metastable behavior for the time–dependent problem.

For the time–dependent problem, our numerical computations and the results in [77] and [16] suggest that the occurrence of metastable behavior for (2.5) strongly depends on the initial condition. In particular, from [16], a sufficient condition as $\varepsilon \to 0$ for metastable flame-front dynamics for (2.5) (or equivalently (2.4)) is that the initial data $u_0(x)$ satisfies

$$u_0(x) < 0 \quad \text{for} \quad x \in (0, a)\,, \qquad \text{and} \qquad u_0(x) > 0 \quad \text{for} \quad x \in (a, 1)\,, \tag{2.6}$$

where $a > 0$. For other cases, our numerical computations suggest that a stable equilibrium configuration can usually be attained in an $O(1)$ time interval. In Figure 2.4–2.6 we illustrate the dynamics of the solution u to (2.5) for various initial conditions. Only in Figure 2.4, where the initial data satisfies (2.6), is an exponentially slow motion observed.

Therefore, when the initial data satisfies (2.6) and when $\varepsilon \ll 1$, we have three different time behaviors under (2.4): a transient $O(1)$ phase where the parabolic–shaped flame–front interface is formed; an exponentially slow phase where the tip of the parabolic

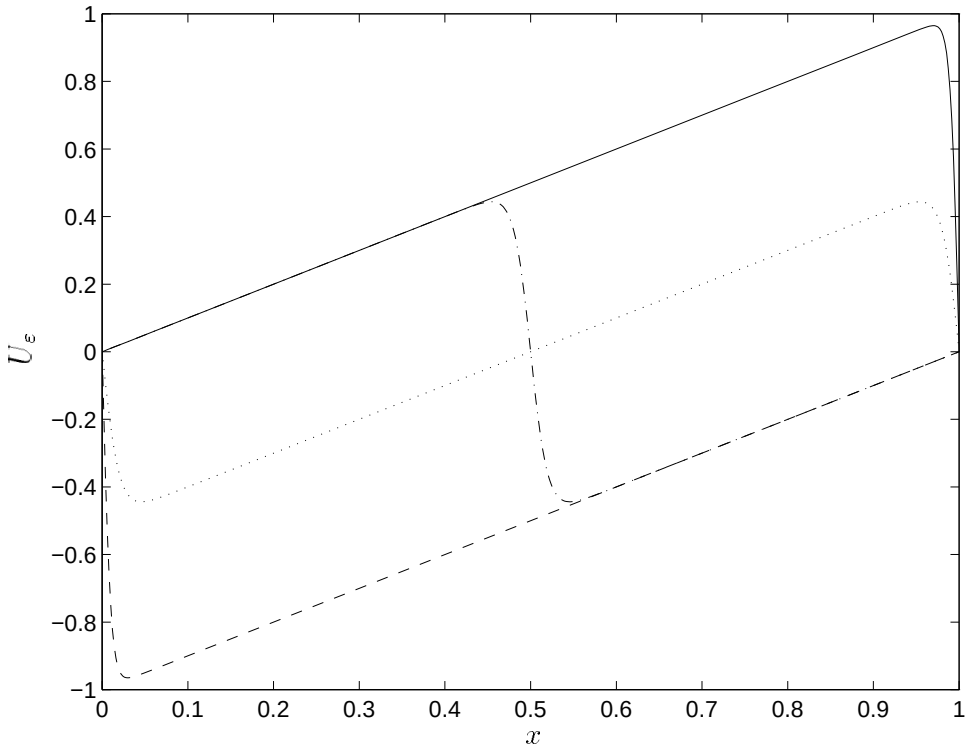

Figure 2.3: Plots of four equilibrium solutions $U(x)$ versus x for (2.5) with $\varepsilon = 0.005$. The solid line and the dashed line represent the positive equilibrium solution U_ε^+ and the negative equilibrium solution U_ε^-, respectively. The dotted line and the dash–dotted line show two unstable equilibrium solutions $U_{\varepsilon,1}^-$ and $U_{\varepsilon,1}^+$. The solution $U_{\varepsilon,1}^-$ is closely related to the metastable parabolic–shaped flame front.

flame–front drifts towards one of the walls; an $O(1)$ collapse phase where the flame-front collapses against the wall and attains its equilibrium configuration. In terms of $u(x,t)$, the first two phases are clearly seen in Figure 2.4. The fact that the time interval corresponding to the second phase may become exceptionally long when ε is small creates an illusion that the flame–front has reached some final equilibrium. However, this phase is merely a quasi–equilibrium transient phase that persists for an exponentially long time interval. If the initial data has several interior zeros, then we would expect that shock layers would quickly be formed with each shock layer connecting two adjacent segments

where u is roughly linear in x. Numerical computations, which we do not give, show that in certain cases metastable patterns may happen.

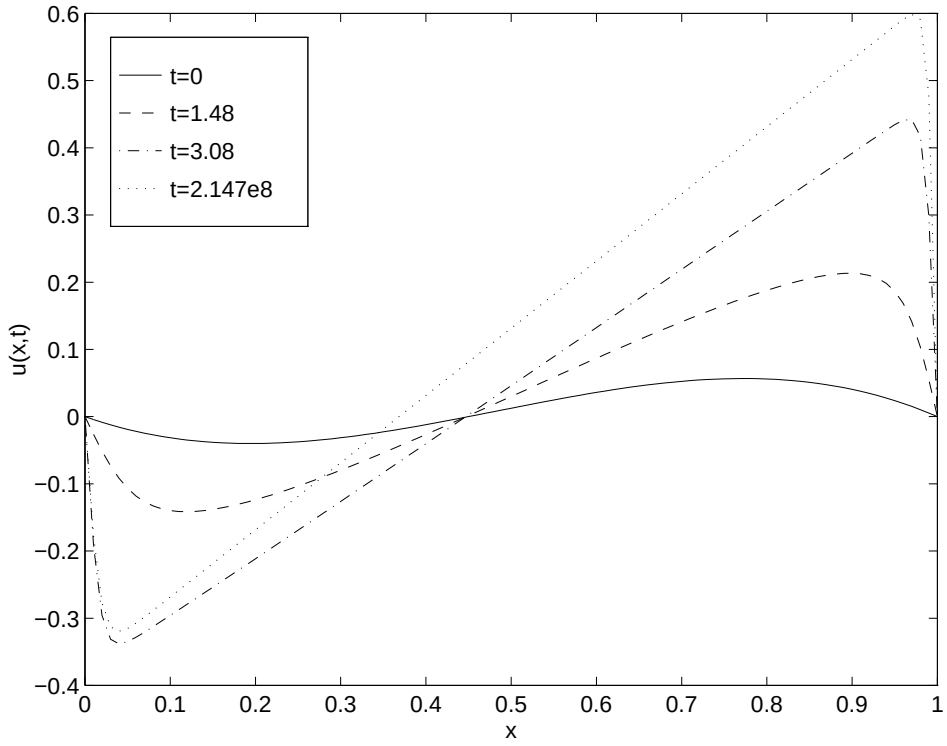

Figure 2.4: Plot of the solution to (2.5) at various times with $\varepsilon = 0.003$, $x_0^0 = 0.45$, and initial data $u(x,0) = x(1-x)(x-x_0^0)$. Notice that the zero of u, which is the tip of the parabolic flame-front interface, moves slowly towards the wall at $x = 0$.

One of our objectives is to use the projection method to give an explicit asymptotic characterization of metastable flame–front motion for (2.4), (2.5) in the limit $\varepsilon \to 0$. The asymptotic results complement the rigorous, but qualitative, metastability result obtained in [16]. Using the method of matched asymptotic expansions, a quasi-steady concave parabolic–shaped flame–front interface for (2.4) can be expressed in terms of $u(x,t)$ as $u(x,t) \sim \tilde{u}^{\varepsilon}[x; x_0(t)]$, where

$$\tilde{u}^{\varepsilon}[x; x_0] \equiv x - x_0 + u_l\left[\varepsilon^{-1}x; x_0\right] + u_r\left[\varepsilon^{-1}(1-x); x_0\right] . \tag{2.7}$$

Here $u_l(y; x_0)$ and $u_r(y; x_0)$ are boundary layer functions that tend to zero exponentially

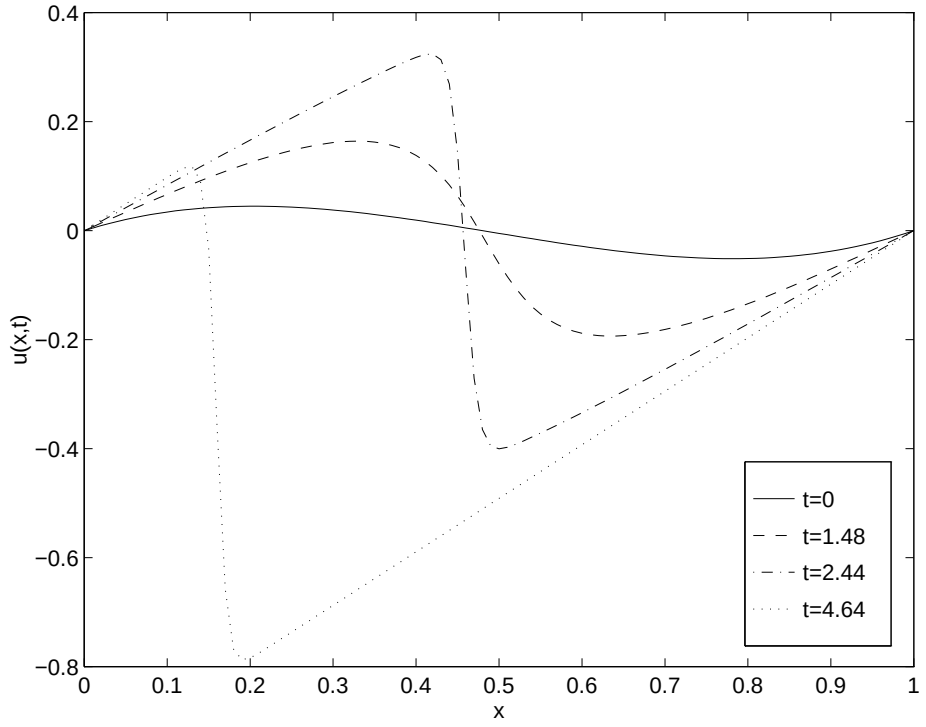

Figure 2.5: Plot of the solution to (2.5) at various times with $\varepsilon = 0.003$, $x_0^0 = 0.48$, and initial data $u(x,0) = -x(1-x)(x-x_0^0)$. A shock-layer is formed in an $O(1)$ time interval and no metastable behavior is observed.

as $y \to \infty$, and the unknown x_0 satisfies $x_0 \in (0,1)$. Thus, to within exponentially small terms, x_0 is the zero of u. Since $y_x = -u$, it follows that $x_0 = x_0(t)$ also represents the trajectory of the tip of the parabolic–shaped flame–front interface for (2.4). For a fixed x_0 satisfying $x_0 \in (0,1)$, we show below that the principal eigenvalue associated with the linearization of (2.5) around $\tilde{u}^\varepsilon$ is exponentially small and has the asymptotic estimate

$$\lambda_0 \sim \frac{1}{\varepsilon}\left[x_0\left(x_0 - c\varepsilon^{1/2}\right)e^{-x_0^2/2\varepsilon} + (1-x_0)\left((1-x_0) - c\varepsilon^{1/2}\right)e^{-(1-x_0)^2/2\varepsilon}\right], \qquad (2.8)$$

as $\varepsilon \to 0$, where $c = (8/\pi)^{1/2}$. This eigenvalue is responsible for the metastable behavior.

For the time–dependent problem, we use the projection method to derive an asymptotic ordinary differential equation for $x_0(t)$, which explicitly characterizes the metastable

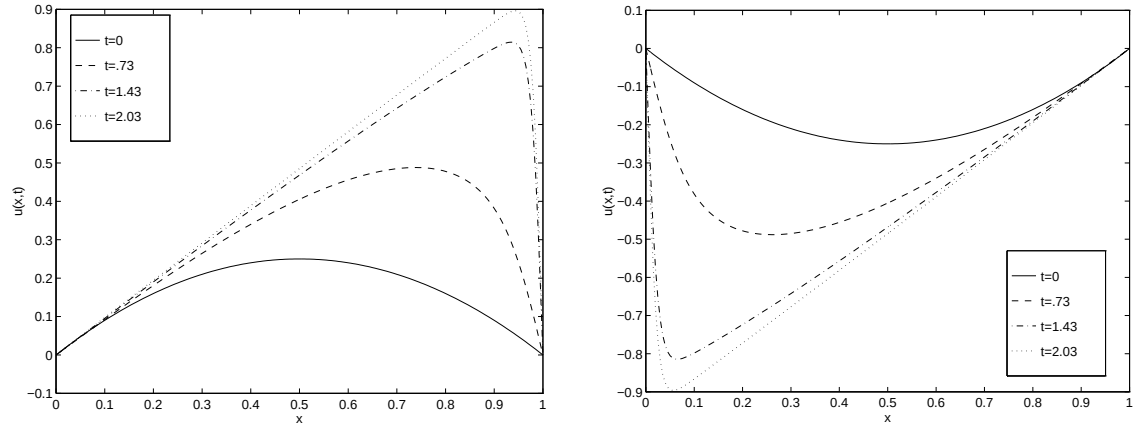

Figure 2.6: Plots of the solutions to (2.5) at various times with $\varepsilon = 0.01$ and initial data $u(x,0) = x(1-x)$, (left figure) and $u(x,0) = -x(1-x)$, (right figure). Metastable behavior does not occur for these initial data.

flame–front motion. This method is based on a quasi-steady linearization of (2.5) around $\tilde{u}^\varepsilon$ given in (2.7). Since λ_0 is exponentially small, a limiting solvability condition must hold in the limit $\varepsilon \to 0$ for the linearized problem. From this condition, we will derive that $x_0(t)$ satisfies

$$x_0' \sim \sqrt{\frac{2}{\pi\varepsilon}} \left[\left((1-x_0)^2 + \frac{\pi^2\varepsilon}{3} \right) e^{-(1-x_0)^2/2\varepsilon} - (x_0^2 + \frac{\pi^2\varepsilon}{3}) e^{-x_0^2/2\varepsilon} \right] . \tag{2.9}$$

Rather than focusing exclusively on (2.5), we instead analyze the following generalized form of (2.5):

$$u_t + f'(u)u_x - f'(u) = \varepsilon u_{xx}, \qquad 0 < x < 1, \quad t > 0, \tag{2.10a}$$

$$u(0,t) = u(1,t) = 0; \quad u(x,0) = u_0(x)\,. \tag{2.10b}$$

Here $f(u)$ is smooth, convex, and satisfies $f(0) = f'(0) = 0$. The special case $f(u) = u^2/2$ yields (2.5). This generalized problem exhibits a very similar metastable behavior as that for (2.5) and is no more difficult to analyze.

The chapter is organized as follows. In §2.2, we construct an asymptotic expansion for a certain equilibrium solution of (2.10) and we outline an application of the projection

method to (2.10). In §2.3 we derive a two–term asymptotic expansion for the principal eigenvalue λ_0 associated with the corresponding linearized problem and we compare this expansion with full numerical results for λ_0. In §2.4, the asymptotic projection method is used to derive an ordinary differential equation characterizing the metastability in (2.10). The results are then applied to the special case $f(u) = u^2/2$, and we show how to recover the flame–front interface $y(x,t)$ satisfying (2.4). In §2.5, we use a full numerical method to compute metastable behavior for (2.10). The numerical results are found to compare very favorably with the corresponding asymptotic results in §2.4.

2.2 The Equilibrium Problem

We first consider the equilibrium problem for (2.10) in the limit $\varepsilon \to 0$

$$\varepsilon u_{xx} - f'(u)u_x + f'(u) = 0, \qquad 0 < x < 1\,, \tag{2.11a}$$

$$u(0) = 0\,, \quad u(1) = 0\,. \tag{2.11b}$$

Here $f(u)$ is smooth, convex, and satisfies $f(0) = f'(0) = 0$. This problem admits multiple equilibria. However, we will only construct a solution to (2.11) having the form given in (2.7), since it is this solution that is closely related to metastable behavior in the corresponding time–dependent problem.

The outer approximation for this solution is clearly $u \sim x - x_0$ for some $x_0 \in (0,1)$. This outer solution satisfies the differential equation (2.11a) exactly, but not the boundary conditions (2.11b). Therefore, there are boundary layers near the end points $x = 0$ and $x = 1$. In the boundary layer near $x = 0$ we let $y = \varepsilon^{-1}x$ and $u_l(y) = u(\varepsilon y)$, and we expand

$$u_l(y) = -x_0 + u_{l_0}(y) + \varepsilon[y + u_{l_1}(y)] + \cdots\,. \tag{2.12}$$

Substituting (2.12) into (2.11), collecting powers of ε, and matching to the outer solution,

we obtain

$$u''_{l_0} - f'(-x_0 + u_{l_0})u'_{l_0} = 0\,, \qquad 0 < y < \infty\,, \tag{2.13a}$$

$$u_{l_0}(0) = x_0\,, \qquad u_{l_0}(y) \sim a_{l_0} e^{-\nu_l y} \quad \text{as} \quad y \to \infty\,, \tag{2.13b}$$

and

$$u''_{l_1} - [f'(-x_0 + u_{l_0})u_{l_1}]' = y f''(-x_0 + u_{l_0})u'_{l_0}\,, \qquad 0 < y < \infty\,, \tag{2.14a}$$

$$u_{l_1}(0) = 0\,, \qquad u_{l_1}(y) \sim a_{l_1} y^2 e^{-\nu_l y} + b_{l_1} y e^{-\nu_l y} \quad \text{as} \quad y \to \infty\,. \tag{2.14b}$$

Here $a_{l_1} = f''(-x_0)a_{l_0}/2$ and $b_{l_1} = 2a_{l_1}/\nu_l$. Upon integrating (2.13), we find that the positive constants ν_l and a_{l_0} are given by

$$\nu_l = -f'(-x_0)\,, \tag{2.15a}$$

$$\log a_{l_0} = \log x_0 - \nu_l \int_{-x_0}^{0} \left[\frac{1}{f(s) - f(-x_0)} - \frac{1}{f'(-x_0)(s + x_0)} \right] ds\,. \tag{2.15b}$$

The asymptotic form in (2.14b) is obtained from (2.14a) by using the far-field behavior of $u_{l_0}(y)$ as $y \to \infty$. By integrating (2.13) we obtain the equivalent first order equation

$$u'_{l_0} = f(u_{l_0} - x_0) - f(-x_0)\,, \quad u_{l_0}(0) = x_0\,, \quad \text{with} \quad u'_{l_0}(0) = -f(-x_0)\,. \tag{2.16}$$

Similarly, in the boundary layer near $x = 1$ we let $y = \varepsilon^{-1}(1-x)$ and $u_r(y) = u(1-\varepsilon y)$, and we expand

$$u_r(y) = 1 - x_0 + u_{r_0}(y) + \varepsilon[u_{r_1}(y) - y] + \cdots\,. \tag{2.17}$$

From (2.17) and (2.11) we obtain the boundary layer equation

$$u''_{r_0} + f'(1 - x_0 + u_{r_0})u'_{r_0} = 0\,, \qquad 0 < y < \infty\,, \tag{2.18a}$$

$$u_{r_0}(0) = x_0 - 1 < 0\,, \qquad u_{r_0}(y) \sim -a_{r_0} e^{-\nu_r y} \quad \text{as} \quad y \to \infty\,. \tag{2.18b}$$

A similar equation holds for u_{r_1}. Here a_{r0} and ν_r are defined by

$$\nu_r = f'(1-x_0), \tag{2.19a}$$

$$\log a_{r_0} = \log(1-x_0) + \nu_r \int_0^{1-x_0} \left[\frac{1}{f(1-x_0)-f(s)} + \frac{1}{f'(1-x_0)(s-1+x_0)} \right] ds. \tag{2.19b}$$

Consider the left boundary layer expansion (2.12). Using the asymptotic behavior of u_{l_0} and u_{l_1} as $y \to \infty$, we observe that (2.12) becomes disordered (i.e., $\varepsilon u_{l_1} \ll u_{l_0}$ does not hold) as $y \to \infty$ when $\varepsilon y^2 = O(1)$ or, equivalently, when $x = O(\varepsilon^{1/2})$. Thus, (2.12) holds on the interval $y = O(\varepsilon^q)$, where $-\frac{1}{2} < q \leq 0$. A similar comment can be made for the boundary layer expansion (2.17) near $x = 1$. This observation is used in §2.3 and §2.4 to help evaluate certain integrals asymptotically.

A composite expansion for this equilibrium solution, valid for $x \in [0,1]$, is obtained by combining (2.12) and (2.17). This yields,

$$u \sim \tilde{u}^{\varepsilon}[x;x_0] \equiv x - x_0 + u_{l_0}[\varepsilon^{-1}x;x_0] + u_{r_0}[\varepsilon^{-1}(1-x);x_0] + \cdots . \tag{2.20}$$

Here u_{l_0} and u_{r0} satisfy (2.13) and (2.18), respectively. In (2.20), we have emphasized the parametric dependence of u_{l0}, u_{r0} and $\tilde{u}^{\varepsilon}$ on the unknown constant x_0, which satisfies $0 < x_0 < 1$. When $f(u) = u^2/2$, this constant represents the tip of the equilibrium parabolic–shaped flame–front interface. The difficulty in analytically determining the correct value for x_0 still persists even after calculating higher order boundary layer corrections near each endpoint. By symmetry, when $f(u)$ is even, the correct value is clearly $x_0 = 1/2$. However, to determine x_0 analytically for general $f(u)$ we must retain exponentially small terms in the asymptotic expansion of the solution. One way to do this is to use the projection method as shown below.

2.2.1 An Application of the Projection Method

We now outline how this method can be used to determine the equilibrium value for x_0 in (2.20) and to analyze metastability for the time–dependent problem (2.10). To analyze metastable behavior for (2.10), we seek a solution to (2.10) for $t \gg 1$ in the form

$$u(x,t) = \tilde{u}^{\varepsilon}[x; x_0(t)] + v(x,t)\,, \tag{2.21}$$

where $v \ll \tilde{u}^{\varepsilon}$ and $v_t \ll \partial_t \tilde{u}^{\varepsilon}$. Linearizing (2.10) around $\tilde{u}^{\varepsilon}$, we obtain that v satisfies the quasi-steady problem

$$L_{\varepsilon} v = -R + x_0' \partial_{x_0} \tilde{u}^{\varepsilon}\,, \qquad 0 < x < 1\,, \tag{2.22a}$$

$$v(0,t) = -\tilde{u}^{\varepsilon}(0; x_0)\,, \quad v(1,t) = -\tilde{u}^{\varepsilon}(1; x_0)\,. \tag{2.22b}$$

Here the operator L_{ε} and the residual $R = R(x; x_0)$ are defined by

$$L_{\varepsilon} v \equiv \varepsilon v_{xx} - [f'(\tilde{u}^{\varepsilon}) v]_x + v f''(\tilde{u}^{\varepsilon})\,, \tag{2.23a}$$

$$R \equiv \varepsilon \tilde{u}^{\varepsilon}_{xx} - f'(\tilde{u}^{\varepsilon}) \tilde{u}^{\varepsilon}_x + f'(\tilde{u}^{\varepsilon})\,. \tag{2.23b}$$

Now consider the homogeneous operator L_{ε} where x_0 is a parameter. Let λ_j, ϕ_j for $j \geq 0$ be the normalized eigenpairs of the associated eigenvalue problem

$$L_{\varepsilon} \phi = \lambda \phi\,, \qquad 0 < x < 1\,; \qquad \phi(0) = \phi(1) = 0\,. \tag{2.24}$$

The λ_j are real and the ϕ_j satisfy the orthogonality relations

$$(\phi_j, \phi_k)_{\omega} = \delta_{jk}, \quad j,k = 0, 1, \ldots\,. \tag{2.25}$$

Here the inner product is defined by $(u,v)_{\omega} \equiv \int_0^1 uv\omega\, dx$, where the weight function $\omega = \omega(x)$ is given by

$$\omega(x) \equiv \exp\left(-\varepsilon^{-1} \int_{x_0}^{x} f'\left[\tilde{u}^{\varepsilon}(z; x_0)\right]\, dz \right)\,. \tag{2.26}$$

Upon integrating by parts, we obtain Lagrange's identity for any two smooth functions v and ϕ,

$$(\phi, L_\varepsilon v)_\omega = (\varepsilon\phi\omega v_x - \varepsilon\phi_x\omega v)\Big|_0^1 + (L_\varepsilon\phi, v)_\omega \ . \tag{2.27}$$

Next, we expand the solution v to (2.22) in terms of the eigenfunctions ϕ_j as

$$v = \sum_{j=0}^{\infty} \frac{c_j}{\lambda_j}\phi_j \ . \tag{2.28}$$

The coefficients c_j, obtained from (2.22) and (2.27) are

$$c_j = -\varepsilon\phi_{jx}\omega\tilde{u}^\varepsilon\Big|_0^1 - (R, \phi_j)_\omega + x_0'\,(\partial_{x_0}\tilde{u}^\varepsilon, \phi_j)_\omega \ . \tag{2.29}$$

As shown in §2.3, the severe indeterminacy in selecting the correct x_0 for the equilibrium problem results in an exponentially small principal eigenvalue for (2.24). Since $L_\varepsilon[\partial_{x_0}\tilde{u}^\varepsilon]$ is uniformly small on $[0,1]$ and $\partial_{x_0}\tilde{u}^\varepsilon$ is of one sign, this suggests that ϕ_0 is proportional to $\partial_{x_0}\tilde{u}^\varepsilon$. Since $\lambda_0 \to 0$ as $\varepsilon \to 0$, a necessary condition for the solvability of (2.22) is that $c_0 \to 0$ as $\varepsilon \to 0$. Setting $c_0 = 0$ in (2.29) we obtain an asymptotic differential equation for $x_0 = x_0(t)$:

$$x_0'\,(\phi_0, \partial_{x_0}\tilde{u}^\varepsilon)_\omega = (R, \phi_0)_\omega + \varepsilon\phi_{0x}\omega\tilde{u}^\varepsilon\Big|_0^1 \ . \tag{2.30}$$

This differential equation will be valid for time intervals over which $x_0 \gg O(\varepsilon)$ and $1 - x_0 \gg O(\varepsilon)$ (i.e., away from the endpoints). The metastable dynamics for (2.10) is then characterized by $u(x,t) \sim \tilde{u}^\varepsilon[x; x_0(t)]$, where $\tilde{u}^\varepsilon$ is defined in (2.20). The equilibrium value for x_0, corresponding to the equilibrium solution for u, is obtained by setting $x_0' = 0$ in (2.30), which yields the algebraic condition

$$(R, \phi_0)_\omega = -\varepsilon\phi_{0x}\omega\tilde{u}^\varepsilon\Big|_0^1 \ . \tag{2.31}$$

In §2.3 we will estimate ϕ_0 and λ_0 as $\varepsilon \to 0$, and in §2.4 we will evaluate the inner products in (2.30) and (2.31) asymptotically. These calculations allow us to explicitly determine the equilibrium value for x_0 from (2.31) and the form of the ODE for $x_0(t)$ in (2.30).

2.3 Asymptotics and Numerics for the Principal Eigenpair

We now estimate the principal eigenpair λ_0, ϕ_0 for (2.24). Let $\tilde{\phi}_0$ be a trial function for ϕ_0. Then, from Lagrange's identity (2.27), we get

$$\lambda_0 \left(\tilde{\phi}_0, \phi_0\right)_\omega = \left(L_\varepsilon \tilde{\phi}_0, \phi_0\right)_\omega + \varepsilon \phi_{0x} \omega \tilde{\phi}_0 \Big|_0^1 . \tag{2.32}$$

To a get a very rough estimate for λ_0 take $\tilde{\phi}_0 = 1$ for which $L_\varepsilon 1$ is exponentially small for $O(\varepsilon) \ll x \ll 1 - O(\varepsilon)$. Then, substituting $\phi_0 \sim \partial_{x_0} \tilde{u}^\varepsilon$ into (2.32), and using the fact that ω is exponentially small unless $|x - x_0| = O(\varepsilon)$, it is readily clear that $\lambda_0 = O(e^{-c/\varepsilon})$ for some $c > 0$.

To get a precise estimate for λ_0, we first replace (2.24) with the approximate equation $L_\varepsilon \phi_0 = 0$. Then, in §2.3.1, we use boundary layer theory to construct ϕ_0 for $\varepsilon \to 0$. The outer solution for ϕ_0 is clearly $\phi_0 \sim 1$ (apart from a normalization constant). In §2.3.2 we use (2.32) to estimate λ_0, and in §2.3.3 we compute λ_0 numerically.

2.3.1 Asymptotics for Principal Eigenfunction

In the left boundary layer we let $y = \varepsilon^{-1} x$, $\phi_l(y) = \phi_0(\varepsilon y)$, and we expand ϕ_l as

$$\phi_l(y) = 1 + \phi_{l_0}(y) + \varepsilon \phi_{l_1}(y) + \cdots . \tag{2.33}$$

Substituting (2.33) into $L_\varepsilon \phi_0 = 0$, and using (2.12), we obtain that ϕ_{l_0} satisfies

$$\phi_{l_0}'' - \left[f'(-x_0 + u_{l_0})(1 + \phi_{l_0})\right]' = 0 , \quad 0 < y < \infty , \quad \phi_{l_0}(0) = -1 , \ \phi_{l_0}(\infty) = 0 . \tag{2.34}$$

Comparing (2.34) with (2.13), we conclude that $\phi_{l_0} = -\partial_{x_0} u_{l_0}$. Therefore, we have

$$\phi_{l_0}'(0) = -f'(-x_0) , \qquad \phi_{l_0}(y) \sim (a_{l_0} \nu_l' y - a_{l_0}')\, e^{-\nu_l y} , \quad \text{as} \quad y \to \infty . \tag{2.35}$$

Here and in the formulae to be derived below, the primes on the constants a_{l_0}, a_{r_0}, ν_l and ν_r denote derivatives with respect to x_0.

Similarly, in the right boundary layer we let $y = \varepsilon^{-1}(1-x)$, $\phi_r(y) = \phi_0(1-\varepsilon y)$, and we expand ϕ_r as

$$\phi_r(y) = 1 + \phi_{r_0}(y) + \varepsilon\phi_{r_1}(y) + \cdots . \tag{2.36}$$

Substituting (2.36) and (2.17) into $L_\varepsilon\phi_0 = 0$, we get to leading order that

$$\phi_{r_0}'' + [f'(1-x_0+u_{r_0})(1+\phi_{r_0})]' = 0\,, \qquad 0 < y < \infty\,, \tag{2.37a}$$

$$\phi_{r_0}(0) = -1\,, \qquad \phi_{r_0}(\infty) = 0\,. \tag{2.37b}$$

Comparing (2.37) with (2.18), we have $\phi_{r_0} = -\partial_{x_0} u_{r_0}$.

For similar reasons as outlined following (2.19) above, the expansions (2.33) and (2.36) hold only on the interval $y = O(\varepsilon^q)$, where $-1/2 < q \le 0$. A composite expansion for ϕ_0, valid for $x \in [0,1]$, is

$$\phi_0(x) = 1 + \phi_{l_0}(\varepsilon^{-1}x) + \phi_{r_0}[\varepsilon^{-1}(1-x)] + \cdots . \tag{2.38}$$

This asymptotic eigenfunction can then be suitably normalized.

In the derivation below to estimate λ_0 we require certain formulae involving the ratios ϕ_{r_0}'/u_{r_0}' and ϕ_{l_0}'/u_{l_0}'. The first identity is obtained by combining (2.13) and (2.34) to get

$$\frac{d}{dy}\left(\frac{\phi_{l_0}'}{u_{l_0}'}\right) = f''(-x_0+u_{l_0})\,(\phi_{l_0}+1)\,, \qquad 0 < y < \infty\,, \tag{2.39a}$$

$$\frac{\phi_{l_0}'(0)}{u_{l_0}'(0)} = \frac{f'(-x_0)}{f(-x_0)}\,, \quad \frac{\phi_{l_0}'(y)}{u_{l_0}'(y)} = \nu_l' y - \frac{(a_{l_0}\nu_l)'}{a_{l_0}\nu_l} + o(1)\,, \quad \text{as } y \to \infty\,. \tag{2.39b}$$

In a similar way, combining (2.18) and (2.37) we obtain

$$\frac{d}{dy}\left(\frac{\phi_{r_0}'}{u_{r_0}'}\right) = -f''(1-x_0+u_{r_0})\,(\phi_{r_0}+1)\,, \qquad 0 < y < \infty\,, \tag{2.40a}$$

$$\frac{\phi_{r_0}'(0)}{u_{r_0}'(0)} = \frac{f'(1-x_0)}{f(1-x_0)}\,, \quad \frac{\phi_{r_0}'(y)}{u_{r_0}'(y)} = \nu_r' y - \frac{(a_{r_0}\nu_r)'}{a_{r_0}\nu_r} + o(1)\,, \quad \text{as } y \to \infty\,. \tag{2.40b}$$

2.3.2 Asymptotics for the Principal Eigenvalue

To estimate λ_0 from (2.32) we choose the comparison function $\tilde{\phi}_0 = 1$ and use (2.20) and (2.38) for $\tilde{u}^\varepsilon$ and ϕ_0, respectively. Substituting (2.38) and $\tilde{\phi}_0 = 1$ into (2.32) we get

$$\lambda_0 \left(1, \phi_0\right)_\omega \sim \left(L_\varepsilon 1, 1\right)_\omega + \left(L_\varepsilon 1, \phi_{l_0}\right)_\omega + \left(L_\varepsilon 1, \phi_{r_0}\right)_\omega - \phi'_{r_0}(0)\omega(1) - \phi'_{l_0}(0)\omega(0)\,, \qquad (2.41)$$

where $\left(u, v\right)_\omega \equiv \int_0^1 uw\omega\, dx$ and $\omega = \omega(x)$ is defined in (2.26). From (2.23a), we calculate

$$L_\varepsilon 1 = f''(\tilde{u}^\varepsilon)\left(1 - \tilde{u}^\varepsilon_x\right)\,. \qquad (2.42)$$

To evaluate the three integrals on the right side of (2.41) we break the range of integration for each integral into the three regions $x \in [0, \varepsilon^p]$, $x \in [\varepsilon^p, 1-\varepsilon^p]$, and $x \in [1-\varepsilon^p, 1]$. Here the choice $1/2 < p < 1$ gives an intermediate scaling between the outer and boundary layer regions and is needed to ensure that the leading order terms in the expansions for ϕ_0 and $\tilde{u}^\varepsilon$ in the boundary layer regions are asymptotically valid (see the remark following (2.19) above). To determine which integrals are asymptotically dominant we make the following observations: $\omega = O(1)$ for $|x - x_0| = O(\varepsilon)$; $\omega =$ t.s.t. for $|x - x_0| \gg O(\varepsilon)$; $\phi_{l_0} =$ t.s.t for $x \gg O(\varepsilon^p)$; $\phi_{r_0} =$ t.s.t for $1 - x \gg O(\varepsilon^p)$. From these considerations, we can reduce (2.41) asymptotically to

$$\lambda_0 \left(1, 1\right)_\omega \sim \Big(I_1 - \phi'_{l_0}(0)\omega(0)\Big) + \Big(I_2 - \phi'_{r_0}(0)\omega(1)\Big) + I_3\,, \qquad (2.43)$$

where

$$I_1 \equiv \int_0^{\varepsilon^p} \omega(1+\phi_{l_0})L_\varepsilon 1\, dx\,,\;\; I_2 \equiv \int_{1-\varepsilon^p}^1 \omega(1+\phi_{r_0})L_\varepsilon 1\, dx\,,\;\; I_3 \equiv \int_{\varepsilon^p}^{1-\varepsilon^p} \omega L_\varepsilon 1\, dx\,. \qquad (2.44)$$

We first estimate I_1. Letting $y = \varepsilon^{-1}x$ and using (2.20) and (2.42) we get

$$I_1 \sim -\int_0^{\varepsilon^{p-1}} \omega u'_{l_0}(y) f''[-x_0 + u_{l_0}(y)]\left(1 + \phi_{l_0}(y)\right)\, dy\,. \qquad (2.45)$$

As shown in (A.5) of the Appendix, $\omega u'_{l_0}$ is asymptotically constant on $[0, \varepsilon^{p-1}]$. Then, substituting (2.39a) into (2.45) we get

$$I_1 \sim -\omega(0)u'_{l_0}(0)\int_0^{\varepsilon^{p-1}} \frac{d}{dy}\left(\frac{\phi'_{l_0}}{u'_{l_0}}\right) dy \sim -\omega(0)u'_{l_0}(0)\left(\frac{\phi'_{l_0}}{u'_{l_0}}\right)\Big|_0^{\varepsilon^{p-1}} . \tag{2.46}$$

Therefore, using (2.39b), we obtain

$$I_1 - \phi'_{l_0}(0)\omega(0) \sim -\omega(0)u'_{l_0}(0)\left[\nu'_l\varepsilon^{p-1} - \frac{(a_{l_0}\nu_l)'}{a_{l_0}\nu_l}\right] . \tag{2.47}$$

The integral I_2 can be estimated in a similar way by using (2.40) and (A.7) of the Appendix to derive

$$I_2 - \phi'_{r_0}(0)\omega(1) \sim -\omega(1)u'_{r_0}(0)\left[\nu'_r\varepsilon^{p-1} - \frac{(a_{r_0}\nu_r)'}{a_{r_0}\nu_r}\right] . \tag{2.48}$$

Asymptotic formulae for $\omega(0)u'_{l_0}(0)$ and $\omega(1)u'_{r_0}(0)$ are given in (A.6) and (A.7) of the Appendix, respectively.

Next we estimate I_3. Using (2.42) and (2.20) we can decompose I_3 as

$$I_3 \sim I_{3L} + I_{3R}\,;\;\; I_{3L} \equiv -\int_{\varepsilon^p}^{1-\varepsilon^p} \omega f''(\tilde{u}^\varepsilon)u_{l_{0x}}\,dx\,,\quad I_{3R} \equiv -\int_{\varepsilon^p}^{1-\varepsilon^p} \omega f''(\tilde{u}^\varepsilon)u_{r_{0x}}\,dx\,. \tag{2.49}$$

For $x \in [\varepsilon^p, 1-\varepsilon^p]$ we have from (A.1) of the Appendix that $\omega(x) = \exp[-f(x-x_0)/\varepsilon](1+$ t.s.t.). Thus, using the decay behavior (2.13b) for u_{l_0} and $\tilde{u}^\varepsilon \sim x - x_0$, I_{3L} becomes

$$I_{3L} \sim \varepsilon^{-1}a_{l_0}\nu_l\int_{\varepsilon^p}^{1-\varepsilon^p} f''(x-x_0)e^{-h_l(x)/\varepsilon}\,dx\,, \qquad h_l(x) \equiv \nu_l x + f(x-x_0)\,, \tag{2.50}$$

where $\nu_l = -f'(-x_0)$. Clearly $h_l(x)$ has a minimum on $[\varepsilon^p, 1-\varepsilon^p]$ at $x = \varepsilon^p$. Thus, for $\varepsilon \to 0$, the dominant contribution to I_{3L} arises from the region near $x = \varepsilon^p$. Let $x = \varepsilon^p + s$ in I_{3L} and expand $h_l(x)$ and $f''(x-x_0)$ near $x = \varepsilon^p$ to get

$$\begin{aligned} I_{3L} \;\sim\; & \varepsilon^{-1}a_{l_0}\nu_l e^{-f(-x_0)/\varepsilon}\int_0^\infty [f''(-x_0) + sf'''(-x_0) + \cdots] \\ & \times \exp\left[-\frac{1}{2\varepsilon}f''(-x_0)\left(s^2 + 2\varepsilon^p s + \varepsilon^{2p}\right)\right] ds\,. \end{aligned} \tag{2.51}$$

Then, using Laplace's method and the bound $1/2 < p < 1$, we obtain as $\varepsilon \to 0$

$$I_{3L} \sim a_{l_0}\nu_l e^{-f(-x_0)/\varepsilon}\left[\left(\frac{\pi}{2\varepsilon}\right)^{1/2}[f''(-x_0)]^{1/2} - \varepsilon^{p-1}f''(-x_0) + \frac{f'''(-x_0)}{f''(-x_0)}\right]. \tag{2.52}$$

A similar calculation, which we shall omit, can be used to calculate I_{3R} as $\varepsilon \to 0$. We find,

$$I_{3R} \sim a_{r_0}\nu_r e^{-f(1-x_0)/\varepsilon}\left[\left(\frac{\pi}{2\varepsilon}\right)^{1/2}[f''(1-x_0)]^{1/2} - \varepsilon^{p-1}f''(1-x_0) - \frac{f'''(1-x_0)}{f''(1-x_0)}\right]. \tag{2.53}$$

Finally, we estimate $(1,1)_\omega$ in (2.43). The dominant contribution to this integral arises from the region near $x = x_0$. Assuming that $f''(0) > 0$, we obtain upon using (A.1) of the Appendix and Laplace's method that

$$(1,1)_\omega \sim \int_{-\infty}^{\infty} e^{-f(x-x_0)/\varepsilon}\,dx \sim \varepsilon^{1/2}\theta_0\left(1 + \varepsilon\theta_1 + \cdots\right), \tag{2.54a}$$

$$\theta_0 = \left(\frac{2\pi}{f''(0)}\right)^{1/2}, \qquad \theta_1 = \left(-\frac{f''''(0)}{8[f''(0)]^2} + \frac{5[f'''(0)]^2}{24[f''(0)]^3}\right). \tag{2.54b}$$

To obtain our asymptotic estimate for λ_0 we substitute (2.47), (2.48), (2.49), (2.52), (2.53) and (2.54) into (2.43). This leads to the following result:

Proposition 2.1 *Let $f(u)$ be smooth, convex, and satisfy $f(0) = f'(0) = 0$ with $f''(0) > 0$. Then, for $\varepsilon \to 0$ and $0 < x_0 < 1$, the principal eigenvalue λ_0 for (2.24) satisfies*

$$\begin{aligned}\lambda_0 \sim \frac{[f''(0)]^{1/2}}{2\varepsilon}\Big(&a_{l_0}\nu_l e^{-f(-x_0)/\varepsilon}\left[b_{l_0} + \varepsilon^{1/2}b_{l_1} + \cdots\right] \\ &+ a_{r_0}\nu_r e^{-f(1-x_0)/\varepsilon}\left[b_{r_0} + \varepsilon^{1/2}b_{r_1} + \cdots\right]\Big),\end{aligned} \tag{2.55}$$

where

$$b_{l_0} = [f''(-x_0)]^{1/2}, \qquad b_{l_1} = \left(\frac{2}{\pi}\right)^{1/2}\left[\frac{f'''(-x_0)}{f''(-x_0)} - \frac{(a_{l_0}\nu_l)'}{a_{l_0}\nu_l}\right], \tag{2.56a}$$

$$b_{r_0} = [f''(1-x_0)]^{1/2}, \quad b_{r_1} = -\left(\frac{2}{\pi}\right)^{1/2}\left[\frac{f'''(1-x_0)}{f''(1-x_0)} - \frac{(a_{r_0}\nu_r)'}{a_{r_0}\nu_r}\right]. \tag{2.56b}$$

Here a_{l_0}, ν_l, a_{r_0}, and ν_r, which depend on x_0, are defined in (2.15) and (2.19). The primes on these coefficients indicate differentiation with respect to x_0.

This estimate for λ_0 characterizes the ill-conditioning of the equilibrium problem (2.11). Since $\lambda_0 > 0$ it also indicates that the equilibrium solution is marginally unstable.

2.3.3 Numerics for the Principal Eigenvalue

We now verify (2.55) by comparing it with full numerical results for λ_0 computed from (2.24) for two choices of $f(u)$ and for various values of x_0 and ε. Numerical methods to compute eigenvalues include the software packages SLEDGE and SLEIGN, and the NAG library code SL02FM (cf. [10], [11], [83], [84]). Our approach to compute λ_0 is to use the boundary value ODE solver COLSYS [6] with a suitable initial guess.

To numerically evaluate the operator L_ε in (2.24) we must first determine $\tilde{u}^\varepsilon$ given in (2.20). In general, this requires us to numerically compute the boundary layer functions u_{l_0} and u_{r_0} satisfying (2.13) and (2.18) using COLSYS. Then, to compute λ_0 we re-write (2.24) as a first order system. Using $\lambda_0 = 0$ and (2.38) for ϕ_0 as initial guesses, we found that COLSYS readily converged to the principal eigenvalue for (2.24).

Example 2.1: Let $f(u) = u^2/2$, which corresponds to the flame–front problem (2.5). For this problem, we calculate from (2.15) and (2.19) that $a_{l_0} = 2x_0$, $\nu_l = x_0$, $a_{r_0} = 2(1-x_0)$, and $\nu_r = 1 - x_0$. Thus, (2.55) becomes

$$\begin{aligned} \lambda_0 \;\sim\; \varepsilon^{-1} \Bigg(& x_0 \left[x_0 - \left(\frac{8\varepsilon}{\pi} \right)^{1/2} \right] e^{-x_0^2/2\varepsilon} \\ & + (1-x_0) \left[(1-x_0) - \left(\frac{8\varepsilon}{\pi} \right)^{1/2} \right] e^{-(1-x_0)^2/2\varepsilon} \Bigg) . \end{aligned} \tag{2.57}$$

For this example, $u_{l_0}(y;x_0)$ and $u_{r_0}(y;x_0)$ can be found analytically as

$$u_{l_0}(y) = x_0 - x_0 \tanh\left(\frac{x_0 y}{2} \right) , \quad u_{r_0}(y) = (1-x_0) \left[\tanh \frac{(1-x_0)y}{2} - 1 \right] . \tag{2.58}$$

Thus, the composite expansion $\tilde{u}^\varepsilon$, which is needed in (2.24), is obtained explicitly.

Example 2.2: Here we choose the function $f(u) = u - 2 + 4/(u+2)$, which is not even. A careful calculation from (2.15) and (2.19) yields

$$\nu_l = -1 + \frac{4}{(2-x_0)^2}, \qquad a_{l_0} = x_0 \exp\left[4(2-x_0)^{-2} \log\left(\frac{4-x_0}{2}\right)\right], \tag{2.59a}$$

$$\nu_r = 1 - \frac{4}{(3-x_0)^2}, \quad a_{r_0} = (1-x_0) \exp\left[4(3-x_0)^{-2} \log\left(\frac{5-x_0}{2}\right)\right]. \tag{2.59b}$$

Substituting (2.59) into (2.55) gives the asymptotic result for λ_0. For this example the boundary layer functions, and hence L_ε, must be computed numerically.

ε	λ_0 (num.)	λ_0 (2.57) 1-term	rate1	λ_0 (2.57) 2-term	rate2
0.004	0.2676×10^{-11}	0.3351×10^{-11}	0.252	0.2674×10^{-11}	-6.13×10^{-4}
0.006	0.5626×10^{-7}	0.7465×10^{-7}	0.327	0.5619×10^{-7}	-1.23×10^{-3}
0.008	0.7333×10^{-5}	0.1023×10^{-4}	0.395	0.7312×10^{-5}	-2.88×10^{-3}
0.010	0.1276×10^{-3}	0.1863×10^{-3}	0.461	0.1269×10^{-3}	-5.57×10^{-3}
0.012	0.8182×10^{-3}	0.1247×10^{-2}	0.524	0.8111×10^{-3}	-8.70×10^{-3}

Table 2.1: **Example 2.1**: Comparison of asymptotic and numerical values for λ_0 with $f(u) = u^2/2$ and $x_0 = 0.50$.

ε	λ_0 (num.)	λ_0 (2.57) 1-term	rate1	λ_0 (2.57) 2-term	rate2
0.002	0.2443×10^{-11}	0.3068×10^{-11}	0.256	0.2442×10^{-11}	-3.52×10^{-4}
0.003	0.4168×10^{-7}	0.5548×10^{-7}	0.331	0.4163×10^{-7}	-1.31×10^{-3}
0.004	0.4893×10^{-5}	0.6854×10^{-5}	0.401	0.4878×10^{-5}	-3.08×10^{-3}
0.006	0.4920×10^{-3}	0.7526×10^{-3}	0.530	0.4868×10^{-3}	-1.05×10^{-2}
0.008	0.4369×10^{-2}	0.7244×10^{-2}	0.658	0.4290×10^{-2}	-1.81×10^{-2}
0.010	0.1476×10^{-1}	0.2680×10^{-1}	0.815	0.1458×10^{-1}	-1.22×10^{-2}

Table 2.2: **Example 2.1**: Comparison of asymptotic and numerical values for λ_0 with $f(u) = u^2/2$ and $x_0 = 0.35$.

In Table 2.1–2.4 we display the asymptotic and numerical results for λ_0 for each of the two examples. In each of these tables, the second column gives the numerical results

ε	λ_0 (num.)	λ_0 (2.55) 1-term	rate1	λ_0 (2.55) 2-term	rate2
0.00325	0.3888×10^{-11}	0.5267×10^{-11}	0.354	0.3791×10^{-11}	-2.49×10^{-2}
0.00350	0.3210×10^{-10}	0.4405×10^{-10}	0.372	0.3124×10^{-10}	-2.68×10^{-2}
0.00400	0.9736×10^{-9}	0.1371×10^{-8}	0.408	0.9448×10^{-8}	-2.96×10^{-2}
0.00450	0.1358×10^{-7}	0.1961×10^{-7}	0.444	0.1314×10^{-7}	-3.24×10^{-2}
0.00500	0.1101×10^{-6}	0.1629×10^{-6}	0.480	0.1063×10^{-6}	-3.45×10^{-2}
0.00550	0.6026×10^{-6}	0.9129×10^{-6}	0.515	0.5798×10^{-6}	-3.78×10^{-2}
0.00600	0.2458×10^{-5}	0.3809×10^{-5}	0.549	0.2357×10^{-5}	-4.11×10^{-2}

Table 2.3: **Example 2.2**: Comparison of asymptotic and numerical values for λ_0 with $f(u) = u - 2 + 4/(u+2)$ and $x_0 = 0.40$.

ε	λ_0 (num.)	λ_0 (2.55) 1-term	rate1	λ_0 (2.55) 2-term	rate2
0.00225	0.4172×10^{-12}	0.5519×10^{-12}	0.323	0.4082×10^{-12}	-2.16×10^{-2}
0.00250	0.9997×10^{-11}	0.1346×10^{-10}	0.347	0.9769×10^{-11}	-2.28×10^{-2}
0.00300	0.1137×10^{-8}	0.1584×10^{-8}	0.393	0.1107×10^{-8}	-2.64×10^{-2}
0.00350	0.3239×10^{-7}	0.4659×10^{-7}	0.439	0.3145×10^{-7}	-2.90×10^{-2}
0.00425	0.1077×10^{-5}	0.1621×10^{-5}	0.506	0.1041×10^{-5}	-3.34×10^{-2}
0.00550	0.4114×10^{-4}	0.6645×10^{-4}	0.615	0.3937×10^{-4}	-4.30×10^{-2}
0.00650	0.2637×10^{-3}	0.4489×10^{-3}	0.702	0.2500×10^{-3}	-5.20×10^{-2}

Table 2.4: **Example 2.2**: Comparison of asymptotic and numerical values for λ_0 with $f(u) = u - 2 + 4/(u+2)$ and $x_0 = 0.35$.

for λ_0, while the third and fifth columns show the asymptotic expansion (2.55) with one term and two terms in the pre-exponential factors, respectively. In the fourth and sixth columns we display the relative error

$$\text{rate} = \frac{\lambda_0(\text{asy.}) - \lambda_0(\text{num.})}{\lambda_0(\text{num.})}\,. \tag{2.60}$$

Here λ_0(asy.) denotes the asymptotic result with either one or two terms in the pre-exponential factors.

From these tables we observe that a two–term asymptotic expansion for the pre–exponential factor of λ_0 is certainly needed to obtain close quantitative agreement with

the numerical results for λ_0. A similar situation was found in [67] for some related problems with exponentially small eigenvalues. From Tables 2.1 and 2.2 we find that, in most cases, the relative errors for the two–term expansion in most cases are below 1 %, while they are only between 20 % and 70 % for the one–term expansion. Similar behavior is observed in Tables 2.3 and 2.4 for the relative errors for Example 2.2.

2.4 Derivation of the Metastable Dynamics

We now asymptotically evaluate the various terms in (2.30) to obtain an explicit ODE for $x_0 = x_0(t)$. The metastable dynamics for (2.10) is then given by $u(x,t) \sim \tilde{u}^\varepsilon[x; x_0(t)]$, where $\tilde{u}^\varepsilon$ is defined in (2.7).

Similar considerations as given following (2.42) above show that (2.30) reduces asymptotically to

$$-x_0'\,(1,1)_\omega \sim I_1 + I_2 + I_3\,, \tag{2.61}$$

where the I_j, for $j = 1,2,3$, are defined by

$$I_1 \equiv \int_0^{\varepsilon^p} \omega(1+\phi_{l_0}) R\,dx\,, \quad I_2 \equiv \int_{1-\varepsilon^p}^1 \omega(1+\phi_{r_0}) R\,dx\,, \quad I_3 \equiv \int_{\varepsilon^p}^{1-\varepsilon^p} \omega R\,dx\,. \tag{2.62}$$

Here R is defined in (2.23b) and $1/2 < p < 1$ gives the intermediate scaling used in §2.3. We note that the boundary term $\varepsilon\phi_{0x}\omega\tilde{u}^\varepsilon \Big|_0^1$ in (2.30) can be neglected in comparison to each I_j since it involves the product of the two exponentially small terms ω and $\tilde{u}^\varepsilon$ at $x = 0, 1$. To calculate R we substitute (2.20) into (2.23b) and use (2.13a) and (2.18a) to get

$$R \sim \left[f'(-x_0 + u_{l_0}) - f'(\tilde{u}^\varepsilon)\right] u_{l_{0x}} + \left[f'(1 - x_0 + u_{r_0}) - f'(\tilde{u}^\varepsilon)\right] u_{r_{0x}}\,. \tag{2.63}$$

The inner product $(1,1)_\omega$ in (2.61) was calculated for $\varepsilon \to 0$ in (2.54).

We first estimate I_1. In the region $0 < x < \varepsilon^p$ we can approximate R by $R \sim -f''(-x_0 + u_{l_0}) x u_{l_{0x}}$. Substituting this expression into I_1 and letting $y = \varepsilon^{-1}x$ we obtain,

upon using (2.39a) and (A.5) of the Appendix, that

$$\begin{aligned} I_1 &\sim -\varepsilon \int_0^{\varepsilon^{p-1}} \omega u_{l_0}' y f''(-x_0 + u_{l_0})\,(1+\phi_{l_0})\,dy \\ &\sim -\varepsilon\omega(0)u_{l_0}'(0)\int_0^{\varepsilon^{p-1}} y\frac{d}{dy}\left(\frac{\phi_{l_0}'}{u_{l_0}'}\right)\,dy\,. \end{aligned} \tag{2.64}$$

Then, since $\phi_{l_0}' = -\partial_{x_0} u_{l_0}'$ and $u_{l_0}' < 0$ we can re-write (2.64) after integrating by parts as

$$I_1 \sim \varepsilon\omega(0)u_{l_0}'(0)\partial_{x_0}\left[y\log(-u_{l_0}')\,\Big|_0^{\varepsilon^{p-1}} - \int_0^{\varepsilon^{p-1}} \log\left(-u_{l_0}'\right)\,dy\right]\,. \tag{2.65}$$

Recall from (2.13b) that $u_{l_0}' \sim -a_{l_0}\nu_l e^{-\nu_l y}$ as $y \to \infty$. Since $\varepsilon^{p-1} \to \infty$ as $\varepsilon \to 0$ for $1/2 < p < 1$ we can use this decay behavior to estimate $\log(-u_{l_0}')$ at the upper endpoint $y = \varepsilon^{p-1}$. In addition, we can add and subtract the term $\log(a_{l_0}\nu_l) - \nu_l y$ inside the integrand in (2.65) so that the resulting integral converges when the upper limit of integration is set to infinity. In this way, we obtain that

$$I_1 \sim \varepsilon\omega(0)u_{l_0}'(0)\left(-\frac{\nu_l'}{2}\varepsilon^{2p-2} + \beta_l\right)\,. \tag{2.66}$$

Here $\nu_l' \equiv d\nu_l/dx_0 = f''(-x_0)$ from (2.15a), and $\beta_l = \beta_l(x_0)$ is defined by

$$\beta_l \equiv -\frac{d}{dx_0}\left(\int_0^{\infty}\left[\log\left(-u_{l_0}'(y)\right) - \log(a_{l_0}\nu_l) + \nu_l y\right]\,dy\right)\,. \tag{2.67}$$

A very similar calculation can be done to estimate I_2 in (2.62). In the region $1-\varepsilon^p < x < 1$, we have $R \sim -f''(1-x_0+u_{r_0})(x-1)u_{r_{0x}}$ in (2.62). Thus, upon using (A.7) of the Appendix and (2.40a), I_2 becomes

$$\begin{aligned} I_2 &\sim -\varepsilon \int_0^{\varepsilon^{p-1}} \omega u_{r_0}' y f''(1-x_0+u_{r_0})\,(1+\phi_{r_0})\,dy \\ &\sim \varepsilon\,\omega(1)u_{r_0}'(0)\int_0^{\varepsilon^{p-1}} y\frac{d}{dy}\left(\frac{\phi_{r_0}'}{u_{r_0}'}\right)\,dy\,. \end{aligned} \tag{2.68}$$

Then, since $\phi_{r_0}' = -\partial_{x_0} u_{r_0}'$ and $u_{r_0}' > 0$ we can re-write (2.68) after integrating by parts as

$$I_2 \sim -\varepsilon\omega(1)u_{r_0}'(0)\partial_{x_0}\left[y\log(u_{r_0}')\,\Big|_0^{\varepsilon^{p-1}} - \int_0^{\varepsilon^{p-1}} \log\left(u_{r_0}'\right)\,dy\right]\,. \tag{2.69}$$

Finally, using $u'_{r_0} \sim a_{r_0}\nu_r e^{-\nu_r y}$ as $y \to \infty$ in (2.69) we obtain, in analogy with (2.66), that

$$I_2 \sim -\varepsilon\omega(1)u'_{r_0}(0)\left(-\frac{\nu'_r}{2}\varepsilon^{2p-2} + \beta_r\right) . \tag{2.70}$$

Here $\nu'_r \equiv -f''(1-x_0)$ and β_r is defined by

$$\beta_r \equiv -\frac{d}{dx_0}\left(\int_0^\infty \left[\log\left(u'_{r_0}(y)\right) - \log(a_{r_0}\nu_r) + \nu_r y\right] dy\right) . \tag{2.71}$$

Next we estimate I_3 in (2.62). Using (2.63) we first decompose I_3 as $I_3 \sim I_{3L} + I_{3R}$, where

$$I_{3L} \sim \int_{\varepsilon^p}^{1-\varepsilon^p} \omega u_{l_{0x}}\left[f'(-x_0+u_{l_0}) - f'(\tilde{u}^\varepsilon)\right] dx , \tag{2.72a}$$

$$I_{3R} \sim \int_{\varepsilon^p}^{1-\varepsilon^p} \omega u_{r_{0x}}\left[f'(1-x_0+u_{r_0}) - f'(\tilde{u}^\varepsilon)\right] dx . \tag{2.72b}$$

The dominant contribution to I_{3L} arises from the region near $x = \varepsilon^p$. To calculate I_{3L} we use (A.1) of the Appendix to estimate ω, (2.13b) to evaluate $u_{l_{0x}}$, and we expand $f'(-x_0+u_{l_0}) - f'(\tilde{u}^\varepsilon)$ for $x \to 0$. This yields,

$$I_{3L} \sim \varepsilon^{-1}a_{l_0}\nu_l \int_{\varepsilon^p}^{1-\varepsilon^p}\left(xf''(-x_0) + \frac{x^2}{2}f'''(-x_0) + \cdots\right) e^{-h_l(x)/\varepsilon}\, dx , \tag{2.73}$$

where $h_l(x) \equiv \nu_l x + f(x-x_0)$. It is clear that $h_l(x)$ is minimized on $[\varepsilon^p, 1-\varepsilon^p]$ at $x = \varepsilon^p$. Therefore, we can use Laplace's method to evaluate (2.73) by expanding $h_l(x)$ as $x \to 0$. In this way, we obtain for $\varepsilon \to 0$ that

$$I_{3L} \sim a_{l_0}\nu_l e^{-f(-x_0)/\varepsilon}\left(1 - \frac{\varepsilon^{2p-1}}{2}f''(-x_0) + \cdots\right) . \tag{2.74}$$

A similar calculation, which we shall omit, can be done to calculate I_{3R} as $\varepsilon \to 0$, with the result

$$I_{3R} \sim -a_{r_0}\nu_r e^{-f(1-x_0)/\varepsilon}\left(1 - \frac{\varepsilon^{2p-1}}{2}f''(1-x_0) + \cdots\right) . \tag{2.75}$$

Then, I_3 in (2.62) is given by $I_3 \sim I_{3L} + I_{3R}$.

Finally, an explicit ODE for $x_0 = x_0(t)$ is obtained by substituting (2.54), (2.66), (2.70), (2.74) and (2.75) into (2.61). The formulae (A.6) and (A.7) of the Appendix are used to evaluate $\omega(0)u'_{l_0}(0)$ and $\omega(1)u'_{r_0}(0)$, respectively. This leads to our main result.

Proposition 2.2 (Metastable Dynamics): *Let $f(u)$ be smooth, convex, and satisfy $f(0) = f'(0) = 0$ with $f''(0) > 0$. Then, for $\varepsilon \to 0$ and $t \gg 1$, the metastable dynamics for (2.10) is given by $u(x,t) \sim \tilde{u}^\varepsilon[x; x_0(t)]$, where $\tilde{u}^\varepsilon$ is given in (2.20) and $x_0(t)$ satisfies the asymptotic nonlinear ODE*

$$x_0' \sim \varepsilon^{-1/2}\theta_0^{-1}\,(1+\varepsilon\theta_1)^{-1}\left[a_{r_0}\nu_r\,(1+\varepsilon\beta_r)\,e^{-f(1-x_0)/\varepsilon} - a_{l_0}\nu_l\,(1-\varepsilon\beta_l)\,e^{-f(-x_0)/\varepsilon}\right]. \quad (2.76)$$

The coefficients a_{l_0}, ν_l, a_{r_0}, ν_r, β_l and β_r, which all depend on x_0, are defined in (2.15), (2.19), (2.67) and (2.71). In addition, θ_0 and θ_1 are given in (2.54b).

The following equilibrium result is obtained by setting $x_0' = 0$ in (2.76):

Corollary 2.1 (Equilibrium): *The (unstable) equilibrium solution to (2.10) of the form given in (2.7) is $u \sim \tilde{u}^\varepsilon[x; x_0^m]$, where x_0^m satisfies the nonlinear algebraic equation*

$$a_{r_0}\nu_r\,(1+\varepsilon\beta_r)\,e^{-f(1-x_0)/\varepsilon} \sim a_{l_0}\nu_l\,(1-\varepsilon\beta_l)\,e^{-f(-x_0)/\varepsilon}. \quad (2.77)$$

The special case $f(u) = u^2/2$ corresponds to the flame–front problem (2.4) (or equivalently (2.5)). For this special case, $a_{l_0} = 2x_0$, $\nu_l = x_0$, $a_{r_0} = 2(1-x_0)$ and $\nu_r = 1 - x_0$. In addition, since u_{l_0} and u_{r_0} are given analytically in (2.58), we can calculate β_l and β_r explicitly as

$$\beta_r = 2\frac{d}{dx_0}\left(\int_0^\infty \log\left[1+e^{-(1-x_0)y}\right]\,dy\right) = \frac{\pi^2}{6(1-x_0)^2}, \qquad \beta_l = -\frac{\pi^2}{6x_0^2}. \quad (2.78)$$

In addition, when $f(u) = u^2/2$, we have $\theta_0 = (2\pi)^{1/2}$ and $\theta_1 = 0$. Substituting these formulae into (2.76) yields the following explicit metastability result for (2.4) (or (2.5):

Corollary 2.2 (Metastable Flame–Front Dynamics): *For $\varepsilon \to 0$ and $t \gg 1$, the tip $x_0 = x_0(t)$ of the metastable parabolic–shaped flame–front interface for (2.4) satisfies the asymptotic nonlinear ODE*

$$x_0' \sim \sqrt{\frac{2}{\pi\varepsilon}} \left[\left((1-x_0)^2 + \frac{\pi^2\varepsilon}{3} \right) e^{-(1-x_0)^2/2\varepsilon} - (x_0^2 + \frac{\pi^2\varepsilon}{3}) e^{-x_0^2/2\varepsilon} \right] . \tag{2.79}$$

Some trends can be observed from these results. Let $x_0^0 \equiv x_0(0)$ denote the initial condition for (2.76). Then, since for $x_0^0 < x_0^m$ ($x_0^0 > x_0^m$) we have $x_0' < 0$ ($x_0' > 0$) from (2.76), it follows that $x_0(t)$ will not approach x_0^m as $t \to \infty$, but instead will eventually hit the wall at $x = 0$ ($x = 1$). In addition, when $O(\varepsilon) \ll x_0 \ll 1 - O(\varepsilon)$, (2.76) shows that x_0' is exponentially small and hence the motion is metastable. It is also clear that unless x_0^0 is within an $O(\varepsilon)$ neighborhood of x_0^m only one of the exponentials on the right side of (2.76) is significant for $\varepsilon \to 0$. Finally, in the case when $f(u)$ is even, it is easy to see from the definitions of the coefficients in (2.77) that $\beta_l = -\beta_r$, $a_{l_0} = a_{r_0}$ and $\nu_l = \nu_r$. Hence, in this case we have $x_0^m = 1/2$ as expected.

2.5 Comparison of Asymptotic and Numerical Results

We now compare the asymptotic results (2.76), (2.77) and (2.79) with corresponding full numerical results computed directly from (2.5), (2.10) and (2.11) using the TMOL in §1.3.

The metastability results (2.76) and (2.79) are valid only after the completion of an $O(1)$ transient period that describes the formation of the quasi–equilibrium solution (2.20) from initial data. As discussed in §2.1, a metastable quasi–equilibrium solution will not be formed for arbitrary initial data $u_0(x)$. A sufficient condition on $u_0(x)$ for metastability to occur is given in (2.6). To eliminate the effect of the initial transient, in the computations below we took $u(x,0) = \tilde{u}^\varepsilon[x; x_0^0]$ as the initial data for (2.10) and (2.5). Here $\tilde{u}^\varepsilon$ is the quasi–equilibrium profile given in (2.20) and $x_0^0 \in (0,1)$ is the initial

zero of u. The value x_0^0 is then used as the initial condition for the asymptotic ODE's (2.76) and (2.79) (i. e. $x_0(0) = x_0^0$). With this initial condition, these ODE's are solved for $t = t(x_0)$ using a numerical quadrature.

Asymptotic and numerical results for $t = t(x_0)$ are compared for $f(u) = u^2/2$ and for the asymmetric $f(u)$ of Example 2.2 in §2.3.3 given by

$$f(u) = u - 2 + \frac{4}{u+2}\,. \tag{2.80}$$

For this latter form of $f(u)$, explicit formulas for ν_l, a_{l_0}, ν_r, and a_{r_0} are given in (2.59). However, the functions $\beta_l(x_0)$ and $\beta_r(x_0)$ in (2.76) are calculated from a numerical quadrature after first using COLSYS to solve for the boundary layer functions u'_{l_0} and u'_{r_0}. For the $f(u)$ of (2.80) we have $\theta_0 = (2\pi)^{1/2}$ and $\theta_1 = 3/32$ in (2.76).

x_0	t(num.)	t(asy.)
0.3999125	0.196752251×10^5	0.192198642×10^5
0.3972259	0.554179455×10^6	0.541388563×10^6
0.3943236	0.997547019×10^6	0.974550456×10^6
0.3829263	0.197541881×10^7	0.193020273×10^7
0.3636165	0.235602159×10^7	0.230237584×10^7
0.3094434	0.245565007×10^7	0.240006441×10^7
0.2514594	0.245728124×10^7	0.240171229×10^7
0.2005907	0.245732411×10^7	0.240176186×10^7
0.1122723	0.245732918×10^7	0.240176776×10^7

Table 2.5: A comparison of the asymptotic and numerical results for the tip $t = t(x_0)$ of the flame–front for (2.5) with $\varepsilon = 0.004$ and $x_0^0 = 0.4$.

For $f(u) = u^2/2$, in Table 2.5 and 2.6, we compare the asymptotic and numerical results for the tip $t = t(x_0)$ of the flame–front interface for $\varepsilon = 0.004$ and $\varepsilon = 0.002$, respectively. The initial tip location of the interface was $x_0^0 = 0.4$ for $\varepsilon = 0.004$ and $x_0^0 = 0.3$ for $\varepsilon = 0.002$. The asymptotic and numerical results for the elapsed time agree to roughly within 2% for each of these examples. In Figure 2.7 we plot, at different times,

x_0	t(num.)	t(asy.)
0.2996765	0.110811891 $\times 10^7$	0.108295000 $\times 10^7$
0.2958542	0.109730472 $\times 10^8$	0.107247855 $\times 10^8$
0.2907243	0.180669282 $\times 10^8$	0.176594370 $\times 10^8$
0.2875337	0.205054498 $\times 10^8$	0.200430705 $\times 10^8$
0.2704028	0.245669157 $\times 10^8$	0.240128133 $\times 10^8$
0.2500379	0.250251570 $\times 10^8$	0.244610251 $\times 10^8$
0.2306506	0.250644804 $\times 10^8$	0.244996311 $\times 10^8$
0.1811032	0.250699164 $\times 10^8$	0.245050448 $\times 10^8$
0.0903085	0.250699778 $\times 10^8$	0.245051150 $\times 10^8$

Table 2.6: A comparison of the asymptotic and numerical results for the tip $t = t(x_0)$ of the flame–front for (2.5) with $\varepsilon = 0.002$ and $x_0^0 = 0.3$.

the numerical solution to (2.5) for $\varepsilon = 0.002$ with the initial data $u(x,0) = \tilde{u}^\varepsilon(x; x_0^0)$, where $x_0^0 = 0.3$. In Figure 2.8 we compare the asymptotic and numerical tip trajectories $t = t(x_0)$ for different initial conditions x_0^0 when $\varepsilon = 0.005$. A logarithmic (base 10) scale is used for the vertical axis and the horizontal axis represents the parabolic tip location x_0. On this logarithmic scale, the asymptotic and numerical results are virtually indistinguishable.

For the asymmetric $f(u)$ of (2.80), in Tables 2.7 and 2.8 we give a similar comparison between the asymptotic and numerical results for $t = t(x_0)$ for $\varepsilon = 0.004$ and $\varepsilon = 0.003$, respectively. The initial zeroes x_0^0 of u are given in the captions of these Tables. For both values of ε , the agreement between the asymptotic and numerical results is slightly closer than that for the case $f(u) = u^2/2$. For the $f(u)$ in (2.80), in Figure 2.9 we plot the numerical solution to (2.10) at different times when $\varepsilon = 0.004$. In Figure 2.10 we compare some asymptotic and numerical trajectories for $t = t(x_0)$ for different initial conditions x_0^0 when $\varepsilon = 0.006$.

For the asymmetric $f(u)$ of (2.80), we now verify the asymptotic result (2.77) for the equilibrium location $x_0 = x_0^m$ corresponding to the equilibrium solution $u \sim \tilde{u}^\varepsilon(x; x_0^m)$.

x_0	t(num.)	t(asy.)
0.3999931	0.131068167 $\times 10^6$	0.133057866 $\times 10^6$
0.3999216	0.149606553 $\times 10^7$	0.151644288 $\times 10^7$
0.3983913	0.277759851 $\times 10^8$	0.281609517 $\times 10^8$
0.3904987	0.103529490 $\times 10^9$	0.105057930 $\times 10^9$
0.3750825	0.140377491 $\times 10^9$	0.142599219 $\times 10^9$
0.3202282	0.146999074 $\times 10^9$	0.149374926 $\times 10^9$
0.2574865	0.147019482 $\times 10^9$	0.149396440 $\times 10^9$
0.2020624	0.147019608 $\times 10^9$	0.149396594 $\times 10^9$
0.0898295	0.147019614 $\times 10^9$	0.149396603 $\times 10^9$

Table 2.7: A comparison of the asymptotic and numerical results for $t = t(x_0)$ for the asymmetric $f(u)$ of (2.80) with $\varepsilon = 0.004$ and $x_0^0 = 0.4$.

In Table 2.9 we compare asymptotic and numerical results for x_0^m at different values of ε. The asymptotic result for x_0^m was computed from (2.77) using Newton's method. The numerical value for x_0^m was computed from (2.11) using COLSYS (cf. [6]). These full numerical equilibrium solutions are plotted versus x for various ε in Figure 2.11 for the asymmetric $f(u)$ of (2.80) as well as $f(u) = u^2/2$. As expected, the asymptotic results provide a closer determination of the corresponding numerical result as ε is decreased.

Finally, we show how to recover the solution $y(x,t)$ to (2.4) from $u(x,t)$. Since $u = -y_x$, we have

$$y(x,t) = h(t) - \int_0^x u(s,t)\, ds\,, \tag{2.81}$$

where $h(t)$ is to be found. To determine $h(t)$, we substitute (2.81) into (2.4a) to derive

$$h'(t) = -\varepsilon u_x(0) + \int_0^1 \int_0^x u(s,t)\, ds\, dx\,. \tag{2.82}$$

Since (2.4a) is invariant under a constant shift in y, we can take $h(0) = 0$. Therefore,

$$h(t) = \int_0^t \left\{ -\varepsilon u_x(0) + \int_0^1 \int_0^x u(s,t)\, ds\, dx \right\} dt\,. \tag{2.83}$$

To determine $h(t)$ during the metastable evolution we substitute $u(x,t) \sim \tilde{u}^\varepsilon[x; x_0(t)]$ into (2.81) and (2.83). Here $\tilde{u}^\varepsilon$ is given by (2.7), where u_{l_0} and u_{r_0} are given in (2.58).

x_0	t(num.)	t(asy.)
0.3499993	0.112330078 $\times 10^5$	0.111349461 $\times 10^5$
0.3499269	0.132980269 $\times 10^7$	0.134879406 $\times 10^7$
0.3493105	0.120121899 $\times 10^8$	0.121708663 $\times 10^8$
0.3476808	0.359540384 $\times 10^8$	0.364335772 $\times 10^8$
0.3380873	0.102874830 $\times 10^9$	0.104310107 $\times 10^9$
0.3005508	0.126006321 $\times 10^9$	0.127873597 $\times 10^9$
0.2503833	0.126203956 $\times 10^9$	0.128078207 $\times 10^9$
0.2012807	0.126205089 $\times 10^9$	0.128079463 $\times 10^9$
0.0884271	0.126205114 $\times 10^9$	0.128079498 $\times 10^9$

Table 2.8: A comparison of the asymptotic and numerical results for $t = t(x_0)$ for the asymmetric $f(u)$ of (2.80) with $\varepsilon = 0.003$ and $x_0^0 = 0.35$.

This yields,

$$\begin{aligned} y(x,t) &= h(t) - \Big\{ \frac{1}{2}x^2 - x_0 x + 2\varepsilon \log 2 - 2\varepsilon \log(1 + e^{-x_0 x/\varepsilon}) \\ &\quad + 2\varepsilon \left[\log(1 + e^{-(1-x_0)/\varepsilon}) - \log(1 + e^{-(1-x_0)(1-x)/\varepsilon}) \right] \Big\}, \end{aligned} \tag{2.84a}$$

where $h(t)$ is defined by

$$\begin{aligned} h(t) &= \int_0^t \left\{ -\frac{\pi^2 \varepsilon^2}{6x_0(1-x_0)} + \varepsilon(\log 4 - 1) + \frac{1}{2}x_0^2 - \frac{1}{2}x_0 + \frac{1}{6} + 2\varepsilon \log(1 + e^{-(1-x_0)/\varepsilon}) \right. \\ &\quad \left. + \frac{1}{2}(1-x_0)^2 \left[1 - \tanh^2 \frac{1-x_0}{2\varepsilon} \right] - 2\varepsilon^2 \left[\frac{\mathrm{g}(1 + e^{-x_0/\varepsilon})}{x_0} + \frac{\mathrm{g}(1 + e^{-(1-x_0)/\varepsilon})}{1-x_0} \right] \right\} dt \\ &\sim \int_0^t \left\{ -\frac{\pi^2 \varepsilon^2}{6x_0(1-x_0)} + \varepsilon(\log 4 - 1) + \frac{1}{2}x_0^2 - \frac{1}{2}x_0 + \frac{1}{6} \right\} dt\,. \end{aligned} \tag{2.84b}$$

Here $g(x)$ is the Dilogarithm function defined by $\mathrm{g}(x) = \int_0^x \frac{\log t}{1-t} dt$, which satisfies $\mathrm{g}(x) \sim 1 - x$ as $x \to 1$. To determine $y(x,t)$ during the metastable evolution we solve the ODE (2.79) numerically and obtain $h(t)$ from a numerical quadrature. Equation (2.84a) then yields $y(x,t)$.

In Figure 2.2 and Figure 2.12 we plot the metastable solution $y(x,t)$ versus x with $\varepsilon = 0.0115$ and $\varepsilon = 0.006$, respectively, at several values of t. For the example in

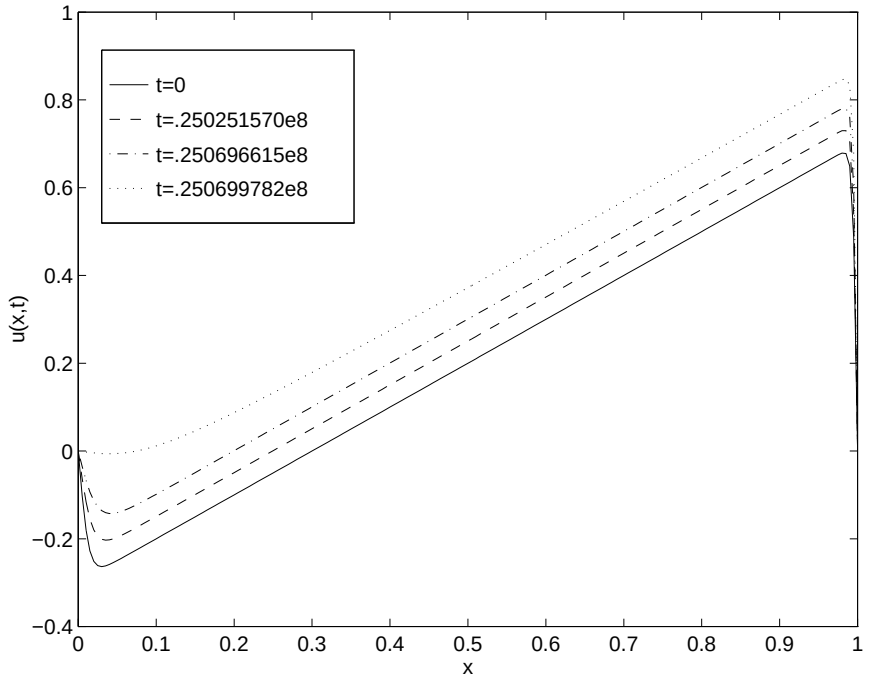

Figure 2.7: Plot of the numerical solution to (2.5) at different times. Here $\varepsilon = 0.002$ and $x_0^0 = 0.3$.

Figure 2.2 it takes a time $t \approx 117.1$ for the tip of the parabola to move from its initial position $x_0^0 = 0.45$ to its final equilibrium state at $x_0 = 0$. The height $h(t)$ of the parabola increases by roughly 5.86 during this evolution. A similar observation was observed in the numerical computations of [77] (see Figure 3 of [77]). When ε is decreased, the height $h(t)$ can increase dramatically as shown in Figure 2.12. This can be explained from (2.84b) since for $\varepsilon \to 0$

$$h(t) \sim \int_0^t \left(\frac{1}{2} x_0^2 - \frac{1}{2} x_0 + \frac{1}{6} \right) \, dt \geq \frac{1}{24} t \, . \tag{2.85}$$

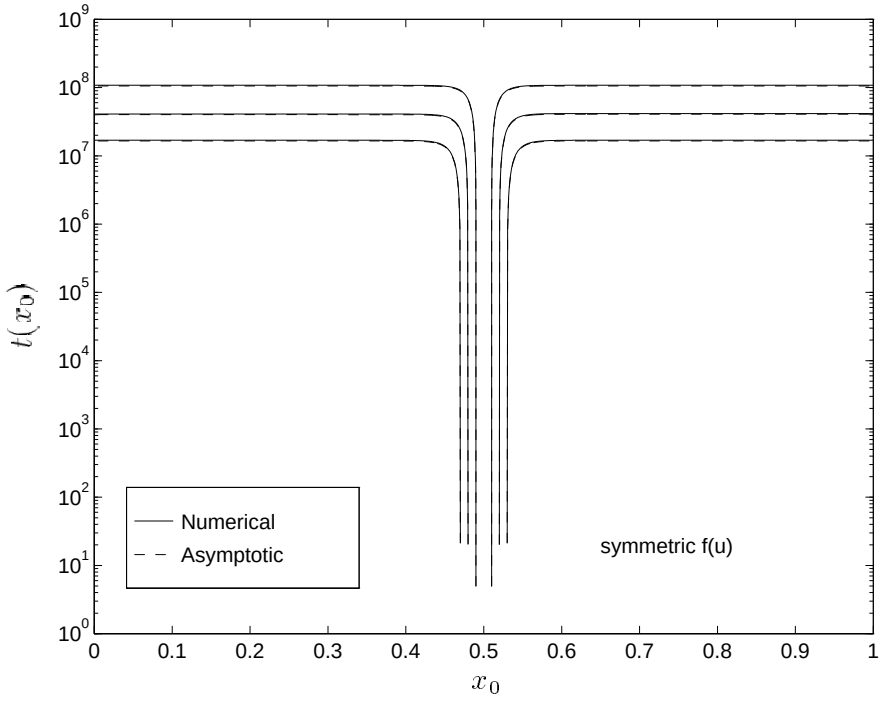

Figure 2.8: Plots of asymptotic and numerical results for the tip location $t = t(x_0)$ of the parabolic–shaped flame–front interface for (2.5) with $\varepsilon = 0.005$. A logarithmic (base 10) scale is used for the vertical axis.

ε	x_0^m (asy.)	x_0^m (num.)
0.004	0.4412712	0.4412866
0.005	0.4420214	0.4420579
0.006	0.4427894	0.4428554
0.007	0.4435751	0.4436858
0.008	0.4443787	0.4445542
0.009	0.4452002	0.4454679
0.010	0.4460395	0.4464367
0.011	0.4468968	0.4474730
0.012	0.4477721	0.4485919
0.013	0.4486654	0.4498109

Table 2.9: The equilibrium location of x_0^m for the asymmetric $f(u)$ of (2.80).

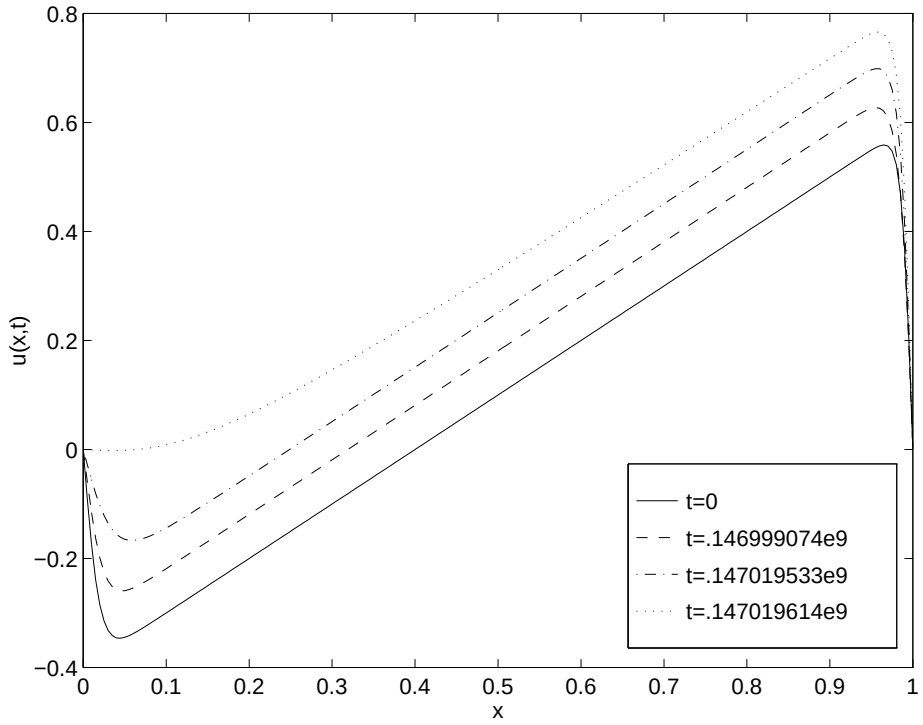

Figure 2.9: Plot of the numerical solution to (2.10) with the asymmetric $f(u)$ of (2.80) at different times. Here $\varepsilon = 0.004$, and $x_0^0 = 0.4$.

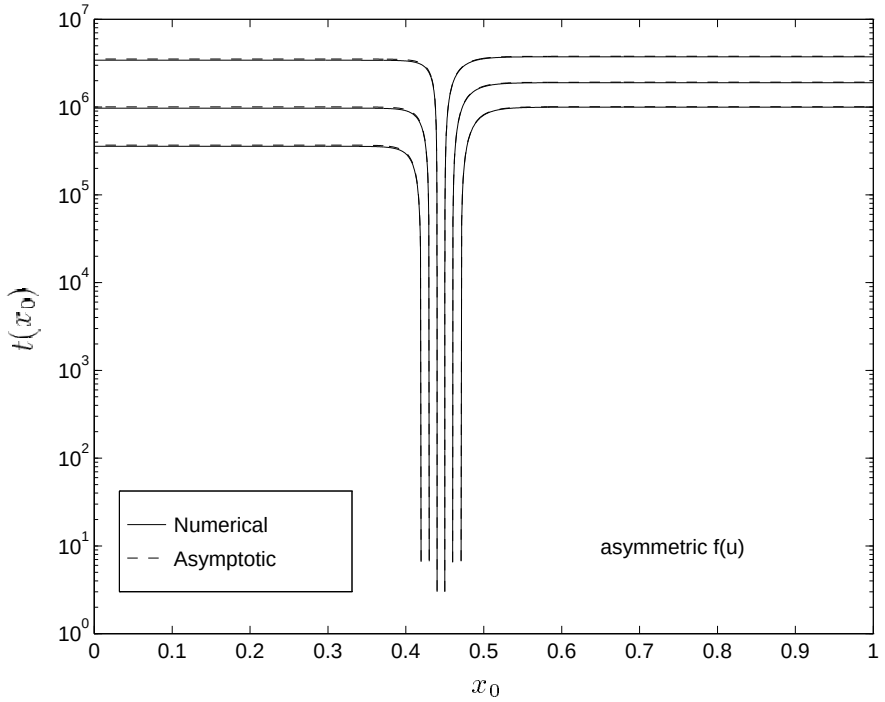

Figure 2.10: Plots of asymptotic and numerical results for $t = t(x_0)$ for (2.10) with the asymmetric $f(u)$ of (2.80) with $\varepsilon = 0.006$. A logarithmic (base 10) scale is used for the vertical axis.

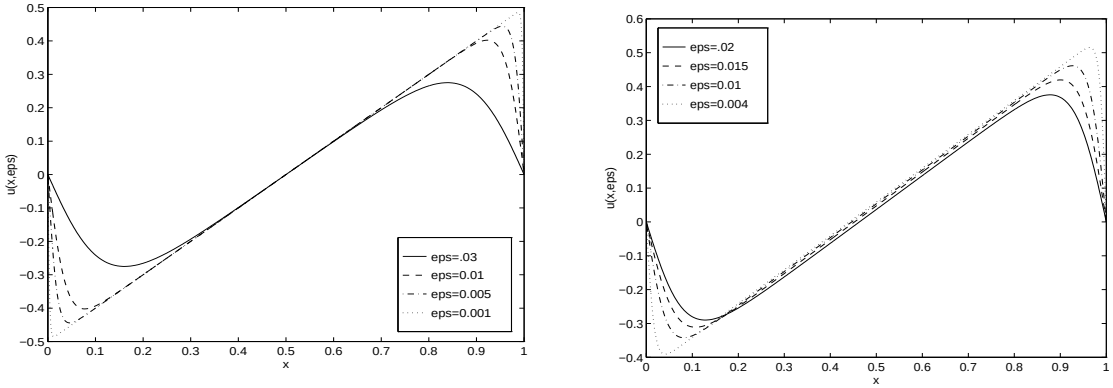

Figure 2.11: Plots of the equilibrium solutions to (2.11) versus x for various ε: (a) For $f(u) = u^2/2$, $x_0^m \equiv \frac{1}{2}$; (b) For an asymmetric $f(u)$ of (2.80), x_0^m are given in Table 2.9.

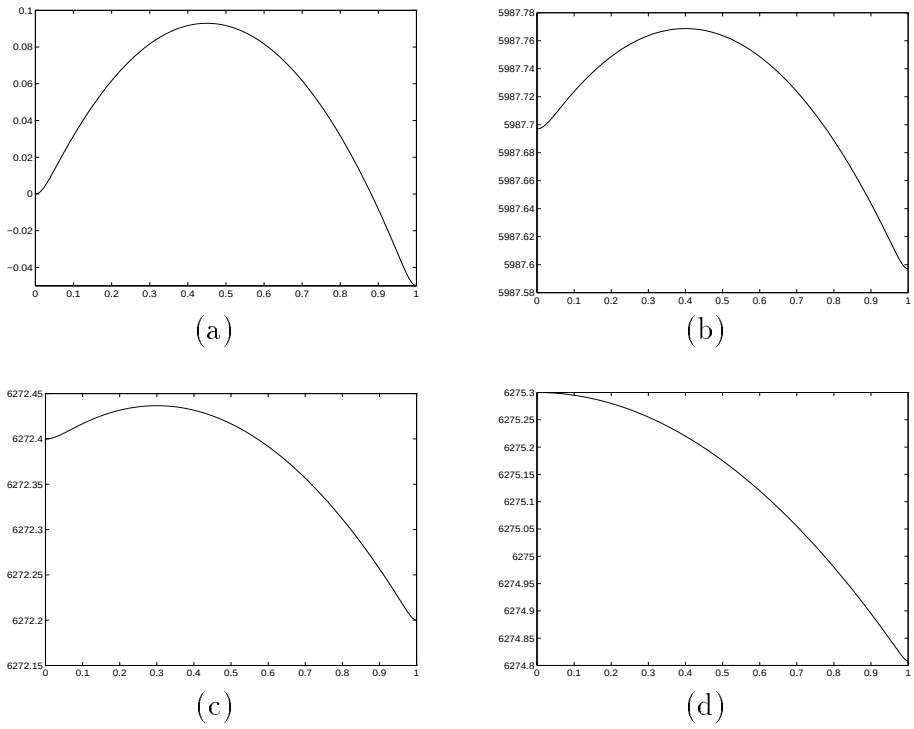

Figure 2.12: Plot of $y(x,t)$ versus x given by (2.84) with $\varepsilon = .006$ that approximates the metastable behavior in (2.4). (a) initial quasi–equilibrium solution $y(x,t)$ with tip location $x_0 = 0.45$ at $t = 0$; (b) quasi–equilibrium solution with $x_0 = 0.4$ at $t = 130745$; (c) quasi–equilibrium solution with $x_0 = 0.3$ at $t = 136353$; (d) final stable equilibrium solution at $t \geq 136394$.

Chapter 3

Metastability in Slowly Varying Geometry Problems

3.1 Convection-Diffusion-Reaction Equations in Thin Domains

In this chapter, we study two singularly perturbed evolution equations exhibiting metastable dynamics in a weakly inhomogeneous medium. The first problem we consider is the following generalized Ginzburg-Landau equation, which models the slow propagation of an internal layer in a thin channel

$$u_t = \frac{\varepsilon^2}{A}\,(Au_x)_x + Q(u)\,, \qquad 0 < x < 1\,, \quad t > 0\,, \tag{3.1a}$$

$$u_x(0,t) = u_x(1,t) = 0\,, \qquad u(x,0) = u_0(x)\,. \tag{3.1b}$$

Here $\varepsilon > 0$ is a small parameter and $A = A(x,\varepsilon) > 0$ is the local cross-sectional area of the channel, which is specified below. In addition, $Q(u)$ is a smooth function with exactly three zeroes on the interval $[s_-, s_+]$ located at $u = s_- < 0$, $u = 0$ and $u = s_+ > 0$. Introducing the double-well potential $V(u)$ by $V(u) \equiv -\int_{s_-}^{u} Q(\eta)\,d\eta$, we assume that

$$Q'(s_\pm) < 0\,, \qquad Q'(0) > 0\,, \qquad V(s_+) = 0\,. \tag{3.2}$$

A typical example is $Q(u) = 2(u - u^3)$ for which $s_\pm = \pm 1$ and $V(u) = \frac{1}{2}(1-u^2)^2$.

The motivation for studying (1.1) is related to the problem of determining the conditions for the existence of stable spatially inhomogeneous steady-state solutions to the Ginzburg-Landau equation

$$u_t = \triangle u + Q(u)\,, \quad x \in D\,; \qquad \partial_n u = 0\,, \quad x \in \partial D\,. \tag{3.3}$$

Here D is a bounded domain in R^N and ∂_n denotes the outward normal derivative to ∂D. In a convex domain it is well-known that (3.3) does not admit a stable spatially inhomogeneous steady-state solution (cf. [28], [73]). However, this non-existence result does not hold for non-convex domains (cf. [45], [57], [73]). In Appendix B we show how (3.1) arises from an asymptotic reduction of (3.3) when D is a thin, axially symmetric domain as shown in Fig. 3.1. In this context, x represents the direction along the axis of the channel and A represents the local cross-sectional area of the channel. When $A \equiv 1$, which yields a constant channel cross-section, it is well-known that the propagation of an internal layer for (3.1) is exponentially slow as $\varepsilon \to 0$ (i. e. metastable) and that a stable spatially inhomogeneous solution for (3.1) does not exist (see [26], [39], [62], [109]). When $A \equiv 1$, the metastability is a consequence of an exponentially small eigenvalue for the linearization of (3.1) around an internal layer solution.

This exponential ill-conditioning suggests that the dynamics of an internal layer solution for (3.1) will depend very sensitively on the channel cross-section A, when A is slightly offset from the uniform value $A \equiv 1$. In particular, exponentially small changes in $A-1$ should influence the dynamics greatly. Therefore, in §3.2 we study (3.1) as $\varepsilon \to 0$ for an $A(x;\varepsilon)$ of the form

$$A(x;\varepsilon) = 1 + \varepsilon^{\mu} g(x) e^{-\varepsilon^{-1} d}\,. \tag{3.4}$$

Here μ and $d > 0$ are constants and $g(x)$ is smooth. If $g''(x) < 0$ then D is convex and we expect that (3.1) will have no stable spatially inhomogeneous equilibrium solutions. When $g''(x) > 0$ and $0 < d < d_c$, where d_c is some constant, we show in §3.2 that (3.1) can have a stable spatially inhomogeneous equilibrium internal layer solution where the internal layer is located at a zero of $g'(x)$. This phenomenon in which an internal layer or other localized structure is stabilized by a weakly inhomogeneous medium is called pinning. The effect of pinning of other localized structures such as vortices in

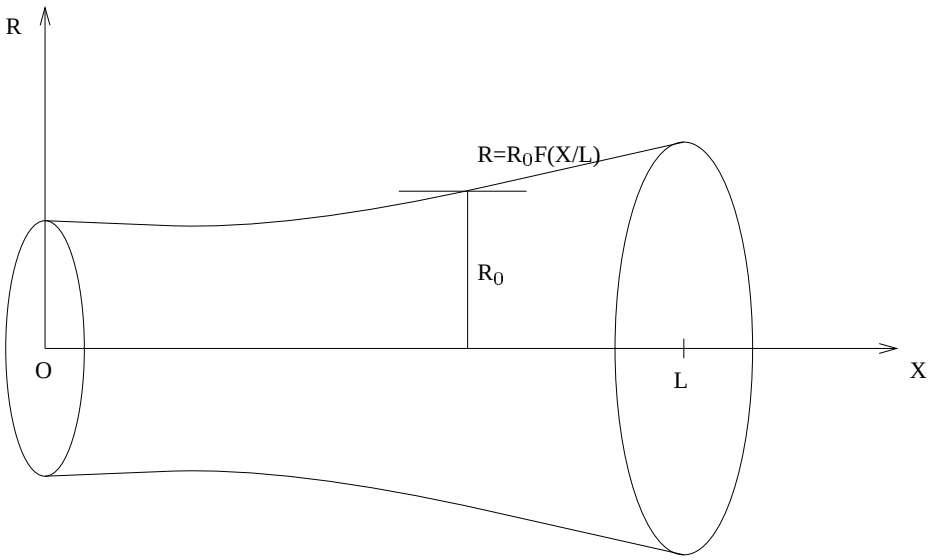

Figure 3.1: A cylinder of revolution with cross-section described in dimensional variables by $R = R_0 F(X/L)$.

superconductivity has been studied in [29], [70]. When $g''(x) > 0$ and $d = d_c$, we show in §3.2 that the internal layer can be pinned at other locations in the interval $[0, 1]$. In §3.2.1 we provide an asymptotic estimate for the principal eigenvalue λ_0 associated with the linearization of (3.8). In §3.2.2 we use the projection method to derive a differential equation for the location $x_0(t)$ of the internal layer, and we determine its limiting behavior as $t \to \infty$. Finally, in §3.2.3 we compare our asymptotic results with corresponding results obtained from a full numerical solution of (3.1).

The second problem we consider is the nonlinear convection-diffusion equation

$$u_t + [f(u)]_x - c(x;\varepsilon)h(u) = \varepsilon u_{xx}\,, \qquad 0 < x < 1\,,\ \ t > 0\,, \tag{3.5a}$$

$$u(0) = \alpha_-\,,\ \ u(1) = \alpha_+\,; \qquad u(x,0) = u_0(x)\,. \tag{3.5b}$$

Here $0 < \varepsilon \ll 1$, $\alpha_- > 0$ and $\alpha_+ < 0$ are constants, and $h(u)$ and $f(u)$ are smooth. The flux function $f(u)$ is assumed to be convex and satisfies

$$f(\alpha_+) = f(\alpha_-)\,, \qquad f(0) = f'(0) = 0\,, \qquad uf'(u) > 0 \quad \text{for} \quad u \neq 0\,. \tag{3.6}$$

The function $c(x;\varepsilon)$ is chosen to be

$$c(x;\varepsilon) = -\varepsilon^{\mu} g'(x) e^{-\varepsilon^{-1} d}\,. \tag{3.7}$$

Here μ and $d > 0$ are constants and $g(x)$ is smooth.

A primary motivation for studying (3.5)-(3.7) is that for the special case when $h(u) = u$ and $f(u) = u^2/2$, this problem models transonic gas flow in a nozzle of cross-sectional area $A(x;\varepsilon)$ given by $c(x;\varepsilon) = -A_x(x;\varepsilon)/A(x;\varepsilon)$ (cf. [53], [51], [71], [94]). Hence, for $\varepsilon \ll 1$, the cross-sectional area $A(x;\varepsilon)$ can be taken precisely as in (3.4). In this context, the nozzle is said to be divergent if $g'(x) > 0$ for all x, convergent if $g'(x) < 0$ for all x, and convergent-divergent if $g'(x)$ has no definite sign. For Burgers equation ($f(u) = u^2/2$) in a straight channel where $g(x) \equiv 0$, it was shown in [61], [64] and [87] that there exists a unique and stable equilibrium shock layer solution centered at $x_0 = \frac{1}{2}$. It was also shown that for the corresponding time-dependent problem, a viscous shock, which gets formed from the initial data, tends toward the steady-state solution only over an asymptotically exponentially long time interval as $\varepsilon \to 0$. This metastable behavior arises from the occurrence of an asymptotically exponentially small principal eigenvalue for the linearization of Burgers equation around the viscous shock solution. In view of this exponential ill-conditioning of Burgers equation, we expect that shock-layer solutions can be significantly altered by perturbing the differential operator by exponentially small terms. The effect of such spatially homogeneous perturbations were considered in [64].

Our primary goal in §3.3 is to study the pinning effect induced by the spatially inhomogeneous term $c(x;\varepsilon)$ in (3.5). In particular, we analyze the existence, stability

and dynamics of equilibrium and time-dependent shock-layer solutions to (3.5). In §3.3.1 we obtain an asymptotic estimate for the principal eigenvalue λ_0 associated with the linearization of (3.5) around a shock-layer profile. In §3.3.2 we use the projection method of [110] to derive a differential equation for the location $x_0(t)$ of the shock-layer trajectory. We then analyze the equilibrium solutions of this differential equation and determine their stability properties. In §3.3.3 we illustrate the results for certain forms of $g(x)$ when $h(u) = u$ and $f(u) = u^2/2$, modeling transonic nozzle flow, and we compare our asymptotic results with corresponding numerical results. Our results show that, under certain assumptions, there can exist stable steady-state shock-layer solutions along a convergent nozzle or in the convergent part of a convergent-divergent nozzle. In contrast, it was shown using a nonlinear stability analysis in [34] that when $c(x;\varepsilon)$ is independent of ε and when the diffusive term εu_{xx} in (3.5) is absent, the corresponding inviscid problem does not admit stable shock waves in these nozzles.

3.2 A Generalized Ginzburg-Landau Equation

We now study (3.1) in the limit $\varepsilon \to 0$ with $A(x;\varepsilon)$ as given in (3.4). A one-layer metastable pattern for (3.1) can be approximated by

$$u(x,t) \sim u_c\left[\varepsilon^{-1}(x - x_0(t))\right] , \tag{3.8}$$

where $u_c(z)$ is the heteroclinic orbit that connects s_+ and s_-, which satisfies

$$u_c''(z) + Q(u_c) = 0\,, \quad -\infty < z < \infty\,,\ u_c(0) = 0\,, \tag{3.9a}$$

$$u_c(z) \sim s_- + a_- e^{\nu_- z}\,, \quad \text{as } z \to -\infty\,; \quad u_c(z) \sim s_+ - a_+ e^{-\nu_+ z}\,, \quad \text{as } z \to \infty\,. \tag{3.9b}$$

Here the positive constants $\nu_\pm$ and $a_\pm$ are defined by

$$\nu_\pm = [-Q'(s_\pm)]^{\frac{1}{2}}\,, \quad \log a_\pm = \log(\pm s_\pm) + \int_0^{s_\pm}\left[\frac{\pm\nu_\pm}{[2V(s)]^{\frac{1}{2}}} + \frac{1}{s - s_\pm}\right] ds\,. \tag{3.10}$$

We now look for a solution to (3.1) for $t \gg 1$ in the form

$$u(x,t) = u_c\left[\varepsilon^{-1}(x - x_0(t))\right] + w(x,t)\,, \tag{3.11}$$

where $w \ll u_c$ and $w_t \ll \partial_t u_c$. The trajectory $x_0 = x_0(t)$ gives the approximate location of the zero of $u(x,t)$ during the metastable evolution. Substituting (3.11) into (3.1), and using (3.9), we obtain that w satisfies the quasi-steady problem

$$L_\varepsilon w = A\left(-\varepsilon^{-1}x_0' u_c'(z) - \varepsilon\frac{A_x}{A}u_c'\right)\,, \quad 0 < x < 1\,, \tag{3.12a}$$

$$w_x(0,t) = u_x(0,t) - \partial_x u_c|_{x=0} \sim -\varepsilon^{-1}a_-\nu_- e^{-\varepsilon^{-1}\nu_- x_0}\,, \tag{3.12b}$$

$$w_x(1,t) = u_x(1,t) - \partial_x u_c|_{x=1} \sim -\varepsilon^{-1}a_+\nu_+ e^{-\varepsilon^{-1}\nu_+(1-x_0)}\,, \tag{3.12c}$$

where $z = \varepsilon^{-1}[x - x_0(t)]$. Here A is given in (3.4) and the operator L_ε is defined by

$$L_\varepsilon w = \varepsilon^2\left(Aw_x\right)_x + AQ'(u_c)w\,. \tag{3.13}$$

3.2.1 The Eigenvalue Analysis

For a fixed $x_0 \in (0,1)$, we now study the eigenvalue problem

$$L_\varepsilon\phi = \lambda\phi\,, \quad 0 < x < 1\,, \tag{3.14a}$$

$$\phi_x(0) = \phi_x(1) = 0\,, \quad (\phi,\phi) = 1\,. \tag{3.14b}$$

Here $(u,v) \equiv \int_0^1 uv\,dx$. For this eigenproblem, the eigenvalues λ_j for $j \geq 0$ are real and the principal eigenvalue λ_0 is exponentially small as $\varepsilon \to 0$. To estimate λ_0 and the corresponding eigenfunction ϕ_0 we use the trial function $\tilde{\phi}_0 \equiv u_c'[\varepsilon^{-1}(x - x_0)]$. Then, upon integrating by parts, we derive

$$\lambda_0\left(\phi_0,\tilde{\phi}_0\right) = \left(\phi_0, L_\varepsilon\tilde{\phi}_0\right) - \varepsilon^2 A\phi_0\tilde{\phi}_{0x}|_0^1\,. \tag{3.15}$$

Using (3.4) and (3.12) we estimate

$$L_\varepsilon\tilde{\phi}_0 = \varepsilon^{\mu+2}g'(x)e^{-\varepsilon^{-1}d}\tilde{\phi}_{0x}\,. \tag{3.16}$$

Since $L_\varepsilon\tilde{\phi}_0$ is exponentially small and $\tilde{\phi}_0$ is of one sign, we have that $\phi_0 \sim N_0\tilde{\phi}_0$ away from $O(\varepsilon)$ regions near the endpoints at $x = 0$ and $x = 1$, where N_0 is a normalization constant. However, this approximate form for ϕ_0 does not satisfy the homogeneous boundary conditions in (3.14b) and so we cannot use it to calculate $\phi_0(0)$ and $\phi_0(1)$. Instead, these quantities are calculated after constructing boundary layer profiles for ϕ_0 near each endpoint.

Since A is exponentially close to 1, the boundary layer analysis given in [109] for the case $A \equiv 1$ can be used to calculate

$$\phi_0(0) \sim 2N_0 a_- \nu_- e^{-\varepsilon^{-1}\nu_- x_0}\,, \qquad \phi_0(1) \sim 2N_0 a_+ \nu_+ e^{-\varepsilon^{-1}\nu_+ (1-x_0)}\,. \tag{3.17}$$

Then, since the dominant contribution to the inner product integrals arises from the region near $x = x_0$, the left side of (3.15) is estimated as

$$\left(\phi_0, \tilde{\phi}_0\right) \sim N_0 \left(\tilde{\phi}_0, \tilde{\phi}_0\right) \sim \varepsilon\beta_0 N_0\,; \quad \beta_0 \equiv \int_{-\infty}^{\infty} \left[u_c'(z)\right]^2\, dz = \int_{s_-}^{s_+} \left[2V(u)\right]^{1/2}\, du\,. \tag{3.18}$$

Next, we use (3.16) to estimate

$$\left(\phi_0, L_\varepsilon\tilde{\phi}_0\right) \sim N_0 \left(\tilde{\phi}_0, L_\varepsilon\tilde{\phi}_0\right) \sim N_0\varepsilon^{\mu+2} e^{-\varepsilon^{-1}d} \int_{-\infty}^{\infty} u_c'(z) g'(x_0 + \varepsilon z) u_c''(z)\, dz\,. \tag{3.19}$$

By using a Taylor series expansion for $g'(x_0 + \varepsilon z)$ we get

$$\left(\phi_0, L_\varepsilon\tilde{\phi}_0\right) \sim -N_0\varepsilon^{\mu+2} e^{-\varepsilon^{-1}d} \sum_{k=0}^{\infty} \varepsilon^k g^{(k+1)}(x_0)\gamma_k\,, \tag{3.20}$$

where the coefficients γ_k are defined by

$$\gamma_k \equiv -\frac{1}{k!} \int_{-\infty}^{\infty} u_c'(z) u_c''(z) z^k\, dz\,, \quad k = 0, 1, \ldots\,. \tag{3.21}$$

The first two coefficients are readily calculated to be

$$\gamma_0 = 0\,, \qquad \gamma_1 = \beta_0/2\,. \tag{3.22}$$

Moreover, if $u_c(z)$ is an even function then $\gamma_{2k} = 0$. Finally, substituting (3.17)–(3.20) into (3.15), we obtain the following key estimate for λ_0:

Proposition 3.1 (Exponentially Small Eigenvalue): *For $\varepsilon \to 0$, the exponentially small eigenvalue of (3.14) satisfies*

$$\begin{aligned}\lambda_0 = \lambda_0(x_0) \;\; &\sim \;\; 2\beta_0^{-1}\left\{a_+^2\nu_+^3 e^{-2\varepsilon^{-1}\nu_+(1-x_0)} + a_-^2\nu_-^3 e^{-2\varepsilon^{-1}\nu_- x_0}\right\} \\ &\quad -\beta_0^{-1}\varepsilon^{\mu+1}e^{-\varepsilon^{-1}d}\sum_{k=1}^{\infty}\varepsilon^k g^{(k+1)}(x_0)\gamma_k\,. \end{aligned} \tag{3.23}$$

Here $\nu_\pm$, $a_\pm$ are defined in (3.10), β_0 is defined in (3.18), and γ_k is defined in (3.21).

3.2.2 The Metastabilty Analysis

We now derive a differential equation for the location $x_0 = x_0(t)$ of the internal layer trajectory. We first expand the solution w to (3.12) in terms of the eigenfunctions ϕ_j of (3.14) as

$$w(x,t) = \sum_{j=0}^{\infty}\frac{c_j(t)}{\lambda_j}\phi_j(x)\,. \tag{3.24}$$

The coefficients c_j, which are found by integrating by parts, are

$$c_j = -\varepsilon^{-1}\left(Ax_0'u_c', \phi_j\right) - \varepsilon\left(A_x u_c', \phi_j\right) - \varepsilon^2 A w_x\phi_j|_0^1\,, \qquad j = 0, 1, \ldots\,. \tag{3.25}$$

Since $\lambda_0 \to 0$ as $\varepsilon \to 0$, a necessary condition for the solvability of (3.12) is that $c_0 \to 0$ as $\varepsilon \to 0$. Setting $c_0 = 0$ in (3.25), we obtain the asymptotic differential equation for $x_0 = x_0(t)$

$$\varepsilon^{-1}x_0'\left(Au_c', \phi_0\right) \sim -\varepsilon\left(A_x u_c', \phi_0\right) - \varepsilon^2\phi_0 A w_x|_0^1\,. \tag{3.26}$$

To obtain an explicit differential equation for $x_0(t)$ we must evaluate the inner product integrals and the boundary terms in (3.26). The dominant contributions to the inner product integrals arise from the region near $x = x_0$.

First, the boundary terms in (3.26) can be calculated asymptotically from (3.12) and (3.17) as

$$\varepsilon^2 A\phi_0 w_x|_0^1 \sim 2N_0\varepsilon\left(-a_+^2\nu_+^2 e^{-2\varepsilon^{-1}\nu_+(1-x_0)} + a_-^2\nu_-^2 e^{-2\varepsilon^{-1}\nu_- x_0}\right)\,. \tag{3.27}$$

Now to evaluate $\left(A_x u_c^{'}, \phi_0\right)$ we use (3.4) and $\phi_0 \sim N_0 u_c^{'}$ to get

$$\left(A_x u_c^{'}, \phi_0\right) \sim N_0 \varepsilon^{\mu+1} e^{-\varepsilon^{-1} d} \int_{-\infty}^{\infty} g'(x_0 + \varepsilon z)[u_c'(z)]^2 \, dz \, . \tag{3.28}$$

By using a Taylor series expansion of $g(x_0 + \varepsilon z)$ we obtain

$$\left(A_x u_c^{'}, \phi_0\right) \sim N_0 \varepsilon^{\mu+1} e^{-\varepsilon^{-1} d} \sum_{k=0}^{\infty} \varepsilon^k g^{(k+1)}(x_0) \beta_k \, , \tag{3.29}$$

where the coefficients β_k are defined by

$$\beta_k = \frac{1}{k!} \int_{-\infty}^{\infty} [u_s'(z)]^2 z^k \, dz \, , \qquad k = 0, 1, \ldots \, . \tag{3.30}$$

Upon integrating by parts, we can show that $\beta_k = 2\gamma_{k+1}$ for $k \geq 0$, where γ_k is defined in (3.21). Next, for $\varepsilon \to 0$, we estimate the left side of (3.26) to get

$$\varepsilon^{-1} x_0^{'} \left(A u_c^{'}, \phi_0\right) \sim N_0 \beta_0 x_0^{'} \, . \tag{3.31}$$

Finally, substituting (3.27), (3.29) and (3.31) into (3.26) we obtain our main result for the metastable dynamics associated with the generalized Ginzburg-Landau equation (3.1):

Proposition 3.2 (Metastable Dynamics): *For $\varepsilon \to 0$ and $t \gg 1$, a one-layer metastable pattern for (3.1) is represented by $u(x,t) \sim u_c[\varepsilon^{-1}(x - x_0(t))]$, where the internal layer trajectory $x_0(t)$ satisfies the asymptotic differential equation*

$$\begin{aligned} x_0^{'} \sim h(x_0) \quad \equiv \quad & 2\varepsilon \beta_0^{-1} \left[a_+^2 \nu_+^2 e^{-2\varepsilon^{-1} \nu_+ (1 - x_0)} - a_-^2 \nu_-^2 e^{-2\varepsilon^{-1} \nu_- x_0} \right] \\ & - \varepsilon^{\mu+2} e^{-\varepsilon^{-1} d} \beta_0^{-1} \sum_{k=0}^{\infty} \varepsilon^k \beta_k g^{(k+1)}(x_0) \, . \end{aligned} \tag{3.32}$$

Here $\nu_\pm$, $a_\pm$ are defined in (3.10), β_k for $k \geq 0$ is defined in (3.30), and $u_c(z)$ is defined in (3.9).

The following equilibrium result is obtained by setting $x_0^{'} = 0$ in (3.32):

Corollary 3.1 (Equilibrium): *For $\varepsilon \to 0$ an equilibrium solution $U(x;\varepsilon)$ to (3.1) corresponding to a one-layer pattern is given by $U(x;\varepsilon) \sim u_c\left[\varepsilon^{-1}(x - x_0^m)\right]$, where $u_c(z)$ is defined in (3.9) and x_0^m satisfies the nonlinear algebraic equation $h(x_0) = 0$, i.e.,*

$$a_+^2\nu_+^2 e^{-2\varepsilon^{-1}\nu_+(1-x_0)} - a_-^2\nu_-^2 e^{-2\varepsilon^{-1}\nu_- x_0} = \frac{1}{2}\varepsilon^{\mu+1}e^{-\varepsilon^{-1}d}\sum_{k=0}^{\infty}\varepsilon^k\beta_k g^{(k+1)}(x_0)\,. \tag{3.33}$$

We now discuss the behavior of the equilibrium solutions for $x_0(t)$. We first observe that in (3.32), $h(0) < 0$ and $h(1) > 0$ for $\varepsilon \to 0$. Thus, there exists at least one equilibrium value x_0^m for $x_0(t)$. The existence of any other equilibrium value for x_0 depends on the constants d and μ and the function $g'(x)$. For example, when $d > 0$ is sufficiently large, the terms in (3.33) proportional to $e^{-\varepsilon^{-1}d}$ are insignificant and consequently, the equilibrium value for x_0 is given uniquely by

$$x_0^m \sim \frac{\nu_+}{\nu_- + \nu_+} - \frac{\varepsilon}{\nu_- + \nu_+}\log\left[\frac{a_+\nu_+}{a_-\nu_-}\right]\,. \tag{3.34}$$

Alternatively, when $d > 0$ is sufficiently small, the right side of (3.33) dominates the left side of (3.33) and, consequently, for $\varepsilon \to 0$, (3.33) has a root x_0^m near each zero of $g'(x)$. As shown in the examples below, when d is near some critical value so that the right and left sides of (3.33) balance as $\varepsilon \to 0$, we can have equilibrium internal layer solutions centered at different points on the interval $[0,1]$.

Although the only stable equilibrium solutions to (3.3) in a convex domain are constants, the generalized G-L equation (3.1) may admit stable spatially dependent equilibrium solution with an internal layer structure. Let x_0^m satisfy $h(x_0^m)=0$. Then, since $\beta_k = 2\gamma_{k+1}$, as seen by comparing (3.21) and (3.30), we can show that $h'(x_0^m) = 2\lambda_0(x_0^m)$, where λ_0 is given in (3.23). This shows that the decay rate for the differential equation (3.32) associated with infinitesimal perturbations about x_0^m is $2\lambda_0^m$, where $\lambda_0^m \equiv \lambda_0(x_0^m)$. This leads to the following criterion for the stability of the equilibrium internal layer solutions:

Corollary 3.2 (Stability of Equilibrium): *Let* x_0^m *satisfy* $h(x_0^m) = 0$. *Then the equilibrium solution to (3.1) has the form* $U \sim u_c[\varepsilon^{-1}(x - x_0^m)]$ *and is stable (unstable) if* $\lambda_0(x_0^m) < 0$ $(\lambda_0(x_0^m) > 0)$. *Here* $u_c(z)$, $\lambda_0(x_0)$ *and* $h(x_0)$ *are given in (3.9), (3.23) and (3.32).*

Using this corollary, it follows that an equilibrium solution with an internal layer located at $x_0 = x_0^m$ is unstable when $g''(x_0^m) < 0$. Since $g''(x) < 0$ corresponds to a convex domain in higher dimensions, this result re-states the conclusion in [28] and [73] concerning the instability of non-constant steady-state solutions to (1.3) in convex domains. However, when $g''(x_0^m) > 0$, then λ_0^m can be negative for certain choices of μ and d, resulting in a stable internal layer solution centered at x_0^m. The key point to construct a stable equilibrium solution is to guarantee that (3.32) has multiple equilibria corresponding to simple zeroes of $h(x_0)$. Then, we must have exactly one stable equilibrium of (3.32) between every two consecutive unstable equilibria. We will see from the examples below that this can be realized by selecting the cross-sectional profile $A(x, \varepsilon)$ (i. e. $g(x)$) appropriately.

3.2.3 Comparison of Asymptotic and Numerical Results

We now compare the asymptotic results obtained above with the corresponding full numerical results computed directly from (3.1). We also show the existence of stable equilibrium solutions with an internal layer structure to the generalized G-L equation (3.1).

In all of the calculations below, we have taken $Q(u) = 2(u - u^3)$, for which $a_+ = a_- = 2$, $\nu_+ = \nu_- = 2$ and $u_s(z) = \tanh(z)$. In addition, we calculate that $\beta_0 = 4/3$, $\gamma_1 = 2/3$, $\gamma_3 = (\pi^2 - 6)/36$ and $\gamma_{2k} = 0$ for $k \geq 0$. Thus, (3.23) becomes

$$\lambda_0 = \lambda_0(x_0) \quad \sim \quad 48\left[e^{-4\varepsilon^{-1}(1-x_0)} + e^{-4\varepsilon^{-1}x_0}\right]$$

$$-\frac{1}{2}\varepsilon^{\mu+2}e^{-\varepsilon^{-1}d}\left[g''(x_0)+\frac{\pi^2-6}{24}g^{(4)}(x_0)\varepsilon^2+\cdots\right]. \qquad (3.35)$$

Noting that $\beta_k = 2\gamma_{k+1}$, the differential equation (3.32) becomes

$$\begin{aligned} x_0' \sim h(x_0) &= 24\varepsilon\left[e^{-4\varepsilon^{-1}(1-x_0)}-e^{-4\varepsilon^{-1}x_0}\right] \\ &\quad -\varepsilon^{\mu+2}e^{-\varepsilon^{-1}d}\left[g'(x_0)+\frac{\pi^2-6}{24}g^{(3)}(x_0)\varepsilon^2+\cdots\right]. \qquad (3.36) \end{aligned}$$

To check the validity of (3.36), we solved (3.1) numerically for a number of choices of $g(x)$, three of which are described below.

To compute numerical solutions to (3.1) we use a transverse method of lines approach (cf. [7]). This method is based on replacing the time derivative in (3.1) by a difference approximation and then solving the resulting boundary value problems in space. More specifically, we convert the time-dependent problem (3.1) to a set of boundary value problems using the second order Backward Differential Formulas (BDF) [7], which we solve at each time step using the boundary value solver COLSYS [6]. Since the motion of the internal layer solutions is exponentially slow, we found it necessary to implement a time-stepping control strategy to efficiently track the solutions to (3.1) over long time intervals. To achieve this, we used the l_2-norm of the difference between the solutions of the second order and the third order BDF schemes as an error indicator to reject large inaccurate time steps or to enlarge unnecessary small time steps. See [100] for details of these algorithms, where they were used in a different context.

The metastablity result (3.36) is valid only after the completion of an $O(1)$ transient period that describes the formation of an internal layer from initial data. In the computations below we took $u(x,0) = u_c(\varepsilon^{-1}[x-x_0^0])$ as the initial data for (3.1), where $u_c(z)$ is defined in (3.9) and $x_0^0 \in (0,1)$ is the initial zero of u. To eliminate any unwanted transient effects we computed the solution to (3.1) with this initial data until $t = 5$. At this time, x_0^0 is reset to be the zero of u predicted by the numerical method. This

new value for x_0^0 is used as the initial condition for (3.36). The differential equation (3.36) is then solved numerically for $x_0(t)$ using the initial value solver DP12 [27] and for $t(x_0)$ using a numerical quadrature, and the results are compared with corresponding numerical results for the zero of u computed from the finite difference scheme.

x_0	t(asy.)	t(num.)
0.3991489	0.100998498×10^5	$0.100998673\ \times10^5$
0.3902339	0.111103064×10^6	$0.111104540\ \times10^6$
0.3459655	0.515111092×10^6	$0.515123233\ \times10^6$
0.3013976	0.818109359×10^6	$0.818137253\ \times10^6$
0.2646857	0.102010258×10^7	$0.102014660\ \times10^7$
0.2024301	0.127991981×10^7	$0.127995306\ \times10^7$
0.1683312	0.133126841×10^7	$0.133127901\ \times10^7$
0.1350323	0.133755526×10^7	$0.133756144\ \times10^7$
0.0753443	0.133805967×10^7	$0.133806497\ \times10^7$

Table 3.1: **Example 3.1**: A comparison of the asymptotic and numerical results for $t = t(x_0)$ for $Q(u) = 2(u - u^3)$ and $g(x) = -\frac{1}{2}(x - \frac{1}{2})^2$ with $\varepsilon = 0.05$, $\mu = 0$, $d = 0.4$ and $x_0(0) = 0.4$.

Example 3.1: Let $g(x) = -\frac{1}{2}(x-\frac{1}{2})^2$, which corresponds to a convex domain. Then a solution to the equilibrium problem $h(x_0) = 0$ for (3.36) is $x_0^m = 1/2$, independent of the constants μ and d. This is the only solution to $h(x_0) = 0$, since $g''(x_0) < 0$ implies that $h'(x_0) > 0$ for $x_0 \in [0, 1]$. This unique equilibrium solution $x_0^m = 1/2$ is unstable since $\lambda_0(1/2) > 0$ in (3.35). This conclusion is confirmed by the full numerical results shown in Table 3.1. This table displays the asymptotic and numerical results for the elapsed time as a function of the internal layer location x_0 for $\varepsilon = 0.05$, $\mu = 0$ and $d = 0.4$, when the initial location is $x_0(0) = 0.4$. The results for $t = t(x_0)$ agree to at least four significant decimal places.

Example 3.2: We choose $g(x) = \frac{1}{2}(x - \frac{1}{2})^2$, which corresponds to a non-convex domain. Again, $x_0^m = 1/2$ is an equilibrium solution to (3.36) for any μ and d. However,

this solution can be stable depending on the values of μ and d. From (3.35), a simple calculation gives $\lambda_0(1/2) = -\frac{1}{2}\varepsilon^{\mu+2}e^{-\varepsilon^{-1}d} + 96e^{-2\varepsilon^{-1}}$. Let d_c be the zero of $\lambda_0(1/2)$ as a function of d, i.e., $d_c = 2 - \varepsilon\log 192 + (\mu+2)\varepsilon\log\varepsilon$. Then, from Corollary 2.4, the equilibrium $x_0^m = 1/2$ is stable (unstable) when $d < d_c\,(d > d_c)$. Given $\mu = -2$ and $\varepsilon = 0.1$, we have $d_c \approx 1.4742$. In Fig. 3.2 we plot the numerical solution to (3.1) at different times for $d = 1.4$ and $d = 1.5$. For $d = 1.5$ and $x_0(0) = 0.49$ we observe that the internal layer located at $x_0(t)$ moves at an accelerating speed away from $x_0^m = \frac{1}{2}$ and eventually, it collapses against the wall at $x = 0$. Alternatively, for $d = 1.4$ and $x_0(0) = 0.45$ the layer drifts toward its equilibrium location at $x_0^m = \frac{1}{2}$ at an exceedingly slow rate. Thus, this example demonstrates the influence of the constants μ and d on the stability of the equilibrium solution. Comparisons between the asymptotic and numerical results for the internal layer trajectories are displayed in Table 3.2a for $d = 1.4$ and in Table 3.2b for $d = 1.5$. They agree to at least 3–4 significant digits.

t	x_0(asy.)	x_0(num.)
0.1009705×10^4	0.4500052	0.4500052
0.5824404×10^5	0.4503374	0.4503374
0.6115657×10^6	0.4541856	0.4541852
0.1266815×10^7	0.4600576	0.4600546
0.3232563×10^7	0.4790305	0.4790227
0.4510299×10^7	0.4875179	0.4875137
0.8933232×10^7	0.4981489	0.4981502
0.1586249×10^8	0.4999096	0.4999098
0.2243776×10^9	0.5	0.5

Table 3.2a: **Example 3.2**: A comparison of the asymptotic and numerical internal layer trajectories for $Q(u) = 2(u - u^3)$ and $g(x) = \frac{1}{2}(x - \frac{1}{2})^2$ with $\varepsilon = 0.1$, $\mu = -2$, $d = 1.4$ and $x_0(0) = 0.45$.

By plotting $h(x_0)$ in (3.36) versus x_0 we can show that $x_0^m = 1/2$ is the only equilibrium to (3.36) when it is unstable. Alternatively, if the equilibrium $x_0^m = 1/2$ is stable

x_0	t(asy.)	t(num.)
0.4899742	0.255661494×10^5	$0.255661329\ \times10^5$
0.4892876	0.679551367×10^6	$0.679517141\ \times10^6$
0.4758890	0.747594011×10^7	$0.747469530\ \times10^7$
0.4519193	0.105770564×10^8	$0.105738718\ \times10^8$
0.4263499	0.113221195×10^8	$0.113185051\ \times10^8$
0.4015483	0.115273938×10^8	$0.115236708\ \times10^8$
0.3522899	0.116191551×10^8	$0.116153855\ \times10^8$
0.3018846	0.116312395×10^8	$0.116274632\ \times10^8$
0.2021744	0.116330380×10^8	$0.116292599\ \times10^8$
0.0794917	0.116330716×10^8	$0.116292938\ \times10^8$

Table 3.2b: **Example 3.2**: A comparison of the asymptotic and numerical internal layer trajectories for $Q(u) = 2(u - u^3)$ and $g(x) = \frac{1}{2}(x - \frac{1}{2})^2$ with $\varepsilon = 0.1$, $\mu = -2$, $d = 1.5$ and $x_0(0) = 0.49$.

then (3.36) has two additional (unstable) equilibria that emerge from a pitchfork bifurcation as d is decreased below $d = d_c$. In particular, for the parameter values $\varepsilon = 0.1$, $\mu = -2$ and $d = 1.4$, we calculate that there are two other equilibria at $x_0^m \approx 0.4435$ and $x_0^m \approx 0.5565$. For a more general $g(x)$, the set of equilibria to (3.36) consists, for $\varepsilon \to 0$, of the zeroes of $g'(x_0)$ and probably one or two others near the endpoints provided that $d < 2\min(\nu_- x_m, \nu_+(1 - x_M))$, where x_m and x_M are the smallest and largest zeros of $g'(x)$ on the interval $[0, 1]$. Since the equilibrium solution closest to the endpoint $x = 0$ or $x = 1$ is unstable, a stable equilibrium x_0^m must be near those zeros of $g'(x)$ satisfying $g''(x_0^m) > 0$. This analysis is illustrated in the next example.

Example 3.3: We now consider $g(x) = \int_0^x (s - \frac{1}{3})(s - \frac{2}{3})\, ds$, which has one maximum at $x_1 = \frac{1}{3}$ and one minimum at $x_2 = \frac{2}{3}$. From the discussion before, since $g''(x_1) < 0$ ($g''(x_2) > 0$), we expect that when $d > 0$ is sufficiently small the equilibrium of (3.36) near x_1 (x_2) is unstable (stable). This is confirmed by the numerical results plotted in Fig. 3.3, where $\varepsilon = 0.08$, $\mu = 0$ and $d = 0.2$. Fig. 3.3a shows that the internal

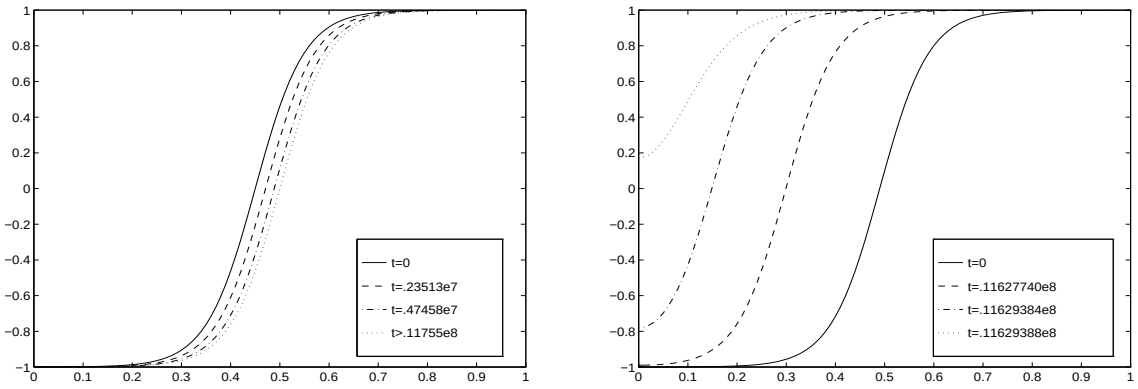

(a) (b)

Figure 3.2: **Example 3.2**: Plots of the numerical solutions to (3.1) at different times with $Q(u) = 2(u - u^3)$ and $g(x) = \frac{1}{2}(x - \frac{1}{2})^2$, where $\varepsilon = 0.1$, $\mu = -2$ with initial condition $u_0(x) = u_c(\varepsilon^{-1}[x - x_0^0])$. (a) When $d = 1.4$ and $x_0^0 = 0.45$ the internal layer moves towards its equilibrium $x_0^m = 1/2$; (b) When $d = 1.5$ and $x_0^0 = 0.49$ the internal layer moves towards the left and collides with $x = 0$.

layer drifts slowly towards the stable equilibrium location at $x_{02}^m \approx 0.6608$ when its initial location is at $x_0(0) = 0.4$. However, in Fig. 3.3b, the internal layer with initial location $x_0(0) = 0.333$ moves slowly towards the left and finally collapses against the wall at $x = 0$. This shows that there is an unstable equilibrium near x_1, which is calculated from (3.36) to be $x_{01}^m \approx 0.3401$. Corollary 2.3 and 2.4 suggests that there is another unstable equilibrium x_{03}^m between x_2 and the right endpoint. We compute from (3.36) that $x_{03}^m \approx 0.7762$. To confirm this conjecture, we compute the solution to (3.1) numerically for two different initial locations of the internal layer and we plot the corresponding numerical results at different times in Fig. 3.4. From this figure we observe that when $x_0(0) > x_{03}^m$ or $x_{02}^m < x_0(0) < x_{03}^m$, the internal layer moves exponentially slowly away from x_{03}^m until it eventually collides with the endpoint $x = 1$ or it reaches its stable equilibrium location at x_{02}^m, respectively. In summary, this example has three equilibrium internal layer solutions. The ones located at x_{01}^m and x_{03}^m are unstable, and the other one located at x_{02}^m is stable.

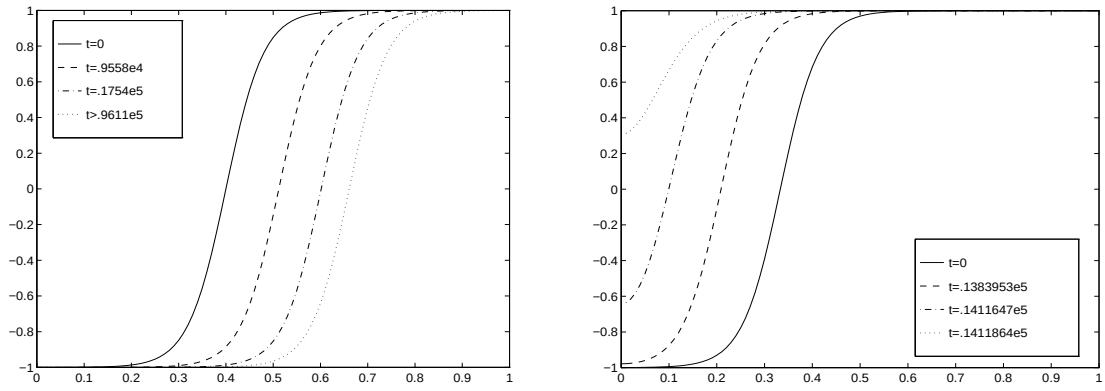

(a) (b)

Figure 3.3: **Example 3.3**: Plots of the numerical solutions to (3.1) at different times with $Q(u) = 2(u - u^3)$ and $g(x) = \int_0^x (s - \frac{1}{3})(s - \frac{2}{3})\, ds$, where $\varepsilon = 0.08$, $\mu = 0$, $d = 0.2$ with initial condition $u_0(x) = u_c(\varepsilon^{-1}[x - x_0^0])$. (a) When $x_0^0 = 0.4$ the internal layer moves towards $x_{02}^m \approx 0.6608$; (b) When $x_0^0 = 0.333$ the internal layer moves towards the left and collides with $x = 0$.

For this example, in Table 3.3a and Table 3.3b we give a comparison between the asymptotic and numerical results for the evolution of the internal layers corresponding to Fig. 3.3a and Fig. 3.3b, respectively. In these tables the second column gives the numerical results for $x_0(t)$ or $t(x_0)$ while the third and fourth columns show the corresponding asymptotic results from (3.36) with the one term and the two term expansions for the second pair of brackets in (3.36), respectively. Since it may happen that $g'(x_0)$ is close to zero during the evolution of an internal layer, the higher order term in (3.36) proportional to $g'''(x_0)$ can be quantitatively significant in some cases. In most cases, we find that the relative errors for the two-term expansion are below 0.002% in Table 3.3a and 0.02% in Table 3.3b, while they are only about 3% in Table 3.3a and 50% in Table 3.3b for the one-term expansion. Thus, a two-term asymptotic expansion for (3.36) is certainly needed to obtain close quantitative agreement with the numerical results.

We finally remark that by taking $g(x)$ to be a periodic function it is possible to construct a domain profile $A(x, \varepsilon)$ such that (3.1) has arbitrarily many (stable) equilibrium

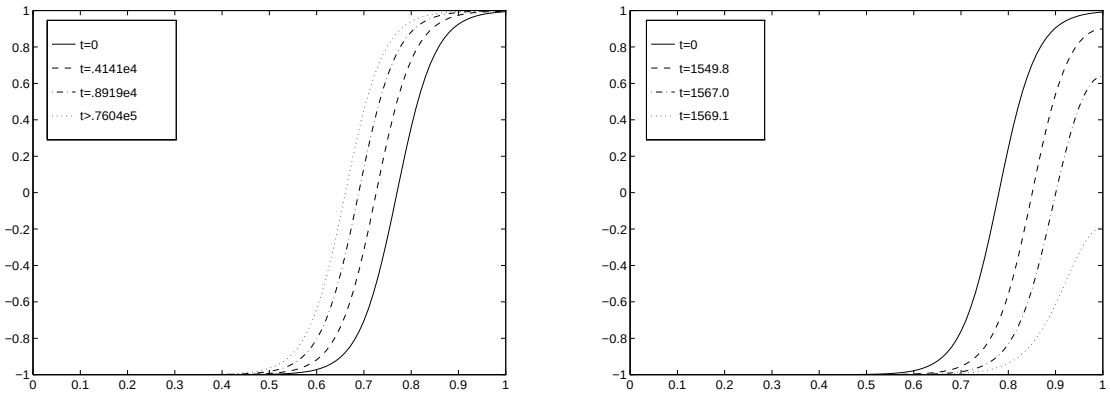

(a) (b)

Figure 3.4: **Example 3.3**: Plots of the numerical solutions to (3.1) at different times with $Q(u) = 2(u - u^3)$ and $g(x) = \int_0^x (s - \frac{1}{3})(s - \frac{2}{3})\, ds$, where $\varepsilon = 0.08$, $\mu = 0$, $d = 0.2$ with initial condition $u_0(x) = u_c(\varepsilon^{-1}[x - x_0^0])$. (a) When $x_0^0 = 0.76$ the internal layer moves towards $x_{02}^m \approx 0.6608$; (b) When $x_0^0 = 0.79$ the internal layer moves towards the right and collides with $x = 1$.

solutions.

3.3 A Burgers-like Convection-Diffusion-Reaction Equation

We now study (3.5) in the limit $\varepsilon \to 0$ with $c(x;\varepsilon)$ as given in (3.7). The viscous shock solution for (3.5) can be approximated by

$$u(x,t) \sim u_s\left[\varepsilon^{-1}(x - x_0(t))\right], \tag{3.37}$$

where the viscous shock profile $u_s(z)$ satisfies

$$u_s'(z) = f[u_s(z)] - f(\alpha_-), \quad -\infty < z < \infty; \quad u_s(0) = 0, \tag{3.38a}$$

$$u_s(z) \sim \alpha_- - a_- e^{\nu_- z}, \ z \to -\infty; \quad u_s(z) \sim \alpha_+ + a_+ e^{-\nu_+ z}, \ z \to +\infty. \tag{3.38b}$$

The positive constants $\nu_\pm$ and $a_\pm$ are defined by

$$\nu_\pm = \mp f'(\alpha_\pm), \qquad \log(\mp\frac{a_\pm}{\alpha_\pm}) = \mp\nu_\pm \int_0^{\alpha_\pm} \left[\frac{1}{f(s) - f(\alpha_\pm)} \pm \frac{1}{\nu_\pm(s - \alpha_\pm)}\right] ds\ . \tag{3.39}$$

t	x_0(num.)	x_0(asy.) 1-term	x_0 (asy.) 2-term
0.4531527×10^4	0.446231116	0.452053925	0.446234119
0.7487310×10^4	0.484045085	0.493797390	0.484052581
0.8965202×10^4	0.503953307	0.515317905	0.503963248
0.1339888×10^5	0.560669741	0.574424596	0.560683682
0.2881822×10^5	0.650108735	0.658569607	0.650107041
0.4544450×10^5	0.660137084	0.666792280	0.660135732
0.5741542×10^5	0.660748955	0.667250946	0.660748242
0.1175766×10^6	0.660847732	0.667319903	0.660847282
0.5677799×10^8	0.660847731	0.667319905	0.660847287

Table 3.3a: **Example 3.3**: A comparison of the asymptotic and numerical internal layer trajectories for $Q(u) = 2(u-u^3)$ and $g(x) = \int_0^x (s-\frac{1}{3})(s-\frac{2}{3})\,ds$, with $\varepsilon = 0.08$, $\mu = 0$, $d = 0.2$ and $x_0(0) = 0.4$.

We now look for a solution to (3.5) in the form

$$u(x,t) = u_s\left[\varepsilon^{-1}(x - x_0(t))\right] + v(x,t)\,, \tag{3.40}$$

where $v \ll u_s$ and $v_t \ll \partial_t u_s$. The trajectory $x_0 = x_0(t)$ gives the approximate location of the zero of $u(x,t)$ during the metastable evolution. Substituting (3.40) into (3.5), and using (3.38), we obtain that v satisfies the quasi-steady problem

$$\varepsilon v_{xx} - \left[f'(u_s)v\right]_x + c\,h'(u_s)v = -c\,h(u_s) - \varepsilon^{-1}x_0' u_s'(z)\,, \quad 0 < x < 1\,, \tag{3.41a}$$

$$v(0,t) = \alpha_- - u_s(-\varepsilon^{-1}x_0) \sim a_- e^{-\nu_-\varepsilon^{-1}x_0}\,, \tag{3.41b}$$

$$v(1,t) = \alpha_+ - u_s(\varepsilon^{-1}[1-x_0]) \sim -a_+ e^{-\nu_+\varepsilon^{-1}(1-x_0)}\,, \tag{3.41c}$$

where $z = \varepsilon^{-1}(x - x_0(t))$.

As in [87], it is convenient to transform (3.41) to self-adjoint form by introducing a new variable $w(x,t)$ defined by

$$v(x,t) = w(x,t)\psi(z)\,, \quad \psi(z) \equiv \left[u_s'(z)/u_s'(0)\right]^{\frac{1}{2}}\,, \quad z = \varepsilon^{-1}(x - x_0)\,. \tag{3.42}$$

x_0	t(num.)	t(asy.) 1-term	t (asy.) 2-term
0.3327547	0.340885709 $\times 10^5$	0.153239646 $\times 10^6$	0.340916775$\times 10^5$
0.3316803	0.147718828 $\times 10^6$	0.444448389 $\times 10^6$	0.147738247$\times 10^6$
0.3058932	0.744277679 $\times 10^6$	0.120475205 $\times 10^7$	0.744387573$\times 10^6$
0.2457738	0.101699029 $\times 10^7$	0.148559051 $\times 10^7$	0.101710846$\times 10^7$
0.2015392	0.110200256 $\times 10^7$	0.157152695 $\times 10^7$	0.110210654$\times 10^7$
0.1500169	0.116129605 $\times 10^7$	0.163121386 $\times 10^7$	0.116139950$\times 10^7$
0.1145554	0.117455785 $\times 10^7$	0.164451780 $\times 10^7$	0.117466741$\times 10^7$
0.1014824	0.117521955 $\times 10^7$	0.164518040 $\times 10^7$	0.117532979$\times 10^7$
0.0747960	0.117546167 $\times 10^7$	0.164542305 $\times 10^7$	0.117557243$\times 10^7$

Table 3.3b: **Example 3.3**: A comparison of the asymptotic and numerical internal layer trajectories for $Q(u) = 2(u - u^3)$ and $g(x) = \int_0^x (s - \frac{1}{3})(s - \frac{2}{3})\, ds$, with $\varepsilon = 0.08$, $\mu = 0$, $d = 0.2$ and $x_0(0) = 0.333$.

Substituting (3.42) into (3.41), and using the asymptotic behavior of $\psi(z)$ as $z \to \pm\infty$, we find that $w(x,t)$ satisfies

$$L_\varepsilon w \equiv \varepsilon^2 w_x x - V[x;\varepsilon]w \sim -\varepsilon\psi^{-1}\left(c\, h(u_s) + \varepsilon^{-1} x_0' u_s'(z)\right), \quad 0 < x < 1, \tag{3.43a}$$

$$w(0,t) \sim [a_- f(\alpha_-)/\nu_-]^{\frac{1}{2}}\, e^{-\varepsilon^{-1}\nu_- x_0/2}\,, \tag{3.43b}$$

$$w(1,t) \sim -[a_+ f(\alpha_+)/\nu_+]^{\frac{1}{2}}\, e^{-\varepsilon^{-1}\nu_+ (1-x_0)/2}\,. \tag{3.43c}$$

Here $V(x;\varepsilon)$ is defined by

$$V(x;\varepsilon) \equiv \frac{1}{4}\left[f'(u_s(z))\right]^2 + \frac{1}{2} f''[u_s(z)]u_s'(z) - \varepsilon c h'[u_s(z)]\,, \tag{3.44}$$

where $z = \varepsilon^{-1}(x - x_0)$ and $c = c(x;\varepsilon)$ is given in (3.7).

3.3.1 The Eigenvalue Analysis

For a fixed $x_0 \in (0,1)$, we now study the eigenvalue problem

$$L_\varepsilon \phi = \lambda\phi\,, \quad 0 < x < 1\,, \tag{3.45a}$$

$$\phi(0) = \phi(1) = 0\,, \quad (\phi,\phi) = 1\,. \tag{3.45b}$$

Here $(u,v) \equiv \int_0^1 uv dx$. For this eigenproblem, the eigenvalues λ_j for $j \geq 0$ are real and the principal eigenvalue λ_0 is exponentially small as $\varepsilon \to 0$. We now extend the analysis of [87] to give an estimate for λ_0 and for the corresponding eigenfunction ϕ_0.

We first define the trial function $\tilde{\phi}_0$ by $\tilde{\phi}_0(x) \equiv \psi^{-1}(z)u_s'(z)$, where $z = \varepsilon^{-1}(x - x_0)$ and ψ is defined in (3.42). Then applying Green's identity to ϕ_0 and $\tilde{\phi}_0$, and using (3.7), we get

$$\lambda_0 \left(\phi_0, \tilde{\phi}_0\right) = \left(\phi_0, L_\varepsilon \tilde{\phi}_0\right) + \varepsilon^2 \phi_{0x} \tilde{\phi}_0 |_0^1 , \tag{3.46a}$$

where

$$L_\varepsilon \tilde{\phi}_0 = -\varepsilon^{\mu+1} g'(x) e^{-\varepsilon^{-1} d} h'[u_s(z)] u_s'(z)/\psi(z) . \tag{3.46b}$$

Since $L_\varepsilon \tilde{\phi}_0$ is exponentially small and $\tilde{\phi}_0$ is of one sign, we have that $\phi_0 \sim N_0 \tilde{\phi}_0$, except near the endpoints at $x = 0$ and $x = 1$. Here N_0 is a normalization constant. We must modify $\tilde{\phi}_0$ by inserting boundary layer profiles near the endpoints in order to satisfy the boundary conditions in (3.45b). These boundary layers can be analyzed in the same way as in [87] and from this analysis, we obtain that

$$\phi_{0x}(0) \sim -\varepsilon^{-1} N_0 \nu_- [a_- \nu_- f(\alpha_-)]^{\frac{1}{2}} e^{-\varepsilon^{-1} \nu_- x_0/2} , \tag{3.47a}$$

$$\phi_{0x}(1) \sim \varepsilon^{-1} N_0 \nu_+ [a_+ \nu_+ f(\alpha_+)]^{\frac{1}{2}} e^{-\varepsilon^{-1} \nu_+ (1-x_0)/2} . \tag{3.47b}$$

Since the dominant contribution to each of the inner product integrals in (3.46a) arises from the region near $x = x_0$ we can calculate $\left(\phi_0, \tilde{\phi}_0\right)$ and $\left(\phi_0, L_\varepsilon \tilde{\phi}_0\right)$ using Laplace's method. As in [87], we estimate

$$\left(\phi_0, \tilde{\phi}_0\right) \sim N_0 \left(\tilde{\phi}_0, \tilde{\phi}_0\right) \sim \varepsilon N_0 \int_{-\infty}^{\infty} [u_s'(z)]^2 \psi^{-2}(z)\, dz = \varepsilon N_0 (\alpha_- - \alpha_+) f(\alpha_-) . \tag{3.48}$$

To calculate $\left(\phi_0, L_\varepsilon \tilde{\phi}_0\right)$ we use $\left(\phi_0, L_\varepsilon \tilde{\phi}_0\right) \sim N_0 \left(\tilde{\phi}_0, L_\varepsilon \tilde{\phi}_0\right)$. Substituting $\tilde{\phi}_0 = \psi^{-1} u_s'$ into this expression, and using (3.42) and $u_s'(0) = -f(\alpha_-)$, we derive

$$\left(\phi_0, L_\varepsilon \tilde{\phi}_0\right) \sim N_0 f(\alpha_-) \varepsilon^{\mu+2} e^{-\varepsilon^{-1} d} \int_{-\infty}^{\infty} g'(x_0 + \varepsilon z) u_s'(z) h'[u_s(z)]\, dz . \tag{3.49}$$

A Taylor series expansion for $g'(x_0+\varepsilon z)$ then yields

$$\left(\phi_0, L_\varepsilon \tilde{\phi}_0\right) \sim -N_0 f(\alpha_-)\varepsilon^{\mu+2} e^{-\varepsilon^{-1}d} \sum_{k=0}^{\infty} \varepsilon^k \gamma_k g^{(k+1)}(x_0)\,, \tag{3.50}$$

where the coefficients γ_k in (3.50) are defined by

$$\gamma_k \equiv -\frac{1}{k!}\int_{-\infty}^{\infty} u_s'(z) h'[u_s(z)] z^k\, dz\ , \quad k=0,1,\ldots\,. \tag{3.51}$$

Since we have assumed that $h'(u)$ is bounded on the interval $[\alpha_+,\alpha_-]$, the exponential decay of $u_s'(z)$ as $z\to\pm\infty$ ensures that γ_k is finite for each $k\geq 0$. We can calculate γ_0 explicitly to get

$$\gamma_0 = h(\alpha_-) - h(\alpha_+)\,. \tag{3.52}$$

Notice that if $f(u)$ is even and $h(u)$ is odd we get $\gamma_{2k+1}=0$ for $k\geq 0$. Finally, substituting (3.47), (3.48) and (3.50) into (3.46a) we obtain the following key estimate for λ_0:

Proposition 3.3 (Exponentially Small Eigenvalue): *For $\varepsilon\to 0$, the exponentially small eigenvalue of (3.45) satisfies*

$$\begin{aligned}\lambda_0 = \lambda_0(x_0) \ \sim\ & \frac{-1}{\alpha_- - \alpha_+}\left[a_+\nu_+^2 e^{-\varepsilon^{-1}\nu_+(1-x_0)} + a_-\nu_-^2 e^{-\varepsilon^{-1}\nu_- x_0}\right] \\ & -\frac{\varepsilon^{\mu+1}e^{-\varepsilon^{-1}d}}{\alpha_- - \alpha_+}\sum_{k=0}^{\infty}\varepsilon^k\gamma_k g^{(k+1)}(x_0)\,.\end{aligned} \tag{3.53}$$

Here $\nu_\pm$, $a_\pm$ are defined in (3.39), and γ_k is defined in (3.51).

3.3.2 The Metastability Analysis

We now derive a differential equation for the location $x_0=x_0(t)$ of the internal layer trajectory. We first expand the solution w to (3.43) in terms of the eigenfunctions ϕ_j of (3.45) as

$$w(x,t) = \sum_{j=0}^{\infty}\frac{r_j(t)}{\lambda_j}\phi_j(x)\,. \tag{3.54}$$

The coefficients r_j, which are found by integrating by parts, are

$$r_j = -x_0^{'}\left(\phi_j, \psi^{-1}u_s^{'}\right) - \varepsilon\left(\phi_j, \psi^{-1}ch\right) + \varepsilon^2 w\phi_{jx}|_0^1\,, \tag{3.55}$$

where ψ is defined in (3.42). Since $\lambda_0 \to 0$ as $\varepsilon \to 0$, a necessary condition for the solvability of (3.43) is that $r_0 \to 0$ as $\varepsilon \to 0$. Setting $r_0 = 0$ in (3.55), we obtain the asymptotic differential equation for $x_0 = x_0(t)$

$$x_0^{'}\left(\phi_0, \psi^{-1}u_s^{'}\right) \sim -\varepsilon\left(\phi_0, \psi^{-1}ch\right) + \varepsilon^2 w\phi_{0x}|_0^1\,. \tag{3.56}$$

To obtain an explicit differential equation for $x_0(t)$ we must evaluate the inner product integrals and the boundary terms in (3.56). The dominant contributions to the inner product integrals arise from the region near $x = x_0$.

First, we use (3.43b), (3.43c) and (3.47) to asymptotically calculate the last term on the right side of (3.56) as

$$\varepsilon^2 w\phi_{0x}|_0^1 \sim N_0\varepsilon f(\alpha_-)\left\{a_-\nu_- e^{-\varepsilon^{-1}\nu_- x_0} - a_+\nu_+ e^{-\varepsilon^{-1}\nu_+(1-x_0)}\right\}\,. \tag{3.57}$$

Next, we evaluate the term on the left side of (3.56) as

$$\left(\phi_0, \psi^{-1}u_s^{'}\right) \sim \varepsilon N_0(\alpha_- - \alpha_+)f(\alpha_-)\,, \tag{3.58}$$

which is the same as (3.48). To evaluate the first term on the right side of (3.56), we use $\phi_0 \sim N_0\tilde{\phi}_0$ and $\tilde{\phi}_0 = \psi^{-1}(z)u_s^{'}(z)$ to get

$$\varepsilon\left(\phi_0, \psi^{-1}ch\right) \sim N_0\varepsilon^{\mu+1}e^{-\varepsilon^{-1}d}f(\alpha_-)\int_0^1 g'(x)h(u_s[\varepsilon^{-1}(x-x_0)])\,dx\,. \tag{3.59}$$

Since $h(u_s(z)) \to h(\alpha_\pm)$ exponentially as $z \to \pm\infty$, we can evaluate the integral in (3.59) by decomposing it as

$$\begin{aligned}\int_0^1 g'(x)h(u_s[\varepsilon^{-1}(x-x_0)])\,dx \;\;&\sim\;\; h(\alpha_-)\left[g(x_0) - g(0)\right] + h(\alpha_+)\left[g(1) - g(x_0)\right] \\ &+ \int_0^{x_0}\left[h(u_s) - h(\alpha_-)\right]g'(x)dx + \int_{x_0}^1\left[h(u_s) - h(\alpha_+)\right]g'(x)\,dx\,.\end{aligned} \tag{3.60}$$

The integrands in the two integrals on the right side of (3.60) are localized near $x = x_0$ and can be evaluated using a Taylor expansion to get

$$\int_0^1 g'(x)h(u_s[\varepsilon^{-1}(x-x_0)])\,dx \;\sim\; h(\alpha_-)\,[g(x_0)-g(0)] + h(\alpha_+)\,[g(1)-g(x_0)] + \varepsilon\sum_{k=0}^{\infty}\varepsilon^k\beta_k g^{(k+1)}(x_0)\,, \tag{3.61a}$$

where the coefficients β_k, for $k = 0, 1, \ldots$, are defined by

$$\beta_k = \frac{1}{k!}\int_{-\infty}^{0}(h[u_s(z)]-h(\alpha_-))\,z^k\,dz + \frac{1}{k!}\int_0^{\infty}(h[u_s(z)]-h(\alpha_+))\,z^k\,dz\,. \tag{3.61b}$$

Using integrating by parts it is readily seen that $\beta_k = \gamma_{k+1}$, where γ_k was defined previously in (3.51). We also observe that when $f(u)$ is even and $h(u)$ is odd, then $\beta_{2k} = 0$ for $k \geq 0$.

Finally, substituting (3.57), (3.58), (3.61a) into (3.56) we obtain our main result for the metastable dynamics associated with (3.5):

Proposition 3.4 (Metastable Dynamics): *For $\varepsilon \to 0$ and $t \gg 1$, the metastable viscous shock dynamics for (3.5) is represented by $u(x,t) \sim u_s\,[\varepsilon^{-1}(x - x_0(t))]$, where the internal layer trajectory $x_0(t)$ satisfies the asymptotic differential equation*

$$x_0' \;\sim\; M(x_0) \equiv \frac{1}{\alpha_- - \alpha_+}\left\{a_-\nu_- e^{-\varepsilon^{-1}\nu_- x_0} - a_+\nu_+ e^{-\varepsilon^{-1}\nu_+(1-x_0)}\right\} - \frac{1}{\alpha_- - \alpha_+}\varepsilon^{\mu}e^{-\varepsilon^{-1}d}\times$$
$$\times\left\{h(\alpha_-)\,[g(x_0)-g(0)] + h(\alpha_+)\,[g(1)-g(x_0)] + \varepsilon\sum_{k=0}^{\infty}\varepsilon^k\beta_k g^{(k+1)}(x_0)\right\}. \tag{3.62}$$

Here the coefficients $a_\pm$ and $\nu_\pm$ are defined in (3.39), β_k for $k \geq 0$ is defined in (3.61b), and $u_s(z)$ is defined in (3.38).

The following equilibrium result is obtained by setting $x_0' = 0$ in (3.62):

Corollary 3.3 (Equilibrium): *For $\varepsilon \to 0$ an equilibrium shock-layer solution to (3.5) is given asymptotically by $U \sim u_s[\varepsilon^{-1}(x - x_0^m)]$, where $u_s(z)$ is defined in (3.38) and*

$x_0 = x_0^m$ *satisfies the nonlinear algebraic equation* $M(x_0) = 0$ *, i.e.,*

$$a_-\nu_- e^{-\varepsilon^{-1}\nu_- x_0} - a_+\nu_+ e^{-\varepsilon^{-1}\nu_+(1-x_0)} = \varepsilon^{\mu} e^{-\varepsilon^{-1}d} \times$$
$$\times \left\{ h(\alpha_-)\,[g(x_0) - g(0)] + h(\alpha_+)\,[g(1) - g(x_0)] + \varepsilon \sum_{k=0}^{\infty} \varepsilon^k \beta_k g^{(k+1)}(x_0) \right\} . \quad (3.63)$$

To qualitatively understand the equilibrium problem for $x_0^{'} = M(x_0)$, we first note that $M(0) > 0$ and $M(1) < 0$ as $\varepsilon \to 0$ when $d > 0$. Thus, there is at least one equilibrium solution for (3.62) as $\varepsilon \to 0$. If $d > 0$ is sufficiently large, then the term in (3.62) proportional to $e^{-\varepsilon^{-1}d}$ can be neglected and hence the unique root x_0^m of $M(x_0) = 0$ is given asymptotically by

$$x_0^m \sim \frac{\nu_+}{\nu_- + \nu_+} - \frac{\varepsilon}{\nu_- + \nu_+} \log\left(\frac{a_+\nu_+}{a_-\nu_-}\right) . \quad (3.64)$$

Alternatively, if $d > 0$ is sufficiently small then $M(x_0) = 0$ may have multiple roots for some choices of $g(x)$. This will be illustrated below for some specific examples.

Since $\gamma_k = \beta_{k-1}$, it follows that $M'(x_0) = \varepsilon^{-1}\lambda_0(x_0)$. Thus, the decay rate associated with infinitesimal perturbations about x_0^m is $\varepsilon^{-1}\lambda_0(x_0^m)$. This leads to the following criterion for the stability of the equilibrium shock-layer solution.

Corollary 3.4 (Stability of Equilibrium): *Let* x_0^m *satisfy* $M(x_0^m) = 0$. *Then the equilibrium solution to (3.5) has the form* $U \sim u_s[\varepsilon^{-1}(x - x_0^m)]$ *and is stable (unstable) if* $\lambda_0(x_0^m) < 0$ $(\lambda_0(x_0^m) > 0)$. *Here* $u_s(z)$, $\lambda_0(x_0)$ *and* $M(x_0)$ *are given in (3.38), (3.53) and (3.62).*

It is easy to show that a sufficient condition for $M^{'}(x_0) < 0$ on $x_0 \in [0,1]$ as $\varepsilon \to 0$ is that

$$g^{'}(x_0)\,[h(\alpha_-) - h(\alpha_+)] > 0\,, \qquad \text{for all} \quad x_0 \in [0,1]\,. \quad (3.65)$$

When this condition holds, the shock-layer solution centered at $x_0 = x_0^m$, where x_0^m is the unique root of $M(x_0) = 0$, is stable for $\varepsilon \ll 1$. In particular, (3.65) is satisfied

when $h'(u) > 0$ for $u \in [\alpha_+, \alpha_-]$ and $g'(x) > 0$ on $x \in [0,1]$, which models a diverging nozzle flow as discussed following (3.7) above. More generally, a sufficient condition for the stability of a root x_0^m of $M(x_0) = 0$ is that (3.65) holds at $x_0 = x_0^m$. This stability conclusion for an internal layer solution is consistent with [53].

However, when $g'(x_0)[h(\alpha_-) - h(\alpha_+)] < 0$ on $[0,1]$, the stability of an equilibrium internal layer solution can only be determined by explicitly calculating the sign of $\lambda_0(x_0^m)$, where x_0^m is a root of $M(x_0) = 0$. In this case, multiple equilibrium solutions for $x_0' = M(x_0)$ are possible (see the examples below). We now illustrate the existence of multiple equilibria in this case when $d > 0$ is sufficiently small and $\varepsilon \to 0$. Let's suppose that $g'(x_0) < 0$ on $[0,1]$ and $h(\alpha_-) > h(\alpha_+) > 0$. Then, when $d > 0$ is sufficiently small and $\varepsilon \to 0$, there is a root x_{02}^m of $M(x_0) = 0$ that is $O(\varepsilon)$ close to the unique solution of

$$h(\alpha_-)\,[g(x_0) - g(0)] + h(\alpha_+)\,[g(1) - g(x_0)] = 0\,. \tag{3.66}$$

The assumption $g'(x_{02}^m)[h(\alpha_-) - h(\alpha_+)] < 0$ then yields that $M'(x_{02}^m) > 0$ when $d > 0$ is sufficiently small and $\varepsilon \to 0$. Hence, this root is unstable. However, when $d > 0$ and $\varepsilon \to 0$, we calculate that $M(0) > 0$, $M(1) < 0$, $M'(0) < 0$, $M'(1) < 0$. Hence, there must exist additional roots x_{01}^m and x_{03}^m to $M(x_0) = 0$ that satisfy $0 < x_{01}^m < x_{02}^m$ and $x_{02}^m < x_{03}^m < 1$ for which $M'(x_{01}^m) < 0$ and $M'(x_{03}^m) < 0$. Thus, these additional roots are stable equilibria of $x_0' = M(x_0)$ and the profiles $u_s\,[\varepsilon^{-1}(x - x_{01}^m)]$ and $u_s\,[\varepsilon^{-1}(x - x_{03}^m)]$ correspond to stable internal layer solutions. Notice, as $d \to 0^+$, $x_{01}^m \to 0$ and $x_{03}^m \to 1$ so that these internal layer solutions become stable boundary layer solutions in agreement with the analysis in [53] for the case $d = 0$.

3.3.3 Comparison of Asymptotic and Numerical Results

We now compare the asymptotic results obtained above with the corresponding full numerical results computed directly from (3.5). For all of the calculations below we

consider the case

$$f(u) = u^2/2\,, \qquad h(u) = u\,, \qquad -\alpha_+ = \alpha_- = \alpha\,. \tag{3.67}$$

As discussed in [94], and following (3.7) above, this problem models the transonic flow through a nozzle of cross-sectional area $A(x;\varepsilon) = 1 + \varepsilon^{\mu} e^{-\varepsilon^{-1}d} g(x)$. We will consider nozzles of different cross-sectional areas by varying the term $g(x)$ in (3.53), (3.62) and (3.63). Recall that the nozzle is said to be divergent if $g'(x) > 0$ for all x, convergent if $g^{'}(x) < 0$ for all x, and convergent-divergent if $g^{'}(x)$ has no definite sign. We use a similar numerical method as described in §3.2.3 above to compute numerical solutions to (3.5) and to compare with the corresponding asymptotic results.

When $f(u) = u^2/2$ and $\alpha_- = -\alpha_+ = \alpha$, we have $a_{\pm} = 2\alpha$ $\nu_{\pm} = \alpha$ and $u_s(z) = -\alpha \tanh(\alpha z/2)$. We also calculate that $(\gamma_0, \gamma_1, \gamma_2, \gamma_3, \ldots) = (2\alpha, 0, \pi^2/3\alpha, 0, \ldots)$. From (3.53) the principal eigenvalue $\lambda_0(x_0)$ satisfies

$$\lambda_0 \sim -\alpha^2 \left(e^{-\varepsilon^{-1}\alpha(1-x_0)} + e^{-\varepsilon^{-1}\alpha x_0} \right) - \varepsilon^{\mu+1} e^{-\varepsilon^{-1}d} \left[g'(x_0) + \frac{\pi^2 \varepsilon^2}{6\alpha^2} g'''(x_0) + \ldots \right]. \tag{3.68}$$

In addition, since $\beta_k = \gamma_{k+1}$ for $k \geq 0$, (3.62) becomes

$$\begin{aligned} x_0^{'} \sim M(x_0) \;\; &= \;\; \alpha \left(e^{-\varepsilon^{-1}\alpha x_0} - e^{-\varepsilon^{-1}\alpha(1-x_0)} \right) \\ &\quad -\varepsilon^{\mu} e^{-\varepsilon^{-1}d} \left[\left(g(x_0) - \frac{g(0)+g(1)}{2} \right) + \frac{\pi^2 \varepsilon^2}{6\alpha^2} g''(x_0) + \ldots \right]. \end{aligned} \tag{3.69}$$

In most cases, the higher order terms in the square brackets on the right sides of (3.68) and (3.69) make only very minor improvements to the results. Thus, except when specified otherwise, they are ignored when making the comparisons below.

Example 3.4: We first consider a **divergent nozzle**, where $g(x) = Cx$ for some $C \geq 0$. From (3.68) and (3.69) the only equilibrium value for $x_0(t)$ is $x_0^m = \frac{1}{2}$ and the principal eigenvalue $\lambda_0(1/2)$ is always negative for any μ and $d > 0$, $C \geq 0$. Thus, from Corollary 3.3 and 3.4, there is a unique shock-layer solution centered at $x = \frac{1}{2}$ and it

is stable. This agrees with the conclusion in [34] and [71] that flows along a divergent nozzle are always stable. The case $C = 0$ was well-studied in [61], [64] and [87] and comparisons between asymptotic and numerical results can be found in [64] and [87].

Example 3.5: We now consider a **convergent nozzle**, where $g(x) = Cx$ for some $C < 0$. In this case, $x_0^m = 1/2$ is still a root of $M(x_0) = 0$ in (3.69), but now from (3.68) we calculate $\lambda_0(1/2)$ as

$$\lambda_0(1/2) \sim -2\alpha^2 \varepsilon^{-1} e^{-\varepsilon^{-1}\alpha/2} - \varepsilon^{\mu} e^{-\varepsilon^{-1} d} C\,. \tag{3.70}$$

Thus, the stability of $x_0^m = 1/2$ is determined by the values of μ, d and C. For example, if $\mu = -1$ and $d = \alpha/2$, then the shock layer located at $x_0^m = \frac{1}{2}$ is stable (unstable) if $C > -2\alpha^2$ $(C < -2\alpha^2)$. If $\mu = -1$ and $C = -2\alpha^2$, then it is stable (unstable) if $d > \alpha/2$ $(d < \alpha/2)$. These stability results are fully confirmed by the numerical results displayed in Table 4 and Table 5. In these tables, we give the asymptotic and numerical results for $x_0(t)$ in the second and third columns respectively, and the error representing the difference between the asymptotic and numerical results in the fourth column. The asymptotic results agree with the numerical ones to at least five decimal places. From these tables we observe that when the equilibrium $x_0^m = \frac{1}{2}$ is unstable, the shock layer will move away from $x_0^m = \frac{1}{2}$ to somewhere else, but not to the endpoints $x = 0, 1$. This suggests the existence of other stable equilibria for (3.69). For this example, it is easy to show that when $x_0^m = \frac{1}{2}$ is unstable (i.e., $\lambda_0(\frac{1}{2}) > 0$), then $M(x_0)$ has exactly two more zeros that are symmetric about $x_0^m = \frac{1}{2}$. They correspond to two stable equilibrium values for $x_0(t)$. When $x_0^m = \frac{1}{2}$ is stable, then it is the only zero of $M(x_0)$. This analysis is illustrated by plotting $M(x_0)$ in Fig. 3.5.

Therefore, there exists either one or two stable steady-state solutions of the form $u \sim u_s[\varepsilon^{-1}(x - x_0^m)]$ along the convergent nozzle we are considering. The analysis of [34]

t	$x_0(t)$(asy.)	$x_0(t)$(num.)	error
$.7466667\times10^{1}$	.212682157	.212676330	$.582\times10^{-5}$
$.5013333\times10^{2}$	.236113084	.236101298	$.117\times10^{-4}$
$.3754166\times10^{3}$	.285065717	.285059434	$.628\times10^{-5}$
$.3879890\times10^{4}$	.352169342	.352167776	$.156\times10^{-5}$
$.2523277\times10^{5}$	.404404274	.404403590	$.683\times10^{-6}$
$.4144176\times10^{6}$	.465271835	.465271222	$.613\times10^{-6}$
$.3061509\times10^{7}$	.489469516	.489468465	$.105\times10^{-5}$
$.8745862\times10^{7}$	.496984897	.496983905	$.991\times10^{-6}$
$.8407137\times10^{8}$	.499999999	.499999999	$-.204\times10^{-9}$

Table 3.4a: **Example 3.5**: A comparison of the asymptotic and numerical shock layer trajectories for (3.5) with $f(u) = u^2/2$ and $g'(x) = -1.9$. Here $\varepsilon = 0.03$, $\mu = -1$, $d = 0.5$, $\alpha = 1$ and $x_0^0 = 0.205712482$.

for the inviscid problem

$$u_t + uu_x - c(x)u = 0\,, \tag{3.71}$$

proved that standing shock waves in a convergent nozzle (i.e. $c(x) > 0$ for all x) or in the convergent portion of a convergent-divergent nozzle are unstable. Our example has shown that the effect of viscosity and the boundary conditions in (3.5) allows for the existence of a stable standing wave in a convergent nozzle when $c(x)$ is replaced by the form in (3.7).

Example 3.6: Next, we let $\alpha = 1$ and consider a **convergent-divergent nozzle** where $g(x) = (x-a)^2$, and the constant a satisfies $\frac{1}{2} < a < 1$. Now the algebraic equation $2g(x_0) - g(0) - g(1) = 0$ has one root $x^* \in (0, a)$. If we choose d so that $0 < d < x^*$, then it is easy to see that for $\varepsilon \to 0$ the function $M(x_0)$ in (3.69) will have three zeros x_{01}^m, x_{02}^m and x_{03}^m, satisfying $0 < x_{01}^m < x_{02}^m < x^*$ and $a < x_{03}^m < 1$. These zeros are illustrated in Fig. 3.6 for the parameter values $\varepsilon = 0.04$, $\alpha = 1$, $\mu = -1$, $d = 0.171244968$ and $a = 0.8$. From the discussion following Corollary 3.4, it is clear that x_{01}^m and x_{03}^m are stable equilibria and that x_{02}^m is unstable. In Fig. 3.7, we verify

t	$x_0(t)$(asy.)	$x_0(t)$(num.)	error
$.2988174\times10^4$	.494997385	.494997382	$.346\times10^{-8}$
$.1725713\times10^6$	.494847418	.494847363	$.548\times10^{-7}$
$.4950768\times10^7$	.489521616	.489522250	$-.633\times10^{-6}$
$.7862987\times10^7$	.486497884	.486497678	$.206\times10^{-6}$
$.9804466\times10^7$	.485206361	.485204630	$.173\times10^{-5}$
$.1465816\times10^8$	.483947388	.483944120	$.326\times10^{-5}$
$.1659964\times10^8$	.483811685	.483908521	$.316\times10^{-5}$
$.2242408\times10^8$	.483701958	.483699155	$.280\times10^{-5}$
$.8697827\times10^8$	.483689263	.483686417	$.284\times10^{-5}$

Table 3.4b: **Example 3.5**: A comparison of the asymptotic and numerical shock layer trajectories for (3.5) with $f(u) = u^2/2$ and $g'(x) = -2.1$. Here $\varepsilon = 0.03$, $\mu = -1$, $d = 0.5$, $\alpha = 1$ and $x_0^0 = 0.494999996$.

the stability of x_{01}^m and x_{03}^m by plotting the numerical solution to (3.5) at different times for two initial values x_0^0. The two initial values x_0^0 in Fig. 3.7a and Fig. 3.7b are so close that there is only one unstable equilibrium for $x_0(t)$ between them, which is x_{02}^m.

Example 3.7: Finally, we give an example to illustrate that it is possible to construct a nozzle geometry to guarantee an **arbitrary** number of steady state internal layer solutions. We take $g(x) = \sin(n\pi x)$ where n is a positive integer. Let $x_i^* = i/n$ for $i = 0, .., n$ be the i-th zero of $g(x)$. In this case, the differential equation (3.62) for $x_0(t)$ becomes

$$x_0^{'} \sim \alpha\left[e^{-\varepsilon^{-1}\alpha x_0} - e^{-\varepsilon^{-1}\alpha(1-x_0)}\right] - \varepsilon^{\mu} e^{-\varepsilon^{-1}d}\zeta\sin(n\pi x_0)\,, \quad \zeta = 1 - \frac{n^2\pi^4\varepsilon^2}{6\alpha^2} + \ldots. \quad (3.72)$$

It is easy to see if d is chosen such that $0 < d < x_1^*$, then for $\varepsilon \to 0$, there exists $N \equiv n + (n-1)\mathrm{mod}2$ equilibria x_{0i}^m, $i = 1, 2, \ldots, N$. Among these equilibria, x_{0i}^m for $i = 1, 3, \ldots, N$ are stable and the rest are unstable. Note that if $d \geq x_1^*$, then the number of the equilibria may be less than N.

We now implement a numerical experiment to illustrate this analysis. We choose $n = 4$, $\alpha = 1$, $\mu = 0$, $d = 0.19$ and $\varepsilon = 0.02$. In this case, we have three stable

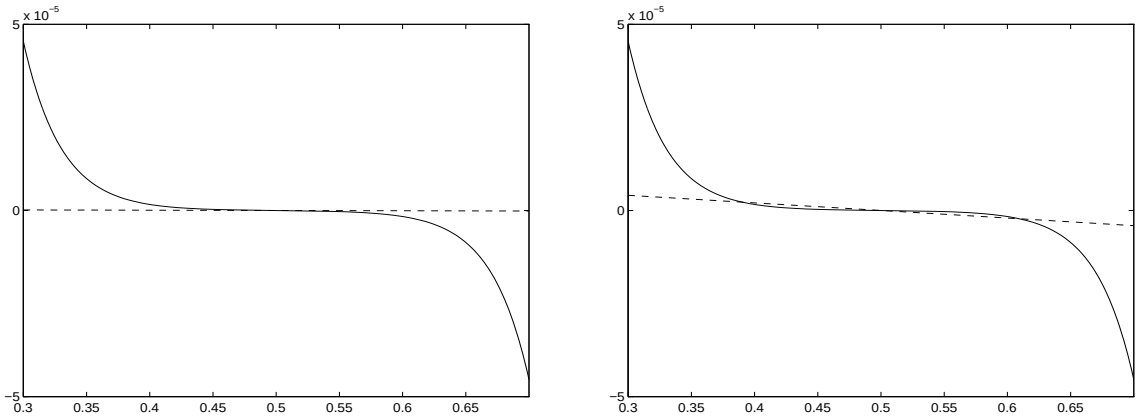

Figure 3.5: **Example 3.5**: Plots of $M_1(x_0) \equiv \alpha(-e^{-\varepsilon^{-1}\alpha(1-x_0)} + e^{-\varepsilon^{-1}\alpha x_0})$ (solid lines) and $M_2(x_0) \equiv \varepsilon^{\mu} e^{-\varepsilon^{-1}d} C(x_0 - \frac{1}{2})$ (dash lines) versus x_0, where $\alpha = 1$, $\varepsilon = 0.03$, $\mu = -1$ and $C = -2$. The intersection(s) of $M_1(x_0)$ and $M_2(x_0)$ is the zero(s) of $M(x_0)$. (a) $d = 0.55$: we have $\lambda_0(\frac{1}{2}) < 0$, and the only equilibrium $x_0^m = \frac{1}{2}$ is stable; (b) $d = 0.45$: we have three zeros of $M(x_0)$ given by $x_{01}^m \approx 0.3902$, $x_{02}^m = 0.5$ and $x_{03}^m \approx 0.6097$. Here $x_{02}^m = 0.5$ is unstable and the rest are stable.

equilibria at $x_{01}^m \approx 0.2044$, $x_{03}^m = 0.5$ and $x_{05}^m \approx 0.7955$, and two unstable equilibria at $x_{02}^m \approx 0.2440$ and $x_{04}^m \approx 0.7559$, which we compute from (3.72) using a two-term expansion for ζ. We choose the initial values $x_0^0 = 0.24$ and $x_0^0 = 0.25$ when computing the numerical solution to (3.5). The asymptotic and numerical results are shown in Tables 6a and 6b. These tables also display the asymptotic result (3.72) with both the one-term and the two-term expansions for ζ. The error terms in the fourth and sixth columns represent the difference between the asymptotic and numerical results. Since the higher order terms in ζ in (3.72) are significant, we observe from Table 6 that a two-term expansion for η is certainly needed to obtain close quantitative agreement with the numerical results for $x_0(t)$. Finally, in Fig. 3.8 we plot the shock layer evolution corresponding to the data in Table 6, which shows that x_{01}^m and x_{03}^m are stable equilibria, while x_{02}^m is an unstable equilibrium.

t	$x_0(t)$(asy.)	$x_0(t)$(num.)	error
$.1270000\times10^{2}$	.216714648	.216706869	$.777\times10^{-5}$
$.4765000\times10^{2}$	.235153498	.235142419	$.110\times10^{-4}$
$.3321062\times10^{3}$	.281796238	.281790749	$.548\times10^{-5}$
$.1271548\times10^{4}$	.320208345	.320206583	$.176\times10^{-5}$
$.1494813\times10^{5}$	.392954938	.392955455	$-.517\times10^{-6}$
$.1429582\times10^{6}$	.457781790	.457782599	$-.808\times10^{-6}$
$.5020859\times10^{6}$	.488305699	.488306411	$-.712\times10^{-6}$
$.1608928\times10^{7}$	.499637394	.499637666	$-.271\times10^{-6}$
$.5455925\times10^{8}$	.500000000	.499999999	$.582\times10^{-9}$

Table 3.5a: **Example 3.5**: A comparison of the asymptotic and numerical shock layer trajectories for (3.5) with $f(u) = u^2/2$ and $g'(x) = -2$. Here $\varepsilon = 0.03$, $\mu = -1$, $d = 0.55$, $\alpha = 1$ and $x_0^0 = 0.205646164$.

t	$x_0(t)$(asy.)	$x_0(t)$(num.)	error
$.3895482\times10^{3}$	.494967222	.494967221	$.946\times10^{-9}$
$.7976059\times10^{4}$	.494295191	.494295125	$.658\times10^{-7}$
$.3291548\times10^{5}$	.491389800	.491389298	$.502\times10^{-6}$
$.8279433\times10^{5}$	.480483494	.480480756	$.273\times10^{-5}$
$.1491332\times10^{6}$	.445338979	.445330373	$.860\times10^{-5}$
$.1690847\times10^{6}$	.429122276	.429116007	$.626\times10^{-5}$
$.2249490\times10^{6}$	.395546688	.395541088	$.560\times10^{-5}$
$.3072491\times10^{6}$	.390353158	.390348796	$.436\times10^{-5}$
$.2905679\times10^{10}$	.390284916	.390281195	$.372\times10^{-5}$

Table 3.5b: **Example 3.5**: A comparison of the asymptotic and numerical shock layer trajectories for (3.5) with $f(u) = u^2/2$ and $g'(x) = -2$. Here $\varepsilon = 0.03$, $\mu = -1$, $d = 0.45$, $\alpha = 1$ and $x_0^0 = 0.494999513$.

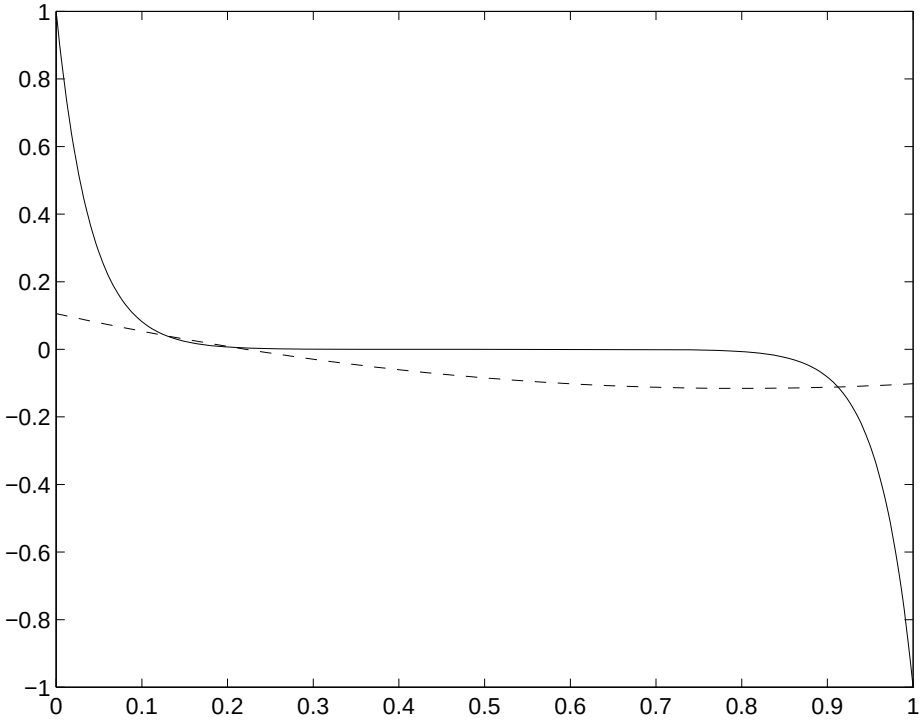

Figure 3.6: **Example 3.6**: Plots of $M_1(x_0) \equiv \alpha(-e^{-\varepsilon^{-1}\alpha(1-x_0)} + e^{-\varepsilon^{-1}\alpha x_0})$ (solid lines) and $M_2(x_0) \equiv \varepsilon^{\mu} e^{-\varepsilon^{-1}d}((x_0 - a)^2 - \frac{1}{2}[a^2 + (1-a)^2] + \pi^2\alpha^{-2}\varepsilon^2/3)$ versus x_0, where $\varepsilon = 0.04$, $a = 0.8$, $\alpha = 1$, $\mu = -1$ and $d = 0.1712\ldots$. The intersections of $M_1(x_0)$ and $M_2(x_0)$, which are the zeros of $M(x_0)$, are $x_{01}^m \approx 0.1286$, $x_{02}^m \approx 0.2077$, and $x_{03}^m \approx 0.9122$. Here the equilibrium x_{02}^m is unstable, and the other two are stable.

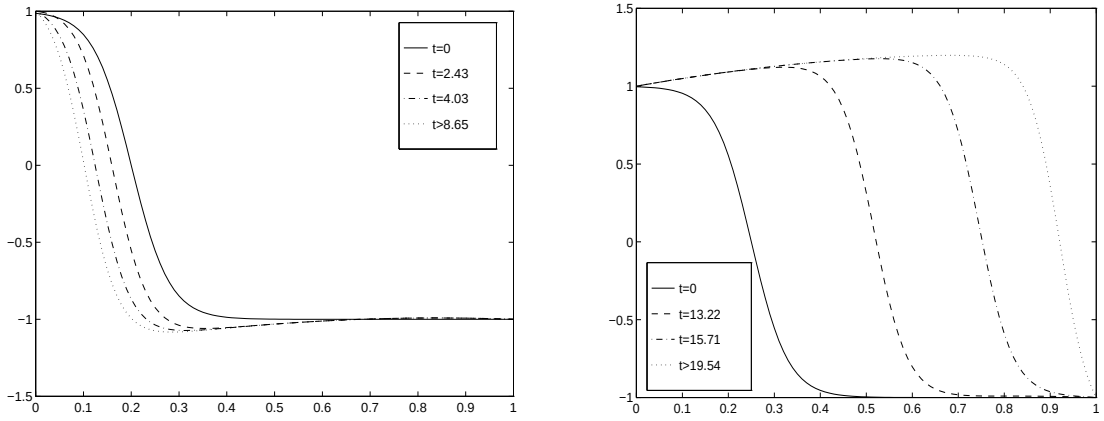

(a) (b)

Figure 3.7: **Example 3.6:** Plots of the numerical solutions to (3.5) at different times with $f(u) = u^2/2$ and $g(x) = (x-a)^2$, where $\varepsilon = 0.04$, $a = 0.8$, $\alpha = 1$, $\mu = -1$, $d = 0.1712\ldots$ and initial condition $u_0(x) = u_s[\varepsilon^{-1}(x - x_0^0)]$. (a) $x_0^0 = 0.2$: shock layer moves towards left; (b) $x_0^0 = 0.25$: shock layer moves towards right.

t	$x_0(t)$(num.)	(3.72) 1-term	error1	(3.72) 2-term	error2
$.1133545\times10^3$	.239718703	.239610666	$-.108\times10^{-3}$	.239726721	$.801\times10^{-5}$
$.5512484\times10^3$	.238497828	.237864222	$-.633\times10^{-3}$	.238543918	$.460\times10^{-4}$
$.1135106\times10^4$	.236387221	.234724657	$-.166\times10^{-2}$	.236505117	$.117\times10^{-3}$
$.2580156\times10^4$	.228182044	.222194243	$-.598\times10^{-2}$	.228599741	$.417\times10^{-3}$
$.4255100\times10^4$	.214978265	.206459679	$-.851\times10^{-2}$	.215700702	$.722\times10^{-3}$
$.6061413\times10^4$	.206403299	.201517420	$-.488\times10^{-2}$	.206902782	$.499\times10^{-3}$
$.8360356\times10^4$	.204368747	.200989316	$-.337\times10^{-2}$	.204672929	$.304\times10^{-3}$
$.1606592\times10^5$	.204187662	.200966538	$-.322\times10^{-2}$	.204461290	$.273\times10^{-3}$
$.6239090\times10^5$	.204187642	.200966538	$-.322\times10^{-2}$	.204461248	$.273\times10^{-3}$

Table 3.6a: **Example 3.7**: A comparison of the asymptotic and numerical shock layer trajectories for (3.5) with $f(u) = u^2/2$ and $g(x) = \sin(4\pi x)$. Here $\varepsilon = 0.02$, $\alpha = 1$, $\mu = 0$, $d = 0.19$ and $x_0^0 = 0.239991525$.

t	$x_0(t)$(num.)	(3.72) 1-term	error1	(3.72) 2-term	error2
$.9389256\times10^{2}$	.250384983	.250386816	$.183\times10^{-5}$	.250384917	$-.664\times10^{-7}$
$.5804413\times10^{3}$	.252677437	.252755503	$.780\times10^{-4}$	.252672223	$-.521\times10^{-5}$
$.1650848\times10^{4}$	.261513735	.262616867	$.110\times10^{-2}$	.261438939	$-.748\times10^{-4}$
$.3207804\times10^{4}$	.296383726	.306534177	$.101\times10^{-1}$	.295721003	$-.662\times10^{-3}$
$.4969111\times10^{4}$	.398142523	.424482167	$.263\times10^{-1}$	.396102752	$-.204\times10^{-2}$
$.6545529\times10^{4}$	.469337132	.481526941	$.121\times10^{-1}$	.468203669	$-.113\times10^{-2}$
$.9610786\times10^{4}$	.497704786	.498961715	$.125\times10^{-2}$	.497567194	$-.137\times10^{-3}$
$.1570298\times10^{5}$	.499987099	.499996630	$.953\times10^{-5}$	.499985677	$-.142\times10^{-5}$
$.6945472\times10^{6}$	.5	.5	$.573\times10^{-9}$	.5	$-.274\times10^{-9}$

Table 3.6b: **Example 3.7**: A comparison of the asymptotic and numerical shock layer trajectories for (3.5) with $f(u) = u^2/2$ and $g(x) = \sin(4\pi x)$. Here $\varepsilon = 0.02$, $\alpha = 1$, $\mu = 0$, $d = 0.19$ and $x_0^0 = 0.250022546$.

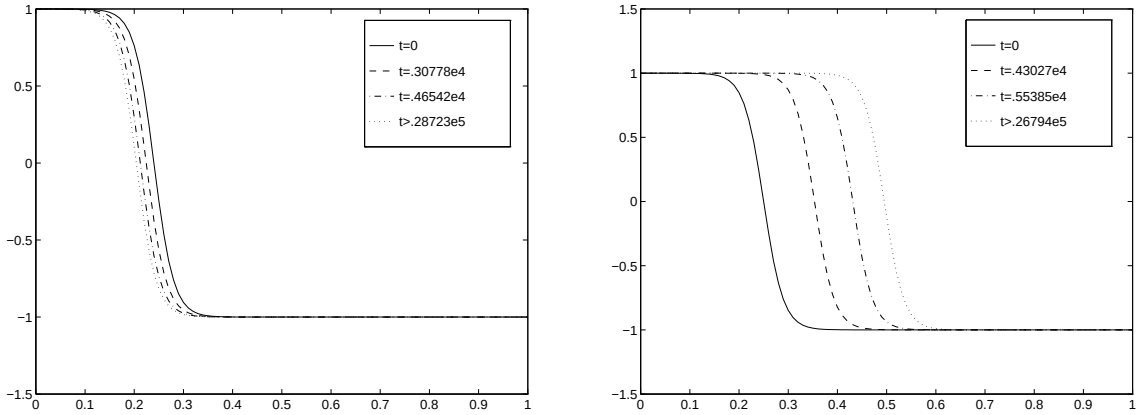

(a) (b)

Figure 3.8: **Example 3.7**: Plots of the numerical solutions to (3.5) at different times with $f(u) = u^2/2$ and $g(x) = \sin(4\pi x)$, where $\varepsilon = 0.02$, $\alpha = 1$, $\nu = 0$, $d = 0.19$ and initial condition $u_0(x) = u_s[\varepsilon^{-1}(x - x_0^0)]$. (a) $x_0^0 = 0.24$: shock layer moves towards left; (b) $x_0^0 = 0.25$: shock layer moves towards right.

Chapter 4

Phase Separation Models in One Spatial Dimension

4.1 The Viscous Cahn-Hilliard Equation

Numerous attempts have been made in recent years to explain the dynamics of phase separation in binary alloys. When a binary alloy, composed of species A and B, is prepared in a state of isothermal equilibrium at a temperature T_1, greater than the critical temperature T_c, the alloy's composition is spatially uniform with the concentration u, of B taking the constant value u_m. Suppose now that the two component system is quenched (rapidly cooled) to a uniform temperature T_2 less that T_c. Then the cooled system will separate itself out into a coexistence of two phases, one phase rich in species A and the other rich in B.

A rough description of the behavior of such systems can be provided by consideration of the Gibbs free energy $G(u,T)$, which is single welled for $T > T_c$, but has the double well form shown in Figure 4.1 for $T < T_c$. The interval (u_a^s, u_b^s) is called the spinodal interval, where u_a^s and u_b^s are spinodal points and are defined by the conditions $\frac{\partial^2 G}{\partial u^2} < 0$ in (u_a^s, u_b^s) and $\frac{\partial^2 G}{\partial u^2} > 0$ outside the interval $[u_a^s, u_b^s]$. Near the two local minima are the binodal values u_a and u_b, which are the two unique tangent points of the curve with the supporting tangent. A state u is said to be stable, metastable or unstable according to whether it corresponds to a homogeneous state which is a global minimizer, local but not global minimizer, or local non-minimizer respectively, for the free energy functional

$$F(u) = \int_\Omega G(u(x), T) dx \ , \tag{4.1}$$

at constant average concentrations (i.e., $\int_\Omega u dx$ is constant). For G as in Fig.4.1, the spinodal region $u_a^s \le u \le u_b^s$ is unstable, states satisfying $u \le u_a$ or $u \ge u_b$ are stable, and the remaining intervals are metastable. A mixture, initially with a homogeneous spatial composition taking values in the spinodal interval, will quickly evolve from this unstable state to an equilibrium configuration consisting of two coexisting phases with a spatial pattern composed of "grains" rich in either A or B. Such an evolution is called phase separation or spinodal decomposition. Then, a coarsening or ripening process ensues on a much slower time scale, as the system losses some of the grains, tending toward more stable patterns.

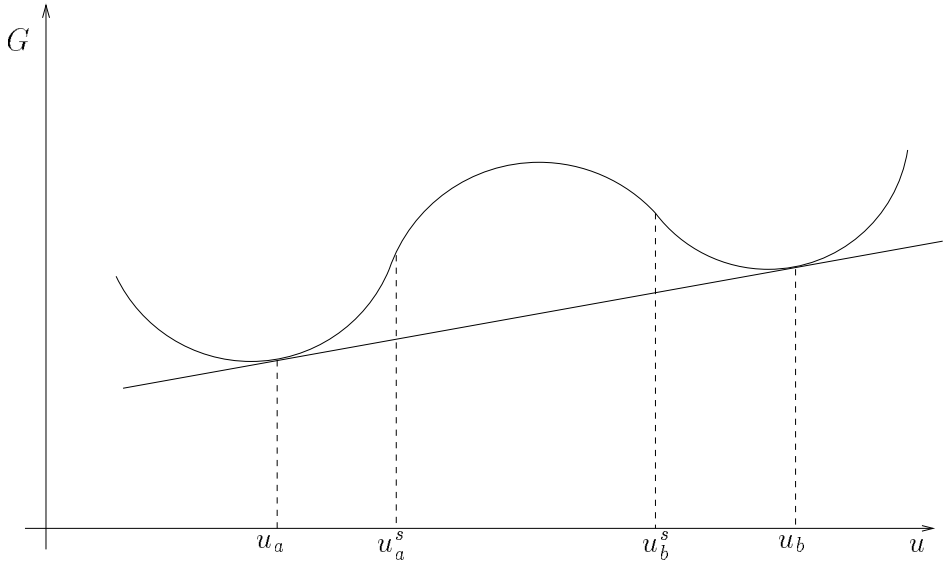

Figure 4.1: Free energy of the system below the critical temperature.

A naive attempt to extrapolate the dynamics of phase separation from the energy minimization of (4.1) would lead to a backward-forward heat equation

$$u_t = - \triangle Q(u) \,, \quad \text{with} \;\; Q(u) \equiv -G'(u) \,. \tag{4.2}$$

Here the diffusion coefficient $Q'(u)$ is positive in the spinodal interval. Thus, the initial value problem is classically ill-posed from the mathematical viewpoint. Experimental

data (cf. [46]) showed the importance of gradient energy effects to the phase separation and coarsening process. One way to obtain a physically justifiable regularization for equation (4.2) is due to Cahn and Hilliard [24] who included the energy contributions in their definition of the free energy. They modified the free energy $G(u)$ of the system by adding a gradient term $\varepsilon|\bigtriangledown u|^2/2$ to get

$$\hat{G}(u) = G(u) + \frac{\varepsilon^2}{2}|\bigtriangledown u|^2 \ . \tag{4.3}$$

Here $\varepsilon \to 0$ is the interfacial energy parameter, $G(u)$ is called the homogeneous free energy and $\hat{G}(u)$ is known as the Landau-Ginzburg free energy. Given that the mass u_m is fixed, the Cahn-Hilliard model for the equilibrium description of phase separation is characterized by minimizing the total energy viz.

$$\min I(u) \equiv \int_\Omega \left\{ G(u) + \frac{\varepsilon^2}{2}|\bigtriangledown u|^2 \right\} dx \quad , \quad \text{subject to} \quad \int_\Omega u(x)dx = u_m|\Omega| \ . \tag{4.4}$$

The kinetics of phase separation can be modeled using non-equilibrium thermodynamics. For an isothermal binary mixture, the mass flux J is proportional to the gradient of the intrinsic chemical potential μ,

$$J = -M \bigtriangledown \mu \ , \tag{4.5}$$

where $M > 0$ denotes the mobility and the chemical potential μ is the variational derivative of the energy $I(u)$:

$$\mu = \frac{\delta I}{\delta u} = -\varepsilon^2 \bigtriangleup u - Q(u) \ . \tag{4.6}$$

Then, from the diffusion equation, $u_t + \bigtriangledown \cdot J = 0$, assuming the mobility $M = 1$, one obtains the Cahn-Hilliard equation

$$u_t = \bigtriangleup(-\varepsilon^2 \bigtriangleup u - Q(u)) \ . \tag{4.7}$$

When the viscous stresses arising from the relative fluxes of the two components are taken into account, the diffusion equation as suggested in [78] gets modified to $u_t = \bigtriangleup(\mu + \gamma u_t)$,

where the term γu_t represents the viscous effects in the mixture. Taking the chemical potential μ as in (4.6), Novick-Cohen [78] obtained the following viscous Cahn-Hilliard equation describing the dynamics of viscous first order phase transitions

$$u_t = \triangle(-\varepsilon^2 \triangle u - Q(u) + \gamma u_t) \ . \tag{4.8}$$

Here the terms $-\varepsilon^2 \triangle^2 u$ and $\gamma \triangle u_t$ represent a gradient energy regularization and a viscous stress regularization, respectively, of the ill-posed backward-forward heat equation (4.2). Boundary conditions may be taken to be of Neumann type

$$\boldsymbol{n} \cdot \bigtriangledown(Q(u) - \varepsilon^2 \triangle u + \gamma u_t) = 0 \ \text{ (no flux)} \ , \quad \boldsymbol{n} \cdot \bigtriangledown u = 0 \ \text{ (variational)} \ , \tag{4.9}$$

where $\boldsymbol{n}$ is the outward unit normal to $\partial\Omega$. Another model for phase separation, which was introduced by Rubinstein and Sternberg [85] as a particular limit of the viscous Cahn-Hilliard equation, is the constrained (non-local) Allen-Cahn equation

$$u_t = \varepsilon^2 \triangle u + Q(u) - \frac{1}{|\Omega|} \int_\Omega Q(u) dx \ , \ \ x \in \Omega \ , \ \ t > 0 \ , \tag{4.10a}$$

$$\frac{\partial u}{\partial \boldsymbol{n}} = 0 \ , \quad x \in \partial\Omega \ , \ \ t > 0 \ . \tag{4.10b}$$

Note that these phase separation models (4.7), (4.8) and (4.10) can also be recovered from the phase-field equations which arise in the modeling of solidification of super-cooled liquids (cf. [8], [20], [21], [81]) in particular parameter limits.

There has been much recent work analyzing the dynamics associated with the phase separation models (4.7), (4.8) and (4.10). These studies have revealed that the phenomenon of phase separation and coarsening process in a binary alloy does occur in these models. In one dimensional setting, the dynamics associated with these models typically proceeds in two stages when ε is small: a relatively fast stage during which a pattern of internal layers is formed from initial data in an $O(1)$ time interval, followed by

an exponentially slow coarsening process during which the internal layers move exponentially slowly in time until they collapse together in pairs. For the Cahn-Hilliard equation, the existence of metastable internal layer motion has been proved in [2], [9], [15], [17], [32], [76], etc. and an explicit characterization of metastability is given in [15] (see also [35]) using a dynamical system approach. In [88] and [86] an asymptotic projection method is used to obtain similar explicit results for the viscous Cahn-Hilliard equation and the constrained Allen-Cahn equation, respectively. In a multi-dimensional setting, dynamic metastability can also occur for the phase separation models that conserve mass. For the Cahn-Hilliard equation, the motion of radially symmetric internal layer solutions, referred to in [3] as bubble solutions, has been shown to exhibit metastable behavior in [3] and [4]. In [112] the projection method is employed to give an explicit asymptotic description of metastable bubble motion for the constrained Allen-Cahn equation.

In this chapter, one of our main goals is to study the similarities and differences of the dynamics of an n-layer ($n \geq 2$) metastable pattern associated with the three phase separation models in one spatial dimension mentioned above and to compare our results with those of Bates and Xun [15] and Eyre [35]. The second goal is to use a hybrid algorithm based on our asymptotic information and the conservation of mass condition to characterize the entire coarsening process for these models. To do so, we consider the viscous Cahn-Hilliard equation in the following form

$$(1-\alpha)u_t = -(\varepsilon^2 u_{xx} + Q(u) - \alpha\kappa u_t)_{xx}\ ,\ \ -1 < x < 1\ ,\ \ t > 0\ , \tag{4.11a}$$

$$u_x(\pm 1, t) = u_{xxx}(\pm 1, t) = 0\ ;\quad u(x,0) = u_0(x)\ , \tag{4.11b}$$

where $u(x,t)$ is the concentration of one of the two components in the alloy. Here $\kappa > 0$ is the viscous parameter, $\varepsilon \to 0$ is the interfacial energy parameter, α is a homotopy parameter satisfying $0 \leq \alpha \leq 1$, and $Q(u) = -G'(u)$ where $G(u)$ is a double-well potential with wells of equal depth. More specifically, we assume that $Q(u)$ has exactly

three zeros on the interval $[s_-, s_+]$, located at $u = s_- < 0$, $u = 0$ and $u = s_+ > 0$, with

$$Q'(s_\pm) < 0 \ , \ \ Q'(0) > 0 \ , \ \ G(s_\pm) = 0 \ .$$

Prototypical is $Q(u) = 2(u - u^3)$, for which $s_\pm = \pm 1$ and $G(u) = (1-u^2)^2/2$. When $0 \leq \alpha < 1$, the mass $2u_m \equiv \int_{-1}^{1} u(x,t)dx$ is conserved for (4.11). We assume below that the initial value $u_0(x)$ is such that $s_- < u_m < s_+$. The importance of the homotopy parameter α is to distinguish three cases: (i) $\alpha = 0$, (ii) $0 < \alpha < 1$, $\kappa \neq 0$ and (iii) $\alpha = 1$, $\kappa \neq 0$. In case (i), equation (4.11) reduces to the Cahn-Hilliard equation for spinodal decomposition. In case (iii), we can integrate the right side of (4.11a) twice, explicitly impose a mass constraint, and re-scale t to obtain the constrained Allen-Cahn equation. Case (ii) corresponds to the viscous Cahn-Hilliard equation. Thus, the homotopy parameter α enables us to understand how three different models are related by studying only (4.11).

The organization of the chapter is as follows. In §4.2, we describe the asymptotic differential algebraic equations (DAEs) of motion, derived in [88], for the locations of the internal layers corresponding to an n-layer metastable pattern for (4.11), and compare these asymptotic results with corresponding full numerical results. In §4.3, by decoupling this system of DAEs, we study the metastable dynamics associated with the three phase separation models and compare our results for the Cahn-Hilliard equation with those in [15] and [35]. Finally, in §4.4, we propose a hybrid algorithms based on this DAE system and an interface realignment technique to simulate the entire coarsening process associated with these models.

4.2 Dynamics of an n-layer Metastable Pattern

In [88], a system of differential-algebraic equations that describes the metastable dynamics of an n-layer pattern for (4.11) was derived by applying the projection method. From

this DAE system, the metastable behavior associated with patterns of two internal layers was obtained and the asymptotic results for the layer dynamics were shown to compare very favorably with corresponding full numerical results. However, for a general pattern having $n > 2$ internal layers, this DAE system was not verified in [88] nor were general properties of the layer dynamics obtained. Here we first present the main asymptotic results in [88] and then supplement it with some numerical results.

Let $u_s(z)$ be the unique heteroclinic orbit connecting s_- and s_+, which satisfies

$$u_s''(z) + Q\left[u_s(z)\right] = 0\,, \quad -\infty < z < \infty\,; \quad u_s(0) = 0\,; \;\; u_s'(z) = 0\,; \tag{4.12a}$$

$$u_s(z) \sim s_+ - a_+ e^{-\nu_+ z}\,, \;\; z \to +\infty\,; \;\; u_s(z) \sim s_- + a_- e^{\nu_+ z}\,, \;\; z \to -\infty\,. \tag{4.12b}$$

The positive constant $\nu_\pm$ and $a_\pm$ in (4.12b) are defined by

$$\nu_\pm = [-Q'(s_\pm)]^{\frac{1}{2}}\;, \;\; \log a_\pm = \log(\pm s_\pm) + \int_0^{s_\pm} \left(\frac{\pm\nu_\pm}{[2G(\eta)]^{\frac{1}{2}}} + \frac{1}{\eta - s_\pm} \right) d\eta\;. \tag{4.13}$$

For $j = 0, 1, \ldots, n$, we define $\xi_j = (-1)^j \xi_0$, where $\xi_0 = \pm 1$ specifies the orientation of the internal layer closest to $x = -1$. For $j = 0, 1, \ldots, n$, the triplet (a_j, ν_j, s_j) is defined by

$$(a_j, \nu_j, s_j) = \begin{cases} (a_+, \nu_+, s_+)\,, & \text{when } \xi_j = -1\,, \\ (a_-, \nu_-, s_-)\,, & \text{when } \xi_j = +1\,. \end{cases} \tag{4.14}$$

Then an n-layer metastable pattern for (4.11) shown in Figure 4.2 is represented by the approximate form $u \sim u^*(x)$, where

$$u^*(x) = u^*(x; x_0, x_1, \ldots, x_{n-1}) \equiv u_s[\varepsilon^{-1}\xi_0(x - x_0)] + \sum_{j=1}^{n-1} \left(u_s[\varepsilon^{-1}\xi_j(x - x_j)] - s_j \right). \tag{4.15}$$

Here $x_j = x_j(t)$ for $j = 0, 1, \ldots, n-1$ and $x_{j-1}(t) < x_j(t)$. Since $u_s(0) = 0$, the curves $x = x_i(t)$, $\;i = 0, 1, \ldots, n-1$, closely determine the locations of the zeros of $u(x,t)$ during the slow evolution. The internal layer distances $d_j = d_j(t)$ are given by $d_j = x_j - x_{j-1}$ for $j = 0, 1, \ldots, n$, where we have introduced the fictitious layers x_{-1} and

x_n by $x_{-1} = -2 - x_0$ and $x_n = 2 - x_{n-1}$. The layers are assumed to be well-separated in the sense that $d_j(t) = O(1)$ as $\varepsilon \to 0$ for $j = 0, 1, \ldots, n$. A lengthy calculation in [88] leads to the following results for the metastable dynamics in the viscous Cahn-Hilliard equation (4.11).

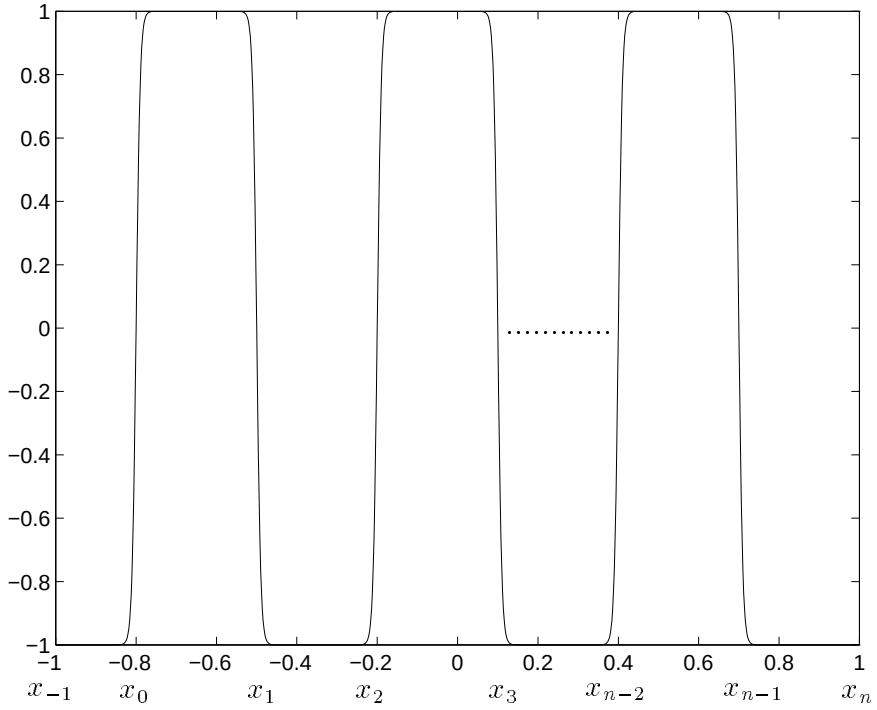

Figure 4.2: An n-layer metastable pattern for the viscous Cahn-Hilliard equation (4.11).

Proposition 4.1 *(From [88]) For $\varepsilon \to 0$, an n-layer metastable pattern for (4.11) with widely separated layers is represented by (4.15), where $x_i(t)$, $i = 0, 1, \ldots, n-1$, and an unknown function $\sigma_c(t)$ satisfy the explicit DAE system*

$$\alpha\kappa\beta\varepsilon^{-1}\dot{x}_j + (1-\alpha)\sum_{k=0}^{n-1}\dot{x}_k b_{jk} \sim \sigma_c\xi_j(s_+ - s_-) + H_j\,,\ j = 0, 1, \ldots, n-1\,, \quad (4.16a)$$

$$\sum_{k=0}^{n} s_k(x_k - x_{k-1}) \sim m - \varepsilon n(\theta_- - \theta_+)\,. \quad (4.16b)$$

Here the exponentially weak forces H_j for $j = 0, 1, \ldots, n-1$ and the coupling coefficients

b_{jk} for $j,k = 0,1,\ldots,n-1$ are defined by

$$H_j = 2\left(a_{j+1}^2\nu_{j+1}^2 e^{-\varepsilon^{-1}\nu_{j+1}d_{j+1}} - a_j^2\nu_j^2 e^{-\varepsilon^{-1}\nu_j d_j}\right), \tag{4.17a}$$

$$b_{jk} = \int_{-1}^{1}\left(u_s[\varepsilon^{-1}\xi_k(x-x_k)] - s_k\right)\left(u_s[\varepsilon^{-1}\xi_j(x-x_j)] - s_{j+1}\right)dx, \tag{4.17b}$$

where

$$\beta = \int_{-\infty}^{\infty}[u_s'(z)]^2 dz\,,\quad \theta_- = \int_{-\infty}^{0}[u_s(\eta)-s_-]\,d\eta\,,\quad \theta_+ = \int_0^{\infty}[s_+ - u_s(\eta)]\,d\eta\,. \tag{4.18}$$

To validate the DAE system (4.16) numerically, we compare the asymptotic and numerical results for the internal layer locations x_j corresponding to an n-layer metastable pattern for (4.11) with $Q(u) = 2(u-u^3)$ and $\kappa = 1$. For this form of $Q(u)$, the heteroclinic orbit constants needed in (4.16) and (4.17) can be obtained analytically as

$$a_\pm = 2\,,\quad \nu_\pm = 2\,,\quad s_\pm = \pm 1\,,\quad \beta = 4/3\,,\quad \theta_\pm = \log 2\,.$$

In the comparisons below, we chose different values of α resulting in different types of phase separation models and took $u(x,0) = u^*(x;x_0^0,\ldots,x_{n-1}^0)$ as the initial data for (4.11). Here u^* is the n-layer metastable pattern (4.15) and $x_j^0 \in (-1,1)\,, j = 0,1,\ldots,n-1$ are initial zeros of u. To eliminate any unwanted transient effects, we computed the full numerical solution to (4.11) with these initial data until $t = t_c$, where t_c was some positive constant, and reset x_j^0 to be the zeros of the numerical approximation u^h at time $t = t_c$. With these new values of x_j^0 as its initial data, the DAE system (4.16) was solved numerically and results were compared with corresponding full numerical results.

We solved the DAE system (4.16) using the implicit-ODE solver LSODI (cf. [48]). This solver requires the initial values of $\sigma_c(t)$, $x_i(t)$ for $i = 0,\ldots,n-1$ and their derivatives. For given initial values of x_i, for $i = 0,\ldots,n-1$, in our computations, $\sigma_c(0)$ was determined by the asymptotic estimate (4.25b) or (4.34) below, $\dot\sigma_c(0)$ was set to zero

and $\dot{x}_i(0)$ were obtained by solving (4.16a) which was treated as a linear system of $\dot{x}_i$. In addition, instead of calculating the coefficients b_{jk} in (4.16a) precisely from (4.17a), we used (4.24) below to evaluate them.

To compute numerical solutions to the evolution problem (4.11), we used the transverse method of lines approach introduced in §1.3, with a slight modification. Since the right hand side of (4.11) contains the derivative u_t, it is convenient to rewrite (4.11) in the form

$$\alpha\kappa u_t = \varepsilon^2 u_{xx} + Q(u) - \sigma\,, \qquad u_x(\pm 1, t) = 0\,, \tag{4.19a}$$

$$(1-\alpha)u_t = -\sigma_{xx}\,, \qquad \sigma_x(\pm 1, t) = 0\,, \tag{4.19b}$$

with $u(x,0) = u_0(x)$. Then, by replacing the time derivatives u_t in (4.19) by the backward differential formulas (BDF), this problem can be converted into a set of boundary value problems with two unknowns u_n and σ_n at each time step. These boundary value problems were solved by applying COLSYS [6]. This procedure works for $0 \le \alpha < 1$, since (4.19) is not well-defined when $\alpha = 1$ unless a mass constraint is imposed. For the special case $\alpha = 1$, we computed solutions to the constrained Allen-Cahn equation

$$u_t = \varepsilon^2 u_{xx} + Q(u) - \frac{1}{2}\int_{-1}^{1} Q(u)dx\,, \quad u_x(\pm 1, t) = 0\,, \;\; u(x,0) = u_0(x)\,. \tag{4.20}$$

After u_t is discretized by the BDF schemes, we obtain

$$\sum_{j=0}^{k} \beta_j u_{n-j}(x) = \beta_{n+1}\left(\varepsilon^2 (u_n)_{xx} + Q(u_n) - \frac{1}{2}\int_{-1}^{1} Q(u_n)dx\right)\,, \;\; (u_n)_x(\pm 1) = 0\,, \tag{4.21}$$

where k and β_j are same as in §1.3. Since these boundary value problems are non-local, we introduce the new variables $\boldsymbol{z} = (z_1, \ldots, z_4)^T$ with

$$z_1 = u_n\,, \;\; z_2 = (u_n)_x\,, \;\; z_3 = \int_{-1}^{1} Q(u_n)dx\,, \;\; z_4 = \int_{-1}^{x} Q(u_n)dx \Big/ \int_{-1}^{1} Q(u_n)dx\,. \tag{4.22}$$

With these new variables, (4.21) is reduced to a local problem

$$\boldsymbol{z}_x = F(\boldsymbol{z})\,, \quad z_2(-1) = z_2(1) = z_4(-1) = 0\,, \;\; z_4(1) = 1\,, \tag{4.23}$$

where nonlinear function $F : R^4 \to R^4$ can be easily derived from (4.21) and (4.22). Again, COLSYS was used to solve the boundary value problem (4.23) at each time step.

It has been clear from [15] and [88] that for the phase separation models specified by (4.11), the closest layers will move towards each other at an extremely slow rate and eventually undergo a collapse phase, leaving behind a metastable pattern with two fewer layers. In Tables 4.1 – 4.3, we give a comparison between the asymptotic and numerical results for the evolution of these collapse layers for three types of phase separation models corresponding to $\alpha = 0, \frac{1}{2}$ and 1. In these tables, the initial values of x_j for $j = 0, \ldots, n-1$ with $n = 6$ were chosen to be near -0.7, -0.4, -0.1, 0.15, 0.5 and 0.8, so the second and third columns compare the numerical and asymptotic elapsed time necessary for the distance d_3 to be given by the values in the first column. These elapsed times are found to agree to more than three significant digits. In Figure 4.3 – 4.5, we plot the full numerical solutions at different time to (4.11) corresponding to the parameter values used for Table 4.1 – 4.3, respectively. The behavior of the solution during the metastable phase and the collapse phase shown in these figures will be discussed in the next few sections.

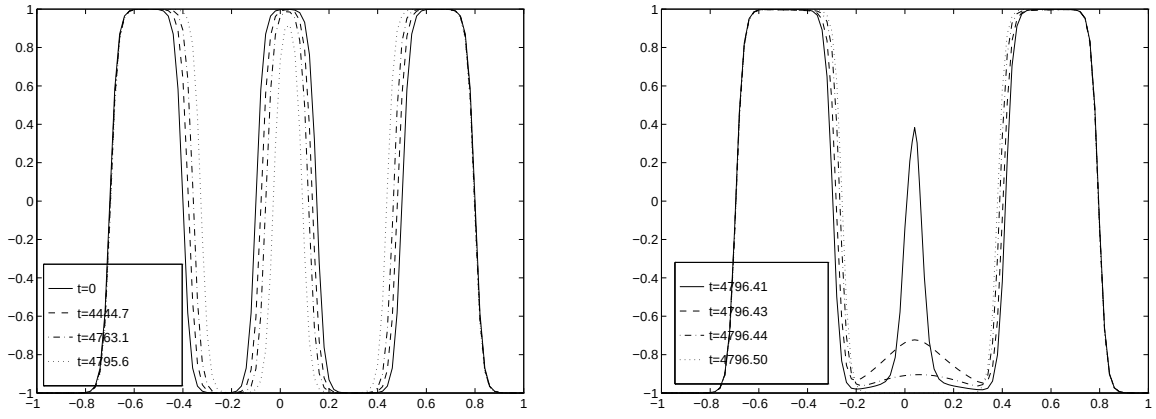

Figure 4.3: Plot of the numerical solution to the Cahn-Hilliard equation at different times corresponding to the parameter values given in Table 4.1.

d_3	t(num.)	t(asy.)
0.2499637	0.11805135 $\times 10^2$	0.11805099 $\times 10^2$
0.2490057	0.31421876 $\times 10^3$	0.31423049 $\times 10^3$
0.2457128	0.12120381 $\times 10^4$	0.12121263 $\times 10^4$
0.2353902	0.30076767 $\times 10^4$	0.30080758 $\times 10^4$
0.2221106	0.40610571 $\times 10^4$	0.40615483 $\times 10^4$
0.2049384	0.45628835 $\times 10^4$	0.45634494 $\times 10^4$
0.1503616	0.47902868 $\times 10^4$	0.47909376 $\times 10^4$
0.1028643	0.47961152 $\times 10^4$	0.47967273 $\times 10^4$
0.0697038	0.47963267 $\times 10^4$	0.47971114 $\times 10^4$

Table 4.1: A comparison of the asymptotic and numerical results for $t = t(d_3)$ for the Cahn-Hilliard equation ($\alpha = 0$) with $\varepsilon = 0.03$. The initial values of x_j for $j = 0, \ldots, 5$ were -0.7000000, -0.3999999, -0.0999999, 0.1499999, 0.4999999, 0.8000000.

4.3 Properties of the Metastable Dynamics

The DAE system (4.16) provides a quantitative characterization of metastable internal layer motion for the viscous Cahn-Hilliard equation (4.11). However, it is not easily analyzed and thus gives little analytical information about the metastable dynamics unless the system is asymptotically simplified. In this section, we decouple the DAE system (4.16) and then study this reduced system to reveal the analytical behavior of the metastable dynamics associated with the three phase separation models.

4.3.1 Simplification of the DAE System (4.16)

In [88], the coefficients b_{jk} defined by (4.17b) have been evaluated asymptotically as

$$\begin{aligned} b_{jk} &\sim -(-1)^{j+k}(x_j - x_k)(s_+ - s_-)^2 \\ &\quad -\varepsilon\left(1 - (-1)^{j+k}\right)\xi_j(s_+ - s_-)(\theta_- - \theta_+)\ , \ \text{for } j > k\ , \\ b_{jj} &\sim -\varepsilon\mu\ , \ b_{jk} = O(e^{-\varepsilon^{-1}c})\ , \ \text{for } j < k\ . \end{aligned} \tag{4.24}$$

d_3	t(num.)	t(asy.)
0.2499080	0.10960657 $\times 10^2$	0.10947517 $\times 10^2$
0.2457898	0.45001770 $\times 10^3$	0.45013814 $\times 10^3$
0.2354383	0.11982005 $\times 10^4$	0.11986815 $\times 10^4$
0.2268495	0.15722918 $\times 10^4$	0.15731235 $\times 10^4$
0.2068120	0.20064226 $\times 10^4$	0.20078002 $\times 10^4$
0.1687788	0.22184970 $\times 10^4$	0.22204742 $\times 10^4$
0.1484624	0.22420676 $\times 10^4$	0.22442599 $\times 10^4$
0.1016572	0.22539916 $\times 10^4$	0.22564691 $\times 10^4$
0.0545736	0.22551925 $\times 10^4$	0.22576482 $\times 10^4$

Table 4.2: A comparison of the asymptotic and numerical results for $t = t(d_3)$ for the viscous Cahn-Hilliard equation ($\alpha = 0.5$) with $\varepsilon = 0.04$. The initial values of x_j for $j = 0, \ldots, 5$ were -0.7000000, -0.3999999, -0.0999996, 0.1499996, 0.5000000, 0.8000000.

Here $\mu = \int_{-\infty}^{\infty} [s_+ - u_s(\eta)][u_s(\eta) - s_-] d\eta$ and c is a positive constant that is proportional to the distance $x_k - x_j$. If we write the left side of (4.16a) in the matrix form $B\dot{\boldsymbol{x}}$, then the matrix B is lower triangular to within exponentially small terms. Moreover, if $0 < \alpha \leq 1$, then the entries in the matrix B that are below the main diagonal are $O(\varepsilon)$ smaller than the entries along the main diagonal. In this case, a simplified form of the DAE system (4.16) was obtained in [88], although only a preliminary description of the metastable behavior was given there. In addition, numerical verification of the asymptotic results in [88] are needed to make the work in [88] complete.

For $0 < \alpha \leq 1$, we follow [88] and introduce the decoupled form of (4.16). Since B is a diagonal matrix to within $O(\varepsilon)$ terms, the system (4.16) can be asymptotically decoupled for this range of α to obtain

$$\alpha\kappa\beta\dot{x}_j \sim \varepsilon\xi_j n^{-1}(s_+ - s_-)^{-1} \sum_{k=0}^{n-1} (s_k - s_{k+1}) H_k + \varepsilon H_j \,, \quad j = 0, \ldots, n-1 \,, \tag{4.25a}$$

$$\sigma_c \sim n^{-1}(s_+ - s_-)^{-2} \sum_{k=0}^{n-1} (s_k - s_{k+1}) H_k \,. \tag{4.25b}$$

This form is an exact reformulation of (4.16) when $\alpha = 1$. Let $n \geq 2$ and label the

d_3	t(num.)	t(asy.)
0.2499500	0.11561895×10^2	0.11528481×10^2
0.2494742	0.12103537×10^3	0.12102348×10^3
0.2450228	0.10128793×10^4	0.10130617×10^4
0.2370225	0.21550525×10^4	0.21555446×10^4
0.2201322	0.34372605×10^4	0.34383206×10^4
0.2058314	0.39218631×10^4	0.39233456×10^4
0.1635920	0.43265906×10^4	0.43291128×10^4
0.1171353	0.43761505×10^4	0.43793961×10^4
0.0497620	0.43813902×10^4	0.43846704×10^4

Table 4.3: A comparison of the asymptotic and numerical results for $t = t(d_3)$ for the constrained Allen-Cahn equation ($\alpha = 1$) with $\varepsilon = 0.04$. The initial values of x_j for $j = 0, \ldots, 5$ were -0.7000000, -0.4000000, -0.0999997, 0.1499996, 0.5000000, 0.8000000.

initial layer separations $d_j(0)$ for $j = 0, \ldots, n$ by $d_j^0 = d_j(0)$. Assume that there is some J with $J \neq 0$ and $J \neq n$ such that $\nu_J d_J^0 < \nu_j d_j^0$ for all $j = 0, \ldots, n$ and $j \neq J$. Then, from (4.25a), it is easy to show that the distance $d_J(t)$ between x_J and x_{J-1} satisfies the approximate evolution equation

$$d_j' \sim -\frac{4\varepsilon}{\alpha\kappa\beta}\left(1 - \frac{2}{n}\right) a_J^2 \nu_J^2 e^{-\varepsilon^{-1}\nu_J d_J}\,, \qquad d_J(0) = d_J^0 > 0\,. \tag{4.26}$$

Integrating (4.26), we obtain

$$d_J(t) \sim d_J^0 + \frac{\varepsilon}{\nu_J}\log[1 - t/t_s]\,, \qquad t_s \equiv \frac{\alpha\kappa\beta[1-2/n]^{-1}}{4a_J^2\nu_J^3} e^{\varepsilon^{-1}\nu_J d_J^0}\,. \tag{4.27}$$

Thus, $d_J = O(\varepsilon)$ when $t \approx t_s$. Since the right hand sides of (4.25a) do not depend on α, it is clear that the viscous Cahn-Hilliard equation ($0 < \alpha < 1$) has the same metastable dynamics as the constrained Allen-Cahn equation ($\alpha = 1$) except for the scale of the collapse time.

For the Cahn-Hilliard equation ($\alpha = 0$), an asymptotic simplification of (4.16) is not so straightforward. Using (4.24), adding up two consecutive ODEs in (4.16a), differentiating

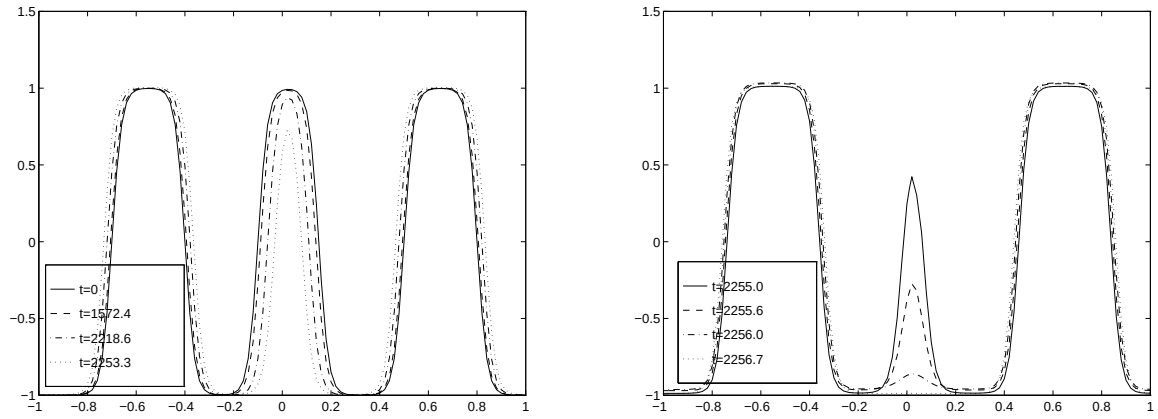

Figure 4.4: Plot of the numerical solution to the viscous Cahn-Hilliard equation at different times corresponding to the parameter values given in Table 4.2.

(4.16b) and performing certain rescalings, we can obtain

$$\begin{pmatrix} 1-\varepsilon\mu_0 & -\varepsilon\mu_0 & 0 & 0 & \dots & 0 & 0 \\ -1 & 1-\varepsilon\mu_1 & -\varepsilon\mu_1 & 0 & \dots & 0 & 0 \\ 1 & -1 & 1-\varepsilon\mu_2 & -\varepsilon\mu_2 & \dots & 0 & 0 \\ & & & \vdots & & & \\ (-1)^n & -(-1)^n & (-1)^n & -(-1)^n & \dots & 1-\varepsilon\mu_{n-2} & -\varepsilon\mu_{n-2} \\ 1 & -1 & 1 & -1 & \dots & (-1)^{n-1} & (-1)^n \end{pmatrix} \begin{pmatrix} \dot{x}_0 \\ \dot{x}_1 \\ \dot{x}_2 \\ \vdots \\ \dot{x}_{n-2} \\ \dot{x}_{n-1} \end{pmatrix} \sim \begin{pmatrix} r_0 \\ r_1 \\ r_2 \\ \vdots \\ r_{n-2} \\ 0 \end{pmatrix}, \tag{4.28}$$

where μ_k and r_k are defined by, for $0 \le k \le n-2$,

$$\mu_k = \frac{\mu}{(x_{k+1}-x_k)(s_+-s_-)^2}, \tag{4.29a}$$

$$\begin{aligned} r_k &= \frac{1}{(x_{k+1}-x_k)(s_+-s_-)^2}\,(H_k + H_{k+1}) \\ &= \frac{2}{(x_{k+1}-x_k)(s_+-s_-)^2}\left(a_{k+2}^2\nu_{k+2}^2 e^{-\varepsilon^{-1}\nu_{k+2}d_{k+2}} - a_k^2\nu_k^2 e^{-\varepsilon^{-1}\nu_k d_k}\right). \end{aligned} \tag{4.29b}$$

From the first three rows of (4.28), it is not hard to derive that $\dot{x}_0 \sim \varepsilon\mu_0\dot{x}_1 + r_0$, $\dot{x}_1 \sim \varepsilon\mu_1\dot{x}_2 + r_0 + r_1$ and $\dot{x}_2 \sim \varepsilon\mu_2\dot{x}_3 + r_1 + r_2 + \varepsilon\mu_1(r_0+r_1)$. In general, we can use the

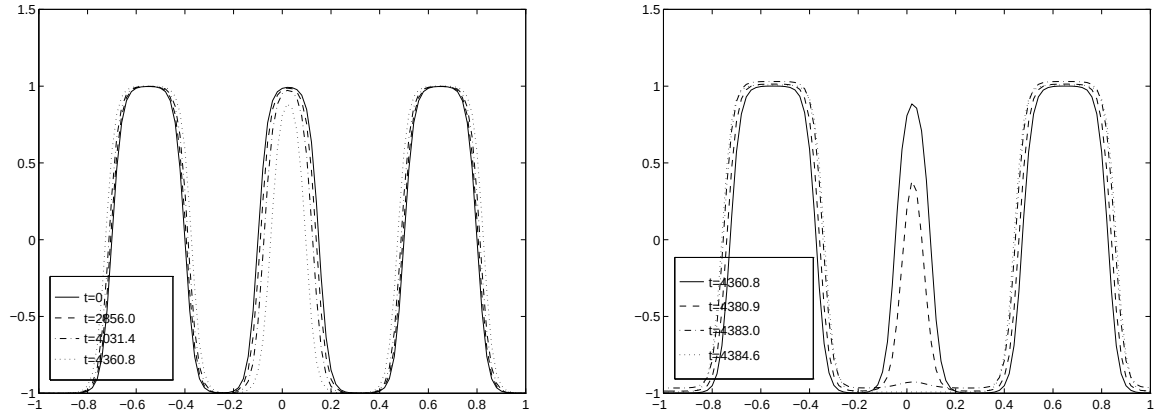

Figure 4.5: Plot of the numerical solution to the constrained Allen-Cahn equation at different times corresponding to the parameter values given in Table 4.3.

induction principle to show that

$$\dot{x}_j \sim \varepsilon\mu_j\dot{x}_{j+1} + \sum_{k=1}^{j} \varepsilon^{j-k}\,(r_{k-1} + r_k) \prod_{l=k}^{j-1} \mu_l\,, \qquad \text{for } 1 \le j \le n-2\,. \tag{4.30}$$

Multiplying the last row of (4.28) by $(-1)^{n-1}$ and adding it to the second to last row, we have

$$-\varepsilon\mu_{n-2}\dot{x}_{n-2} + (1-\varepsilon\mu_{n-2})\dot{x}_{n-1} \sim r_{n-2}\ , \tag{4.31}$$

which can be combined with (4.30) to yield

$$\dot{x}_{n-1} \sim \sum_{k=0}^{n-2} \varepsilon^{n-2-k} r_k \prod_{l=k+1}^{n-2} \mu_l\ . \tag{4.32}$$

Substituting (4.32) into (4.30), we can obtain $\dot{x}_j$ for $j = n-2, \ldots, 0$, recursively. Specifically, the internal layer locations $x_j(t)$ for $j = 0, \ldots, n-1$ satisfy

$$\dot{x}_j \sim \sum_{k=j}^{n-2} \varepsilon^{k-j} r_k \prod_{l=j}^{k-1} \mu_l + \sum_{k=0}^{j-1} \varepsilon^{j-1-k} r_k \prod_{l=k+1}^{j-1} \mu_l\ , \tag{4.33}$$

where μ_k and r_k are given in (4.29). From (4.16a) and (4.33) with $j = 0$, it is straightforward to get the following estimate for $\sigma_c(t)$

$$\sigma_c \sim -\frac{1}{\xi_0(s_+ - s_-)} \left(H_0 + \varepsilon\mu \sum_{k=0}^{n-2} \varepsilon^k r_k \prod_{l=0}^{k-1} \mu_l \right)\ . \tag{4.34}$$

Since $\mu r_k = \mu_k(H_k + H_{k+1})$, we can neglect some higher order terms in this estimate to obtain

$$\sigma_c \sim -\frac{1}{\xi_0(s_+ - s_-)} \sum_{k=0}^{n-1} \varepsilon^k H_k \prod_{l=0}^{k-1} \mu_l \ . \tag{4.35}$$

As a partial check on our simplified results, the estimates for σ_c in (4.25b), (4.34) and (4.35) were evaluated for various sets of internal layer locations and were found to compare very favorably with corresponding numerical results computed directly from (4.16) using LSODI. The results are shown in Table 4.4 and 4.5.

(x_0, x_1, x_2, x_3)	σ_c (num.)	σ_c (4.34)	σ_c (4.35)
$(-0.9, -0.4, 0, 0.6)$	0.336661×10^{-7}	0.336380×10^{-7}	0.329785×10^{-7}
$(-0.4, -0.1, 0.1, 0.5)$	-0.117992×10^{-8}	-0.109940×10^{-8}	-0.104577×10^{-8}
$(-0.5, -0.2, 0.2, 0.8)$	$-0.149581 \times 10^{-11}$	$-0.149597 \times 10^{-11}$	$-0.144732 \times 10^{-11}$
$(-0.6, -0.2, 0.2, 0.6)$	$-0.697625 \times 10^{-16}$	$-0.696720 \times 10^{-16}$	$-0.679726 \times 10^{-16}$
$(-0.7, -0.3, 0.25, 0.6)$	$-0.729543 \times 10^{-16}$	$-0.725283 \times 10^{-16}$	$-0.707289 \times 10^{-16}$

Table 4.4: A comparison of the asymptotic and numerical results for σ_c for the Cahn-Hilliard equation ($\alpha = 0$) with $\varepsilon = 0.02$ and $Q(u) = 2(u - u^3)$. Here $n = 4$ and $\xi_0 = 1$.

(x_0, x_1, x_2, x_3)	σ_c (num.)	σ_c (4.25b)
$(-0.5, -0.1, 0.1, 0.5)$	0.127273×10^{-4}	0.129567×10^{-4}
$(-0.7, -0.3, 0, 0.5)$	0.162085×10^{-7}	0.164682×10^{-7}
$(-0.5, -0.1, 0.3, 0.7)$	$-0.213520 \times 10^{-10}$	$-0.209847 \times 10^{-10}$
$(-0.75, -0.25, 0.2, 0.75)$	0.738668×10^{-12}	0.747657×10^{-12}

Table 4.5: A comparison of the asymptotic and numerical results for σ_c for the viscous Cahn-Hilliard equation ($\alpha = \frac{1}{2}$) with $\varepsilon = 0.03$ and $Q(u) = 2(u - u^3)$. Here $n = 4$ and $\xi_0 = 1$.

4.3.2 Comparisons of the Internal Layer Dynamics

Using the decoupled ODE systems (4.25) and (4.33), we are able to study analytically the metastable behavior associated with the viscous Cahn-Hilliard equation (4.11). We first consider the Cahn-Hilliard equation ($\alpha = 0$). Let $n \geq 4$ in (4.33) and label the initial layer separation $d_j(0)$ for $j = 0, \ldots, n$ by $d_j^0 = d_j(0)$. Assume that for some J with $2 \leq J \leq n-2$, we have that $\nu_J d_J^0 < \nu_j d_j^0$ for all $j = 0, \ldots, n$ and $j \neq J$. Then, from (4.29b), it is easy to show that

$$r_{J-2} \sim \frac{2}{d_{J-1}(s_+ - s_-)^2} a_J^2 \nu_J^2 e^{-\varepsilon^{-1}\nu_J d_J}, \qquad r_J \sim -\frac{2}{d_{J+1}(s_+ - s_-)^2} a_J^2 \nu_J^2 e^{-\varepsilon^{-1}\nu_J d_J}, \quad (4.36)$$

and the rest of the r_j's are exponentially small, compared with r_{J-2} and r_J. Now, from (4.33), we have

$$\dot{x}_{J-2} \sim r_{J-2} > 0\,, \quad \dot{x}_{J-1} \sim r_{J-2} > 0\,, \quad \dot{x}_J \sim r_J < 0\,, \quad \dot{x}_{J+1} \sim r_J < 0\,. \quad (4.37)$$

This means that the interfaces of the annihilating interval (x_{J-1}, x_J) will approach each other and eventually disappear, while the nearest neighboring intervals move together in an asymptotically rigid way. For the layers that are left of x_{J-2} and right of x_{J+1}, we can find from (4.33) that

$$\dot{x}_{J-k} \sim \varepsilon^{k-2} r_{J-2} \prod_{l=J-k}^{J-3} \mu_l \sim O(\varepsilon^{k-2} e^{-\varepsilon^{-1}\nu_J d_J}) > 0\,, \quad k \geq 2\,, \quad (4.38a)$$

$$\dot{x}_{J+k} \sim \varepsilon^{k-1} r_J \prod_{l=J+1}^{J+k-1} \mu_l \sim -O(\varepsilon^{k-1} e^{-\varepsilon^{-1}\nu_J d_J}) < 0\,, \quad k \geq 1\,. \quad (4.38b)$$

Therefore, we expect that the layers x_{J-1} and x_{J-2} (x_J and x_{J+1}) will move at the same speed and direction to the right (left), and that the other layers on the left (right) will move in the same direction as x_{J-1} and x_{J-2} (x_J and x_{J+1}), but at a successive slower speed, i.e., x_{J-k_1} with $k_1 \geq 3$ (x_{J+k_2} with $k_2 \geq 2$) is $O(\varepsilon)$ slower than its right neighbor x_{J-k_1+1} (left neighbor x_{J+k_2-1}). This analysis has been verified numerically (e.g., see

Figure 4.3). From (4.36) and (4.37), it is easy to show that the distance $d_J(t)$ between x_J and x_{J-1} satisfies

$$d_J' \sim -\frac{2}{(s_+ - s_-)^2} a_J^2 \nu_J^2 e^{-\varepsilon^{-1}\nu_J d_J} \left(d_{J-1}^{-1} + d_{J+1}^{-1} \right) , \qquad d_J(0) = d_J^0 > 0 . \tag{4.39}$$

Since the distances d_{J-1} and d_{J+1} are constant to within $O(\varepsilon)$ terms before the layer collapse, we integrate (4.39) to obtain

$$d_J(t) \sim d_J^0 + \frac{\varepsilon}{\nu_J} \log\left(1 - t/t_s\right), \quad t_s \equiv \frac{\varepsilon (s_+ - s_-)^2 \left({d_{J-1}^0}^{-1} + {d_{J+1}^0}^{-1} \right)^{-1}}{2 a_J^2 \nu_J^3} e^{\varepsilon^{-1}\nu_J d_J^0}. \tag{4.40}$$

Here t_s is the approximate collapse time for the Cahn-Hilliard equation.

We now return to study the motion of the layers characterized by the ODE system (4.25a) for the viscous Cahn-Hilliard equation with $0 < \alpha \leq 1$. We note that in this case the metastable dynamics is insensitive to the value of α except for the time scale of the motion. Let $n \geq 3$ and assume that there is some J with $1 \leq J \leq n-1$ such that $\nu_J d_J^0 < \nu_j d_j^0$ for all $j = 0, \ldots, n$ and $j \neq J$. Then, from (4.17a), we have $H_J \sim -H_{J-1} \sim -2a_J^2 \nu_J^2 e^{-\varepsilon^{-1}\nu_J d_J}$, while the other H_j's are exponentially small compared with H_J and H_{J-1}. Thus, using (4.25a), it is easy to obtain that

$$\alpha\kappa\beta \dot{x}_{J-1} \sim \varepsilon H_{J-1}[1 - 2/n] > 0 \; ; \; \alpha\kappa\beta \dot{x}_J \sim -\varepsilon H_{J-1}[1 - 2/n] < 0 \; ; \tag{4.41a}$$

$$\alpha\kappa\beta \dot{x}_{J-i} \sim \frac{2\varepsilon}{n}(-1)^i H_{J-1} \; , \; \; i \geq 2 \; ; \; \; \alpha\kappa\beta \dot{x}_{J+i} \sim \frac{2\varepsilon}{n}(-1)^i H_{J-1} \; , \; \; i \geq 1 \, . \tag{4.41b}$$

Therefore, when $0 < \alpha \leq 1$, as the collapse layers move toward each other, the other layers move asymptotically at speeds of a same order as the collapse layers and in alternate left and right directions (see Figure 4.4 and 4.5). In other words, the mass of the disappearing "island" will be consumed *evenly* by the rest of the "islands" by expanding their widths. This has been verified by the full numerical results in Figure 4.4 – 4.6.

Now let's analyze the motion of internal layers with collapse layers close to the boundaries. For the Cahn-Hilliard equation, let $n \geq 3$ and assume that for $J = 0, 1, n-1$ or n,

we have that $\nu_J d_J^0 < \nu_j d_j^0$ for all $j = 0, \ldots, n$ and $j \neq J$. If $J = n-1$, then

$$r_{n-3} \sim \frac{2}{d_{n-2}(s_+ - s_-)^2} a_{n-1}^2 \nu_{n-1}^2 \, e^{-\varepsilon^{-1}\nu_{n-1} d_{n-1}}$$

will be dominant, as the other r_j's are exponentially small compared with r_{n-3}. Thus, we obtain from (4.33) that

$$\dot{x}_j \sim \varepsilon^{n-3-j} r_{n-3} \prod_{l=j}^{n-4} \mu_l > 0\,, \qquad \text{for } 0 \le j \le n-4\,, \tag{4.42a}$$

$$\dot{x}_{n-3} \sim r_{n-3} > 0\,, \quad \dot{x}_{n-2} \sim r_{n-3} > 0\,, \quad \dot{x}_{n-1} \sim \varepsilon \mu_{n-2} r_{n-3} > 0\,. \tag{4.42b}$$

Using these asymptotic estimates, it follows that all layers will move to the right, but their speeds are different: while the layers x_{n-3} and x_{n-2} are shifting at the same speed r_{n-3} , other layers are almost static. This is verified in Figure 4.6(a). In Figure 4.6–4.8, we plot the full numerical solutions to the viscous Cahn-Hilliard equation (4.11) for the metastable phase in parts (a), (c) and (e) and for the collapse phase in parts (b), (d) and (f). In each of these figures, we plot the solutions at different times for (4.11) corresponding to $\alpha = 0$, $\alpha = \frac{1}{2}$ and $\alpha = 1$. From (4.42b), we have that

$$\dot{d}_{n-1} \sim -\frac{2}{d_{n-2}(s_+ - s-)^2} a_{n-1}^2 \nu_{n-1}^2 e^{-\varepsilon^{-1}\nu_{n-1} d_{n-1}}\,, \tag{4.43}$$

and d_{n-2} is constant to within $O(\varepsilon)$ terms before the annihilation. Hence, we can integrate (4.43) to obtain

$$d_{n-1}(t) \sim d_{n-1}^0 + \frac{\varepsilon}{\nu_{n-1}} \log\left(1 - t/t_s\right)\,, \qquad t_s \equiv \frac{\varepsilon (s_+ - s_-)^2 d_{n-2}^0}{2 a_{n-1}^2 \nu_{n-1}^3} \, e^{\varepsilon^{-1}\nu_{n-1} d_{n-1}^0}\,. \tag{4.44}$$

Next, consider the Cahn-Hilliard equation with $J = n$. Then

$$r_{n-2} \sim \frac{2}{d_{n-1}(s_+ - s_-)^2} \, a_n^2 \nu_n^2 \, e^{-\varepsilon^{-1}\nu_n d_n}$$

will be dominant in this case. From (4.33), it is easy to show that

$$\dot{x}_j \sim \varepsilon^{n-2-j} r_{n-2} \prod_{l=j}^{n-3} \mu_l > 0\,, \qquad \text{for } 0 \le j \le n-3\,, \tag{4.45a}$$

$$\dot{x}_{n-2} \sim r_{n-2} > 0\,, \qquad \dot{x}_{n-1} \sim r_{n-2} > 0\,. \tag{4.45b}$$

Thus, the layers x_{n-2} and x_{n-1} will move to the right at the same speed r_{n-2}, while other layers will move in the same direction, but at a much slower speed. This is verified in Figure 4.7(a). In a similar way as in the derivation of (4.44), we can estimate the length of the annihilating interval (x_n, x_{n-1}) as

$$d_n(t) \sim d_n^0 + \frac{\varepsilon}{\nu_n} \log\left(1 - t/t_s\right) , \qquad t_s \equiv \frac{\varepsilon (s_+ - s_-)^2 d_{n-1}^0}{4 a_n^2 \nu_n^3}\, e^{\varepsilon^{-1} \nu_n d_n^0} . \tag{4.46}$$

For $J = 0$ or $J = 1$, it is clear by symmetry that the metastable behavior of a pattern of n internal layers is similar to that for the case $J = n$ or $J = n - 1$, respectively.

For the viscous Cahn-Hilliard equation (4.11) with $0 < \alpha \le 1$, let $n \ge 2$ and assume that for $J = 0$ or $J = n$, we have that $\nu_J d_J^0 < \nu_j d_j^0$ for all $j = 0, \ldots, n$ and $j \ne J$. When $J = n$, we have from (4.17a) that $H_{n-1} \sim 2 a_n^2 \nu_n^2\, e^{-\varepsilon^{-1} \nu_n d_n}$ and that other H_j's are exponentially small compared with H_{n-1}. Thus, (4.25a) reduces to

$$\alpha \kappa \beta \dot{x}_{n-1} \sim \varepsilon (1 - \frac{1}{n}) H_{n-1} , \quad \alpha \kappa \beta \dot{x}_j \sim \frac{\varepsilon}{n} (-1)^{n-j} H_{n-1} , \quad \text{for } 0 \le j \le n-2 . \tag{4.47}$$

This means that x_{n-1} will collapse at the boundary and other layers will be shifting at the same speed and at opposite directions. As a results, the change of the mass due to the annihilation of x_{n-1} will be compensated by the remaining layers evenly. This is verified in Figure 4.7(c) and (e). Using $\dot{d}_n = -2 \dot{x}_{n-1}$ and (4.47), we have

$$d_n(t) \sim d_n^0 + \frac{\varepsilon}{\nu_n} \log\left(1 - t/t_s\right) , \qquad t_s \equiv \frac{\alpha \kappa \beta [1 - 1/n]^{-1}}{4 a_n^2 \nu_n^3}\, e^{\varepsilon^{-1} \nu_n d_n^0} . \tag{4.48}$$

The dynamics is similar when $J = 0$.

Next, we consider the dynamics of an n-layer metastable pattern which has two smallest neighboring "islands". Specifically, we assume that $n \ge 4$ and there is some J with $2 \le J \le n - 2$ such that $\nu_J d_J^0 = \nu_{J+1} d_{J+1}^0 < \nu_j d_j^0$ for all $j = 0, \ldots, n$ and $j \ne J, J+1$. For the sake of simplicity, we let $Q(u)$ be an odd nonlinearity for which $a_+ = a_- \equiv a$ and $\nu_+ = \nu_- \equiv \nu$. In this case, $d_J^0 = d_{J+1}^0$ and thus we further assume that

$d \equiv d_J \sim d_{J+1}$ as $\varepsilon \to 0$ during the metastable phase. Defining $H \equiv 2a^2\nu^2\, e^{-\varepsilon^{-1}\nu d}$, we obtain from (4.16) that $H_{J-1} \sim H$ and $H_{J+1} \sim -H$, and that the remaining H_j's are asymptotically negligible. From now on in this section, we use the notation $f = o'(g)$, by which we mean that f is exponentially small with respect to g as $\varepsilon \to 0$. For the viscous Cahn-Hilliard equation with $0 < \alpha \leq 1$, we can find from (4.25) that $\sigma_c = o'(H)$ and

$$\alpha\kappa\beta\dot{x}_{J-1} \sim \varepsilon H_{J-1} > 0\,, \quad \alpha\kappa\beta\dot{x}_{J+1} \sim \varepsilon H_{J+1} < 0\,, \quad \dot{x}_j = o'(H)\,, \tag{4.49}$$

for $j \neq J-1,\, J+1$. Thus, we can claim that during the metastable phase, the layers x_{J-1} and x_{J+1} move towards each other, while the other layers, including the interface x_J joining the smallest intervals (x_{J-1}, x_J) and (x_J, x_{J+1}), remains stationary in time to within exponentially small precision. For the Cahn-Hilliard equation ($\alpha = 0$), it is easy to show from (4.29b) and (4.33) that

$$\begin{aligned} r_{J-2} &\sim \frac{1}{d_{J-1}(s_+ - s_-)^2}\, H_{J-1}\,, \qquad r_{J-1} \sim \frac{1}{d_J(s_+ - s_-)^2}\, H_{J-1}\,, \\ r_J &\sim \frac{1}{d_{J+1}(s_+ - s_-)^2}\, H_{J+1}\,, \qquad r_{J+1} \sim \frac{1}{d_{J+2}(s_+ - s_-)^2}\, H_{J+1}\,, \\ r_j &= o'(H)\,, \qquad \text{for } j \neq J \pm 1,\, J \pm 2\,. \end{aligned} \tag{4.50}$$

Therefore, the internal layer locations $x_j(t)$ satisfy

$$\begin{aligned} \dot{x}_{J-2} &\sim r_{J-2} > 0\,, \qquad \dot{x}_{J-1} \sim r_{J-1} + r_{J-2} > 0\,, \\ \dot{x}_{J+2} &\sim r_{J+1} < 0\,, \qquad \dot{x}_{J+1} \sim r_J + r_{J+1} < 0\,, \\ \dot{x}_j &= O(\varepsilon H)\,, \qquad \text{for } j \neq J \pm 1,\, J \pm 2\,. \end{aligned} \tag{4.51}$$

Here we have to assume $d^0_{J-1} = d^0_{J+2}$ to ensure that our former assumption $d_J \sim d_{J+1}$ is valid. Therefore, the internal layers whose motion is most noticeable during the metastable phase are x_{J-2}, x_{J-1} that move to the right and x_{J+1}, x_{J+2} that move to the left. The other layers remain stationary to within at least $O(\varepsilon)$ precision. In addition, from (4.51), it is clear that $x_{J\pm1}$ moves at a higher speed than does $x_{J\pm2}$. The

numerical evidence supporting the analysis given above can be observed in Figure 4.8(a), (c) and (e).

4.3.3 Other Explicit ODE Systems

There are some other systems of ODEs for the motion of the internal layers for the Cahn-Hilliard equation (cf. [15] and [35]) and it is of interest to determine if these seemingly different systems are consistent with (4.16). In our notation, the ODE system (4.36) in [15] can be rewritten as

$$\dot{x}_j \sim r_j + r_{j-1} \ , \quad \text{for } 1 \le j \le n-2 \, , \quad \dot{x}_0 \sim r_0 \, , \ \ \dot{x}_{n-1} \sim r_{n-2} \, , \tag{4.52}$$

where $r_j's$ are defined in (4.29b). Comparing this system with (4.33), we find that if the "higher order terms" in (4.33) (i.e., $\sum_{k=j+1}^{n-2} \varepsilon^{k-j} r_k \prod_{l=j}^{k-1} \mu_l + \sum_{k=0}^{j-2} \varepsilon^{j-1-k} r_k \prod_{l=k+1}^{j-1} \mu_l$) are omitted, then our ODE system (4.33) reduces to (4.52). However, it is clear that these "higher order terms" may be significantly greater than the remaining $r_j's$. For example, suppose J with $2 \le J \le n-2$ ($n \ge 4$) is the index of a unique annihilating interval. Then our asymptotic formula (4.38) indicates that the internal layer x_j for $j = J-k$ with $k \ge 2$ and $j = J+k$ with $k \ge 1$ will move at an algebraic slower speed than the annihilating layers. On the other hand, from (4.52), the corresponding internal layers x_j will satisfy $\dot{x}_j = o'(\dot{x}_J)$, i.e., they move exponentially slower than the collapsing layers. Thus, the results in [15] provide useful information for the motion of layers for the annihilating interval and its two nearest neighborhoods, but may be inaccurate for other layers. Similarly, for the case corresponding to Figure 4.7(a) and (b), where the annihilating interval is (x_{n-1}, x_n), the system (4.52) yields $x_j' = o'(r_{n-1})$ for $j \le n-3$. In contrast, our ODE system (4.33) gives (4.45a) instead. Here we illustrate that (4.45a) is correct by giving the full numerical results for the locations x_j, their deviations $e_j \equiv x_j - x_j^0$ and the ratios $\rho_j \equiv e_j/e_{j+1}$ at two different times in

Table 4.6. From (4.45), we expect that the ratio ρ_j with $j \leq n-3$ should be $O(\varepsilon)$, and the deviation e_j should satisfy $O(\varepsilon^{n-2-j} e_{n-2})$ for $j \leq n-3$. This is exactly what is obtained in Table 4.6.

Eyre [35] also derived an explicit ODE system using a collocation technique, but we can't find any similarities between his results and our asymptotic and full numerical results.

	$t = 140.22$			$t = 156.02$		
j	x_j	e_j	ρ_j	x_j	e_j	ρ_j
0	-.800000	.000000	-	-.800000	.000000	-
1	-.499998	.000002	.05	-.499995	.000005	.04
2	-.099961	.000039	.05	-.099861	.000139	.05
3	.200718	.000718	.04	.202578	.002578	.04
4	.617812	.017812	1.04	.671481	.071481	.81
5	.917114	.017114		.987852	.087852	

Table 4.6: Numerical results (using TMOL) for the Cahn-Hilliard equation ($\alpha = 0$) at two different times corresponding to the parameter values used for Figure 4.7(a) and (b). Here, x_j for $j = 0, \ldots, 5$ are the locations of internal layers, $e_j \equiv x_j - x_j^0$ and $\rho_j \equiv e_j / e_{j+1}$.

4.4 Simulation of the Entire Coarsening Process

The DAE system (4.16) is not valid when two internal layers, or an internal layer and a wall, become closely separately by an amount of $O(\varepsilon)$. In particular, when two approaching internal layers become closely separated, the layers will undergo a strong local interaction which leads to an annihilation of two internal layers, leaving behind a metastable pattern with two fewer layers. This strong local interaction of two approaching internal layers during annihilation is very complicated (see Figure 4.3–4.8) and will not be discussed. Instead, we will find an approximation of the interface realignment after an

annihilation, using the explicit characterization of motion of the layers in the previous section. Here interface realignment refers to an algorithm that maps interface locations before an annihilation to locations immediately after an annihilation. Since an annihilation event takes place on a much faster time scale than metastable dynamics, we believe that incorporating the interface realignment into the metastable evolution described by the DAE system (4.16) could provide, approximately, a complete quantitative description of the coarsening process associated with the phase separation models.

In our discussion below, we assume that at any time, the interval having the least length is unique, i.e., there is some J with $0 \le J \le n$ such that $\nu_J d_J < \nu_j d_j$ for all $j = 0, \ldots, n$ and $j \ne J$. Another assumption is that the solution $u(x,t)$ is a piecewise constant with $u = s_+$ or $u = s_-$ during the metastable phase. This is reasonable when ε is small since the interfaces of the metastable pattern (4.15) have length $O(\varepsilon)$. Under this assumption, the mass constraint is equivalent to the length conservation conditions that both $\sum_{i \text{ odd}} d_i$ and $\sum_{i \text{ even}} d_i$ are constant. Here and only here the interval lengths d_0 and d_n represent $x_0 + 1$ and $1 - x_{n-1}$, respectively. Since the interval with the least length annihilates first, the layers x_{J-1} and x_J will be referred to as the left and right annihilating interfaces, while the layers x_{J-2} and x_{J+1} will be referred to as the left and right nearest interfaces. During the annihilation of the J-th interval, the interface number decreases by two (one if $J = 0$ or n). Let the locations of the resulting interfaces immediately after the annihilation be denoted by x'_j for $j = 0, \ldots, J-2, J+1, \ldots, n-1$, where we assume that the set $\{0, \ldots, J-2\}$ ($\{J+1, \ldots, n-1\}$) is empty if $J < 2$ ($J > n-2$).

We now describe how the interface realignment is realized. First, consider the viscous Cahn-Hilliard equation with $0 < \alpha \le 1$, and assume $J(\ne 0, n)$ is the index of the only annihilating interval. It has been found in §4.3 that the annihilating interfaces approach each other and eventually coalesce and that the other interfaces move at the same speed

and in opposite directions. So the new locations of the internal layers after an annihilation can be approximated by

$$x_j' = x_j + (-1)^{j-J}\delta\ ,\ \ j = 0, \ldots, n-1,\ \ j \neq J-1, J\ , \tag{4.53}$$

where $\delta > 0$ is a constant. Using the length conservation conditions, we have $\delta = d_J/(n-2)$. If $J = 0$ or n, then the new internal layer locations after an annihilation will approximately be

$$x_j' = x_j + (-1)^{j-J}\delta\ ,\quad j = 0, \ldots, n-1,\ \ j \neq (1-\frac{1}{n})J\ , \tag{4.54}$$

with $\delta = d_J/2(n-1)$.

For the Cahn-Hilliard equation, the asymptotic analysis and numerical experiments in §4.3 indicate that when $2 \leq J \leq n-2$ $(n \geq 4)$, the nearest interfaces x_{J-2} and x_{J+1} will move at the same speeds and directions as the corresponding annihilating interfaces x_{J-1} and x_J, while all other interfaces remain unchanged to within at least $O(\varepsilon)$ precision. Thus, the new locations of the interfaces can be approximately represented by

$$x_{J-2}' = x_{J-2} + \delta d_J\ ,\qquad x_{J+1}' = x_{J-2}' + d_{J-1} + d_{J+1}\ , \tag{4.55a}$$

$$x_j' = x_j\ ,\qquad j = 0, \ldots, J-3, J+2, \ldots, n-1\ . \tag{4.55b}$$

Here $\delta > 0$ is a constant to be determined. To find an approximation for δ, we compare the speeds of the nearest interfaces during the metastable phase. It is clear from (4.37) that the annihilating interfaces move towards each other, each being followed by its nearest interface moving at approximately the same speed. The ratio of the speeds of these two rigid motions is equal to the inverse ratio of the distances between the pairs of the nearest and annihilating interfaces. So, we obtain

$$\delta = \frac{d_{J+1}}{d_{J-1} + d_{J+1}}\ .$$

Note that if $d_{J-1} = d_{J+1}$, then $\delta = \frac{1}{2}$ and the length of the annihilated interval is redistributed equally to its neighboring intervals. The above arguments are limited to the annihilating intervals that are separated from the boundary by at least two intervals. When the annihilating interfaces are near the boundary, it is not hard to see from (4.42) and (4.45) that if $J = n-1$ or n, then the interface(s) x_j for $J-1 \le j \le n-1$ will eventually disappear. Since, during this annihilation, the interfaces x_j for $0 \le j \le J-2$ are almost unchanged, the new location of the left nearest interface x_{J-2} can be calculated using the length conservation conditions. Specifically, we have

$$x'_{n-3} = x_{n-1} - d_{n-2}\,, \quad x'_j = x_j\,, \quad \text{for } j = 0, \ldots, n-4\,, \quad \text{if } J = n-1, \tag{4.56a}$$

$$x'_{n-2} = 1 - d_{n-1}\,, \qquad x'_j = x_j\,, \quad \text{for } j = 0, \ldots, n-3\,, \quad \text{if } J = n\,. \tag{4.56b}$$

The interface realignment for $J = 0$ or 1 can be implemented similarly. Our discussions here are motivated by the work of Eyre (see [35]) for the Cahn-Hilliard equation. Comparing (4.55) and (4.56) with the corresponding equations for the interface motion during annihilation in [35], we find they are essentially equivalent.

We now present a procedure, that is conceived to be able to approximately describe the entire coarsening process associated with the phase separation models. We first integrate the DAE system (4.16) until a collapse criterion is satisfied. Then we use the interface realignment technique to determine the new locations of the interfaces after an annihilation, and with these new interface locations as initial values, we return to integrate the DAE system again. We repeat the procedure above for each successive collapse event until a stable equilibrium state with only one internal layer is achieved. Using this procedure, we calculate and plot the interface locations as a function of time for the Cahn-Hilliard equation and the constrained Allen-Cahn equation in Figure 4.9. This figure shows the entire coarsening process associated with the phase separation models and the two distinct time scales of the fast annihilation and the metastable interface

motion.

Next, we explain a prominent phenomenon that we can observe from Figure 4.3–4.8. These figures show that for the viscous Cahn-Hilliard equation with $0 < \alpha \leq 1$, the tops of the non-collapse "islands" and the bottoms of the non-collapse "valleys" will deviate some visible distance vertically from the original positions $u \sim s_{\pm}$. This deviation, however, does not occur for the Cahn-Hilliard equation ($\alpha = 0$) during the coarsening process. By examining the version (4.19) of the viscous Cahn-Hilliard equation, we conjecture that this behavior may result from the different signs and values of $\sigma(x,t)$ for different models. Specifically, we can expect from the graph for $Q(u)$ that if $\sigma < 0$ ($\sigma > 0$), then the top of an "island" and the bottom of an "valley" will go up (down), and furthermore, the deviated distance will depend on the value of σ. Now we derive asymptotic expressions for $\sigma(x,t)$ for different models to interpret this difference.

It has been shown in [88] that we can decompose $\sigma(x,t)$ as

$$\sigma(x,t) = (1-\alpha)\sum_{j=0}^{n-1} \dot{x}_j M_j(x;x_j) + \sigma_c(t)\,, \tag{4.57}$$

where M_j defined by $M_j \equiv \int_{-1}^{x} \left(u^*[\varepsilon^{-1}\xi_j(\eta - x_j)] - s_j\right) d\eta$ satisfies

$$M_j \sim 0 \quad \text{if } x < x_j\,, \quad M_j \sim \xi_j(s_+ - s_-)(x - x_j) + \varepsilon(\theta_- - \theta_+) \quad \text{if } x > x_j\,, \tag{4.58}$$

and $\sigma_c(t)$ is asymptotically determined by (4.16). For the viscous Cahn-Hilliard equation with $0 < \alpha \leq 1$, let $n \geq 3$ and assume that there is some J with $1 \leq J \leq n-1$ such that $\nu_J d_J^0 < \nu_j d_j^0$ for all $j = 0, \ldots, n$ and $j \neq J$. Then, the dominant H_j's can be found from (4.17a) to be

$$H_{J-1} \sim 2a_J^2 \nu_J^2\, e^{-\varepsilon^{-1}\nu_J d_J} \equiv H \qquad \text{and} \qquad H_J \sim -H\,. \tag{4.59}$$

Thus, using (4.25b), we can estimate σ_c as

$$\sigma_c \sim 2\,\xi_J\, n^{-1}(s_+ - s_-)^{-1} H\,.$$

For $x < x_0$, it is obvious from (4.57) and (4.58) that $\sigma \sim \sigma_c$. For $x > x_0$, we calculate $\sigma(x,t)$, using (4.41), (4.57) and (4.58), to obtain

$$\sigma = \sigma_c \left[1 + (1-\alpha)O(\varepsilon)\right] .$$

Therefore, for the constrained Allen-Cahn equation ($\alpha = 1$), $\sigma = \sigma_c(t)$ is constant and its sign depends only on ξ_J. If $\xi_J < 0$, then the non-collapse "islands" and "valleys" will shift up, and otherwise, they will shift down. For the viscous Cahn-Hilliard equation with $0 < \alpha < 1$, $\sigma(x,t)$ differs from $\sigma_c(t)$ by only a relative error $O(\varepsilon)$ and thus, the movement of these "islands" and "valleys" are the same as for the constrained Allen-Cahn equation. This analysis agrees with the numerical results shown in Figures 4.4–4.8. For example, in Figures 4.4 and 4.5, we have that $\xi_J = 1$ with $J = 3$ and σ_c is positive. Thus, the metastable pattern on the non-collapse intervals seems to be lifted up during the coarsening process.

For the Cahn-Hilliard equation, let $n \geq 4$ and assume that for some J with $2 \leq J \leq n-2$, we have $\nu_J d_J^0 < \nu_j d_j^0$ for all $j = 0, \ldots, n$ and $j \neq J$. Then, the dominant H_j's are also H_{J-1} and H_J satisfying (4.59). From (4.35), we have

$$\sigma_c \sim -\frac{1}{\xi_0(s_+ - s_-)} \varepsilon^{J-1} H (1 - \varepsilon\mu_{J-1}) \prod_{l=0}^{J-2} \mu_l \,. \tag{4.60}$$

For $x_{k-1} < x < x_k$ with $0 \leq k \leq J-1$, we can derive from (4.38a), (4.57) and (4.58) that

$$\sigma \sim \sum_{j=0}^{k-1} \xi_j (s_+ - s_-)(x - x_j) \varepsilon^{J-j-2} \mu^{-1} H \prod_{l=j}^{J-2} \mu_l + \sigma_c \,,$$

which gives

$$\sigma \sim -\xi_k \, H \, \varepsilon^{J-k-1} \, C \,. \tag{4.61}$$

where $C > 0$ is a constant. For $x_{k-1} < x < x_k$ with $J-1 \leq k \leq J+1$, it can be similarly obtained that $\sigma \sim \xi_J \, H \, C$, for some $C > 0$, which yields that the sign of σ

determined only by ξ_J is the same on the collapse interval and its two nearest neighbors. By symmetry, when $x_{k-1} < x < x_k$, $J+1 \le k \le n$, σ can be naturally expected to satisfy

$$\sigma \sim -\xi_k \, H \, \varepsilon^{k-J-1} \, C \,, \tag{4.62}$$

where $C > 0$. We notice from (4.61) and (4.62) that the sign of σ changes when x crosses the interface x_k $(k \neq J-1, J)$. More specifically, if $\xi_k = 1\,(-1)$ with $k \neq J$, which means that $u \sim s_-\,(s_+)$ in the k-th interval (x_{k-1}, x_k), then since σ is negative (positive) on this interval, the bottom (top) of the corresponding "valley" ("island") will move towards $u = 0$ during the metastable phase and then move back to its original position at the end of the collapse phase. Therefore, the metastable pattern will contract vertically and will not go beyond $u = -1$ and $u = 1$. In addition, from (4.61) and (4.62), we believe that during the collapse phase, σ will be $O(1)$ only on the collapse interval and its left and right nearest neighbors, but will be at most $O(\varepsilon^{J-k-1})$ $(O(\varepsilon^{k-J-1}))$ on the k-th interval with $k \le J-1$ $(k \ge J+1)$. So we anticipate that the changes of these tops and bottoms are virtually indistinguishable when they are far away from the collapse interval. The full numerical results in Figures 4.3, 4.6 and 4.7 show that the solution $u(x,t)$ to the Cahn-Hilliard equation satisfies $-1 \le u \le 1$ and the local maximums or minimums on all intervals except the collapse interval and its nearest neighbor(s) are almost unchanged during both the metastable phase and the collapse phase.

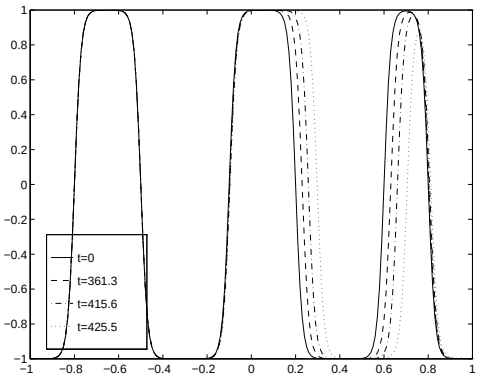

(a): $\alpha = 0\,,\ \varepsilon = 0.03$

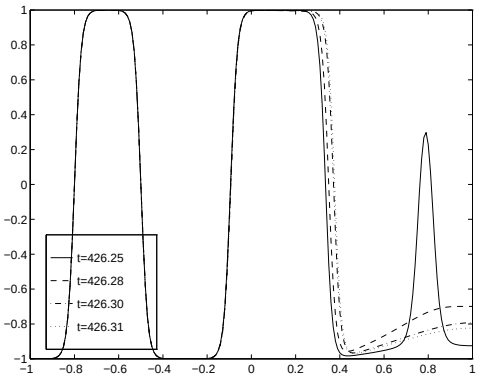

(b): $\alpha = 0\,,\ \varepsilon = 0.03$

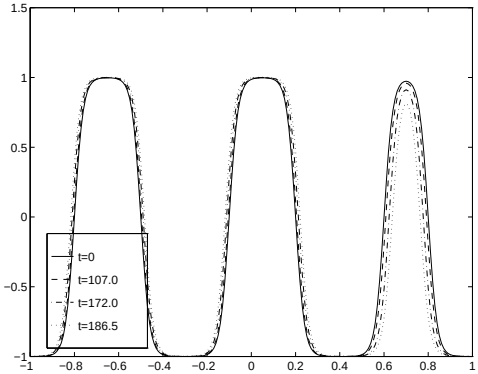

(c): $\alpha = 0.5\,,\ \varepsilon = 0.04$

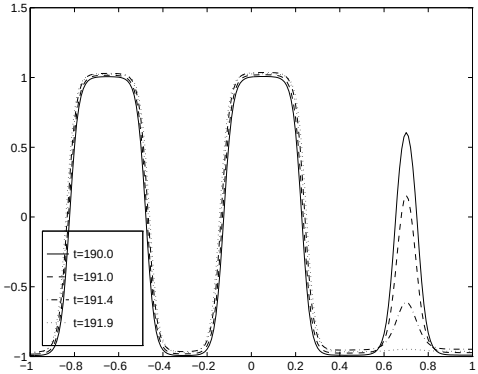

(d): $\alpha = 0.5\,,\ \varepsilon = 0.04$

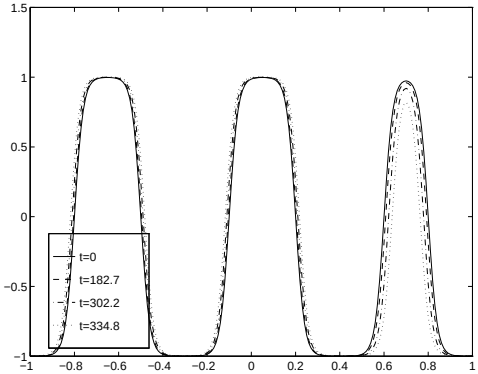

(e): $\alpha = 1\,,\ \varepsilon = 0.04$

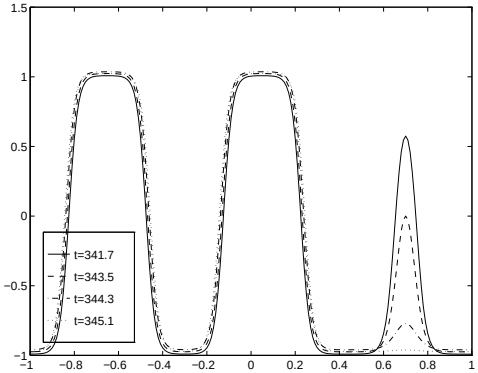

(f): $\alpha = 1\,,\ \varepsilon = 0.04$

Figure 4.6: Plots of the full numerical solutions (using TMOL) to the viscous Cahn-Hilliard equation (4.11) with $Q(u) = 2(u - u^3)$ and $\kappa = 1$ at different times for various values of α and ε. Here the initial data $u(x,0) \equiv u^*(x;\boldsymbol{x}^0)$ with $\boldsymbol{x}^0 = (-0.8,\ -0.5,\ -0.1,\ 0.2,\ 0.6,\ 0.8)$ and u^* defined by (4.15).

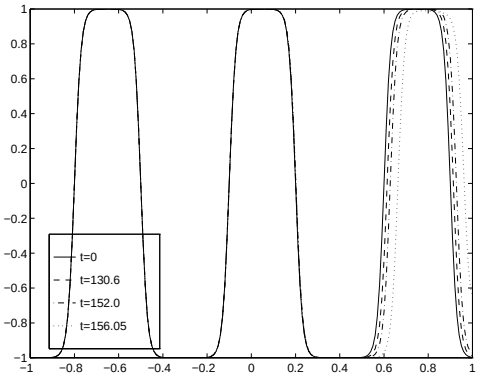

(a): $\alpha = 0\,,\ \varepsilon = 0.03$

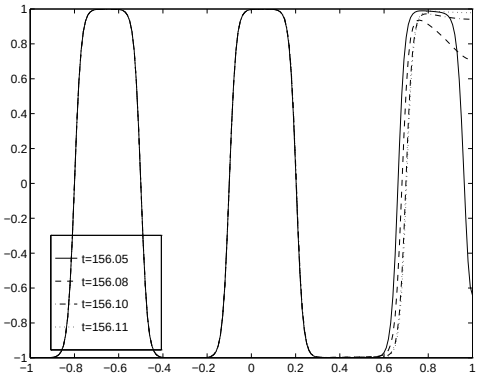

(b): $\alpha = 0\,,\ \varepsilon = 0.03$

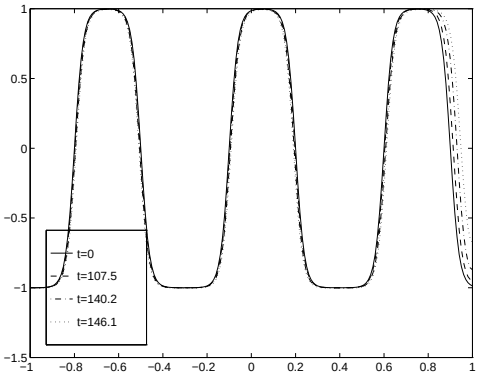

(c): $\alpha = 0.5\,,\ \varepsilon = 0.04$

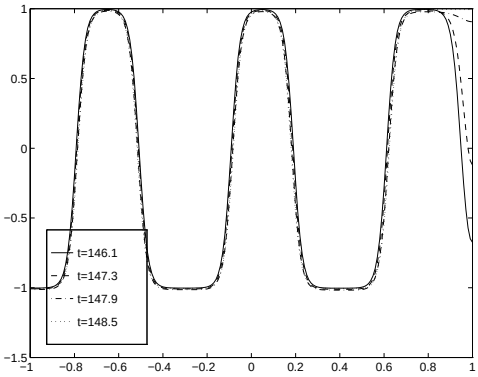

(d): $\alpha = 0.5\,,\ \varepsilon = 0.04$

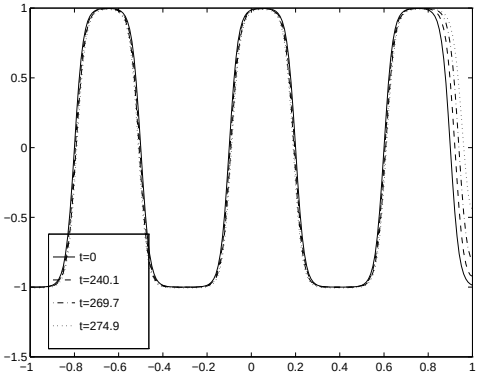

(e): $\alpha = 1\,,\ \varepsilon = 0.04$

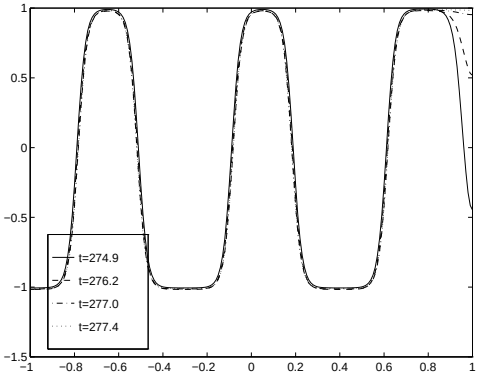

(f): $\alpha = 1\,,\ \varepsilon = 0.04$

Figure 4.7: Plots of the full numerical solutions (using TMOL) to the viscous Cahn-Hilliard equation (4.11) with $Q(u) = 2(u - u^3)$ and $\kappa = 1$ at different times for various values of α and ε. Here the initial data $u(x,0) \equiv u^*(x;\boldsymbol{x}^0)$ with $\boldsymbol{x}^0 = (-0.8, -0.5, -0.1, 0.2, 0.6, 0.9)$ and u^* defined by (4.15).

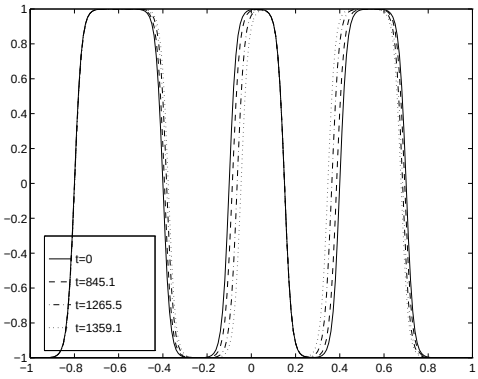

(a): $\alpha = 0\,,\ \varepsilon = 0.032$

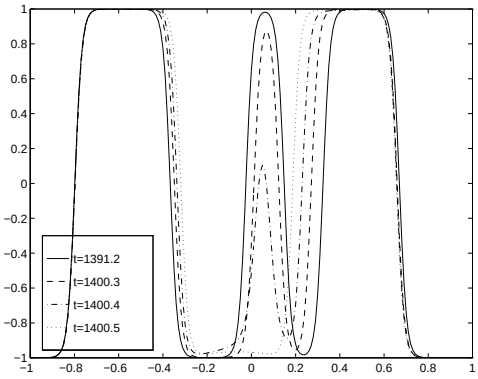

(b): $\alpha = 0\,,\ \varepsilon = 0.032$

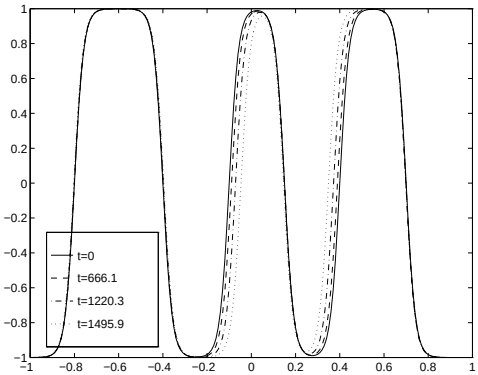

(c): $\alpha = 0.5\,,\ \varepsilon = 0.042$

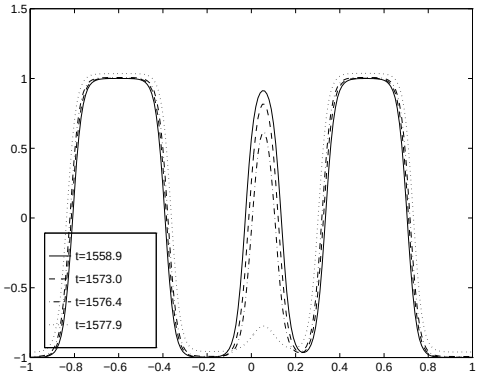

(d): $\alpha = 0.5\,,\ \varepsilon = 0.042$

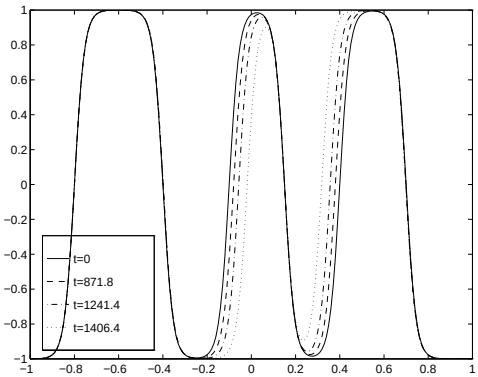

(e): $\alpha = 1\,,\ \varepsilon = 0.045$

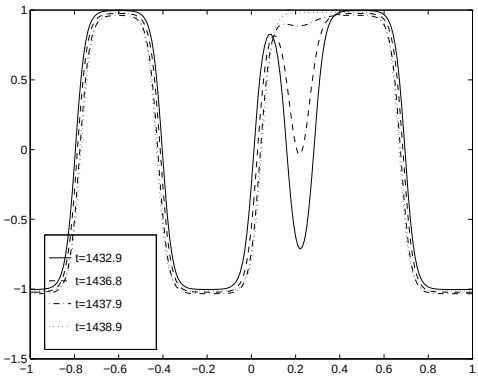

(f): $\alpha = 1\,,\ \varepsilon = 0.045$

Figure 4.8: Plots of the full numerical solutions (using TMOL) to the viscous Cahn-Hilliard equation (4.11) with $Q(u) = 2(u - u^3)$ and $\kappa = 1$ at different times for various values of α and ε. Here the initial data $u(x,0) \equiv u^*(x;\boldsymbol{x}^0)$ with $\boldsymbol{x}^0 = (-0.8,\ -0.4,\ -0.1,\ 0.15,\ 0.4,\ 0.7)$ and u^* defined by (4.15).

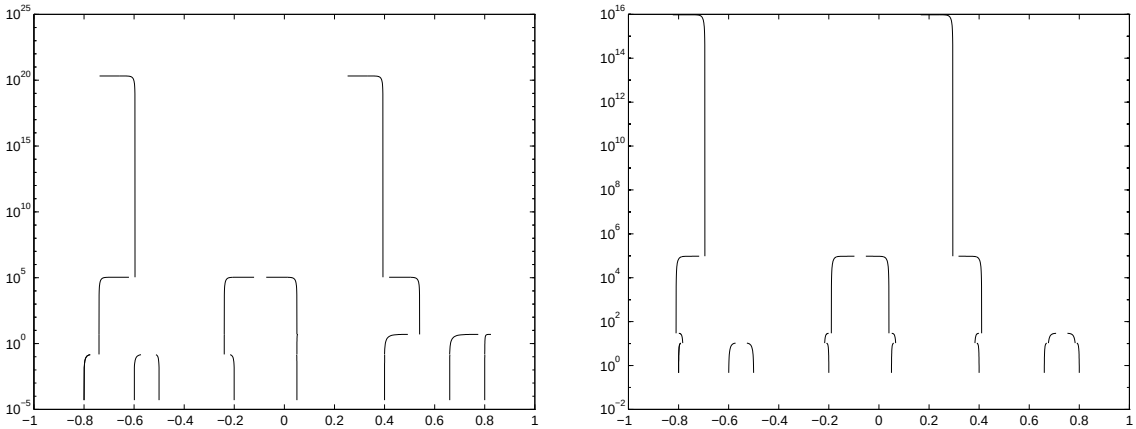

(a) $\alpha = 0$ (b) $\alpha = 1$

Figure 4.9: Plots of the interface locations as a function of time for (4.11) with $\varepsilon = 0.02$, $\kappa = 1$ and $Q(u) = 2(u - u^3)$. Here the initial locations of the interfaces are –0.8, –0.6, –0.5, –0.2, 0.05, 0.4, 0.66, 0.8, and the final stable equilibrium having one interface at $x_0 = -0.01$ is achieved at $t \sim .2096 \times 10^{21}$ for $\alpha = 0$ and $t \sim .9551 \times 10^{16}$ for $\alpha = 1$.

Chapter 5

Numerical Analysis of an Exponentially Ill-Conditioned BVP

In this chapter we give a preliminary approach for the numerical analysis of an exponentially ill-conditioned boundary value problem. Although we do not study how to overcome the difficulties in numerical computations of singularly perturbed problems exhibiting dynamic metastability in a general setting, the detailed analysis of a particular example shows the numerical difficulties encountered in computing these metastable problems.

5.1 Introduction

There have been numerous computational experiments of exponentially ill-conditioned problems such as the viscous shock problem, the exit problem and various phase separation models (cf. [32], [33], [76], [62], [67], [9], [8], [86], [87], [88], etc.). However, little is known of the rigorous nature concerning the convergence and stability of the numerical schemes that compute metastable behavior. As shown in the previous sections, the solution $u(x)$ of an exponentially ill-conditioned boundary value problem, say $L_\varepsilon u = f$, can be exponentially sensitive to all the data in the equation; for example, to the right-hand side f. Suppose $\tilde{L}_\varepsilon$ is the linearization operator of L_ε and λ_0 is its principal eigenvalue which is usually exponentially small. Then, a perturbation $\triangle f$ to f may cause an exponentially large change $\triangle u$ in u, of the order $O(\lambda_0^{-1} \triangle f)$. Since a good discretization scheme often inherits the properties of the corresponding continuous problem such as the sensitivity and stability, it is natural to expect that a truncation error which is usually

much greater than the exponentially small eigenvalue λ_0 may result in such a large error in the numerical solution $u^h(x)$ that renders $u^h(x)$ to be highly inaccurate. To overcome this obstacle, in consequence, one has to require that the truncation error be smaller than the smallest eigenvalue λ_0, which is exponentially small. Thus high-order or spectral-type numerical methods are preferred for solving these problems. A high-order integral equation scheme was implemented to compute boundary value resonance solutions in [67] and a Galerkin spectral method was employed to solve the Cahn-Hilliard equation in [9] and the viscous Cahn-Hilliard equation in [8]. Another approach to overcome the difficulties in solving exponentially ill-conditioned problems is preconditioning; for example, the viscous shock problem and the (constrained) Allen-Cahn equation were successfully studied numerically using a WKB formulation which leads to well-conditioned problems in [87] and [86], respectively.

On the other hand, we notice that many conventional schemes have also been widely used in computing solutions to exponentially ill-conditioned problems and they indeed work rather successfully. Elliott and French [32] studied the metastable dynamics for the Cahn-Hilliard Equation by applying the Galerkin finite element method; the classic finite difference schemes were employed to compute the solutions of the Burgers' equation in [62] and the viscous Cahn-Hilliard equation in [88]; Carr and Pego [26] obtained very nice pictures of the evolution of the solutions to the unconstrained Allen-Cahn equation by using the subroutine LSODI with the methods of lines, taking 801 grid points. The success of application of these traditional numerical methods with moderate mesh sizes gives rise to some queries about the heuristic inference in the previous paragraph. Specifically, is it a necessary condition for a numerical method when solving a very ill-conditioned problem that the truncation error be less than the order of the principal eigenvalue λ_0 of the corresponding linearized elliptic operator? Can we apply the classic finite difference schemes and other numerical methods with moderate mesh sizes to solve

the ill-conditioned problems, instead of using high-order methods or preconditioning? If so, what difficulties will possibly occur in our computations and which type of schemes may be preferred for these problems? Moreover, can we give a rigorous proof of the convergence of a numerical method for an exponentially ill-conditioned problem?

Our goal is to shed some light on the above questions and provide some general guidance or principles in designing numerical schemes for metastable problems by studying the following singularly perturbed boundary value resonance problem (cf. [1], [31], [60], [67], [74], [113])

$$L_\varepsilon u \equiv -\varepsilon u_{xx} + x^{2m+1} p(x) u_x = 0 \ , \quad -1 < x < 1 \ , \tag{5.1a}$$

$$u(-1) = A_{-1} \ , \quad u(1) = A_1 \ . \tag{5.1b}$$

Here $\varepsilon > 0$ is a small parameter, $m \geq 0$ is an integer and $p(x) > 0$ is an even smooth function. This equation corresponds to the equilibrium problem of the exit problem studied in [79] and the references therein. One of the reasons to choose (5.1) as a model problem is that it is linear and its solution can be explicitly written in terms of a quadrature. This makes it easy to perform computations and comparisons. The second reason is that without a stability estimate, this equation still satisfies a comparison principle which is crucial for proving the convergence of a finite difference scheme. Despite its simplicity, we hope that the qualitative results revealed from this model equation are also applicable to other nonlinear metastable problems, for which a rigorous convergence analysis is typically not easy.

Although there have been some error bounds for the finite element Galerkin method for the Cahn-Hilliard equation in [33] and [32], they do not guarantee any accuracy unless we use extremely small step size h. In fact, the constant C in error bounds Ch^r obtained there, where r is the convergence order, is dependent on the small parameter ε and may be very large. Another loss of accuracy comes from the regularity assumption on the

solution u and its derivatives. However, the solutions u to the metastable problems are often associated with sharp boundary layers and/or internal layers where u will possess large derivatives in x as $\varepsilon \to 0$. Therefore, in this section, we will give an analysis of *uniform convergence* introduced below.

A discretization method is called *uniformly convergent* (with respect to ε) of order r in the norm $\|\cdot\|$, if there exists a constant C that is independent of ε and h, such that for all sufficiently small h (independent of ε),

$$\| u - u^h \| \leq C h^r \ . \tag{5.2}$$

Here u^h denotes a numerical solution obtained using this method. For illustration, we consider the singularly perturbed convection diffusion equation

$$\varepsilon u'' + u' = 0 \ , \ \ 0 < x < 1 \ ; \qquad u(0) = 0 \ , \ \ u(1) = 1 \ , \tag{5.3}$$

whose solution $u = (1 - e^{-x/\varepsilon})/(1 - e^{-1/\varepsilon})$ has a boundary layer at $x = 0$. The upwind scheme (see (5.24) below) on an equidistant mesh $I^h = \{x_i = ih; i = 0, 1, \ldots, N, \ Nh = 1\}$ yields the numerical solution $u^h = (u_i)$ with

$$u_i = (1 - \rho^i)(1 - \rho^N)^{-1} \quad , \qquad \text{where } \rho = \frac{\varepsilon}{\varepsilon + h} \, . \tag{5.4}$$

If the solution of (5.3) had bounded derivatives independent of ε, a classical convergence theory for finite difference methods (i.e., consistency+stability $\Rightarrow$ convergence) could guarantee the first order convergence of the upwind scheme. However, this convergence is not uniform in that (5.2) does not hold. In fact, when $h = \varepsilon$, comparing $u_1 = \frac{\frac{1}{2}}{1-(\frac{1}{2})^N}$ and $u(x_1) = \frac{1-e^{-1}}{1-e^{-\frac{1}{\varepsilon}}}$, we can find that $u(x_1) - u_1 \to \frac{1}{2} - e^{-1} \neq 0$ as $h \to 0$, and consequently, the numerical solution u^h does not converge to $u(x)$ as $h \to 0$ uniformly.

There are basically two approaches to construct uniformly convergent finite difference schemes for the following singularly perturbed convection diffusion equation with

Dirichlet boundary conditions

$$-\varepsilon u_{xx} + b(x)u_x + d(x)u = f(x) \ , \quad 0 < x < 1 \ , \tag{5.5}$$

under the assumptions that $b(x) \geq b_0 > 0$ (i.e., no turning points), and $d(x) \geq 0$. One of the approaches is the exponentially fitting technique first introduced by Allen and Southwell [5] and Il'in [55], which yields the Il'in-type scheme. Through introducing an artificial diffusion by means of a fitting factor that enforces the scheme to be exactly satisfied by the boundary layer function in the leading order asymptotic expansion of the solution, the nodal convergence that is uniform with respect to the small parameter ε was proved in [55] and [58]. Since discretization methods on equidistant meshes may have difficulties in representing the solutions that change abruptly in layers, an alternative approach to yield uniform convergence is the use of highly non-equidistant meshes (see [106], [107], [95] and [90] for details). One of the necessary steps in proving the uniform convergence of the numerical approaches above is to establish a *uniform* stability estimate for the discretization operator L^h, such as

$$|u_i| \leq C(\max_j |L^h u_j| + |u_0| + |u_N|) \ , \quad \text{for } i = 0, 1, \ldots, N \ , \tag{5.6}$$

where C is a constant independent of ε and h. Unfortunately, this type of uniform stability estimate obviously does not hold for any discretization of our model problem (5.1) due to its exponential ill-conditioning. To our knowledge, no numerical analysis addressing the uniform convergence of any finite difference scheme or finite element method for any metastable problem has been performed, even for the "simplest" model (5.1).

In this chapter, we will study the uniform convergence of three finite difference schemes for (5.1): the upwind scheme, the coupled scheme and the Il'in scheme . This study is not only significant in understanding the finite difference schemes (and other numerical methods) applied to metastable problems, but is also interesting from the point

of numerical analysis: it provides an example showing that a uniform stability estimate is not a necessary condition for uniform convergence. The chapter is organized as follows. In the rest of this section, we estimate the derivatives of solutions u of (5.1) and we decompose u into a singular part and a less singular part. Using these analytical results, in §5.2, we construct an appropriate mesh generating function and three finite difference schemes and analyze the uniform convergence of these schemes on the corresponding meshes. Finally, in §5.3, we present some numerical results for (5.1) and discuss the numerical computation of some related exponentially ill-conditioned problems.

5.1.1 The Analytical Behavior of Solutions

To study the uniform convergence of our difference approximations, it is necessary to investigate the analytical behavior of the solution to (5.1). The problem (5.1) is exponentially ill-conditioned, so it is obvious that the typical stability inequality

$$\| v \| \leq C \| L_\varepsilon v \| , \quad \text{for all } v \text{ with } v(-1) = v(1) = 0$$

does not hold, where C is a constant independent of ε. However, the comparison principle is still valid (cf. [82]), and its counterparts for difference schemes play an indispensable role in establishing uniform convergence.

Lemma 5.1 *(Comparison principle) Suppose that v and w are functions in $C^2(-1,1) \bigcap C[0,1]$ that satisfy*

$$L_\varepsilon v(x) \leq L_\varepsilon w(x) , \quad \textit{for all } x \in (-1,1)$$

and $v(-1) \leq w(-1)$, $v(1) \leq w(1)$. Then we have

$$v(x) \leq w(x) , \quad \textit{for all } x \in [0,1].$$

Although (5.1) has a turning point at $x = 0$, nothing special happens near this point. For $\varepsilon \to 0$, its leading order boundary layer approximation has the form (cf. [79])

$$u(x) \sim \tilde{u}^{\varepsilon}(x) \equiv \frac{1}{2}(A_{-1} + A_1) + \frac{1}{2}(A_{-1} - A_1)\left(e^{-\xi\frac{1+x}{\varepsilon}} - e^{-\xi\frac{1-x}{\varepsilon}}\right), \tag{5.7}$$

where $\xi \equiv p(\pm 1)$. To estimate the error in our discretization methods, we shall require bounds for the derivatives of the solution u to (5.1) that are valid for all small positive ε. To analyze the Il'in scheme we need more precise information on the behavior of the solution. These results are contained in Lemmas 5.2 and 5.3.

Lemma 5.2 *Let $u(x)$ be the solution of (5.1). Then we have*

$$| u(x) | \leq \max\{| A_{-1} |, | A_1 |\} \tag{5.8}$$

and

$$| u^{(i)}(x) | \leq M\varepsilon^{-i}\left(e^{-\gamma\frac{1+x}{\varepsilon}} + e^{-\gamma\frac{1-x}{\varepsilon}}\right), \quad \text{for } i = 1, 2, \ldots. \tag{5.9}$$

Here γ is any constant satisfying $0 < \gamma \leq \frac{\min p(x)}{2m+2}$ and the constant $M > 0$ is independent of ε.

Proof. The proof of (5.8) is obvious by applying Lemma 5.1 with $v = \pm u$ and the barrier function $w = \max\{| A_{-1} |, | A_1 |\}$. Integrating (5.1) twice yields

$$u(x) = \frac{1}{2}(A_1 + A_{-1}) + \frac{1}{2}(A_1 - A_{-1})\frac{\int_0^x e^{\varepsilon^{-1}\tilde{p}(s)}ds}{\int_0^1 e^{\varepsilon^{-1}\tilde{p}(s)}ds}, \tag{5.10}$$

where $\tilde{p}(s) \equiv \int_0^s t^{2m+1}p(t)dt$. We can show that for $x^{2m+2} \gg \varepsilon$,

$$\int_0^x e^{\varepsilon^{-1}\tilde{p}(s)}ds \sim \frac{\varepsilon}{x^{2m+1}p(x)}e^{\varepsilon^{-1}\tilde{p}(x)}, \qquad \text{as } \varepsilon \to 0. \tag{5.11}$$

Since $\tilde{p}(x) - \tilde{p}(1) = -\frac{p(s_0)}{2m+2}(1 - x^{2m+2})$, where $s_0 \in (x, 1)$, the derivate of u satisfies

$$\begin{aligned} u'(x) &= \frac{1}{2}(A_1 - A_{-1})e^{\varepsilon^{-1}\tilde{p}(x)} / \int_0^1 e^{\varepsilon^{-1}\tilde{p}(s)}ds \leq M\varepsilon^{-1}e^{\varepsilon^{-1}[\tilde{p}(x)-\tilde{p}(1)]} \\ &\leq M\varepsilon^{-1}e^{-\frac{p(s_0)}{2m+2}\varepsilon^{-1}(1-x^{2m+2})}. \end{aligned} \tag{5.12}$$

If we assume γ is a constant satisfying $0 < \gamma \leq \frac{\min p(x)}{2m+2}$, then (5.9) follows with $i = 1$. For $i > 1$, the result is obtained by induction and repeated differentiation of (5.1). □

Lemma 5.3 *Let $u(x)$ be the solution of (5.1). Then it can be decomposed into $u(x) = \tilde{u}^\varepsilon(x) + v(x)$, where $\tilde{u}^\varepsilon(x)$ is given in (5.7) and $v(x)$ satisfies*

$$| v^{(i)}(x) | \leq M\varepsilon^{1-i} \left(e^{-\gamma\frac{1+x}{\varepsilon}} + e^{-\gamma\frac{1-x}{\varepsilon}} \right), \qquad \text{for } i = 0, 1, \ldots, 4. \tag{5.13}$$

Here the constant $M > 0$ is independent of ε and γ is any constant satisfying $0 < \gamma < \frac{\min p(x)}{2m+2}$.

Proof. Since (5.1) is symmetric about $x = 0$, we prove (5.13) on $0 \leq x \leq 1$ only. By symmetry, we have $u(0) = \frac{1}{2}(A_{-1} + A_1)$. So from (5.1) and (5.7), we find that $v = u - \tilde{u}^\varepsilon$ satisfies

$$\tilde{L}_\varepsilon v \equiv -\varepsilon v_{xx} + p(1)v_x = f, \qquad 0 < x < 1, \tag{5.14a}$$

$$v(0) = v(1) = 0, \tag{5.14b}$$

where f is defined by

$$f \equiv \left(p(1) - x^{2m+1}p(x) \right) u' - (A_1 - A_{-1}) (p(1))^2 \varepsilon^{-1} e^{-p(1)\frac{1+x}{\varepsilon}}. \tag{5.15}$$

Given constants k, c and c_1 satisfying $k \geq 0$ and $c > c_1 > 0$, we have $t^k e^{-ct} \leq Ce^{-c_1 t}$ for all $t \geq 0$, where C is a constant. Thus, using Lemma 5.2, we can show that

$$| f^{(i)}(x) | \leq M\varepsilon^{-i} e^{-\gamma\frac{1-x}{\varepsilon}}, \qquad \text{for } i = 0, 1, \ldots, 4, \tag{5.16}$$

where γ is any constant satisfying $0 < \gamma < \frac{\min p(x)}{2m+2}$. Since $\tilde{L}_\varepsilon \left(\exp\left(-\gamma\varepsilon^{-1}(1-x)\right) \right) = \gamma \left(p(1) - \gamma \right) \varepsilon^{-1} \exp\left(-\gamma\varepsilon^{-1}(1-x)\right)$, we may choose M large enough so that

$$\phi(x) = M\varepsilon e^{-\gamma\varepsilon^{-1}(1-x)} \pm v$$

satisfies $\tilde{L}_\varepsilon \phi \geq 0\,,\ \phi(0) \geq 0\,,\ \phi(1) \geq 0$. From the comparison principle, the inequality (5.13) holds for $i = 0\,$.

We now integrate (5.14) twice and obtain

$$v(x) = v_p(x) + K_1 + K_2 \int_x^1 e^{-\varepsilon^{-1} p(1)(1-t)} dt, \tag{5.17}$$

where

$$v_p(x) = -\int_x^1 z(t)dt\ , \quad z(x) = \int_x^1 \varepsilon^{-1} f(t) e^{-\varepsilon^{-1} p(1)(t-x)} dt\,. \tag{5.18}$$

From (5.9) and (5.15),

$$|\ z(x)\ | \leq M e^{-\gamma \varepsilon^{-1}(1-x)}\,. \tag{5.19}$$

Hence $|\ v_p(x)\ | \leq M\varepsilon\,$. The constants K_1 and K_2 must satisfy

$$K_1 = 0\ , \qquad v_p(0) + K_2 \int_0^1 e^{-\varepsilon^{-1} p(1)(1-t)} dt = 0\,.$$

Since $\int_0^1 \exp(-\varepsilon^{-1} p(1)(1-t))dt \geq M\varepsilon\,$, we have $|\ K_2\ | \leq M\,$. Therefore, from (5.17) and (5.19), we find that (5.13) holds with $i = 1$. The proof of (5.13) for $i \geq 1$ follows by induction and repeated differentiation of (5.14). □

Note that throughout this chapter we use M to denote a generic positive constant independent of ε and the mesh width h and it may take different values in different formulas. Some of the constants will also be represented by $M_0\,,\ M_1\,,\ C\,,\ C_0\,,\ c\,,\ c_0\,,$ etc.

5.2 Difference Schemes and their Uniform Convergence

5.2.1 Difference Schemes and Some Preliminaries

Denote the mesh I^h by $I^h = \{x_i : -1 = x_N < x_{-N+1} < \ldots < x_{N-1} < x_N = 1\}$ with mesh widths $h_i = x_i - x_{i-1}$ and $h = \max_i h_i\,$. Two meshes will be used in our discussion:

(1). an equidistant mesh $I_e^h = \{x_i = ih : i = -N, \ldots, N, Nh = 1\}$; and

(2). a non-equidistant mesh $I_n^h = \{x_i : i = -N, \ldots, N\}$, where with $h = 1/N$ and $t_i = ih$,

$$x_i = x(t_i) = \begin{cases} \lambda(t_i + 1) - 1 , & i = -N, \ldots, 0 , \\ 1 - \lambda(1 - t_i) , & i = 1, \ldots, N . \end{cases} \tag{5.20}$$

Here the mesh generating function $\lambda(t)$ (see Figure 5.1) is defined by

$$\lambda(t) = \begin{cases} \psi(t) := -a\varepsilon \ln(1 - t/q) , & t \in [0, \alpha] , \\ \pi(t) := \psi(\alpha) + \psi'(\alpha)(t - \alpha) , & t \in (\alpha, 1] , \end{cases} \tag{5.21}$$

where $q \in (0, 1)$ and $a > 0$ are constants, and $\alpha \in (0, q)$ is determined uniquely by $\pi(1) = 1$. Furthermore, some computations yield

$$q - \alpha = M\varepsilon, \quad \psi(\alpha) = -a\varepsilon \ln(1 - \frac{\alpha}{q}) = -M\varepsilon \ln \varepsilon, \tag{5.22a}$$

$$1 \le \psi'(\alpha) \le (1 - q)^{-1}, \quad 0 \le \lambda'(t) \le \psi'(\alpha), \quad \psi''(\alpha) = M\varepsilon^{-1}. \tag{5.22b}$$

Using these estimates, we can easily show (cf. [104]) that

$$| h_i - h_{i-1} | \le M\varepsilon^{-1}h^2 , \qquad \text{for } i = -N + 2, \ldots, N. \tag{5.23}$$

This non-equidistant mesh I_n^h is called Bakhvalov mesh [12]. If there were an exponentially boundary layer at $x = 0$, then the boundary layer function would be $y = \exp(-\beta x/\varepsilon)$, for some fixed $\beta > 0$. Bakhvalov's idea is to use an equidistant y-grid near $y = 1$ (which corresponds to $x = 0$), then to map this grid back to the x-axis by means of the boundary layer function. That is, grid points near $x = 0$ are defined by $\exp(-\frac{\beta x_i}{\varepsilon}) = 1 - \frac{t_i}{q}$, which is equivalent to $x_i = -a\varepsilon \ln(1 - \frac{t_i}{q})$ with $a = \beta^{-1}$. The definition (5.21) produces a condensed grid near $x = -1$ and $x = 1$, an equidistant grid outside the boundary layers and a gradual transition from the fine to the coarse grids.

Using the usual notations for divided differences,

$$D_+u_i = (u_{i+1} - u_i)/h_{i+1} , \qquad D_-u_i = (u_i - u_{i-1})/h_i ,$$
$$D_0u_i = (u_{i+1} - u_{i-1})/(h_i + h_{i+1}) , \quad D_+D_-u_i = 2(D_+u_i - D_-u_i)/(h_i + h_{i+1}) ,$$

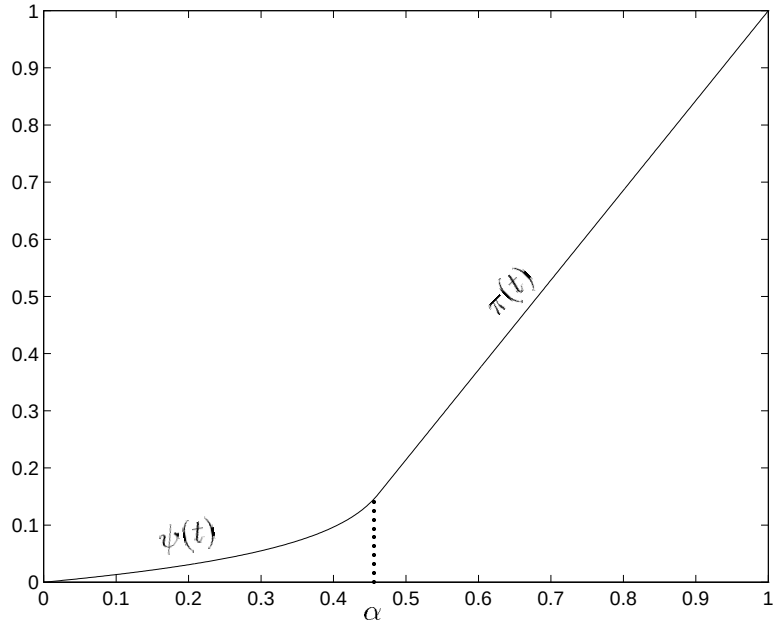

Figure 5.1: The mesh generating function $\lambda(t)$ versus t with $a = 2$, $q = 0.5$ and $\varepsilon = 0.03$. In this case, the tangent point of the curve $\psi(t)$ with the straight line $\pi(t)$ is $\alpha = 0.4618\ldots$

we will consider the following three finite difference schemes.

(1). Upwind scheme on a non-equidistant mesh I_n^h,

$$L_1^h u_i = -\varepsilon D_+ D_- u_i + P_i D' u_i = 0\ ,\ \ -N < i < N\ ,\ \ u_{-N} = A_{-1}\ ,\ \ u_N = A_1\ , \tag{5.24}$$

where $P_i = P(x_i) \equiv x_i^{2m+1} p(x_i)$, and

$$D' u_i = \begin{cases} D_+ u_i\ , & \text{if } P_i \le 0\ , \\ D_- u_i\ , & \text{if } P_i > 0\ . \end{cases}$$

(2). Coupled scheme on a non-equidistant mesh I_n^h,

$$L_2^h u_i = \begin{cases} L_c^h u_i = 0\ , & \text{if } \rho_i \le 1\ , \\ L_a^h u_i = 0\ , & \text{if } \rho_i > 1\ , \end{cases} \qquad -N < i < N, \tag{5.25a}$$

$$u_{-N} = A_{-1}\ ,\ \ u_N = A_1\ , \tag{5.25b}$$

where with $x_{i-\frac{1}{2}} = \frac{1}{2}(x_{i-1} + x_i)$ and $P_{i-\frac{1}{2}} = P(x_{i-\frac{1}{2}})$,

$$\begin{aligned}
\rho_i &= \begin{cases} h_{i+1}P_i/2\varepsilon\ , & \text{if } P_i \geq 0\ , \\ -h_iP_i/2\varepsilon\ , & \text{if } P_i < 0\ , \end{cases} \\
L_c^h u_i &= -\varepsilon D_+D_-u_i + P_iD_0u_i\ , \quad \text{(central scheme [90])}, \qquad (5.26) \\
L_a^h u_i &= -\varepsilon D_+D_-u_i + P_{i\pm\frac{1}{2}}D_\pm u_i\ , \ \text{(Gushchin-Shchennikow scheme [47])}. \qquad (5.27)
\end{aligned}$$

Here "$\pm$" corresponds to whether P_i is negative or positive.

(3). Il'in scheme on an equidistant mesh I_e^h,

$$L_3^h u_i = -\varepsilon\sigma_i D_+D_-u_i + P_iD_0u_i = 0\ ,\ -N < i < N\ ,\ u_{-N} = A_{-1}\ ,\ u_N = A_1\ , \qquad (5.28)$$

where the fitting factor σ_i is defined by $\sigma_i \equiv \frac{P_ih}{2\varepsilon}\coth\frac{P_ih}{2\varepsilon}$. The basic idea in constructing the Il'in scheme (5.28) is to select a fitting factor σ_i such that (5.28) would be accurate if the coefficient function $P(x)$ were a constant $P(x_i)$. For the upwind and coupled schemes, we use a non-equidistant mesh which is dense near the boundary layers at $x = \pm 1$. For such a mesh, we can show that $\mid u'(x)\cdot x'(t)\mid \leq M$. The coupled scheme is made up of a central scheme and a Gushchin-Shchennikow (G-S) scheme. Although the central scheme is usually unstable, the i-th row of its corresponding coefficient matrix is diagonally dominant and has non-positive off-diagonal entries when $\rho_i \leq 1$. On the other hand, in spite of the first order consistency of the G-S scheme, it becomes second order consistent at $x = x_i$ if $\rho_i \geq 1$. So the coupled scheme (5.25) is in fact stable and has second order consistency. The details of the background concerning these difference schemes and meshes can be found in [90], [98], [104], [106], [12], [55], [58] and the references therein.

Here we give an explanation of why the schemes (1)–(3) are expected to be uniformly convergent on the corresponding meshes. First, for the singular perturbation problem (5.5) without turning points, the uniform convergence of these schemes has been proved in

[55], [58], [98], [104], etc. We wish to extend the analysis of uniform convergence in these studies to the exponentially ill-conditioned problem (5.1). Although (5.1) is a turning point resonance problem, the singularity of its solution only occurs in the boundary layers, which is similar to that of (5.5). Near the turning point $x = 0$, the solution of (5.1) is constant to within exponentially small terms and the derivatives are exponentially small for $\varepsilon \ll 1$. In addition, although the (numerical) solution apparently does not satisfy the (discrete) stability estimate for (5.1), the (discrete) comparison principle is still valid for the turning point problem. Therefore, we anticipate that schemes (1)–(3) are uniformly convergent for (5.5) as well as for (5.1).

To provide a rigorous analysis of the convergence of the difference schemes (1)–(3), we require some elementary facts about the difference operators L_k^h, $k = 1, 2, 3$.

Lemma 5.4 *(Discrete Comparison Principle) For $k = 1, 2, 3$, the scheme $L_k^h u_i = 0$, $-N < i < N$, with $u_{-N} = A_{-1}$ and $u_N = A_1$, has a unique solution. If $L_k^h u_i \leq L_k^h v_i$, $-N < i < N$, and if $u_{-N} \leq v_{-N}$, $u_N \leq v_N$, then $u_i \leq v_i$ for $-N \leq i \leq N$.*

Proof. It is easy to show that the coefficient matrix of the scheme $L_k^h u_i = 0$, $-N < i < N$, with u_{-N} and u_N specified, is diagonally dominant and has non-positive off-diagonal entries. In addition, its rows corresponding to $i = -N + 1$ and $i = N - 1$ are strictly diagonally dominant. Hence, this matrix is an irreducible M-matrix and so has a positive inverse. Therefore, the solution u_i, $-N < i < N$, exists and if the v_i are as specified in the lemma, then we have $u_i \leq v_i$ for $-N \leq i \leq N$. □

From Lemmas 5.1 and 5.4 and the symmetry of the continuous problem (5.1) and the difference schemes (1)–(3), we get

$$u_0 = u(0) = A_0 \equiv \frac{1}{2}(A_{-1} + A_1). \tag{5.29}$$

Thus the proof of the convergence of the difference schemes (1)–(3) can be simplified to

studying the convergence of the following schemes

$$L_k^h u_i = 0, \quad i = 1, \ldots, N-1\ , \quad u_0 = A_0,\ u_N = A_1\ , \quad k = 1,2,3, \tag{5.30}$$

for the continuous problem (5.1) on the interval $0 \le x \le 1$. In a similar way as in establishing Lemma 5.4, we can show the following lemma.

Lemma 5.5 *For $k = 1,2,3$, the scheme $L_k^h u_i = 0,\ 0 < i < N$, with $u_0 = A_0$ and $u_N = A_1$, has a unique solution. If $L_k^h u_i \le L_k^h v_i$, $0 < i < N$, and if $u_0 \le v_0$, $u_N \le v_N$, then $u_i \le v_i$ for $0 \le i \le N$.*

The next lemma, with Lemma 5.5, will enable us to convert bounds for the truncation error into bounds for the discretization error.

Lemma 5.6 *There exist positive constants β, C_1 and C_2 depending only on $x^{2m+1}p(x)$ such that, for $k = 1,2,3$,*

$$L_k^h r_{k,i} \ge \begin{cases} \frac{C_1}{\max(\varepsilon, h_i)} r_{k,i}\ , & \text{for} \quad i \ge N_0, \\ -C_2 \varepsilon^l\ , & \text{for} \quad i < N_0, \end{cases} \tag{5.31}$$

where $N_0 \equiv \min\{i : x_i \ge \frac{1}{2}\}$ and l and $r_{k,i}$ with $i = 0,1,\ldots,N$ are defined by

$$l = 1, \qquad r_{k,i} = \prod_{j=i+1}^{N} \frac{\varepsilon}{\varepsilon + \beta h_j}\ , \qquad \text{for } k = 1,2, \tag{5.32}$$

and

$$l = 2, \qquad r_{k,i} = r^{i-N} \quad \text{with } r = e^{\frac{\beta h}{\varepsilon}}\ , \quad \text{for } k = 3. \tag{5.33}$$

Proof. A computation shows that

$$L_1^h r_{1,i} = \frac{\beta}{\varepsilon + \beta h_i} \left(P_i - \frac{2h_i \beta}{h_i + h_{i+1}} \right) r_{1,i}\ . \tag{5.34}$$

If we select β satisfying $0 < \beta < \frac{1}{2} \min_{\frac{1}{2} \le x \le 1} P(x)$, then for $i = N_0, \ldots, N-1$, we have

$$L_1^h r_{1,i} \ge \frac{M}{\varepsilon + \beta h_i} r_{1,i} \ge \frac{C_1}{\max(\varepsilon, h_i)} r_{1,i}\ .$$

For $i = 1, \ldots, N_0 - 1$, since $\sum_{j=i+1}^{N} h_j \geq \frac{1}{2}$ and $\sum_{j=i+1}^{N} h_j^2 \leq cN^{-1}$, we have

$$\begin{aligned} r_{1,i}^{-1} &= \prod_{j=i+1}^{N} (1 + \frac{\beta h_j}{\varepsilon}) \geq \frac{\beta^2}{\varepsilon^2} \sum_{j,k=i+1, j<k}^{N} h_j h_k = \frac{\beta^2}{\varepsilon^2} \left(\left(\sum_{j=i+1}^{N} h_j \right)^2 - \sum_{j=i+1}^{N} h_j^2 \right) \\ &\geq \frac{M}{\varepsilon^2}. \end{aligned}$$

So $| L_1^h r_{1,i} | \leq M(\varepsilon + \beta h_i)^{-1} r_{1,i} \leq C_2 \varepsilon$ and we obtain (5.31) for $i < N_0$.

Next, since

$$\begin{aligned} L_c^h r_{2,i} &= L_1^h r_{2,i} + A r_{2,i} \geq L_1^h r_{2,i}, \\ L_a^h r_{2,i} &= \frac{\beta}{\varepsilon + \beta h_i} \left(P_{i-\frac{1}{2}} - \frac{2 h_i \beta}{h_i + h_{i+1}} \right) r_{2,i}, \end{aligned}$$

where $A = P_i \beta^2 h_i h_{i+1} / \varepsilon(\varepsilon + \beta h_i)(h_i + h_{i+1}) > 0$, a similar argument can be used to obtain (5.31) when $k = 2$.

For $k = 3$, a computation gives

$$L_3^h r_{3,i} = \frac{P_i}{2hr} (r-1)^2 A r_{3,i}, \tag{5.35}$$

where

$$A = \frac{r+1}{r-1} - \coth \frac{P_i h}{2\varepsilon} = \coth \frac{\beta h}{2\varepsilon} - \coth \frac{P_i h}{2\varepsilon} = \sinh \frac{(P_i - \beta)h}{2\varepsilon} / \sinh \frac{\beta h}{2\varepsilon} \sinh \frac{P_i h}{2\varepsilon}.$$

For $i \geq N_0$, (5.31) can be proved in the same way as Lemma 4.2 in [58]. For $i < N_0$, since $c_1 t \leq \sinh t \leq c_2 t$ for $0 \leq t \leq c$, we have $| A | \leq \frac{M\varepsilon}{P_i h}$ if $h \leq \varepsilon$. In this case, using $r^{-1}(r-1)^2 \leq M\varepsilon^{-2} h^2$ and $r_{3,i} \leq M\varepsilon^3$, we obtain (5.31) from (5.35). If $\varepsilon \leq h$, then since $(r+1) \leq c(r-1)$ and $t \coth t \leq c(1+t)$ for $t \geq 0$, from (5.35), we have

$$| L_3^h r_{3,i} | \leq \frac{M P_i r}{h} \coth \frac{P_i h}{2\varepsilon} r_{3,i} \leq M\varepsilon^{-1} r_{3,i+1} \leq C_2 \varepsilon^2.$$

The proof is completed. □

5.2.2 Convergence Analysis

In this section, we derive error bounds for our difference schemes (1)–(3). Let $u(x)$ be the solution of (5.1) and u_i^k the solution of the system $L_k^h u_i^k = 0,\ 1 \le i \le N-1$, with $u_0^k = A_0$ and $u_N^k = A_1$. Our first result is

Theorem 5.1 *Let γ be given in Lemma 5.2 and the non-equidistant mesh I_n^h be defined by (5.20) with $a\gamma \ge 4$. Then the coupled scheme on I_n^h is second order uniformly convergent, i.e.,*

$$| u(x_i) - u_i^2 | \le Mh^2, \qquad i = 0, \ldots, N. \tag{5.36}$$

Proof. We first consider the truncation error associated with the coupled scheme. A computation in [104] has showed that $\tau_i^2 \equiv L_2^h(u(x_i) - u_i^2)$ satisfies

$$| \tau_i^2 | \le M \left((h_{i+1} - h_i)\varepsilon^{-2} V_\varepsilon(x_i) + h_i^2 \varepsilon^{-3} V_\varepsilon(x_{i+1}) \right), \tag{5.37}$$

where $V_\varepsilon(x) \equiv \exp(-\gamma(1-x)/\varepsilon)$. Lemma 5.2 gives that the solution $u(x)$ to (5.1) on [0,1] has the same differentiability properties as the problem (5.5), which does not have any turning points. So the same argument as that in [104] can be used to derive a bound for τ_i^2 as follows

$$| \tau_i^2 | \le C_3 h^2 \left(1 + \frac{1}{\max(\varepsilon, h_i)} r_{2,i} \right), \quad i = 1, \ldots, N-1, \tag{5.38}$$

if $a\gamma \ge 4$. Furthermore, this bound can be improved when $i < N_0$. Since $\varepsilon^{-3} V_\varepsilon(x) \le Me^{-\tilde{\gamma}/\varepsilon}$ for $x \le \frac{1}{2}$, with some $0 < \tilde{\gamma} < \gamma/2$, from (5.23) and (5.37), we have

$$| \tau_i^2 | \le C_4 h^2 e^{-\tilde{\gamma}/\varepsilon}, \quad \text{for } i < N_0. \tag{5.39}$$

Thus to estimate the discretization error $e_i^h \equiv u(x_i) - u_i^2$, we define $w_i = M_1 h^2 \phi_i + M_2 h^2 r_{2,i} \pm e_i^h$, where $\phi_i \equiv 4x_i - x_i^2$. Since $x_{i-\frac{1}{2}} \ge \frac{1}{2} x_i$ for $i \ge 1$, it is clear that

$$L_2^h \phi_i \ge \min\{L_c^h \phi_i,\ L_a^h \phi_i\} \ge C_0(\varepsilon + x_i^{2m+1}), \tag{5.40}$$

where $L_c^h\phi_i = 2\varepsilon + P_i(4 - x_{i-1} - x_{i+1})$ and $L_a^h\phi_i = 2\varepsilon + P_{i-\frac{1}{2}}(4 - x_i - x_{i-1})$. Using (5.38), (5.39), (5.40) and Lemma 5.6, we have

$$h^{-2}L_2^h w_i \geq \begin{cases} M_1C_0(\varepsilon + x_i^{2m+1}) + M_2\frac{C_1}{\max(\varepsilon,h_i)}r_{2,i} - C_3\left(1 + \frac{1}{\max(\varepsilon,h_i)}r_{2,i}\right), & i \geq N_0\,, \\ M_1C_0(\varepsilon + x_i^{2m+1}) - M_2C_2\varepsilon - C_4h^2e^{-\tilde{\gamma}/\varepsilon}\,, & i < N_0\,. \end{cases} \tag{5.41}$$

Noting that $C_0, \ldots, C_4$ are fixed constants, we may first choose $M_2 = M_2(C_1, C_3)$ large enough such that the sum of the coefficients of $r_{2,i}$ in (5.41) is positive. Then we choose $M_1 = M_1(M_2, C_0, C_2, C_3, C_4)$ large enough such that the right hand sides of (5.41) are positive. In addition, it is obvious that $w_0 \geq 0$ and $w_N \geq 0$. Thus, Lemma 5.5 yields $w_i \geq 0$, i.e.,

$$|\, e_i^h \,| \leq M_1h^2\phi_i + M_2h^2r_{2,i} \leq Mh^2\,, \quad \text{for } i = 0, \ldots, N\,. \tag{5.42}$$

□

Similarly, we can prove, for the operator L_1^h,

Theorem 5.2 *Let γ be given in Lemma 5.2 and the non-equidistant mesh I_n^h be defined by (5.20) with $a\gamma \geq 2$. Then the upwind scheme on I_n^h is first order uniformly convergent, i.e.,*

$$|\, u(x_i) - u_i^1 \,| \leq Mh\,, \qquad i = 0, \ldots, N. \tag{5.43}$$

We now give an error bound for the Il'in scheme.

Theorem 5.3 *The solution u_i^3 to the Il'in scheme on the equidistant mesh I_e^h satisfies*

$$|\, u(x_i) - u_i^3 \,| \leq M\frac{h^2}{h+\varepsilon}\,, \qquad i = 0, \ldots, N. \tag{5.44}$$

Proof. Again, since the solutions to (5.1) on $[0,1]$ and (5.5) have the same differentiability properties and both can be decomposed into a singular part $\zeta\exp(-p(1)\varepsilon^{-1}(1-x))$ (ζ is some constant) and a less singular part as in Lemma 5.3, we can use the reasoning in

[58] to obtain the following bound for the truncation error $\tau_i^3 \equiv L_3^h(u(x_i) - u_i^3)$ of the Il'in scheme

$$| \tau_i^3 | \leq C_3(\varepsilon + h)^{-1}h^2\left(1 + \varepsilon^{-1}r_{3,i}\right), \quad i = 1, \ldots, N-1. \tag{5.45}$$

For $i < N_0$, this estimate can be refined. In fact, since $| \sigma_i - 1 | \leq M\varepsilon^{-2}h^2$, using a Taylor expansion, it is easy to show that if $x_i \leq \frac{1}{2}$,

$$| \tau_i^3 | \leq Mh^2\varepsilon^{-3}V_\varepsilon(x_{i+1}) \leq C_4h^2e^{-\tilde{\gamma}/\varepsilon}, \quad \text{with some } 0 < \tilde{\gamma} < \frac{1}{2}\gamma, \tag{5.46}$$

where $V_\varepsilon(x) = exp(-\gamma(1-x)/\varepsilon)$. Let $\phi(x) = 4x - x^2$. Then, noting that $\sigma_i \geq 1$, we have

$$L_3^h\phi_i = 2\varepsilon\sigma_i + P_i(4 - 2x_i) \geq C_0(\varepsilon + x_i^{2m+1}), \quad i = 1, \ldots, N-1. \tag{5.47}$$

If $h \leq \varepsilon$, then we define $w_i = \varepsilon^{-1}h^2(M_1\phi_i + M_2r_{3,i}) \pm (u(x_i) - u_i^3)$. Using (5.45), (5.46), (5.47) and Lemma 5.6, we obtain

$$\varepsilon h^{-2}L_3^hw_i \geq \begin{cases} M_1C_0(\varepsilon + x_i^{2m+1}) + M_2C_1\varepsilon^{-1}r_{3,i} - C_3(1 + \varepsilon^{-1}r_{3,i}), & i \geq N_0, \\ M_1C_0(\varepsilon + x_i^{2m+1}) - M_2C_2\varepsilon^2 - C_4\varepsilon e^{-\tilde{\gamma}/\varepsilon}, & i < N_0. \end{cases} \tag{5.48}$$

Since we can choose suitable positive constants M_1 and M_2 such that the right hand sides of (5.48) are positive, Lemma 5.5 yields $w_i \geq 0$, i.e.,

$$| u(x_i) - u_i^3 | \leq \varepsilon^{-1}h^2(M_1\phi_i + M_2r_{3,i}) \leq M\varepsilon^{-1}h^2, \quad \text{if } h \leq \varepsilon. \tag{5.49}$$

If $\varepsilon \leq h$, let $w_i = h(M_1\phi_i + M_2\varepsilon^{-1}hr_{3,i}) \pm (u(x_i) - u_i^3)$, which satisfies

$$h^{-1}L_3^hw_i \geq \begin{cases} M_1C_0(\varepsilon + x_i^{2m+1}) + M_2\varepsilon^{-1}C_1r_{3,i} - C_3(1 + \varepsilon^{-1}r_{3,i}), & i \geq N_0, \\ M_1C_0(\varepsilon + x_i^{2m+1}) - M_2\varepsilon hC_2 - C_4he^{-\tilde{\gamma}/\varepsilon}, & i < N_0. \end{cases} \tag{5.50}$$

Again, there exist constants $M_1 > 0$ and $M_2 > 0$ such that $L_3^hw_i \geq 0$. So, since $w_0 \geq 0$, $w_N \geq 0$ and $\varepsilon^{-1}hr_{3,i} \leq \varepsilon^{-1}h\exp(-\beta\varepsilon^{-1}h) \leq M$ for $i \leq N-1$, Lemma 5.5 gives

$$| u(x_i) - u_i^3 | \leq h\left(M_1\phi_1 + M_2\varepsilon^{-1}hr_{3,i}\right) \leq Mh, \quad \text{if } \varepsilon \leq h. \tag{5.51}$$

This completes the proof of the theorem. □

5.3 Numerical Experiments and Discussions

The convergence analysis in the previous section indicates that the exponential ill-conditioning of the singularly perturbed resonance problem (5.1) does not cause any special difficulties in its numerical computation different from the non-turning point problem (5.5). Thus the discretization techniques used to construct uniform convergence schemes for (5.5) can lead to uniform difference approximations for (5.1) as well. We now present a few numerical results to examine our analysis.

5.3.1 A Model Problem of (5.1)

To verify the uniform convergence of our schemes (5.24), (5.25) and (5.28) numerically, we consider a specific problem of the form (5.1)

$$-\varepsilon u'' + xu' = 0\,, \quad -1 < x < 1\,, \qquad u(-1) = -3\,,\ \ u(1) = 1\,. \tag{5.52}$$

We solve this problem for various values of ε and h. In Tables 5.1, 5.2 and 5.3, we list the maximum error E_∞^h and the numerical convergence order r of our schemes L_k^h, $k = 1,2,3$ respectively, for $\varepsilon = 0.01, 0.02$ and 0.03, where $E_\infty^h \equiv \max_i \mid u(x_i) - u_i^h \mid$ and $r \equiv (\log E_\infty^h - \log E_\infty^{h/2})/\log 2$. Here $u(x)$ is the analytical solution of (5.52) and u_i^h the solution of one of our schemes with mesh size $h = 1/N$. For $\lambda(t)$ defined in (5.21), we use $q = \frac{1}{2}$ and $a = 2$. The computation here was performed in FORTRAN double precision (approximately 15.95 significant decimal digits) on a HP735 at UBC. The solver for computing the linear systems corresponding to our schemes is Gaussian elimination and the exact solution $u(x)$ is obtained by applying a numerical quadrature with sufficient precision to (5.10). Note that the principal eigenvalue of the eigenvalue problem associated with (5.52) satisfies $\lambda_0 \approx 2.662 \times 10^{-7}$ for $\varepsilon = 0.03$, $\lambda_0 \approx 7.835 \times 10^{-11}$ for $\varepsilon = 0.02$ and $\lambda_0 \approx 1.539 \times 10^{-21}$ for $\varepsilon = 0.01$ (cf. [79]).

Let's analyze Table 5.2 first. Table 5.2 shows that the coupled scheme is uniformly second order convergent only when the number N of mesh points is not too large. For large N, on the contrary, the convergence of the scheme deteriorates, which contradicts the classical convergence theory that the discretization error of a convergent scheme will tend to zero as the mesh size goes to zero. In addition, the smaller ε is, the sooner this deterioration happens as N increases. Since the uniform convergence of the coupled scheme has been established analytically in §5.2, the only explanation of this paradox is that the Gaussian elimination does not give an accurate numerical approximation to the difference scheme because of the round-off errors of a computer. Specifically, we believe that our schemes do converge uniformly in ε as $h \to 0$, and the degeneration of the discretization errors for large N is caused by the round-off errors in computation due to the severe ill-conditioning of the finite difference operators. We partially verify this explanation by calculating and presenting the condition numbers of the coefficient matrices of our schemes in Table 5.4 for different values of ε and h. Note that since these condition numbers are calculated by MATLAB which uses double precision, they may be *NOT accurate* especially when they are greater than about 10^{15}. Comparing Table 5.4 with Table 5.2, we notice that the numerical convergence order r for the coupled scheme, roughly speaking, begins to deviate from the analytical value of 2 when the condition number is close to 10^{15}, which is approximately the reciprocal of the (double) machine precision. Thus, we believe that this degeneration of the convergence can be avoided if we can calculate a difference scheme more precisely. Based on this explanation, it is anticipated that the numerical computations with quadruple precision arithmetic will yield better results than those with double precision. This is verified in Table 5.5, where the second order convergence for the coupled scheme is obviously obtained using quadruple precision arithmetic even for much larger N than those in Table.5.2 and $\varepsilon = 0.01$. On the other hand, we expect that single precision arithmetic will not give good

numerical results in solving our difference schemes. This is also verified numerically in Table 5.6, where we get only very few significant digits of accuracy even for $\varepsilon = 0.03$ and when h is large.

From Tables 5.1 to 5.6, we can notice that our previous observations about the coupled scheme are also applicable to the upwind scheme and the Il'in scheme. Here we give a further discussion of these schemes. It is clear for each scheme that for a fixed h, the condition of a difference scheme becomes worse if ε is smaller. Thus, for a larger value of ε, it is natural that we can solve our schemes accurately over a wider range of values of h. For fixed values of ε and h, we notice that the condition number of the coupled scheme is greater than that of the upwind scheme. That means a higher order scheme can only be solved accurately for a larger h. However, since a higher order scheme with a larger h may give a better result than a lower order scheme with a smaller h, we find from Tables 5.1 and 5.2 that the coupled scheme resolves the exponentially ill-conditioning problem better than does the upwind scheme.

In summary, although the discrete stability estimate is not valid for a numerical scheme of an exponentially ill-conditioned problem, a truncation error τ^h may not result in very large errors in the numerical solution u^h and a scheme may still be uniformly convergent with respect to ε. However, a numerical method will usually inherit the ill-conditioning associated with the continuous problem. This causes the peculiar phenomenon we observed in the computations that a small number of meshpoints N may give better numerical results than does a large value of N. To minimize the effects of round-off errors that may pollute the accuracy of a scheme, higher (such as quadruple) precision arithmetic is preferred in solving the discrete linear systems. Furthermore, our numerical experiments suggest that higher order difference schemes (or other numerical methods) are usually more efficient in computing the numerical solutions of exponentially ill-conditioning problems.

N	$\varepsilon = 0.03$		$\varepsilon = 0.02$		$\varepsilon = 0.01$	
	E_∞^h	r	E_∞^h	r	E_∞^h	r
24	.1491e0	0.93	.1532e0	0.93	.1585e0	0.95
48	.7840e-1	0.97	.8020e-1	0.97	.8211e-1	-1.21
96	.4010e-1	0.99	.4086e-1	0.99	.1897e0	-
192	.2026e-1	0.99	.2060e-1	0.99	-	-
384	.1018e-1	1.00	.1039e-1	0.89	-	-
768	.5105e-2	1.00	.5616e-2	0.80	-	-
1536	.2556e-2	1.00	.3227e-2	-3.29	-	-
3072	.1282e-2	-	.3150e-1	-	-	-

Table 5.1: Numerical results of the upwind scheme for (5.52) using *double precision*.

5.3.2 A Nonlinear Problem and a Time-dependent Problem

Our purpose in carrying out the next two numerical experiments is to illustrate that our preceding analysis regarding the numerical computation of the model problem (5.1) might also be applicable to other types of exponentially ill-conditioned boundary value problems and their corresponding time-dependent equations.

The first test problem is the steady state Ginzburg-Landau equation

$$\varepsilon^2 u_{xx} + Q(u) = 0\,, \quad -1 < x < 1\,, \qquad u_x(-1) = u_x(1) = 0\,, \tag{5.53}$$

with $Q(u) = 2(u - u^3)$. For this nonlinear BVP, one of its solutions that can be asymptotically approximated by $u \sim \tilde{u}^\varepsilon(x) \equiv \tanh(x/\varepsilon)$ has one internal layer at $x = 0$. So, to compute this solution, we use a non-equidistant mesh $I_n^h = \{x_i : \ i = -N, \ldots, N\}$, which is dense near $x = 0$ and equidistant outside the internal layer, where with the same notations as in (5.20),

$$x_i = x(t_i) = \begin{cases} \lambda(t_i)\,, & i = 0, \ldots, N\,, \\ -\lambda(-t_i)\,, & i = -N, \ldots, -1\,. \end{cases} \tag{5.54}$$

N	$\varepsilon = 0.03$		$\varepsilon = 0.02$		$\varepsilon = 0.01$	
	E_∞^h	r	E_∞^h	r	E_∞^h	r
12	.2545e-1	2.41	.2184e-1	1.89	.1900e-1	2.04
24	.4789e-2	2.00	.5872e-2	2.15	.4615e-2	-7.77
48	.1199e-2	1.99	.1319e-2	1.87	1.01	-
96	.3017e-3	1.98	.3598e-3	0.22	-	-
192	.7659e-4	1.99	.3088e-3	-0.25	-	-
384	.1925e-4	1.79	.1466e-2	-1.10	-	-
768	.5558e-5	-0.76	.3136e-2	-0.97	-	-
1536	.9406e-5	-	.6162e-2	-	-	-

Table 5.2: Numerical results of the coupled scheme for (5.52) using *double precision*.

Here $\lambda(t)$ is defined by

$$\lambda(t) = \begin{cases} \psi(t) := -a\varepsilon t/(q-t)\,, & t \in [0,\alpha]\,, \\ \pi(t) := \psi(\alpha) + \psi'(\alpha)(t-\alpha)\,, & t \in (\alpha,1]\,, \end{cases} \tag{5.55}$$

where $q = \frac{1}{2}$, $a = 1.5$, and $\alpha \in (0,q)$ is determined uniquely by $\pi(1) = 1$. This mesh is similar to (5.20) except that α can be calculated explicitly now. On this mesh, we apply the following finite difference scheme

$$\varepsilon^2 D_+ D_- u_i + Q(u_i) = 0\,, \quad -N < i < N\,, \qquad D_+ u_{-N} = D_- u_N = 0 \tag{5.56}$$

to solve (5.53). Since the exact solution of (5.53) we are seeking is constant near the end points $x = \pm 1$ to within exponentially small terms, first order precision in the difference approximations of the boundary conditions will not ruin the second order accuracy of the difference operator on the interior points when ε is small. In addition, it is clear that $\mid d^i\tilde{u}^\varepsilon/dx^i \mid \leq M\varepsilon^{-i}\exp(-\gamma|x|/\varepsilon)$ with some constant $\gamma > 0$, which is similar to the differential properties of the solution of (5.1). So we expect that the scheme (5.56) on the Bakhvalov type mesh (5.54) is second order uniformly convergent with respect to ε as $h \to 0$. In our computations, the nonlinear discrete system corresponding to

N	$\varepsilon = 0.03$		$\varepsilon = 0.02$		$\varepsilon = 0.01$	
	E_∞^h	r	E_∞^h	r	E_∞^h	r
12	.7158e-2	1.06	.3890e-2	0.05	0.100e1	0.00
24	.3424e-2	1.97	.3766e-2	1.49	0.100e1	-
48	.8765e-3	1.93	.1337e-2	1.88	-	-
96	.2296e-3	2.00	.3633e-3	1.99	-	-
192	.5755e-4	1.99	.9157e-4	-1.33	-	-
384	.1447e-4	1.87	.2309e-3	-4.08	-	-
768	.3945e-5	0.90	.3899e-2	-0.94	-	-
1536	.2116e-5	-	.7459e-2	-	-	-

Table 5.3: Numerical results of the Il'in scheme for (5.52) using *double precision*.

N	Upwind scheme (5.24)			Coupled scheme (5.25)			Il'in scheme (5.28)		
	$\varepsilon = .03$	$\varepsilon = .02$	$\varepsilon = .01$	$\varepsilon = .03$	$\varepsilon = .02$	$\varepsilon = .01$	$\varepsilon = .03$	$\varepsilon = .02$	$\varepsilon = .01$
12	4.17e6	5.64e7	6.39e9	8.67e7	4.87e9	7.31e9	1.14e8	2.66e11	1.81e17
24	1.75e8	7.44e9	1.07e13	2.30e11	3.20e13	2.60e14	4.74e8	1.21e12	8.00e16
48	4.94e9	7.98e11	3.46e15	1.64e11	6.31e14	4.04e17	1.89e9	4.77e12	3.07e16
96	8.02e10	4.50e13	1.52e19	5.38e11	4.48e15	1.33e17	7.56e9	1.89e13	4.86e16
192	7.79e11	1.13e15	1.40e17	2.15e12	1.16e16	2.12e17	3.02e10	7.52e13	6.41e16
384	5.20e12	1.46e16	-	8.80e12	5.00e16	-	1.21e11	3.03e14	-

Table 5.4: Numerical results (using Matlab) of the condition numbers $\| A \|_2 \| A^{-1} \|_2$ of the coefficient matrices A of schemes (5.24), (5.25) and (5.28).

(5.56) is solved by Newton's method with $\tilde{u}^\varepsilon(x)$ as the initial guess. The iterations are stopped when the maximum pointwise absolute difference between successive iterations becomes smaller than ε_n, which equals 10^{-10} for double precision arithmetic and 10^{-20} for quadruple precision arithmetic.

The numerical results are compared to the numerical solution obtained by the same method with a sufficiently large $N = N_0$. The corresponding maximum pointwise absolute errors $\tilde{E}_\infty^h$, as well as the numerical rate r_1 and anticipated rate r_2, are presented in Tables 5.7 and 5.8, for $\varepsilon = 0.05$, 0.1 and 0.15, where $r_1 \equiv \tilde{E}_\infty^h / \tilde{E}_\infty^{h/2}$ and r_2 is defined

N	Upwind scheme (5.24)		Coupled scheme (5.25)		Il'in scheme (5.28)	
	E^h_∞	r	E^h_∞	r	E^h_∞	r
48	.8204e-1	0.98	.1225e-2	1.89	.1815e-2	1.45
96	.4153e-1	0.99	.3310e-3	2.00	.6603e-3	1.97
192	.2084e-1	1.00	.8265e-4	2.00	.1675e-3	1.99
384	.1044e-1	1.00	.2064e-4	2.00	.4221e-4	1.97
768	.5222e-2	1.00	.5154e-5	2.00	.1075e-4	1.90
1536	.2611e-2	-	.1286e-5	-	.2875e-5	-

Table 5.5: Numerical results of schemes (5.24), (5.25) and (5.28) using *quadruple precision* arithmetic. Here $\varepsilon = 0.01$.

N	Upwind scheme (5.24)		Coupled scheme (5.25)		Il'in scheme (5.28)	
	E^h_∞	r	E^h_∞	r	E^h_∞	r
12	.2699	0.81	.0289	-7.28	.3584	-0.48
24	.1540	0.63	4.492	4.33	.4987	-0.42
48	.0998	-2.01	.2234	-2.32	.6670	-0.37
96	.4016	-	1.113	-	.8627	-

Table 5.6: Numerical results of schemes (5.24), (5.25) and (5.28) using *single precision* arithmetic. Here $\varepsilon = 0.03$.

below. Note that, from (3.23), the principal eigenvalue of the eigenvalue problem associated with the linearized equation about the one layer solution satisfies $\lambda_0 \approx 2.518 \times 10^{-10}$ for $\varepsilon = 0.15$, $\lambda_0 \approx 4.078 \times 10^{-16}$ for $\varepsilon = 0.1$ and $\lambda_0 \approx 1.733 \times 10^{-33}$ for $\varepsilon = 0.05$. Let us estimate what the values of r_2 should be. Let $h_0 = 1/N_0$ and suppose $h = 2^k h_0$ with some integer $k > 1$. If our scheme is second order uniformly convergent, then we have, by assuming that $u^h(x_i) \sim u(x_i) + c(x_i)h^2$,

$$u^h - u^{h_0} \sim c(2^{2k} - 1)h_0^2, \qquad u^{h/2} - u^{h_0} \sim c(2^{2(k-1)} - 1)h_0^2.$$

So we set the anticipated rate

$$r_2 = \frac{4^k - 1}{4^{k-1} - 1}. \tag{5.57}$$

From Table 5.7, where double precision arithmetic is used, we notice that the values of r_1 and r_2 agree with each other when the number N of the mesh points is not large. However, it is true for all values of ε listed that the numerical rate r_1 begins to diverge from the anticipate rate r_2 when N is greater than about 1024 and Newton's method does not converge when $N \geq 1024$. Although we can't explain exactly what causes this value of 1024, which should depend on the value of ε, to be independent of ε, from our experience in computing the solution to (5.1), we speculate that the disagreement in Table 5.7 stems from the round-off errors in computation. This is verified by Table 5.8, where we use quadruple precision arithmetic. Surprisingly, in Table 5.8, r_1 agrees with r_2 to more than five significant digits when $N \geq 2048$.

		$\varepsilon = 0.15$		$\varepsilon = 0.1$		$\varepsilon = 0.05$	
$N:k$	r_2	$\hat{E}_\infty^h$	r_1	$\hat{E}_\infty^h$	r_1	$\hat{E}_\infty^h$	r_1
16:9	4.0000	.4110e-4	3.8297	.1094e-3	4.0286	.1478e-3	4.0767
32:8	4.0002	.1073e-4	4.0662	.2715e-4	4.0008	.3625e-4	3.9745
64:7	4.0007	.2639e-5	3.9700	.6785e-5	3.9999	.9120e-5	4.0044
128:6	4.0029	.6648e-6	4.0087	.1696e-5	4.0024	.2277e-5	3.9984
256:5	4.0118	.1658e-6	4.0131	.4238e-6	4.0116	.5696e-6	4.0117
512:4	4.0476	.4132e-7	4.0177	.1057e-6	4.0463	.1420e-6	4.0457
1024:3	4.2000	.1029e-7˜	3.5997	.2611e-7˜	3.9447	.3509e-7˜	3.8957
2048:2	5.0000	.2857e-8˜	0.5854	.6619e-8˜	1.5100	.9008e-8˜	0.8692
4096:1	-	.4881e-8˜	-	.4384e-8˜	-	.1036e-7˜	-

Table 5.7: Numerical results of the scheme (5.56) using *double precision*. Here $N_0 = 8192$, $\varepsilon_n = 10^{-10}$. For those $\hat{E}_\infty^h$ ending with "˜", Newton's method does not converge within 20 iterations.

For our second test problem, we consider the time-dependent problem corresponding to (5.1) from [79]

$$u_t = \varepsilon u_{xx} - x u_x\,, \qquad -1 < x < 1\,, \quad t > 0\,, \tag{5.58a}$$

$$u(-1,t) = 2\,, \quad u(1,t) = \frac{1}{2}\,, \quad u(x,0) = \frac{1}{2} + 3(x-1)^2/8\,. \tag{5.58b}$$

		$\varepsilon = 0.15$		$\varepsilon = 0.1$		$\varepsilon = 0.05$	
$N:k$	r_2	$\tilde{E}^h_\infty$	r_1	$\tilde{E}^h_\infty$	r_1	$\tilde{E}^h_\infty$	r_1
32:9	4.0000	.1073e-4	4.0660	.2715e-4	4.0007	.3625e-4	3.9744
64:8	4.0002	.2639e-5	3.9694	.6786e-5	3.9994	.9120e-5	4.0038
128:7	4.0007	.6649e-6	4.0065	.1697e-5	4.0002	.2278e-5	3.9962
256:6	4.0029	.1660e-6	4.0043	.4241e-6	4.0028	.5700e-6	4.0032
512:5	4.0118	.4144e-7	4.0121	.1060e-6	4.0117	.1424e-6	4.0118
1024:4	4.0476	.1033e-7	4.0477	.2641e-7	4.0475	.3549e-7	4.0476
2048:3	4.2000	.2552e-8	4.2000	.6526e-8	4.2000	.8769e-8	4.2000
4096:2	5.0000	.6076e-9	5.0000	.1554e-8	5.0000	.2088e-8	5.0000
8192:1	-	.1215e-9	-	.3107e-9	-	.4176e-9	-

Table 5.8: Numerical results of the scheme (5.56) using *quadruple precision*. Here $N_0 = 16384$, $\varepsilon_n = 10^{-20}$.

It is shown in [79] that the metastable dynamics for (5.58), valid away from an initial time layer, can be asymptotically described by

$$u(x,t) \sim \tilde{u}^\varepsilon[x; A(x,\varepsilon)] \equiv A(t,\varepsilon) + (2 - A(t,\varepsilon))\, e^{-\frac{1+x}{\varepsilon}} + \left(\frac{1}{2} - A(t,\varepsilon)\right) e^{-\frac{1-x}{\varepsilon}}\,, \quad (5.59)$$

where with $\lambda_0 = \sqrt{\frac{2}{\pi\varepsilon}}\,(1 - \varepsilon + O(\varepsilon^2))\, e^{-\frac{1}{2\varepsilon}}$,

$$A(t,\varepsilon) \sim \frac{5}{4} - \frac{3}{8}(1-\varepsilon)e^{-\lambda_0 t}\,. \quad (5.60)$$

To compute $u(x,t)$ numerically, we apply the TMOL in §1.3 to (5.58) except that the BVP solver COLSYS is replaced by our difference scheme (5.24), (5.25) or (5.28), where the mesh generating function $\lambda(t)$ is given in (5.55) instead of (5.21). From our numerical results, we output the value of $u(0,t)$, which gives the numerical prediction for $A(t,\varepsilon)$. In Figure 5.2, 5.3 and 5.4, we plot t versus A for the asymptotic result (5.60) (dotted lines) and the numerical results (solid lines) corresponding to the upwind scheme, the coupled scheme and the Il'in scheme, respectively, for various values of h. Here the computation was performed in double precision arithmetic. The figures indicate that two curves representing the asymptotic and numerical results of $t(A)$ converge as h decreases.

For the center scheme with $N = 400$ and the Il'in scheme with $N \geq 100$, the two curves are virtually indistinguishable. These phenomena suggest that our numerical methods are convergent and can be used to give a numerical verification of the validity of the asymptotic metastable dynamics.

Based on our convergence analysis and numerical experiments, we believe that classic finite difference schemes and other numerical methods may be applied to compute the singularly perturbed problems exhibiting dynamic metastability as long as the mesh size h is suitably selected and ε is not too small. In such cases, the exponentially ill-conditioned singularly perturbed problems do not cause more troubles in numerical computations than other "standard" singular perturbation problems such as (5.5) do.

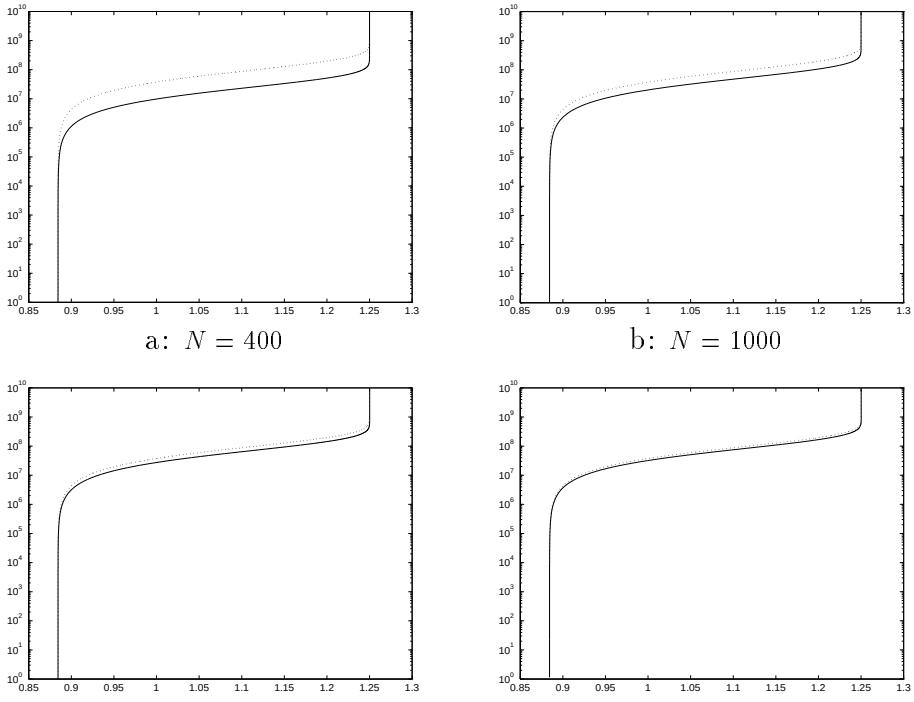

a: $N = 400$ b: $N = 1000$

c: $N = 2000$ d: $N = 4000$

Figure 5.2: Plot of t versus A for (5.58) from the asymptotic approximation (dotted line) and from the full numerical approximation (solid line) using the *upwind scheme* when $\varepsilon = 0.025$.

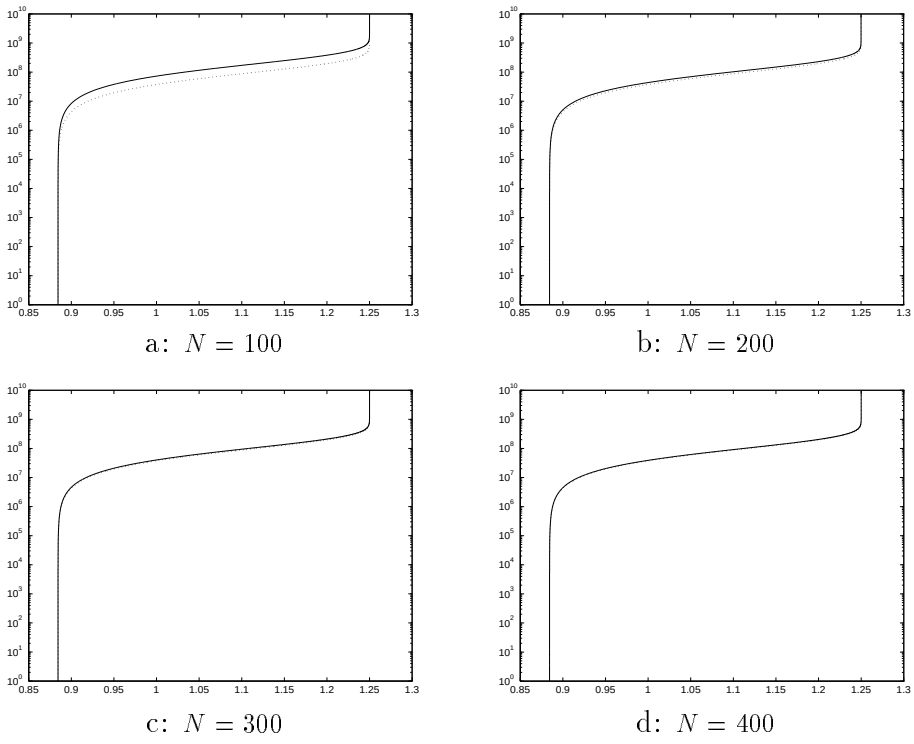

a: $N = 100$ b: $N = 200$

c: $N = 300$ d: $N = 400$

Figure 5.3: Plot of t versus A for (5.58) from the asymptotic approximation (dotted line) and from the full numerical approximation (solid line) using the *coupled scheme* when $\varepsilon = 0.025$.

5.3.3 A Spectral Method

According to our observations in §5.3.1, we believe that higher order numerical methods, which can lead to small discretization errors with a moderate number of mesh points, are usually more effective to compute the numerical solutions of exponentially ill-conditioned problems. Since the spectral methods are known to be able to offer exponential accuracy meaning that the error between the numerical solution and exact solution decays exponentially versus N, we now introduce a new procedure based on coordinate stretching and the Chebyshev pseudo-spectral (PS) method to solve (5.1). Our aim is to see with this procedure if and then how significantly we can improve the numerical results in §5.3.1.

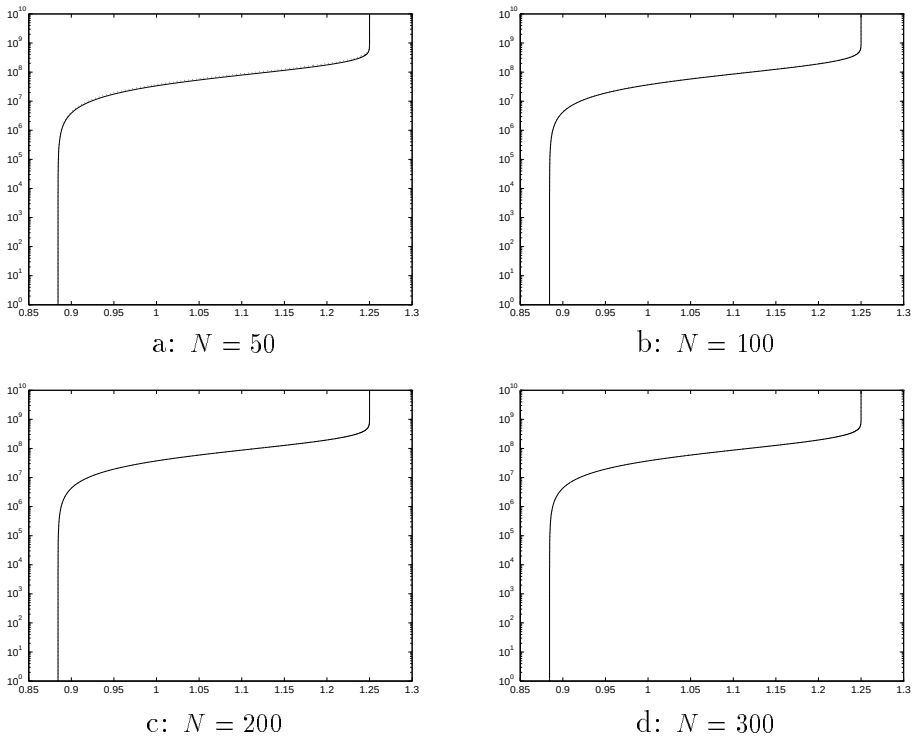

a: $N = 50$ b: $N = 100$

c: $N = 200$ d: $N = 300$

Figure 5.4: Plot of t versus A for (5.58) from the asymptotic approximation (dotted line) and from the full numerical approximation (solid line) using the *Il'in scheme* when $\varepsilon = 0.025$.

It has been found (see [25], [42]) that the PS method is attractive in solving singular perturbation problems having boundary layers by clustering the mesh points toward the boundaries, for example, as in the Chebyshev method ($x_i = \cos \frac{\pi i}{N}, i = 0, \ldots, N$). However, to obtain an accurate solution with a very small parameter ε, a large N is required to guarantee that at least one of the collocation points lies in the boundary layer. To avoid this difficulty, Tang and Trummer [105] introduced a sequence of SINE transformations of the computational domain so that some collocation points are within a distance ε from the boundaries $x = \pm 1$ for $\varepsilon \ll 1$. Indeed these transformations together with the Chebyshev PS method can deal well with very small boundary layers with a fairly small number of collocation points. However, we notice that since the SINE transformation does not make use of the properties of a boundary layer such as (5.9),

it does not ensure that at least one collocation point lies in the boundary layer for all $\varepsilon > 0$. Thus, with a fixed number of the SINE transformations, the number of collocation points required to resolve a boundary layer is still dependent on ε. Instead of the SINE transformation, therefore, we consider the following coordinate transformation, which yields $O(N)$ collocation points, independent of ε, in both the boundary layers and the interior domain:

$$x(t) = \begin{cases} \lambda(t+1) - 1 \ , & t \in [-1, 0] \ , \\ 1 - \lambda(1-t) \ , & t \in (0, 1] \ , \end{cases} \tag{5.61}$$

where

$$\lambda(t) = \begin{cases} \psi(t) := -A\varepsilon \ln \left[1 - 2(1 - \varepsilon^{\frac{1}{K+1}})t\right] \ , & 0 \le t \le \frac{1}{2} \ , \\ \pi(t) := \sum_{k=0}^{K} \frac{1}{k!}\psi^{(k)}(\frac{1}{2})(t - \frac{1}{2})^k + B(t - \frac{1}{2})^{K+1} \ , & \frac{1}{2} < t \le 1 \ . \end{cases} \tag{5.62}$$

Here $A > 0$ is a constant, $K > 0$ is an integer and $B = B(t, \varepsilon)$ is determined such that $x(t)$ is a strictly increasingly function connecting $(-1, -1)$ and $(1, 1)$ on the x-t plane and has certain required smoothness. Another advantage of the coordinate transformation (5.61) over the SINE transformation is that the solution in the computational coordinate t can be as smooth as needed by selecting the integer K (see (5.65) below). This is rather important to the convergence of the spectral methods, since lack of smoothness of a continuous solution is the main source of degradation of the expected infinity-order accuracy for a spectral method due to the Gibbs phenomenon.

The transformed form of (5.1) can be written as

$$-\varepsilon v''(t) + \tilde{P}(t)v'(t) = 0 \ , \ \ -1 < t < 1 \ , \quad v(-1) = A_{-1} \ , \ \ v(1) = A_1 \ , \tag{5.63}$$

where v is the transplant of u, $v(t) = u(x(t))$, and $\tilde{P}(t) \equiv \varepsilon \frac{x''(t)}{x'(t)} + x(t)^{2m+1} p(x(t)) x'(t)$. To ensure that this transformed equation is well defined, we require that $x(t)$ has at least up to second order continuous derivatives and $x'(t) > 0$. It is clear that $\lambda(t)$ is K-th

order continuously differentiable and if we let

$$\pi(1) = 1\,, \qquad \pi''(1) = 0\,, \tag{5.64}$$

then $x(t)$ has up to third order continuous derivatives. In our computations, we let $B = b_0 + b_1(t - \frac{1}{2})$, where b_0 and b_1 are determined by (5.64). Now let us show that for this choice of B, (5.63) is well defined and its solution $v(t)$ has uniformly bounded derivatives up to K-th order except at $t = 0$ when $A\gamma \geq K(K+1)$, i.e.,

$$|\, v^{(k)}(t)\,| \leq M \quad \text{for } 0 < |t| \leq 1 \text{ and } k = 0, \ldots, K\,, \tag{5.65}$$

where γ is the constant given in (5.9) and $M > 0$ is a constant independent of ε.

First, to show (5.63) is well defined, it suffices to prove $\lambda'(t) > 0$. From (5.62), we have

$$\psi^{(k)}(t) = \frac{A(k-1)!q^k\varepsilon}{(1-qt)^k}\,, \qquad \psi^{(k)}(\frac{1}{2}) = A(k-1)!q^k\varepsilon^{1-\frac{k}{K+1}}\,, \tag{5.66}$$

for $k = 1, \ldots, K$, where $q \equiv 2(1 - \varepsilon^{\frac{1}{K+1}})$. Since $\psi^{(k)}(\frac{1}{2}) \to 0$ as $\varepsilon \to 0$, from (5.64), we obtain

$$b_0 \sim 2^K(K+2)\,, \quad b_1 \sim -K2^{K+1}\,, \qquad \text{as } \varepsilon \to 0\,. \tag{5.67}$$

It follows that on $\frac{1}{2} < t \leq 1$,

$$\begin{aligned} \pi'(t) &> b_0(K+1)(t-\frac{1}{2})^K + b_1(K+2)(t-\frac{1}{2})^{K+1} \\ &= (K+2)2^K(t-\frac{1}{2})^K\left(K+2-2K(t-\frac{1}{2})\right) > 0\,, \quad \text{as } \varepsilon \to 0\,. \end{aligned}$$

The proof of $\lambda'(t) > 0$ on $0 \leq t \leq \frac{1}{2}$ is apparent. Next, let's consider (5.65). By symmetry, we only show it on $-1 \leq t < 0$. For $-1 \leq t \leq -\frac{1}{2}$, using (5.9) and (5.66), we have

$$\begin{aligned} |\,\frac{dv}{dt}\,| &= |\,\frac{du}{dx}\cdot\frac{dx}{dt}\,| \leq M\varepsilon^{-1}e^{-\gamma\frac{-A\varepsilon\ln(1-q(t+1))}{\varepsilon}}\cdot\frac{A\varepsilon q}{1-q(t+1)} \\ &\leq M\,(1-q(t+1))^{A\gamma-1} \leq M\,, \qquad \text{if } A\gamma \geq 1 \end{aligned}$$

and similarly, for $k = 1, \ldots, K$,

$$| \frac{d^k v}{dt^k} | \leq M \, (1 - q(t+1))^{A\gamma - k} \leq M \ , \qquad \text{if } A\gamma \geq k \ .$$

For $-\frac{1}{2} \leq t < 0$, since $\lambda(t+1) \geq \psi(\frac{1}{2}) = -A\varepsilon \ln \varepsilon/(K+1)$, we have

$$\begin{aligned} | \frac{d^k v}{dt^k} | &\leq M \, | \frac{d^k u}{dx^k} | \leq M \varepsilon^{-k} e^{-\gamma \varepsilon^{-1} \lambda(t+1)} \\ &\leq M \varepsilon^{\frac{A\gamma}{K+1} - k} \leq M \ , \qquad \text{if } A\gamma \geq k(K+1) \ . \end{aligned}$$

Thus, (5.65) holds when $A\gamma \geq K(K+1)$. It is certain that we can find a mesh generating function $\lambda(t)$ such that (5.65) is true on the whole region of t i.e., including $t = 0$. But since the solution of (5.1) is constant to within exponentially small terms outside the boundary layers, we do not expect doing so will make any significant improvements.

Our numerical procedure is to solve the transformed problem (5.63) using the standard Chebyshev PS method (cf. [25], [42]). The resulting linear system is solved by Gauss elimination in double precision. Our numerical experiments displayed in Table 5.9 show that this procedure is indeed superior to our finite difference schemes in §5.3.1 for (5.1). For example, for $\varepsilon = 0.01$, the least maximum error we can obtain in Table 5.9 is about $O(10^{-6})$, whereas it is only at best $O(10^{-2})$ in Tables 5.1 to 5.3. In addition, we can still obtain four significant digits of accuracy even for (5.52) with $\varepsilon = 0.002$, for which the corresponding principal eigenvalue $\lambda_0 \approx O(10^{-108})$.

N	$\varepsilon = 0.03$	$\varepsilon = 0.02$	$\varepsilon = 0.01$	$\varepsilon = 0.005$	$\varepsilon = 0.002$
10	.5635e-2	.7848e-2	.1753e-1	.3859e-1	.7900e-1
20	.8912e-5	.6488e-5	.6045e-5	.7707e-4	.1222e-3
40	.3107e-6	.6807e-6	.2759e-6	.1831e-5	.2806e-4
80	.2949e-7	.7160e-7	.2487e-6	.1997e-5	.2787e-4
120	.7312e-8	.5419e-7	.8624e-6	.1978e-5	.2790e-4
160	.8513e-8	.6267e-7	.2030e-3	.5149e-5	.2797e-4
200	.9894e-8	.7220e-7	.1724e-1	.6075e-5	.2817e-4
240	.9094e-8	.4613e-7	.1303e0	.1725e-3	.1428e-2[1]

Table 5.9: Maximum errors for the spectral method applied to (5.52) using double precision. Here, $K = 3$ and $A = 8$.

[1]For this entry, N=400

Chapter 6

Summary and Future Work

6.1 Summary

In this thesis we have applied asymptotic and numerical methods to investigate metastable behavior associated with several time-dependent singular perturbation problems, including the generalized Burgers equation modeling an upward flame front propagation in a vertical channel, the viscous Cahn-Hilliard equation modeling the phase separation of a binary mixture and two problems related to exponentially slowly varying geometries. Specifically, we employed the projection method to derive ordinary differential equations (ODEs) or differential algebraic equations (DAEs) for the undetermined constants in the conventional MMAE solutions to the equilibrium problems. From these ODEs/DAEs, the metastable behavior was then studied quantitatively and in detail, and the equilibrium solutions and their stability were also obtained. In addition, the principal eigenvalues of the linearized operators were estimated asymptotically for the flame front problem and the slowly varying geometry problems. Most of our crucial asymptotic results were verified by the full numerical results computed using the TMOL. Another role of our numerical method TMOL is to provide useful information about the metastable solutions in their transient phases and collapse phases during which our asymptotic analysis fails.

For the flame front problem, it was suggested by Berestycki, et al. [16] that the parabolic flame front may be dynamically metastable in the sense that its tip location

remains near its initial location for an exponentially long time. However, to our knowledge, no rigorous proof has been given yet and little is known of its detailed dynamics. In this thesis, we considered a generalized form of the Burgers type equation. It was shown that the principal eigenvalue associated with the linearization around the equilibrium is exponentially small. In addition, the metastable behavior was studied quantitatively by deriving an asymptotic ODE characterizing the slow motion of the tip of a parabolic-shaped interface. Our asymptotic results were shown to compare very favorably with full numerical computations and give a first detailed and quantitative description of the metastable flame-front motion in a vertical channel.

For the Burgers-like convection-diffusion equation which describes one dimensional transonic flow through a nozzle with a slowly varying cross-sectional area, we studied the effect of an exponentially small change in the cross-sectional area upon the existence and stability of the steady state shock layer solution. In particular, using the projection method, we derived an asymptotic ODE characterizing the slow motion of a shock layer. From this ODE, we designed a specific convergent-divergent nozzle where a stable steady state shock layer occurs in the convergent part of the nozzle. This is interesting, because it has been proved by Liu [71] and Embid, et al. [34] for the corresponding inviscid problem that shock waves in the convergent part of the nozzle are not stable. We have found that this discrepancy is due to some situations which were not included in [71] and [34] where exponentially small terms, generated by the viscosity term, have to be resolved. Another slowly varying geometry problem is a generalized Ginzburg-Landau equation that can be employed to study the existence of non-constant stable steady solutions to the Ginzburg-Landau equation in several space dimensions. By studying the metastable dynamics in this equation using the projection method, we are able to construct non-convex domains for which the Ginzburg-Landau equation are believed to admit stable spatially-dependent steady state solutions.

For the viscous Cahn-Hilliard equation, this thesis gives a detailed analysis of the dynamics of an n-layer metastable pattern and uses a hybrid approach to describe the coarsening process until the final stable configuration is reached. From the DAE system derived from applying the projection method, we can trace the metastable dynamics very accurately. For the Cahn-Hilliard equation ($\alpha = 0$), using this DAE system, we found the "missing" small terms which are significant for non-collapse interfaces in the ODE system obtained by Bates, et al. [15]. We also showed that the viscous Cahn-Hilliard equation ($0 < \alpha < 1$) and the constrained Allen-Cahn equation ($\alpha = 1$) have the same metastable dynamics except in the collapse time scale, while the Cahn-Hilliard equation is quite different. During the layer collapse, a hybrid algorithm based on our asymptotic information and the conservation of mass condition is provided to characterize the whole coarsening process. This thesis has revealed the similarities and differences of the dynamics of an n-layer metastable pattern associated with the three phase separation models in one spatial dimension and showed several interesting phenomena associated with the coarsening process for the first time.

The above discussion indicates that our approach based on asymptotic and numerical methods is a powerful and general tool to quantitatively study the metastable behavior associated with various physical problems.

Another topic of the thesis is the numerical analysis of a linear boundary layer resonance problem which is one of the "simplest" metastable models. Our convergence analysis and numerical experiments have shown that several classical finite difference schemes are uniformly convergent with respect to ε, but their coefficient matrices inherit the extreme ill-conditioning from the continuous problem. In particular, the exponentially small principal eigenvalue does not affect the uniform convergence of these schemes. Thus, the exponentially ill-conditioned singularly perturbed problems would not cause

more troubles in numerical computations than other (not metastable) singular perturbation problems provided that we could use sufficiently high (such as quadruple) precision arithmetic. Our observations revealed from this model problem were shown numerically to be also valid for some other types of exponentially ill-conditioned boundary value problems and their corresponding time-dependent equations. Thus, these observations might be used as some guidelines in designing numerical schemes for metastable problems.

6.2 Future Research

In spite of numerous efforts devoted to study metastable dynamics in various physical problems in the past decade, there still remain many interesting unexplored problems, especially in multi-dimensional domains, and for systems of reaction-diffusion equations. Some of these problems I plan to work on are:

1. Kolmogorov's backward equation in two dimensions, which is related to the exit problem of a Brownian particle confined by a finite potential well. We wish to use the projection method to study the exponential ill-conditioning and metastable dynamics in this equation and show that the equilibrium solution is extremely sensitive to small perturbations in the coefficients of the equation due to its exponentially small principal eigenvalue. This supersensitivity might be used to give a linearized sensitivity analysis of a model equation that arises from a diffusive regularization of the shape from shading problem. Parts of this work have been done in [103].

2. Two dimensional flame front problem, modeled by the Mikishev-Rakib-Sivashinsky equation. The goal is to characterize the metastable behavior of a flame front in an axially symmetric vertical channel and to explain experimental evidence showing the slow motion of the flame-front interface. We have noticed an inherent connection between the one-dimensional and multi-dimensional flame front problems, and

thus it is hopeful that we will be able to characterize the metastable dynamics by applying the projection method.

3. Two dimensional bubble problem, modeled by the constrained Allen-Cahn equation with a mixed boundary condition. Cahn [23] observed experimentally that a surface layer — bubble of the wetting phase continues to exist under certain conditions when this phase is no longer stable as a bulk. This observation does not agree with the simulation of the constrained Allen-Cahn equation with a Neumann boundary condition, since with this boundary condition the bubble is unstable and drifts towards the boundary of the domain. We believe that the resolution of this paradox is that the boundary condition corresponding to a surface layer perturbs the exponentially small eigenvalue and allows for the stability of the bubble solution.

4. Bubble problem for the Cahn-Hilliard equation. The goal is to characterize the dynamics of metastable bubble solutions for the fourth order Cahn-Hilliard equation. This would extend previous work which was focused on the dynamics of bubble solutions for the second order constrained Allen-Cahn equation.

In addition, it would be of interest to develop an efficient and robust numerical method to treat problems exhibiting metastable dynamics in two spatial dimensions.

Bibliography

[1] R.C. Ackerberg, R.E. O'Malley, Jr., *Boundary layer problems exhibiting resonance*, Studies in Applied Math. **49**, (1970), pp. 277–295.

[2] N. Alikakos, P.W. Bates, G. Fusco, *Slow motion for the Cahn-Hilliard equation in one space dimension*, J. Diff. Equat. **90**, (1991), pp. 81–135.

[3] N. Alikakos, G. Fusco, *Slow dynamics for the Cahn-Hilliard equation in higher spatial dimensions, part 1: spectral estimates*, Comm. Part. Diff. Equat. **19**, (1994), pp. 1397–1447.

[4] N. Alikakos, G. Fusco, *Slow dynamics for the Cahn-Hilliard equation in higher spatial dimensions: the motion of bubbles*, Arch. Rational Mech. Anal. **141**, (1998), pp. 1–61.

[5] D.N. Allen, R.V. Southwell, *Relaxation methods applied to determine motion, in two dimensions, of a viscous fluid past a fixed cylinder*, J. Mech. Appl. Math. **8**, (1955), pp. 129–145.

[6] U. Ascher, R. Christiansen, R. Russell, *Collocation software for boundary value ODE's*, Math. Comp. **33**, (1979), pp. 659–679.

[7] U. Ascher, R. Mattheij, R. Russell, *Numerical solution of boundary value problems for ordinary differential equations.* Englewood Cliffs, N.J., Prentice Hall, 1988.

[8] F. Bai, C.M. Elliott, A. Gardiner, A. Spence, A.M. Stuart, *The viscous Cahn-Hilliard equation. Part I: computations.* Nonlinearity **8**, (1995), pp. 131–160.

[9] F. Bai, A. Spence, A.M. Stuart, *Numerical computations of coarsening in the one-dimensional Cahn–Hilliard model of phase separation*, Physica D **78**, (1994), pp. 155-166.

[10] P.B. Bailey, B.S. Garbow, H.G. Kaper, A. Zettl, *Eigenvalue and eigenfunction computations for Sturm-Liouville problems.* ACM Trans. on Math. Software **17**, (1991), pp. 491–499.

[11] P.B. Bailey, B.S. Garbow, H.G. Kaper, A. Zettl, *Algorithm 700: A FORTRAN software package for Sturm-Liouville problems.* ACM Trans. on Math. Software **17**, (1991), pp. 500–501.

[12] A.S. Bakhvalov, *On the optimization of methods for solving boundary value problems with boundary layers*, (in Russian) Zh. Vychisl. Mat. i Mat. Fis., **9**, (1969), pp. 841–859.

[13] H. Bateman, *Some recent researches on the motion of fluids*, Monthly Weather Review **43**, (1915), pp. 163–170.

[14] P.W. Bates, P.C. Fife, *Spectral comparison principles for the Cahn-Hilliard and Phase-Field equations, and time scales for coarsening*, Physica D **43**, (1990), pp. 335–348.

[15] P.W. Bates, J. Xun, *Metastable patterns for the Cahn-Hilliard equation: part 1 and 2*, J. Diff. Equat. **111**, (1994), pp. 421–457; J. Diff. Equat. **117**, (1995), pp. 165–216.

[16] H. Berestycki, S. Kamin, G. Sivashinsky, *Nonlinear dynamics and metastability in a Burgers type equation*, Compte Rendus Acad. Sci., Paris t. **321**, Serié 1, (1995), pp. 185–190.

[17] L. Bronsard, D. Hilhorst, *On the slow dynamics for the Cahn-Hilliard equation in one space dimension*, Proc. Roy. Soc. London A. **439**, (1992), pp. 669–682.

[18] J.M. Burgers, *A mathematical model illustrating the theory of turbulence*, Advances Appl. Mechanics **1**, (1948), pp. 171–199.

[19] J.M. Burgers, *The Nonlinear Diffusion Equation*, Reidel, Dordrecht, 1974.

[20] G. Caginalp, *An analysis of a phase-field model of a free-boundary*, Arch. Rat. Anal. Mech. **92**, (1986), pp. 205–245.

[21] G. Caginalp, P. Fife, *Dynamics of layered interfaces arising from phase boundaries*, SIAM J. Appl. Math. **48**, (1988), pp. 506–518.

[22] J.W. Cahn, *On spinodal decomposition*, Acta Metallurgica, **9**, (1961), pp. 795–801.

[23] J.W. Cahn, *Critical point wetting*, J. Chem. Phy. **66**, (1977), pp. 3667–3672.

[24] J.W. Cahn, J.E. Hilliard, *Free energy of a nonuniform system. I. Interfacial free energy*, J. Chem. Phy. **28**, (1958), pp. 258–267.

[25] C. Canuto, M.Y. Hussaini, A. Quarteroni, T.A. Zang, *Spectral Methods in Fluid Dynamics*, Series of Computational Physics, Springer-Verlag, Heidelberg, Berlin, New York, 1988.

[26] J. Carr, R. Pego, *Metastable patterns in solutions of* $u_t = \varepsilon^2 u_{xx} - f(u)$, Comm. Pure Appl. Math. **42**, (1989), pp. 523–576.

[27] J.R. Cash, *The integration of stiff initial value problems in ODEs using modified extended backward differentiation formulae*, Comput. Math. Appl. **9** (1983), pp. 645–657.

[28] R.G. Casten, C.J. Holland, *Instability results for reaction diffusion equations with Neumann boundary conditions*, J. Diff. Equat. **27**, (1978), pp. 266–273.

[29] S.J. Chapman, G. Richardson, *Vortex pinning by inhomogeneities in type-2 superconductors*, Physica D, **108**, (1997), pp. 397-407.

[30] J.D. Cole, *On a quasilinear parabolic equation occurring in aerodynamics*, Quart. Appl. Math. **9**, (1951), pp. 225–236.

[31] P.P.N. deGroen, *The nature of resonance in a singular perturbation problem of turning point type*, SIAM J. Math. Anal. **11**, (1980), pp. 1–22.

[32] C.M. Elliott, D.A. French, *Numerical studies of the Cahn–Hilliard equation for phase separation*, IMA J. Appl. Math. **38**, (1987), pp. 97–128.

[33] C.M. Elliott, S. Zheng, *On the Cahn–Hilliard equation*, Arch. Rat. Mech. Anal. **96**, (1986), pp. 339–357.

[34] P. Embid, J. Goodman, A. Majda, *Multiple steady states for 1-D transonic flow*, SIAM J. Sci. Statist. Comput. **5**, (1984), pp. 21–41.

[35] D.J. Eyre, *Coarsening dynamics for solutions of the Cahn-Hilliard equation in one dimension*, unpublished (1992).

[36] P.C. Fife, L. Hsiao, *The generation and propagation of internal layers*, J. Nonlinear Analysis, **12**, (1988), pp. 19–41.

[37] C.A.J. Fletcher, *Burgers equation: A model for all reasons*, Numerical Solutions of Partial Differential Equations, J. Noye, editor, North–Holland, Amsterdam, 1982, pp. 139–225.

[38] G. Fusco, *A geometric approach to the dynamics of* $u_t = \varepsilon^2 u_{xx} + f(u)$ *for small* ε , Proc. Stuttgart FRG, 1988, Problems Involving Change of Type, K. Kirchgässner(ed.), Lecture Notes in Physics, **359**.

[39] G. Fusco, J.K. Hale, *Slow motion manifolds, dormant instability and singular perturbations*, J. Dyn. Diff. Equat. **1**, (1989), pp. 75–94.

[40] A. Gierer, H. Meinhardt, *A theory of biological pattern formation*, Kybernetik, **12**, (1972), pp. 30–39.

[41] J. Goodman, *Stability of the Kuramoto-Sivashinsky and related systems*, Comm. Pure Appl. Math. **47**, (1994), pp. 293–306.

[42] D. Gottlieb, S.A. Orszag, *Numerical Analysis of Spectral Methods: Theory and Applications*, Society for Industrial and Applied Mathematics, Philadelphia, Pennsylvania, 1977.

[43] C. Grant, *Slow motion in one-dimensional Cahn-Morral systems*, SIAM J. Math. Anal. **26**, (1995), pp. 21–34.

[44] J. Grasman, B. Matkowsky, *A variational approach to singularly perturbed boundary value problems for ordinary and partial differential equations with turning points.*, SIAM J. Appl. Math. **32**, (1977), pp. 588–597.

[45] P. Grindrod, M. A. Lewis, J. D. Murray, *A geometrical approach to wave-type solutions of excitable reaction-diffusion systems*, Proc. Roy. Soc. London, Series A, Vol. 433, No. 1887, (1991), pp. 151-164.

[46] J.O. Gunton, M. San-Miguel, P.S. Sahni, *The dynamics of first-order phase transitions*, Phase Transitions and Critical Phenomena, vol.8, Academic Press, 1983, pp. 267–482.

[47] V.A. Gushchin, V.V. Shchennikov, *On a monotone difference scheme of the second order*, (in Russian), Z. Vycisl. Mat. i Mat. Fiz., **14**, (1974), pp. 789–792.

[48] A.C. Hindmarsh, *Odepack, a systematized collection of ode solvers*, in Scientific Computing, R.S. Stepleman, et al. (eds.), North-Holland, Amsterdam, 1983, pp. 55-64.

[49] E. Hopf, *The partial differential equation* $u_t + uu_x = \mu u_{xx}$, Comm. Pure Appl. Math. **3**, (1950), pp. 201–230.

[50] M.E. Hosea, L.F. Shampine, *Global extrapolation integrators for solving Sturm–Liouville problems by shooting*, IMA J. Numer. Anal. **13**, (1993), pp. 397–411.

[51] F.A. Howes, *Some stability results for advection-diffusion equations*, Stud. Appl. Math. **74**, (1986), pp. 35–53.

[52] F.A. Howes, *Asymptotic stability of viscous shock waves*, in Transactions of the Fourth Army Conference on Applied Mathematics and Computing, No. ARO Report 87-1, 1987.

[53] S. Hsu, T.P. Liu, *Nonlinear singular sturm-liouville problems and an application to transonic flow through a nozzle*, Comm. Pure Appl. Math. **43**, (1990), pp. 31-61.

[54] W. Huang and R.D. Russell, *A Moving Collocation Method for the Numerical Solution of Time Dependent Partial Differential Equations*, Appl. Numer. Math. **20**, (1996), pp. 101-116.

[55] A.M. Il'in, *A difference scheme for a differential equation with a small parameter affecting the highest derivative*, Mat. Zametki, **6**, (1969), pp. 237–248 (in Russian).

[56] D. Iron, *Metastability of the Gierer Meinhardt equations*, M.Sc. Thesis, Dept. of Math., Univ. of British Columbia, 1997.

[57] S. Jimbo, Y. Morita, *Stable solutions with zeros to the Ginzburg-Landau equation with Neumann boundary condition*, J. Diff. Equat. **128**, (1996), pp. 596–613.

[58] R.B. Kellogg, A. Tsan, *Analysis of some difference approximations for a singularly perturbed problem without turning points*, Math. Comp. **32**, (1978), pp. 1025–1039.

[59] B.L. Keyfitz, H.J. Kuiper, *Bifurcation resulting from changes in domain in a reaction-diffusion equation*, J. Diff. Equat. **47**, (1983), pp. 378–405.

[60] H.-O. Kreiss, *Resonance for singular perturbation problems*, SIAM J. Appl. Math. **41**, (1981), pp. 331–344.

[61] G. Kreiss, H. Kreiss, *Convergence to steady state of solutions of Burgers equation*, Appl. Numerical Math. **2**, (1986), pp. 161–179.

[62] J. Laforgue, *Using exponential asymptotics to study the metastability and supersensitivity of shock and transition layers*, Ph.D. Thesis, Dept. of Math., University of Washington, 1994.

[63] J. Laforgue, R.E. O'Malley, *Supersensitive boundary value problems*, In: Asymptotic and Numerical Methods for Partial Differential Equations with Critical Parameters, H.G. Kaper and M. Garbey, editors, kluwer, Dordrecht, (1993), pp. 215–223.

[64] J. Laforgue, R.E. O'Malley, *On the motion of viscous shocks and the super-sensitivity of their steady-state limits*, Method and Appl. of Anal. **1**, (1994), pp. 465–487.

[65] J. Laforgue, R.E. O'Malley, *Shock layer movement for Burgers equation*, SIAM J. Appl. Math. **55**, (1995), pp. 332–348.

[66] C. Lange, *On spurious solutions of singular perturbation problems*, Stud. Appl. Math. **68**, (1983), pp. 227–257.

[67] J.-Y. Lee, M.J. Ward, *On the asymptotic and numerical analysis of exponentially ill-conditioned singularly perturbed boundary value problems*, Studies in Applied Math. **94**, (1995), pp. 271–326.

[68] W. Lick, *Wave propagation in real gases*, Adv. in Appl. Mech. **10**, (1967), pp. 1–72.

[69] M.J. Lighthill, *Viscosity effects in sound waves of finite amplitude*, Surveys in Mechanics, G.K. Batchelor and R.M. Davies, editors, University Press, Cambridge, 1956, pp. 250–351.

[70] F.H. Lin, Q. Du, *Ginzburg-landau vortices: dynamics, pinning and hysteresis*, SIAM J. Math. Anal. **28**, (1997), pp. 1265-1293.

[71] T.P. Liu, *Nonlinear stability and instability of transonic flows through a nozzle*, Commun. Math. Phys. **83**, (1982), pp. 243–260.

[72] D. Ludwig, *Persistence of dynamical systems under random perturbations*, SIAM Review, **17**, (1975), pp. 605–640.

[73] H. Matano, *Asymptotic behavior and stability of solutions of semilinear diffusion equations*, Publ. RIMS, Kyoto Univ. **15**, (1979), pp. 401–454.

[74] B.J. Matkowsky, *On boundary layer problems exhibiting resonance*, SIAM Review 17, (1975), pp. 82–100.

[75] B.J. Matkowsky, Z. Schuss, *The exit problem for randomly perturbed dynamical systems*, SIAM J. Appl. Math. **33**, (1977), pp. 365–382.

[76] W. McKinney, *Ph.D. Thesis*, Dept. of Math., U. of Tennesse, Knoxville (1989).

[77] A.B. Mikishev, G.I. Sivashinsky, *Quasi–equilibrium in upward propagating flames*, Physics Letters A, **175**, (1993), pp. 409–414.

[78] A. Novick-Cohen, *On the viscous Cahn-Hilliard equation*, In: Material Instabilities in Continuum Mechanics and Related Mathematical Problems (J. Ball, editor), Oxford Sci. Publ., Oxford Univ. Press, New York, 1988, pp. 329–342.

[79] R.E. O'Malley, M.J. Ward, *Exponential asymptotics, boundary layer resonance, and dynamic metastability*, in: Mathematics is for Solving Problems, (P. Cook et al. editors), SIAM publication, pp. 189-203.

[80] R.L. Pego, *Front migration in the nonlinear Cahn-Hilliard equation*, Proc. Roy. Soc. London Ser. A **422**, (1989), no. 1863, pp. 261–278

[81] O. Penrose, P. Fife, *Thermodynamically consistent models of the phase-field type for the kinetics of phase transitions*, Physica D, **42**, (1990), pp. 44–62.

[82] M.H. Protter, H.F. Weinberger, *Maximum Principles in Differential Equations*, Prentice-Hall, Englewood Cliffs, 1967.

[83] S. Pruess, C. Fulton, *Mathematical software for Sturm-Liouville problems.* ACM Trans. on Math. Software **19**, (1993), pp. 360–376.

[84] J. Pryce, M. Marletta, *A new multi-purpose software package for Schrödinger and Sturm-Liouville computations.* Comput. Phys. Comm. **62**, (1991), pp. 42-54.

[85] Z. Rakib, G.I. Sivashinsky, *Instabilities in upward propagating flames*, Combust. Sci. and Tech. **54**, (1987), pp. 69–84.

[86] L.G. Reyna, M.J. Ward, *Resolving weak internal layer interactions for the Ginzburg-Landau equation*, European J. Appl. Math. **5**, (1994), pp. 495–523.

[87] L.G. Reyna, M.J. Ward, *On the exponentially slow motion of a viscous shock*, Comm. Pure Appl. Math. **48**, (1995), pp. 79–120.

[88] L.G. Reyna, M.J. Ward, *Metastable internal layer dynamics for the viscous Cahn-Hilliard equation*, Methods and Appl. of Anal. **2**, No. 3, (1995), pp. 285–306.

[89] L.G. Reyna, M.J. Ward, *On exponential ill-conditioning and internal layer behavior*, J. Num. Func. Analysis and Optimization Vol. **16**, No.4, (1995), pp. 475–500.

[90] H.-G. Roos, M. Stynes, L. Tobiska, *Numerical Methods for Singularly Perturbed Differential Equations —Convection-Diffusion and Flow Problems*, Springer series in Computational Mathematics, Springer-Verlag, Berlin, Heidelberg, New York, 1996.

[91] J. Rubinstein, P. Sternberg, *Nonlocal reaction-diffusion equations and nucleation*, IMA J. Appl. Math. **48**, (1992), pp. 249–264.

[92] Z. Schuss, *Singular perturbation methods in stochastic differential equations of mathematical physics*, SIAM J. Review, **22**, (1980), pp. 119–155.

[93] Z. Schuss, B.J. Matkowsky, *The exit problem: a new approach to diffusion across potential barriers*, SIAM J. Appl. Math. **35**, (1979), pp. 604–623.

[94] J.S. Scroggs, D.C. Sorensen, *An asymptotic induced numerical method for the convection-diffusion-reaction equation*, Lecture Notes in Pure and Appl. Math. **120**, (1989), pp. 81–114.

[95] G.I. Shishkin, *Methods of constructing grid approximations for singularly perturbed boundary value problems: condensing grid methods*, Russ. J. Numer. Anal. Math. Modeling, **7**, (1992), pp. 537–562.

[96] G.I. Sivashinsky, *Nonlinear analysis of hydrodynamic instability in laminar flames— I. Derivation of basic equations*, Acta Astronautica **4**, (1977), pp. 1177–1206.

[97] G.I. Sivashinsky, *Instabilities, pattern formation, and turbulence in flames*, Ann. Rev. Fluid Mech. **15**, (1983), pp. 179–199.

[98] X. Sun, *Numerical Solution of a Non-selfadjoint Singular Perturbation Problem on a Nonuniform Mesh.* Journal of Nanjing University, Mathematics Biquarterly, vol. **9**, (1992), pp. 208-216.

[99] X. Sun, *Numerical analysis of an exponentially ill-conditioned boundary value problem*, in preparation.

[100] X. Sun, M. Ward, *Metastability for a generalized Burgers equation with applications to propagating flame fronts*, European Journal of Applied Mathematics, accepted for publication in Jan., 1997.

[101] X. Sun, M. Ward, *Metastability and pinning for convection-diffusion-reaction equations in thin domains*, Methods and Applications of Analysis, submitted, 1998.

[102] X. Sun, M. Ward, *Metastable patterns and coarsening for various phase separation models*, in preparation.

[103] X. Sun, M. Ward, *Exponentially ill-conditioned convection-diffusion equations in multi-dimensional domains*, in preparation.

[104] X. Sun, Q. Wu, *A Coupled Difference Scheme for a Nonselfadjoint Singular Perturbation Problem.* Applied Mathematics and Mechanics, **13**, (1992), pp. 963-971.

[105] T. Tang, M.R. Trummer, *Boundary layer resolving pseudospectral methods for singular perturbation problems*, SIAM J. Sci. Comput. **17**, (1996), pp. 430–438.

[106] R. Vulanović, *On a numerical solution of a type of singularly perturbed boundary value problem by using a special discretization mesh*, Univ. u Novom Sadu Zb. Rad. Prirod.-Mat. Fak. Ser. Mat. **13**, (1983), pp. 187–201.

[107] R. Vulanović, *Some improvements of the nonequidistant Engquist-Osher scheme*, Appl. Math. Comput. **40** (1990), no. 2, part II, pp. 147–164.

[108] M.J. Ward, *Eliminating indeterminacy in singularly perturbed boundary value problems with translation invariant potentials*, Stud. Appl. Math. **87**, (1992), pp. 95–135.

[109] M.J. Ward, *Metastable patterns, layer collapses, and coarsening for a one–dimensional Ginzburg-Landau equation*, Stud. Appl. Math. **91**, (1994), pp. 51–93.

[110] M.J. Ward, *Dynamic metastability and singular perturbations*, in: Boundaries, Interfaces, and Transitions (Michel C. Delfour, ed.) (Banff 95), CRM Proc. Lecture Notes, vol. 13, AMS, Providence, R.I., (1998), pp. 237–263.

[111] M.J. Ward, *An asymptotic analysis of localized solutions for some reaction-diffusion models in multi-dimensional domains*, Studies in Appl. Math. **97**, pp. 103-126.

[112] M.J. Ward, *Metastable bubble solutions for the Allen-Cahn equation with mass conservation*, SIAM J. Appl. Math. **5**, (1996), pp. 1247–1279

[113] W. Wasow, *Linear Turning Point Theory*, Springer–Verlag, New York, (1984).

[114] M. Williams, *Another look at Ackerberg–O'Malley resonance*, SIAM J. Appl. Math. **41**, (1981), pp. 288–293.

Appendix A

Estimating the weight function ω

For $\varepsilon \to 0$, we now calculate the weight function $\omega(x)$, defined in (2.26), in both the outer and the boundary layer regions. In the outer region we use $\tilde{u}^\varepsilon = x - x_0 +$ t.s.t. to obtain

$$\omega(x) = \exp\left[-f(x-x_0)/\varepsilon\right](1 + \text{t.s.t.}) \; . \tag{A.1}$$

In the left boundary layer near $x = 0$ we first integrate (2.13a) to get

$$u_{l_0}'(y) \exp\left(-\int_0^y f'[-x_0 + u_{l_0}(z)]\, dz\right) = u_{l_0}'(0)\,, \qquad \text{for} \quad 0 < y < \infty\,. \tag{A.2}$$

Then, we re-write $\omega(x)$ exactly as

$$\omega(x) = \omega(0) \exp\left(-\varepsilon^{-1} \int_0^x f'[\tilde{u}^\varepsilon(z)]\, dz\right) \; . \tag{A.3}$$

Let $y = x/\varepsilon$ and use $\tilde{u}^\varepsilon(x) \sim -x_0 + u_{l_0}(\varepsilon^{-1}x)$ in (A.3) to get

$$\omega(\varepsilon y) \sim \omega(0) \exp\left(-\int_0^y f'[-x_0 + u_{l_0}(z)]\, dz\right) \; . \tag{A.4}$$

Comparing (A.4) with (A.2) we observe that $\omega(\varepsilon y) u_{l_0}'(y)$ is asymptotically constant and, hence,

$$\omega(\varepsilon y) u_{l_0}'(y) \sim \omega(0) u_{l_0}'(0) \tag{A.5}$$

To calculate $\omega(0)u_{l_0}'(0)$ we evaluate the left side of (A.5) as $y \to \infty$ using (A.1) and the decay behavior (2.13b) for u_{l_0}. This yields the key identity

$$\omega(0) u_{l_0}'(0) \sim -a_{l_0} \nu_l \exp\left(-f(-x_0)/\varepsilon\right) \; , \tag{A.6}$$

where a_{l_0} and ν_l are defined in (2.15).

A similar analysis, which we shall omit, can be done in the right boundary layer region near $x = 0$ to show that the product $\omega(1 - \varepsilon y)u'_{r_0}(y)$ is asymptotically constant in this region. The key identity, analogous to (A.6), is that

$$\omega(1 - \varepsilon y)u'_{r_0}(y) \sim \omega(1)u'_{r_0}(0) \sim a_{r_0}\nu_r \exp\left(-f(1 - x_0)/\varepsilon\right) , \tag{A.7}$$

where a_{r_0} and ν_r are defined in (2.19).

Appendix B

Derivation of Equation (3.1)

Consider the Ginzburg-Landau equation (3.3) with Neumann boundary condition in a cylinder of revolution with cross-section described in dimensional variables by $R = R_0 F\left(X/L\right)$ (see Figure 3.1):

$$U_t = D\left(U_{RR} + R^{-1}U_R + U_{XX}\right) + Q_0 Q(U)\,, \qquad \text{(B.1a)}$$

$$0 < X < L,\ \ 0 < R < R_0 F\left(X/L\right)\,,$$

$$(U_R, U_X)\cdot(1, -L^{-1}R_0 F'\left(X/L\right) = 0\,, \quad \text{on } R = R_0 F\left(X/L\right)\,, \qquad \text{(B.1b)}$$

$$U_X = 0\,, \qquad \text{on } X = 0, L\,. \qquad \text{(B.1c)}$$

Here D and Q_0 are positive constants and $Q(U)$ is described following (3.1). We assume that the cylinder is long and thin so that $R_0 \ll L$. In terms of the dimensionless variables $r = R_0^{-1}R,\ x = L^{-1}X$ and $\tau = DL^{-2}t$, (B.1) becomes

$$U_\tau = \delta^{-2}(U_{rr} + r^{-1}U_r) + U_{xx} + \bar{Q}Q(U)\,, \quad 0 < x < 1,\ \ 0 < r < F(x), \qquad \text{(B.2a)}$$

$$U_r - \delta^2 U_x F'(x) = 0\,, \quad \text{on } r = F(x) \qquad \text{(B.2b)}$$

$$U_x = 0\,, \qquad \text{on } x = 0, 1 \qquad \text{(B.2c)}$$

Here $\delta = R_0/L \ll 1$ and $\bar{Q} = D^{-1}Q_0 L^2$.

We now derive a partial differential equation that is valid for U in the limit $\delta \to 0$. We expand U away from the endpoints at $x = 0, 1$, as $U = U_0 + \delta^2 U_1 + \ldots$. Substituting this expansion into (B.2a) and (B.2b) and collecting powers of δ^2, we obtain

$$U_{0rr} + r^{-1}U_r = 0\,, \quad \text{in } 0 < r < F(x)\,; \qquad U_{0r} = 0\,, \quad \text{on } r = F(x)\,, \qquad \text{(B.3)}$$

and

$$U_{1rr} + r^{-1}U_{1r} = U_{0\tau} - \bar{Q}Q(U_0) - U_{0xx}\ , \quad \text{in } 0 < r < F(x)\,, \tag{B.4a}$$

$$U_{1r} = F'(x)U_{0x}\ , \qquad \text{on} \quad r = F(x)\,. \tag{B.4b}$$

The first equation gives $U_0 = U_0(x,t)$. To determine an evolution equation for U_0 we write (B.4a) as $(rU_{1r})_r = r(U_{0\tau} - \bar{Q}Q(U_0) - U_{0xx})$. Integrating this equation with respect to r from 0 to $F(x)$ and applying the boundary condition (B.4b) we get

$$U_{0\tau} = U_{0xx} + 2F^{-1}F'U_{0x} + \bar{Q}Q(U_0)\ . \tag{B.5}$$

Let A denote the cross-sectional area of the domain, so that $A = \pi F^2$. Then from (B.5) and (B.2c) we get the one-dimensional reaction-diffusion equation

$$U_{0\tau} = \frac{1}{A}(AU_{0x})_x + \bar{Q}Q(U_0)\ , \qquad 0 < x < 1\,, \quad t > 0\,, \tag{B.6a}$$

$$U_{0x}(0,\tau) = U_{0x}(1,\tau) = 0\ . \tag{B.6b}$$

To study the slow motion of internal layers under (B.6), we suppose $\bar{Q} \gg 1$ and so we write $\bar{Q} = \varepsilon^{-2}$ for some $\varepsilon \ll 1$. Then, setting $t = \varepsilon^{-2}\tau$, we find that (B.6) reduces to (3.1) when the cross sectional area $A = A(x,\varepsilon)$ is given by $A(x,\varepsilon) = 1 + \varepsilon^{\mu}g(x)e^{-\varepsilon^{-1}d}$.